PERMANENT MAGNET SYNCHRONOUS MOTOR DRIVE CONTROL SYSTEM BASED ON SILICON CARBIDE MOSFET FOR NEW ENERGY ELECTRIC VEHICLES

By

ZHANG CHI

Thesis Submitted to the School of Graduate Studies,
Universiti Putra Malaysia, in Fulfilment of the Requirements for the Degree of Doctor of Philosophy

December 2024

FK 2024 82

Abstract of thesis presented to the Senate of Universiti Putra Malaysia in fulfilment of the requirement for the degree of Doctor of Philosophy

PERMANENT MAGNET SYNCHRONOUS MOTOR DRIVE CONTROL SYSTEM BASED ON SILICON CARBIDE MOSFET FOR NEW ENERGY ELECTRIC VEHICLES

By

ZHANG CHI

December 2024

Chairman : Associate Professor Jasronita bt Jasni, PhD
Faculty : Engineering

The 21st century faces critical challenges, including fossil fuel dependence, climate change, and rising energy costs. In response, the transition to new energy electric vehicles (NEEVs) is accelerating, replacing internal combustion engine (ICE) vehicles to mitigate the energy crisis and reduce environmental pollution.

This research focuses on developing a permanent magnet synchronous motor (PMSM) drive control system based on silicon carbide metal-oxide-semiconductor field-effect transistor (SiC MOSFET) technology for NEEVs. A comprehensive analysis of key subsystems—electrification levels, power battery packs, and electrical propulsion systems—is conducted. To address switching challenges in SiC MOSFET, an active discontinuous current source gate driver (CSGD) circuit is proposed. Additionally, a three-phase interleaved parallel bidirectional Buck–Boost (TPIPBi-Buck–Boost) converter is

introduced to regulate energy flow between the power battery pack and the motor drive inverter within the high-voltage DC bus, enabling efficient bidirectional voltage conversion. As advancements in NEEVs production demand higher precision, speed, and stability in PMSM systems, a finite control set model predictive torque control (FCS-MPTC) strategy with voltage vector expansion is recommended. However, integrating SiC MOSFET and PMSM poses challenges related to electromagnetic interference (EMI), affecting compliance with electromagnetic compatibility (EMC) standards. To address this, system-level conducted EMI equivalent circuit models are developed, covering key components such as the power battery pack, busbar cables, three-phase inverter, and PMSM.

Simulation and experimental validation confirm the proposed innovations. The novel CSGD circuit maintains a constant gate drive current during both turn-on and turn-off periods, enhancing SiC MOSFET switching performance. The TPIPBi-Buck–Boost converter efficiently manages energy flow—supporting motor performance during acceleration and recovering excess energy during braking. The optimized FCS-MPTC method eliminates weight coefficients from traditional MPTC, improving system performance. Additionally, the system-level EMI equivalent circuit model aids in predicting conducted EMI noise during the design phase, providing a robust theoretical foundation for accurate modeling and effective EMI suppression.

Keywords: Electromagnetic Compatibility, SiC MOSFET, Permanent Magnet Synchronous Motor, Electric Vehicles, Motor Drive Control.

SDG: GOAL 7: Affordable and Clean Energy, GOAL 9: Industry, Innovation and Infrastructure.

Abstrak tesis yang dikemukakan kepada Senat Universiti Putra Malaysia
sebagai memenuhi keperluan untuk ijazah Doktor Falsafah

SISTEM KAWALAN PEMACU MOTOR SYNCHRONOUS MAGNET KEKAL BERASASKAN MOSFET SILIKON KARBIDA UNTUK KENDERAAN ELEKTRIK TENAGA BARU

Oleh

ZHANG CHI

Disember 2024

Pengerusi : Profesor Madya Jasronita bt Jasni, PhD
Fakulti : Engineering

Abad ke-21 menghadapi cabaran kritikal, termasuk pergantungan bahan api fosil, perubahan iklim dan peningkatan kos tenaga. Sebagai tindak balas, peralihan kepada kenderaan elektrik tenaga baharu (NEEVs) semakin pantas, menggantikan kenderaan enjin pembakaran dalaman (ICE) untuk mengurangkan krisis tenaga dan mengurangkan pencemaran alam sekitar.

Penyelidikan ini memberi tumpuan kepada membangunkan sistem kawalan pemacu motor segerak magnet kekal (PMSM) berasaskan teknologi transistor kesan medan logam karbida logam-oksida-semikonduktor (SiC MOSFET) untuk NEEVs. Analisis komprehensif subsistem utama—paras elektrifikasi, pek bateri kuasa dan sistem pendorong elektrik—dijalankan. Untuk menangani cabaran penukaran dalam SiC MOSFET, litar pemacu pintu sumber arus terputus aktif (CSGD) dicadangkan. Selain itu, penukar Buck–Boost (TPIPBi-Buck–Boost) selari berjalin tiga fasa diperkenalkan untuk

mengawal aliran tenaga antara pek bateri kuasa dan penyongsang pemacu motor dalam bas DC voltan tinggi, membolehkan penukaran voltan dua arah yang cekap. Memandangkan kemajuan dalam pengeluaran NEEVs menuntut ketepatan, kelajuan dan kestabilan yang lebih tinggi dalam sistem PMSM, strategi kawalan tork ramalan model set kawalan terhingga (FCS-MPTC) dengan pengembangan vektor voltan adalah disyorkan. Walau bagaimanapun, penyepaduan SiC MOSFET dan PMSM menimbulkan cabaran yang berkaitan dengan gangguan elektromagnet (EMI), menjejaskan pematuhan piawaian keserasian elektromagnet (EMC). Untuk menangani perkara ini, model litar setara EMI yang dikendalikan peringkat sistem dibangunkan, meliputi komponen utama seperti pek bateri kuasa, kabel bar bas, penyongsang tiga fasa dan PMSM.

Simulasi dan pengesahan eksperimen mengesahkan inovasi yang dicadangkan. Litar CSGD novel mengekalkan arus pemacu get yang berterusan semasa kedua-dua tempoh hidup dan mati, meningkatkan prestasi pensuisan SiC MOSFET. Penukar TPIPBi-Buck–Boost dengan cekap mengurus aliran tenaga—menyokong prestasi motor semasa pecutan dan memulihkan tenaga berlebihan semasa brek. Kaedah FCS-MPTC yang dioptimumkan menghapuskan pekali berat daripada MPTC tradisional, meningkatkan prestasi sistem. Selain itu, model litar setara EMI peringkat sistem membantu dalam meramalkan hingar EMI yang dijalankan semasa fasa reka bentuk, menyediakan asas teori yang teguh untuk pemodelan yang tepat dan penindasan EMI yang berkesan.

Kata Kunci: Keserasian Elektromagnet, SiC MOSFET, Motor Segerak Magnet Kekal, Kenderaan Elektrik, Kawalan Pandu Motor.

SDG: MATLAMAT 7: Tenaga Mampu Milik dan Bersih, MATLAMAT 9: Industri, Inovasi dan Infrastruktur.

ACKNOWLEDGEMENTS

I extend my sincere appreciation to my committee members for their invaluable time and constructive academic guidance, significantly contributing to the achievement of my objectives. Special gratitude is owed to the chairperson of my supervisory committee for their provision of professional guidance, academic expertise, personal encouragement, and inspiration throughout this endeavor.

My gratitude extends to my supervisor, Prof. Dr. Jasronita bt. Jasni, for her consistent support and guidance during this research. Her empowering assistance, insightful advice, and supervision have been instrumental in maintaining my focus, motivation, and determination. I deeply appreciate her patient guidance and encouragement during the challenges encountered on this journey. Her unwavering commitment and invaluable mentorship have greatly contributed to the successful completion of this thesis. I express my utmost gratitude to my supervisory committee, led by Prof. Dr. Mohd. Amran bt. Mohd. Radzi, for his exceptional guidance, steadfast support, and dedicated time ensuring the successful completion of my project.

Gratitude is also extended to the entire academic and non-academic staff at Universiti Putra Malaysia, particularly within the Faculty of Engineering and the Graduate Research Office. Additionally, I am thankful to my fellow PhD students and friends at Universiti Putra Malaysia for their academic support and camaraderie throughout this challenging journey. Their support and encouragement have been invaluable, recognizing that the PhD journey is not solitary.

Sincerest thanks.

This thesis was submitted to the Senate of Universiti Putra Malaysia and has been accepted as fulfilment of the requirement for the degree of Doctor of Philosophy. The members of the Supervisory Committee were as follows:

Jasronita bt Jasni, PhD
Associate Professor
Faculty of Engineering
Universiti Putra Malaysia
(Chairman)

Mohd Amran bin Mohd Radzi, PhD
Professor
Faculty of Engineering
Universiti Putra Malaysia
(Member)

ZALILAH MOHD SHARIFF, PhD
Professor and Dean
School of Graduate Studies
Universiti Putra Malaysia

Date: 17 April 2025

TABLE OF CONTENTS

LIST OF TABLES

LIST OF FIGURES

LIST OF ABBREVIATIONS

A/D	analog to digital
AC	alternate current
ADC	Analog-to-Digital Converter
Al-Ni-Co	aluminum-nickel-cobalt
ANSI	American National Standards Institute
APM	auxiliary power module
AT	asymmetric groove gate
BEVs	battery electric vehicles
Bi-DC–DC	bidirectional DC–DC
CAN	controller area network
CC-CV	Constant Current and Constant Voltage
CCM	continuous conduction mode
CCS-MPC	continuous control set model predictive control
Ce	cerium
CENELEC	Comite Europeen de Normalisation Electrotechnique
CGD	conventional gate driver
CHB	cascaded H-bridge
CISPR	International Special Committee on Radio Interference
Clark	static coordinate transformation
CM	common-mode
CO_2	carbon dioxide
CSFPWM	constant switching frequency PWM
CSGD	current source gate driver
DBC	dead-beat control

DC	direct current
DCR	direct current resistance
DIBBC	dual input Buck–Boost converter
DM	differential-mode
DSP	Digital Signal Processor
DT	double groove
DTC	direct torque control
DUT	device under test
DV-MPC	double vector MPC
Dy	dysprosium
ECU	electronic control unit
EMC	electromagnetic compatibility
EMI	electromagnetic interference
EMS	energy management system
Er	erbium
ESL	equivalent series inductance
ESR	equivalent series resistance
ESS	energy storage system
ETSI	European Telecommunication Standards Institute
Eu	europium
EVs	electrical vehicles
FC	flying capacitor
FCC	Federal Communications Commission
FCEVs	fuel cell electric vehicles
FCH-NEEVs	Fuel Cell Hybrid NEEVs
FC-NEEVs	fuel cell new energy electric vehicles

FC-NEEVs	Fuel Cell NEEVs
FCS-MPC	finite control set model predictive control
FCS-MPCC	finite control set model predictive current control
FCS-MPTC	finite control set model predictive torque control
FH-NEEVs	full hybrid NEEVs
FOC	field-oriented control
FPGA	Field Programmable Gate Array
GaN	gallium nitride
Gd	gadolinium
GHG	greenhouse gas
HEVs	hybrid electric vehicles
HEVs	hybrid electric vehicles
H-NEEVs	hybrid new energy electric vehicles
Ho	holmium
IC	integrated circuit
ICC-CV	Improved Constant Current and Constant Voltage
ICE	internal-combustion engine
IEC	International Electrotechnical Commission
IEEE	Institute of Electrical and Electronics Engineers
IPMSM	interior permanent magnet synchronous motor
IPOS	input-parallel output-series
ISO	international Standardization Organization
La	lanthanum
LISN	line impedance stability network
Lu	lutetium
MCC-CV	Multistage Constant Current and Constant Voltage

mH-NEEVs	micro-hybrid NEEVs
MH-NEEVs	mild-hybrid NEEVs
MIL-STD	Military Standards
MOSFET	metal oxide semiconductor field effect transistor
MPC	model predictive control
MPCC	model predictive current control
MPSFPWM	model prediction switching frequency PWM
MPTC	model predictive torque control
MS-MPC	multi-step MPC
Nd	neodymium
Nd-Fe-B	neodymium-iron-boron
NEEVs	new energy electric vehicles
NPC	neutral point clamped
OBC	on-board charger
OBCM	on-board charge module
Park	synchronous rotating coordinate transformation
PCB	printed circuit board
PD	partial discharge
PDC	power distribution center
PEVs	photo-voltaic electric vehicles
PG	planar-gate
PHEVs	plug-in hybrid electric vehicles
PH-NEEVs	plug-in hybrid NEEVs
Pm	promethium
PMSM	permanent magnet synchronous motor
P-NEEVs	pure new energy electric vehicles

P-NEEVs	pure NEEVs
Pr	praseodymium
PSFPWM	period switching frequency PWM
PV	photovoltaic
PWM	pulse width modulation
RE-NEEVs	range extender NEEVs
RGD	resonant gate driver
RSFPWM	random switching frequency PWM
RTCA	Radio Technical Commission for Aeronautics
Sc	scandium
SiC	silicon carbide
Sm	samarium
Sm-Co	samarium-cobalt
SOA	safe operating area
SPMSM	surface permanent magnet synchronous motor
SS-MPC	Single step MPC
SV-MPC	Single Vector MPC
SVPWM	space vector pulse width modulation
Tb	terbium
TG	trench-gate
Tm	thulium
TPIPBi-Buck–Boost	three-phase interleaved parallel bidirectional Buck–Boost
TV-MPC	three vector MPC
VCU	vehicle control unit
VFD	variable frequency drive
VSFPWM	variable switching frequency PWM

VSGD	voltage source gate driver
WBG	wide band gap
WPT	wireless power transfer
y	yttrium
Yb	ytterbium

CHAPTER 1

INTRODUCTION

1.1 Introduction

This chapter presents the introduction of the study. It covers the background of the study that includes permanent magnet synchronous motor drive control system for new energy electric vehicles (NEEVs) based on silicon carbide (SiC) metal oxide semiconductor field effect transistors (MOSFET). The discussion continues with the statement of the problem. aim and objectives of the study, the scope of the study, the significance of the study, contribution and outlines of the research. This chapter ends with the conclusion of chapter one.

1.2 Research Background

The significant challenges in the 21st century is fossil fuels dependence, climate change and incremental energy cost [1-5]. Looming environmental problems and growing concerns about the global energy crisis have prompted people to make new opportunities and technologies to meet the higher demand for clean and sustainable energy systems [6-9]. Electrification of transportation system is a promising way to green transportation system and reduce climate change [10-12]. In recent years, NEEVs have become very popular in the transportation industry and are likely to replace the internal-combustion engine (ICE) to protect the environment from pollution [13,14]. Environmental protection, fossil fuel shortage, and climate change have promoted the research and development of cleaner and sustainable transportation.

For the automotive industry, harmful gas emissions are one of the main pollutants, the vehicles electrification has become the best solution for automotive market that is adapted to environmental regulations [15]. The electrification of transportation systems is a crucial initiative aimed at mitigating the impacts of global climate change and preserving the environment. NEEVs use green renewable energy to grow environmental conservation [16,17]. Due to the use of the most efficient subsystems NEEVs gives better performance than ICE. With green climate and energy saving features, NEEVs are bringing additional advantages relative to traditional renewable energies. NEEVs are more popular because of its merits like economy, less maintenance required, reliability, regenerative breaking, less noise, high performance, and renewable charging energy.

Generally, the NEEVs can be divided into the following types according to the power source: battery electric vehicles (BEVs), hybrid electric vehicles (HEVs), photo-voltaic electric vehicles (PEVs), fuel cell electric vehicles (FCEVs) and plug-in hybrid electric vehicles (PHEVs) [18].

Faced with the increasingly serious energy crisis and environmental pollution problems, traditional internal combustion engine vehicles are receiving more and more resistance, which has rapidly promoted the development of new energy electric vehicles. Permanent magnet synchronous motor (PMSM) because of their simple structure, light weight, small size, and high-power density, the silicon carbide (SiC) metal oxide semiconductor field effect transistor (MOSFET) as a representative of third-generation wide band gap (WBG) materials are widely used in NEEVs [19-21]. With the continuous advancement of production technology, the requirements of accuracy, rapidity, and stability in PMSM drive control system have gradually increased.

1.3 Problem Statement

Although gasoline and diesel fuel processing continue to dominate as the primary energy sources [22], characterized by inefficient heat engines and significant levels of pollutants such as dust [23], carbon dioxide, noise and other pollution [24], posing a serious threat to the survival of the human environment [25-27]. Fortunately, NEEVs have emerged as crucial components in the establishment of sustainable green energy systems [28,29].

To contribute to a comprehensive investigation, this research needs to have thoroughly surveyed the state-of-the-art subsystems and their components for NEEVs applications. The main features, advantages and disadvantages, new technological breakthroughs, challenges, and opportunities are delved deeply.

In large power applications of the NEEVs, the requirements for power switching devices, rectifier diodes, filter capacitors, energy storage inductors, and other parts (active and passive) are becoming much higher than before, which leads to difficulties in circuit design. Therefore, in order to effectively increase power and reduce voltage and current stress of electronic components, enabling convert voltage bidirectionally and regulate electrical energy flow, need to improve the traditional bidirectional Buck–Boost converter.

The use of a three-phase two-level voltage source converter with space vector pulse width modulation (SVPWM) to drive PMSM based on SiC MOSFET power devices. To mitigate voltage and current overshoot and oscillation during SiC MOSFET turn on and off process, a gate drive circuit is able to exhibit significantly increased effective gate current need be proposed.

With the continuous developments of NEEVs, the requirements of accuracy, rapidity, and stability in permanent magnet synchronous motor systems have gradually increased. Therefore, compared to conventional vector control (field-oriented control, FOC), direct torque control (DTC) and constant pressure frequency ratio, an advances control strategy should be made to enhance both the dynamic and the steady-state performance of the PMSM control drive system.

The SiC MOSFET and PMSM can significantly improve efficiency, performance, and power density, making high speed motor controllers possible. However, more serious electromagnetic interference (EMI) noise has also emerged, which makes the motor drive control system difficult to achieve electromagnetic compatibility (EMC) standards. Therefore, it is necessary to conduct mechanism modeling, simulation and experimental verification to study conducted EMI of the motor drive control system.

1.4 Aim and Objectives

The aim of this research is to develop a high switching frequency drive control system of PMSM for NEEVs with SiC MOSFET. In order to achieve these aims, four specific research objectives are specifically formulated as follows:

a. To ensure consistent gate drive current during the turn-on and turn-off cycles of SiC MOSFET in motor drive control system

b. To regulate and manage the flow of electrical energy between the battery pack and the motor drive inverter in the high-voltage direct current bus, where voltage conversion from two directions is necessary.

c. Developing an advanced control strategy for PMSM that prioritizes accuracy, speed, and stability.

d. The integration of SiC MOSFET and PMSM presents challenges in ensuring the motor drive control system meets EMC standards.

These research objectives aim to provide timely insights and a valuable reference regarding the impact of high switching frequency on motor drive control systems.

1.5 Scope of the Study

The research inspects the present status, latest deployment, and future prospects in the implementation of NEEVs and introduces the subsystems and their components: electrification transportation degrees, power battery pack, electrical propulsion system.

The research proposes a novel active gate drive circuit, which ensures a constant gate drive current throughout the turn on and off process of SiC MOSFET for motor drive control system in NEEVs.

In this research, the multi-phase interleaving Buck–Boost converter is proposed and analyzed for new energy electric vehicles applications, which is the core factor of electrical energy flow regulation and management between the power battery pack and motor drive inverter within the high voltage direct current bus and convert the voltage from two directions.

Among many advanced control technologies, this study proposes an optimized model predictive torque control strategy based on multi voltage vector expansion to enhance the performance of the motor drive control system.

In this study, a system level conducted EMI equivalent circuit models about motor drive control system based on PMSM with SiC MOSFET for NEEVs has been proposed to research and analysis conducted EMI noise. On this foundation, in order to meet EMC standards, the principles of suppression and optimization EMI noise are discussed.

1.6 Significance of the Study

In recent years, the consumption of conventional energy sources has increased dramatically. Due to rising fuel costs and environmental concerns, governments around the world have formulated a series of policies such as strategic planning, technology research and market supervision to promote the process of low carbon automobiles and support the development of the NEEVs industry, the time for the final withdrawal of petrol-powered vehicles from the market is approaching. The NEEVs have important economic and social value in alleviating the energy crisis, saving energy, reducing emissions, and promoting the development and upgrade of the clean energy industry.

Meanwhile, The SiC MOSFET and PMSM as advantageous components have been adopted in NEEVs. The motor drive control system of PMSM based on SiC MOSFET achieves higher efficiency and higher power density by having higher switching speeds (reduced switching losses and cooling requirement) and higher switching frequencies (smaller filters).

It is worth mentioning that most researchers in the field could use this research as a more valuable and informative source to provide some knowledge references and possible thoughts for the future development of NEEVs.

1.7 Contribution of the Study

This research reviews the present subsystem configurations, methodologies, advancements, and prospects for NEEVs, focusing on their key technologies and characteristics. It presents the market classification based on transport electrification degrees and evaluates the power battery pack, including chemical secondary batteries and both traditional and advanced charging technologies. The electrical propulsion system, encompassing electromotor drives and control strategies, is also explored in detail.

This research introduces a novel discontinuous current source gate drive (CSGD) that maintains a constant gate drive current throughout the on and off periods for motor drive control in NEEVs. This approach simplifies the design, reduces costs, offering both theoretical and practical benefits for high-frequency SiC MOSFET operations.

To enhance power efficiency and reduce voltage and current stress on electronic components, a three-phase interleaved parallel bidirectional Buck–Boost (TPIPBi-Buck–Boost) converter is analyzed and designed. It regulates electrical energy flow between the power battery pack and motor drive inverter within the high-voltage DC bus, converting voltage bidirectionally.

Among advanced control technologies, this research proposes an optimized model predictive torque control strategy based on voltage vector expansion. This strategy constructs a reference stator flux linkage vector using the analytical relationships between electromagnetic torque, flux linkage amplitude, and rotor flux linkage, optimizing the duty cycle for adjacent voltage vectors and the zero vector.

The research employs a system-level equivalent circuit model, including components such as the power battery pack, busbar cable, three-phase inverter, and PMSM. This model establishes EMI sources and propagation paths, simulating control strategies and operating conditions effectively. This research contributes significantly to predicting conducted EMI noise early in the design phase, reducing the need for additional PCB updates. It provides a reliable theoretical foundation and methodology for accurate modeling and effective EMI suppression.

1.8 Outlines of the Study

This research is organized into five chapters according to thesis format, in which each chapter comprises of introduction, methodology, results and discussion, and conclusions. Brief explanation of each chapter has been discussed in the following section.

Chapter 1 is the introduction chapter. This chapter presents the study background, the problem of statement, aim and objectives, scopes and significance of the study, the contribution and outlines of the study.

Chapter 2 presents a detailed and comprehensive literature review concerning this study. The aim of Chapter 2 is to review the present subsystems configurations, technical methodologies, advancements, and prospects for NEEVs and have discussed in detail with their main technologies and characteristics. In this chapter, an extensive review related to SiC MOSFET, active gate driver, bidirectional Buck–Boost converter, PMSM, model predictive control, EMI are descried.

Chapter 3 portrays the detailed explanation on methodology. First, it introduces the active discontinuous CSGD for SiC MOSFET, three phase interleaved parallel bidirectional Buck–Boost converter, three voltage vector duty cycle optimization strategy of PMSM based on finite set model predictive control, shaft voltage and bearing current of PMSM, EMI harm and protection about motor drive control system.

Chapter 4 focuses on explaining the result analysis and discussions for this work are also discussed according to the sections in the previous chapter.

Finally, Chapter 5 is the last chapter, and it summarizes the work done in the overall study. This chapter also includes future work directions and some suggestions for further development.

CHAPTER 2

LITERATURE REVIEW

2.1 Introduction

Chapter 2 sets out the main concepts, knowledge base, and literature related to the technologies, advancements and prospects of NEEVs. A detailed previous review that covers the topic of this study, beginning with the SiC MOSFET, active gate driver, bidirectional Buck–Boost converter, PMSM, MPC, EMI and EMC followed by technical methodologies for the motor drive control system, as well as a summary of the chapter's content.

2.2 New Energy Electric Vehicles

In recent decades, the greenhouse gas (GHG) emissions, fossil fuel pollution, air contamination in contemporary society, environmental protection and alternative green energy have been receiving attentions for scientific community, particularly among developed countries, and international organizations [30–39]. These factors have converged to develop more efficient, sustainable, and renewable energy systems [40–44]. Transportation is one of the largest undeniable contributors to carbon dioxide (CO_2) emissions, accounting for approximately 24% of total emissions as depicted in Figure 2.1.

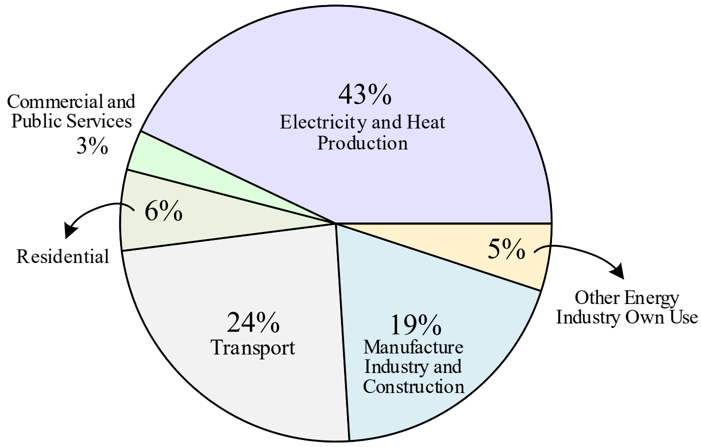

Figure 2.1 : Sector-Wise CO2 Emissions from Transportation Combustion

Environmental protection, fossil fuel shortage, and climate change have fostered research and development into cleaner and sustainable transportation. In particular, the automotive industry, which is a significant contributor to harmful gas emissions, the vehicles electrification has become the best solution for automotive market that is adapted to environmental regulations [45–47]. The adoption of transportation electrification systems has emerged as an essential measure to mitigate the effects of global climate change and protect the environment. The NEEVs are more popular due to superior features, including economy, less maintenance requirements, reliability, regenerative braking, less noise pollution, high performance, and renewable charging energy [48–58].

The NEEVs uses green renewable energy to grow environmental conservation. Due to the use of the most efficient subsystems NEEVs gives better performance than ICE. With green climate and energy saving features, NEEVs are bringing additional advantages relative to traditional renewable energies [59–66].

2.2.1 Electrification Transportation Degrees

Due to fossil fuels pressure and increased carbon dioxide emissions, the NEEVs are gradually reducing their dependence on fossil fuels and reducing greenhouse gas emissions. The NEEVs could be categorized according to their different electrification degrees in Figure 2.2: micro-hybrid NEEVs(mH-NEEVs), mild-hybrid NEEVs (MH-NEEVs), full hybrid NEEVs (FH-NEEVs), plug-in hybrid NEEVs (PH-NEEVs), range extender NEEVs (RE-NEEVs), and pure NEEVs (P-NEEVs) [67–70].

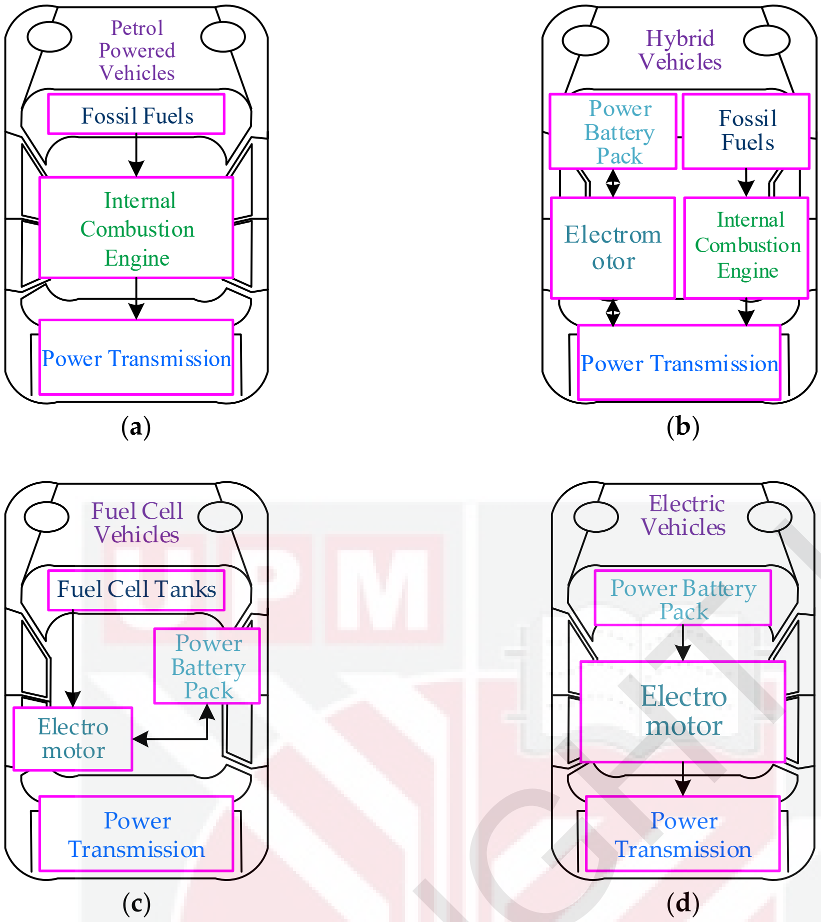

Figure 2.2 : Transportation Electrification Development: (a) Petrol Powered Vehicles; (b) Hybrid Vehicles; (c) Fuel Cell Vehicles; (d) Electric Vehicles

2.2.1.1 Hybrid New Energy Electric Vehicles (H-NEEVs)

The H-NEEVs, characterized by ICE and power battery pack, are commonly referred to as dual-power vehicles. In urban traffic, the NEEVs often start and stop repeatedly. However, H-NEEVs, which charge power battery pack to enable city driving, have emerged as a cost-effective solution [71].

The primary mechanism utilized by H-NEEVs to reduce energy costs is through the use of a power battery pack. The propulsion system consists of a series of components, with either a power battery pack or ICE drives the wheels. The vehicles controllers receive information about electric motor and generator, while electrical components receive electric motor torque and determine the charging and discharging status of power battery pack. When the driver steps on the brake pedal, the generator starts charging the power battery pack and can also obtain electrical energy from power battery pack via electromotor, generators, and power electronics converters. The power distributor is the central control unit of H-NEEVs, directing the operations of the ICE, generator, and electromotor, which function in series or in parallel, as illustrated in Figure 2.3 [72].

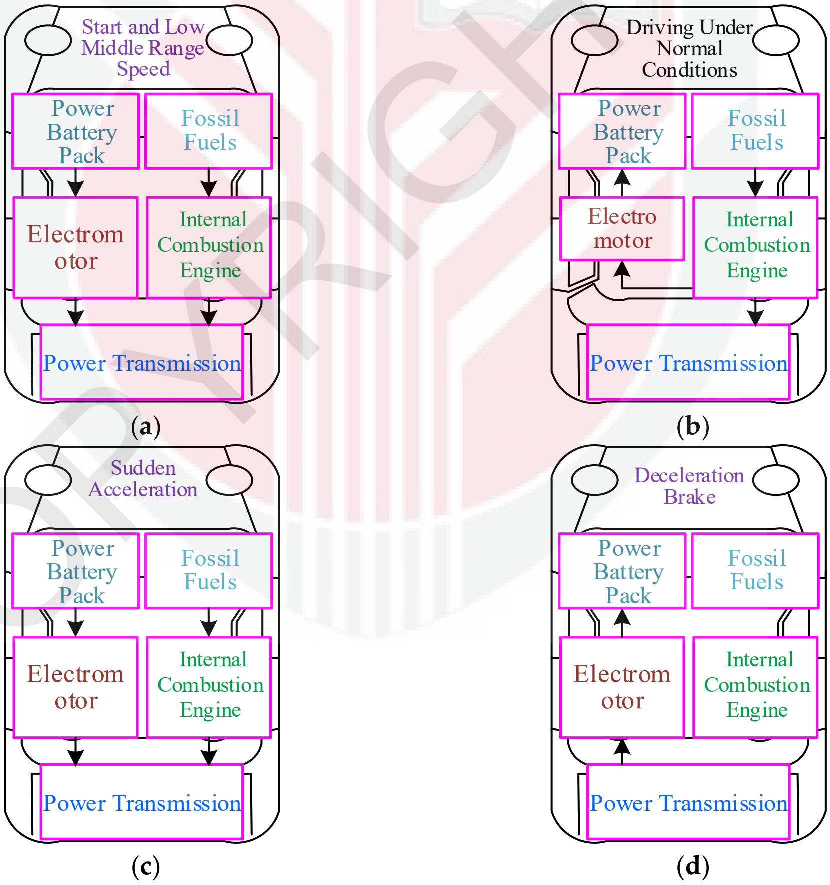

Figure 2.3 : H-NEEVs Operation Modes: (a) Start and Low to Mid-Range Speed; (b) Driving under Normal Conditions; (c) Sudden Acceleration; (d) Deceleration/Brake

2.2.1.2 Fuel Cell New Energy Electric Vehicles (FC-NEEVs)

FC-NEEVs exhaust are zero-emission vehicles that generate no pollutants during operation. Figure 2.4 shows that the FC-NEEVs can be categorized into two types based on their transport configuration: FC-NEEVs and FCH-NEEVs. The FC-NEEVs are well-suited for uniform power demands and low speeds, such as in buses, trolleys, and forklifts for high-speed transmission and additional energy storage systems. The power battery pack can be charged and discharged based on the FC-NEEVs' energy consumption and electric power requirements. [73–77].

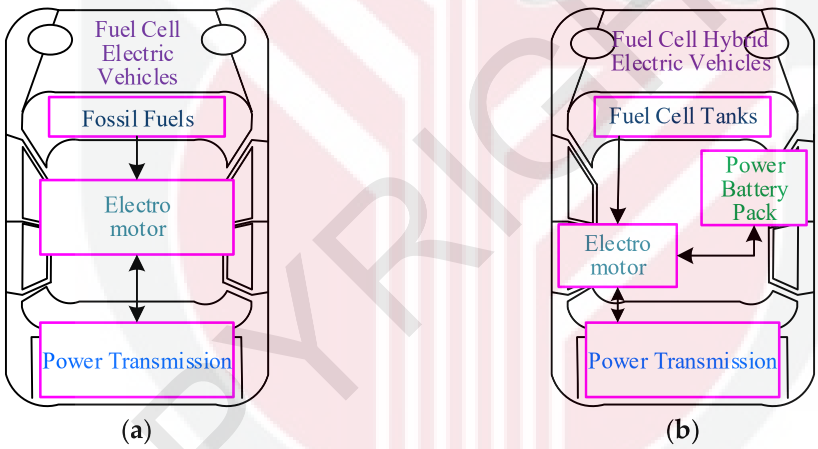

Figure 2.4 : FC-NEEVs Powertrain Configurations: (a) Fuel Cell Electric Vehicles; (b) Fuel Cell Hybrid Electric Vehicles

2.2.1.3 Pure New Energy Electric Vehicles (P-NEEVs)

In light of the numerous potential advantages offered by NEEVs, the experts and professors turn series parallel H-NEEVs into P-NEEVs. Moreover, the state of charge and discharge for the power battery pack can be anticipated by analyzing real-time driving data, such as road slope, vehicle weight, and wind resistance. In P-NEEVs, only a single power battery pack is employed to drive the electromotors [78,79]. As depicted in Figure 2.5, the P-NEEVs represent a more suitable solution for fighting global warming and urban driving than H-NEEVs.

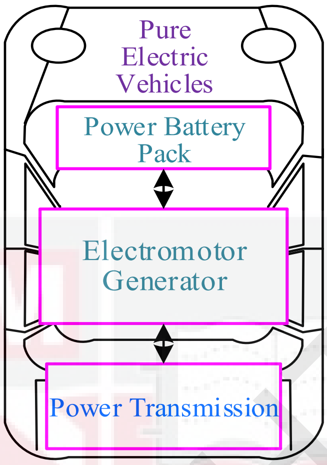

Figure 2.5 : P-NEEVs Work Principles

It is widely known that some typical NEEVs manufacturers are: America Tesla, Japan Toyota, Germany Mercedes-Benz, China BYD, Geely, AITO, Leading Ideal, NIO and Xpeng. Their main advantages are as follows:

a. Zero exhaust emissions;

b. No fossil fuels (coal and oil) are required;

c. Easy charging at home;

d. Start and stop quickly and smoothly;

e. Low overall operating costs

2.2.1.4 Vehicles Propulsion System

The propulsion system of NEEVs, defined as a set of components that work together and provide electromotor torque, are divided into four subsystems in Figure 2.6 [80–86]:

a. Power subsystem: ICE, energy management system (EMS), alternate current AC/DC rectifier and direct current DC/DC chopper;

b. Transmission torque subsystem: transmission shaft, clutch, differential, transfer box and drive shaft;

c. Energy subsystem: power battery pack, direct current DC/DC chopper, auxiliary power module (APM), power distribution center (PDC), on-board charge module (OBCM);

d. Thermal subsystem: radiator, electric water pump, cooling fan, heater, compressor.

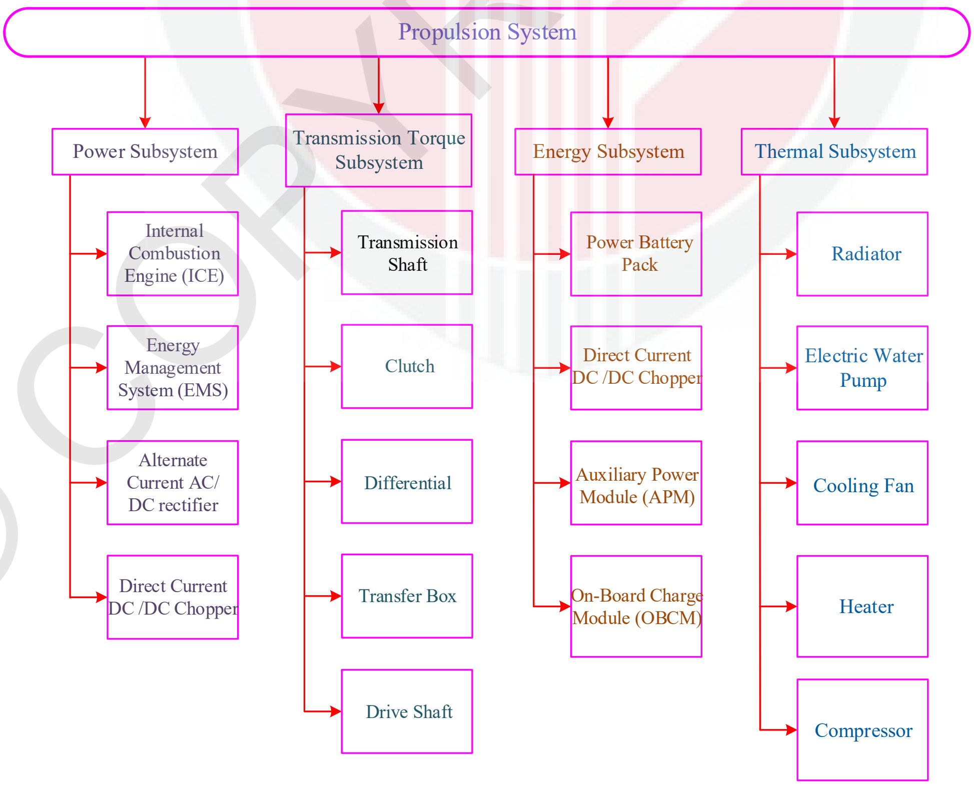

Figure 2.6 : Vehicles Propulsion System Organization Chart

2.2.2 Power Battery Pack

Over the past few years, the quantity of slow and rapid chargers has significantly increased in worldwide. Nevertheless, due to technical, economic and policy obstacles, high cost, short lifecycle, reliability, limited driving range, lengthy charging time and inadequate infrastructure all pose significant challenges to the continued advancement of power battery pack technology for NEEVs [87–90].

2.2.2.1 Conception and Basic Principle

Electric energy is stored and discharged chemically within the power battery pack as illustrated in Figure 2.7. There are two types of batteries: the primary battery is those that only deliver electrical energy during discharge; the secondary battery (charging and discharging) provides electrical energy in whole lifecycle. Therefore, the NEEVs always use secondary battery. In a secondary battery, the conversion of electrical energy to chemical energy (charging time) and chemical energy to electrical energy (discharging time) is achieved through electronic supply (oxidation) and electronic acceptance (reduction). The process is called an oxidation-reduction reaction at the positive and negative poles [91–98]. In power battery pack, one or more batteries are accumulated in series or in to achieve the desired voltage or current.

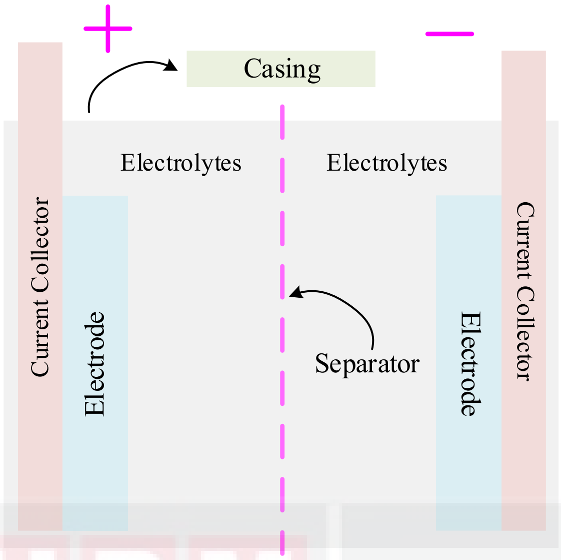

Figure 2.7 : Groundwork Design of Electrochemical Secondary Battery

The performance and reliability of power battery pack for NEEVs are strongly influenced by the specific properties of the electrodes and electrolytes:

a. The electrodes are where the electrochemical reactions take place during power battery pack operation. The specific properties of the electrodes, such as their capacity, power output, and cycle life, are determined by a number of factors, including the active materials, the electrode architecture, and the manufacturing process. For example, increasing the surface area of the electrodes can enlarge their capacity and power output, but also increases the risk of electrode degradation and failure.

b. The choice of electrolytes also plays a critical role in power battery pack performance and reliability. Electrolytes must provide great ionic conductivity between the electrodes, high chemical stability, and low flammability. Various types of electrolytes, such as liquid, polymer, and solid-state, have been developed to meet these requirements. For example, the solid-state electrolytes can provide high energy density and power density, safety, and long cycle life, but may have lower ionic conductivity than liquid or polymer electrolytes.

Therefore, selecting the appropriate combination of electrodes and electrolytes is crucial in designing high performance and high availability power battery pack for NEEVs. This requires a deep understanding of the electrochemical behavior of different materials, as well as the practical constraints of manufacturing and assembly.

By combining electrodes and electrolytes with specific properties allow the manufacture of power battery pack for a wider range of uses. For NEEVs, the energy storage system with high electrical energy, superior power density, capacity and extended lifecycle are necessary. The reliability of power battery pack relies heavily on the length of time throughout which electrical energy can be charged and discharged. Due to unique material and design constraints, the characteristics of power battery pack may vary across different manufacturers.

2.2.2.2 Chemical Secondary Batteries

The cost and lifecycle of different types of power battery packs for NEEVs can vary greatly depending on the type of batteries, including lead-acid, nickel-based, zinc-silver, sodium-sulfur, lithium-ion. Table 2.1 summarizes the performance parameters of different type chemical batteries commercially available the power battery pack of NEEVs.

Table 2.1 : Performance Parameters of Different Type Chemical Batteries

Battery type	Specific Energy (Wh/kg)	Energy Density (W/kg)	Power Density (W/kg)	Energy Efficiency (%)	Life Cycle (80% DOD)
VRLA	30~50	60~100	200~400	70~90	2000~4500
Ni-Cd	40~50	80~100	150~350	60~70	2000~3000
Ni-MH	50~70	100~140	150~300	50~80	500~3000
$Zn\text{-}Br_2$	65~75	60~70	90~130	68~76	300
$Zn\text{-}Cr_2$	65	90	60	NULL	200
Na-S	100	150	120	80	2500~4500
ZEBRA	86	149	150	80	2500~3000
LiAl-FeS	130	220	240	80	<1000
$LiAl\text{-}FeS_2$	180	350	400	NULL	<1000
Li-Polymer	155	200~250	315	70	<1200
Li-ion	120~140	240~280	200~300	70~80	1500~4500

For NEEVs market, the demand for lithium-ion battery is increasing. Generally, lithium oxide is used as a positive pole with a layered structure, while graphite carbon as a negative pole [99–109]. The different types of lithium-ion batteries are as follows:

a. Lithium-Cobalt Oxide: The lithium-cobalt oxide battery is commonly used in laptops that do not require discharge rates. It can provide high specific energy of 175-240Wh/kg, but its thermal stability is very poor.

b. Lithium Manganese Oxide: The lithium manganese oxide battery is made from inexpensive electrode materials, and these cell units are thought to be used as power battery pack due to the specific energy of between 100-150Wh/kg.

c. Lithium Nickel Manganese Cobalt Oxide: The lithium nickel manganese cobalt oxide battery provides the characteristics for power battery pack with a specific energy between 100 and 150Wh/kg, with the highest specific power range when the electrolytes temperature exceeds 300C.

d. Lithium Nickel Cobalt Aluminum Oxide: The maximum specific energy of lithium nickel cobalt aluminum oxide battery is related to relevant chemicals available on market. The similarities between lithium nickel cobalt aluminum oxide and lithium nickel manganese cobalt oxide battery are similar in that they have high specific power and long lifecycle. However, the battery has marginal safety and high cost.

e. Lithium Iron Phosphate Oxide: The lithium oxide iron phosphate battery is considered to have better electrical performance and low internal resistance. Its significant advantages are long cycle life, high rated current, good thermal stability, and safety.

It is widely known that lithium-ion batteries are currently the most popular choice due to their high energy density and long cycle life. They also have a faster charging time compared to other types of batteries. However, the lead-acid batteries are still commonly used in low-speed electric vehicles due to their low cost and simple maintenance. Nickel-cadmium and nickel-metal hydride batteries are also options, although they have a lower energy density and may require more frequent replacement.

When selecting a power battery pack for a particular NEEVs application, the factors such as energy density, power density, operating temperature range, charging time, safety and reliability should be considered. It is important to carefully evaluate the specific requirements such as cost, lifecycle, and performance to determine which type of power battery pack is the best choice.

2.2.2.3 Traditional and Advanced Charging Technologies

In order for NEEVs to be well-suited for long distance travel, their energy storage system must conform to high standards of high energy density, operate effectively across a wide temperature range, and accept repetitive high power repetitive charging and discharging from renewable braking operations. The rate of charging for power battery packs is directly linked to the internal direct current resistance (DCR) of each individual cell unit [110–113]. Ideally, A low DCR value is optimal for ensuring both high efficiency and low calorific output. However, frequent rapid charging and discharging of power battery pack in NEEVs can result in overheating.

For NEEVs, the charging technology adopted by power battery pack is conducive to rapid charging. Several are discussed below:

a. Constant Current and Constant Voltage (CC-CV) Mode

   The CC-CV mode is a traditional charging technology. The main idea is to start charging the power battery pack of NEEVs with a constant maximum current until it reaches a certain maximum voltage, and then continue charging with this voltage until the power battery is charged at a slower speed [114,115]. The CC-CV charging curve is given in Figure 2.8 (a).

b. Multistage Constant Current and Constant Voltage (MCC-CV) Mode

   According to Figure 2.8 (b), the MCC-CV mode is an improved CC-CV mode, which can enhance the charge acceptance rate of power battery pack. In CC-CV, only one constant current is used for charging. In the MCC-CV mode, many step currents are applied up to the threshold voltage [116,117].

c. Improved Constant Current and Constant Voltage (ICC-CV) Mode

   The above two charging modes are traditional and have limitations in their ability to transmit high power due to polarization effect [118–120]. The ICC-CV mode with negative pulses is seen from Figure 2.8 (c), using a variable pulse charging strategy, in which the optimal pulse charging frequency is continuously calculated and optimized so that the ions in the electrolyte are evenly distributed. In Figure 2.8 (d), the pulse charging characteristics increase the charge acceptance with variable frequency.

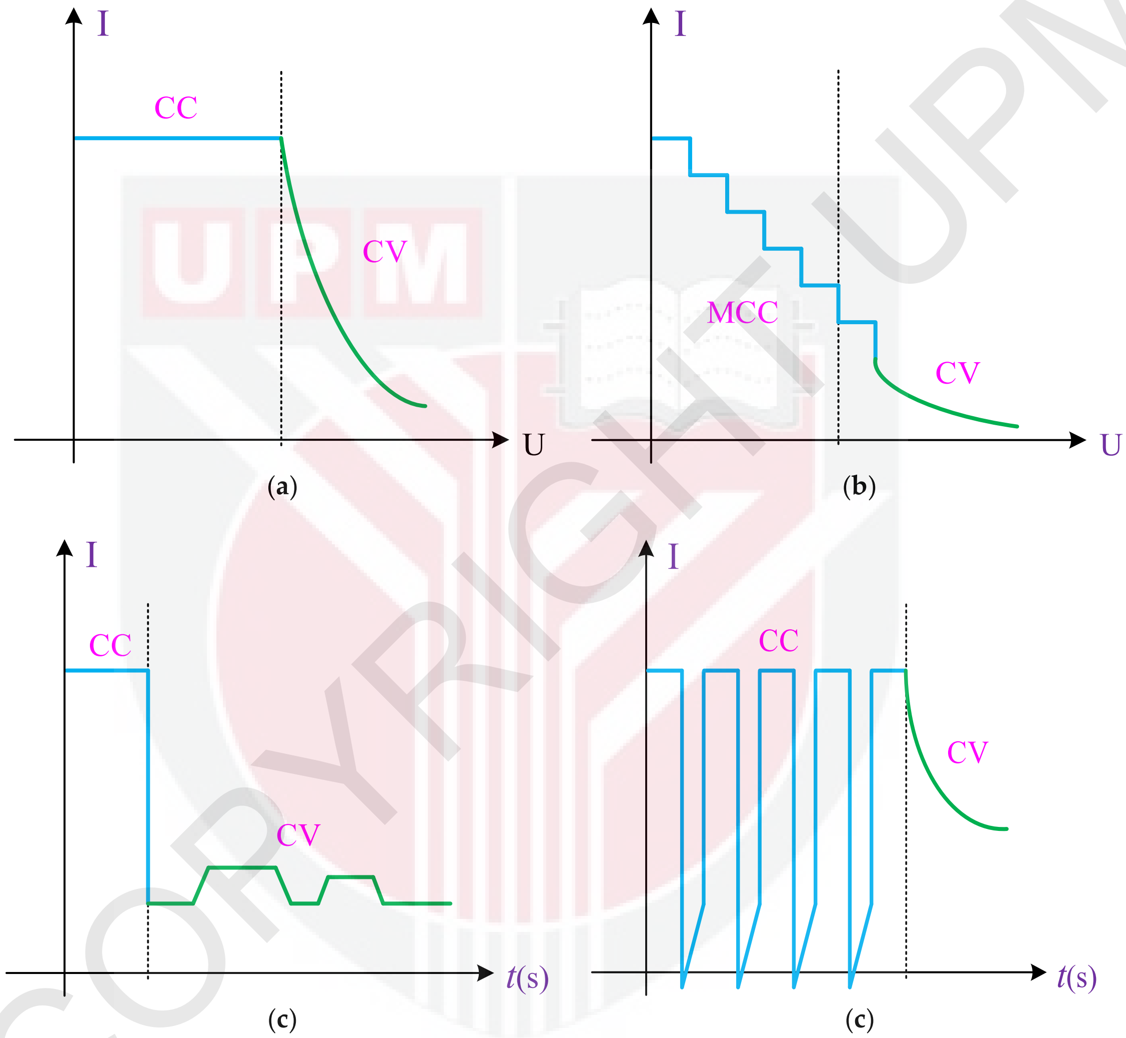

Figure 2.8 : Advanced Charging Modes Curve: (a) CC-CV; (b) MCC-CV; (c) ICC-CV with Negative Pulses; (d) ICC-CV with Variable Frequency

2.2.3 Electrical Propulsion System

Within an electrical propulsion system, the electromotor represents a goat component of energy storage system (ESS). The selection of the most suitable electromotor must account for its simple structure, low acoustic signature, lightweight construction, compact size, cost-effectiveness, and user-friendly electric drive control. Moreover, it is essential for the chosen electromotor to deliver constant power output across a wide range of speeds and offer ultra-fast torque response during emergency driving scenarios [121–125].

Figure 2.9 depicts the typical torque, power and speed characteristics required by electromotor drive and control system. The following points should also be considered for electrical propulsion system:

a. Power battery pack and charging mode;

b. Energy storage system and maximum voltage, current and power;

c. Electromotor and control techniques.

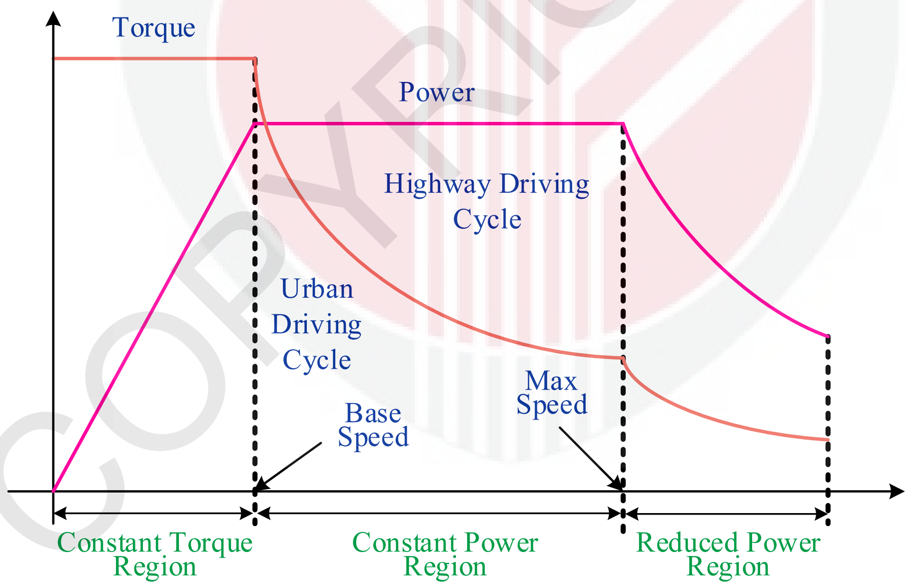

Figure 2.9 : Typical Speed, Torque, Power Characteristics of Electromotor Drive and Control System

2.2.3.1 Drive Electromotor Classification

The general classification of electromotor for NEEVs includes direct current motor (DCM), induction motor (IM), switched reluctance motor (SRM), permanent magnet synchronous motor (PMSM).

a. Direct Current Motor (DCM)

The direct current motor possesses commendable attributes such as favorable starting and speed regulating capabilities, robust overload capacity, and minimal electromagnetic interference. However, despite these benefits, the mechanical wear and sparking resulting from the sliding contact between the commutator and brush represent significant drawbacks that compromise the reliability and longevity of the DCM, ultimately leading to frequent failures, shortened lifecycle, and necessitating increased maintenance workload [126].

b. Induction Motor (IM)

The Induction motor have high torque at low speed, high efficiency at high speed and low torque [127]. Figure 2.10 describes the electrical characteristics with speed variations.

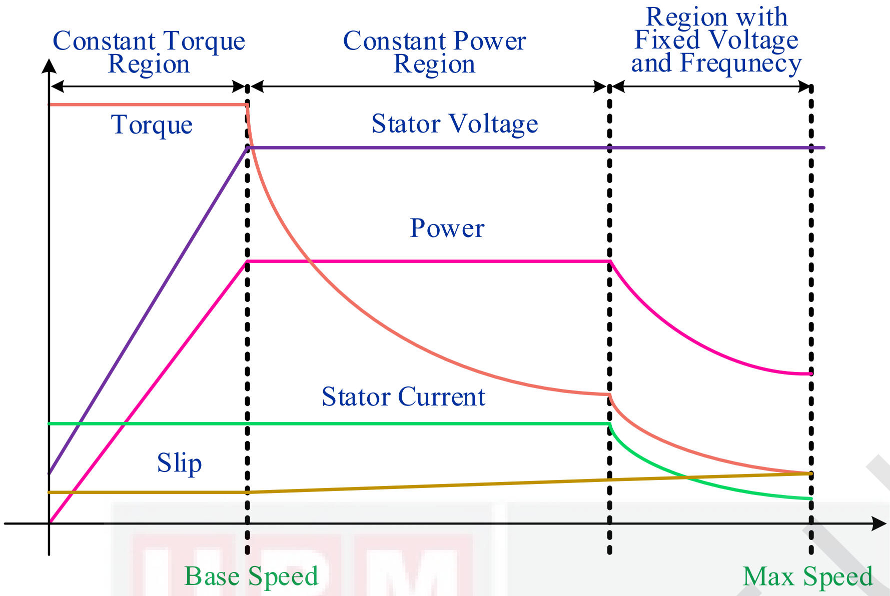

Figure 2.10 : IM Characteristics with Speed Variations

c. Switched Reluctance Motor (SRM)

SRM is a variable reluctance (double salient pole) motor [128]. Due to the limited torque density, it is only suitable for small and service NEEVs, such as golf carts, scooters, or delivery trucks. Some features are as follows:

a. No windings or permanent magnets on rotor, simple, robust, and reliable construction;

b. Without a rotor magnetic bridge, can inhibit mechanical failure, improve safety, and fault tolerance;

c. Both motor and generator modes occur during operation with electrical drive control;

d. Large Torque pulsation and electromagnetic vibration could cause noise pollution to drivers and passengers.

d. Permanent Magnet Synchronous Motor (PMSM)

Presently, the PMSM remains the most commonly utilized motor in NEEVs. Permanent magnets provide excitation source, simplifying the motor's structure, reduces processing and assembly expenses, eliminating commutators and brushes, and enhancing overall operational reliability [129]. Table 2.2 introduces four systems of permanent magnet material: Al-Ni-Co magnet, ferrite magnet, samarium cobalt magnet and neodymium magnet.

Table 2.2 : Physical Properties of Permanent Magnetic Material

Property	AlNiCo	Ferrite	Samarium Cobalt	Neodymium
Residual Induction Br/T	0.7~1.28	0.23~0.41	0.83~1.16	1.00~1.41
Coercitive Force H_C/(kA/m)	37~143	50~290	48~840	760~1030
Maximum Energy Product $(BH)_{max}/(KJ/m^3)$	10.7~71.6	8.35~31.8	130~240	220~366
Electric Resistivity $\rho/(\Omega cm)$	(50~75) $\times 10^{-6}$	10^6	(53~86) $\times 10^{-6}$	100×10^{-6}
Maximum Service Temperature T_{max}/℃	450~550	800	300~350	150
Density d(g/cm^3)	6.8~7.3	4.9	8.4	7.4

2.2.3.2 Electromotor Drive and Control Strategy

The electromotor drive and control strategies can make full use of the electromotor performance, which can be divided into: field-oriented control (FOC), direct torque control (DTC), and model predictive control (MPC) [130–132]. The similarities and differences among them are shown in Table 2.3.

Table 2.3 : Comparison of Electromotor Drive and Control Strategies

Aspect	Field Oriented Control (FOC)	Direct Torque Control (DTC)	Model Predictive Control (MPC)
Structure	One speed PI and two current PI	One speed PI and two hysteresis controllers	One speed PI and predictive controller
	Space vector and modulation required	Switching table required	Cost function required
Merit	Fixed switching frequency	Low switching frequency	Lowest switching frequency
	Low computation burden	Low computation burden	Easy to tune
	Low THD	Fast transient response	Fastest transient response
	Low torque ripple	East to tune	Large current control bandwidth
Weakness	High switching frequency	High THD	High computation burden
	All parameters required except resistance	All parameters required except resistance	Sensitive to parameters
	Modulation required and difficult to tune	Small current control bandwidth	Low robustness
	Slow transient response	Normally combine with other strategies	Sensitive to small-inductance motors
	Small current control bandwidth		
NEEVs	Existing applied in NEEVs	Widely applied in high-power NEEVs	Future trend for direct-drive propulsion system
	Low noise		

2.3 SiC MOSFET

As a representative of the third-generation wide band gap semiconductor material, SiC is the most advanced semiconductor materials all over the world for high temperature, high power, high frequency and high radiation applications, with superior performance such as high frequency, high voltage resistance, high temperature resistance, and strong radiation resistance [133–136]. SiC exhibits significant potential for application in various fields such as NEEVs, photovoltaics, wind power, 5G base stations, and high-speed railways. The swift growth of sub-markets, including automotive electric drive systems, high-voltage fast charging piles, consumer electronic adapters, data centers, and communication base station power supplies, persistently fuels the market demand for SiC MOSFET.

In recent decades, the remarkable progress of SiC technology has prompted major semiconductor manufacturers to augment production techniques and expand manufacturing capabilities [137]. The conventional planar-gate (PG) cell, illustrated in Figure 2.11(a), is widely employed for the majority of SiC MOSFET due to its mature process and simple structure [138,139]. However, advancements in SiC materials technology, encompassing etching, oxide deposition, and deep well implantation, have led to the emergence of groove trench-gate (TG) SiC MOSFET, which offer superior channel carrier mobility and cell density compared to the PG structure [140]. Notably, Rohm and Infineon have introduced two TG products: the double groove (DT) and asymmetric groove gate (AT), depicted in Figure 2.11(b) and (c), respectively.

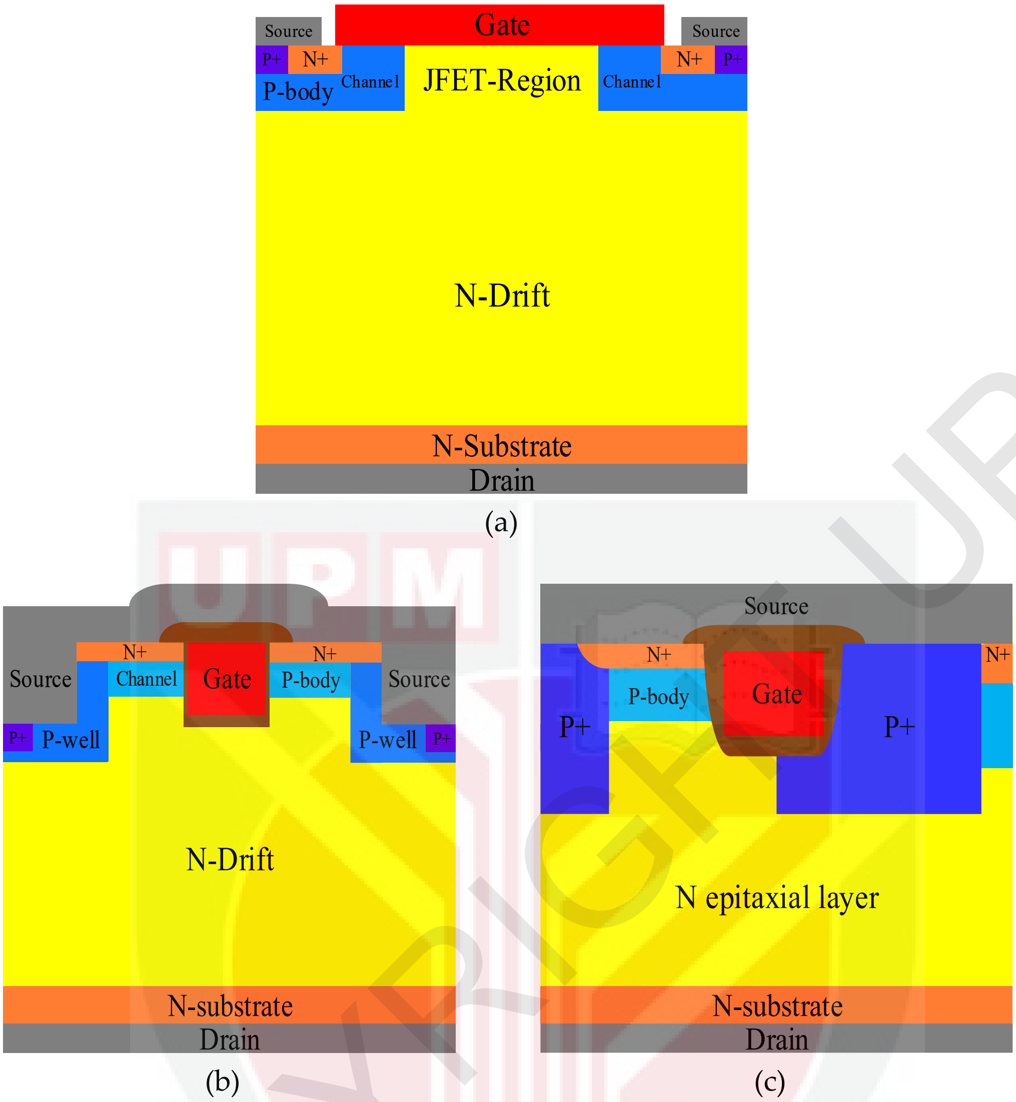

Figure 2.11 : SiC MOSFET Cell Structures (a) PG; (b) DT; (c) Asymmetric TG

SiC MOSFET are operated by manipulating charge within their physical structure, as depicted in Figure 2.12 [141,142]. During turn-on, the objective is to transfer sufficient charge from the power supply to the gate, thus establishing an inversion layer between the source and drain. This enables current flow through the channel. Conversely, during turn-off, the removal of gate charge causes the collapse of the inversion layer, preventing current from flowing through the channel. The movement of gate charge can be analyzed by considering the equivalent device capacitance, including the input capacitance $C_{iss} = C_{gs} + C_{gd}$, output capacitance $C_{oss} = C_{ds} + C_{gd}$, and reverse transfer capacitance $C_{rss} = C_{gd}$. These capacitances are determined by integrating the changes in gate-source voltage V_{GS}, drain current i_{DS}, and drain-source voltage V_{DS}.

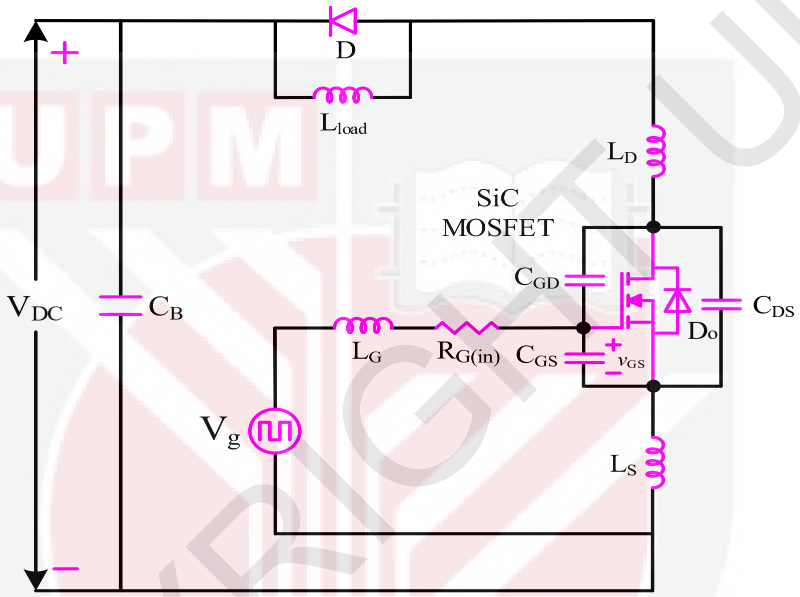

Figure 2.12 : Equivalent SiC MOSFET Circuit during Switching Transients

SiC MOSFET offers significant advantages throughout the energy conversion chain, spanning from power generation to transmission, distribution, energy storage, and consumption. In photovoltaic generation, their implementation results in system cost reduction, enhanced output power, and decreased system volume. For track traction applications, SiC MOSFET enables energy savings of up to 10% and improved system efficiency. Additionally, they contribute to loss reduction and increased energy density in battery systems used for energy storage. Notably, SiC MOSFET are in high demand in the market for NEEVs, especially in scenarios such as 800V automotive electric drive systems and high-pressure fast charging stations. In these cases, SiC MOSFET significantly reduces the size and weight of motor controllers while simultaneously improving energy conversion efficiency.

2.4 Active Gate Driver

The gate drive circuit serves as the crucial interface between the control circuit and power devices, which directly influences the switching characteristics of SiC MOSFET and overall system performance. For efficient and safe operation of SiC MOSFET, an excellent gate drive circuit is imperative. Different gate drive circuits used for the same SiC MOSFET can result in varying switching characteristics. The driving of SiC MOSFET switches raises two main concerns: power consumption and electrical stress. However, reducing power consumption and avoiding electrical stress present a theoretical contradiction, involving turn on loss (E_{on}) and current overshoot (I_{rr}), as well as turn off loss (E_{off}) and voltage overshoot (V_{ov}). As a result, balancing power consumption and electrical stress has become a crucial yet challenging aspect in gate drive technology research [143–145].

In order to answer the aforementioned questions, the conventional gate driver (CGD) has been utilized to regulate the impedance of the gate drive circuit. However, it falls short in meeting the requirements for SiC MOSFET switching frequency, converter efficiency, and system cost simultaneously. To more effectively address the issues of switching transient oscillations and overshoots in SiC MOSFET, researchers have proposed the adoption of an active gate driver (AGD). With the capability to dynamically adjust the current and voltage of the gate drive circuit, AGD proves to be a promising solution in enhancing and optimizing the switching process of SiC MOSFET [146-148].

Active gate driver (AGD) is generally classified as three types: voltage source gate driver (VSGD), current source gate driver (CSGD), and resonant gate driver (RGD) as shown in Figure 2.13. VSGD, commonly employed in power converters, features a straightforward structure and control mechanism where a voltage source, in series with a drive resistor (R_{on}/R_{off}), charges the gate capacitor. However, VSGD is not optimal for high-frequency operation of SiC MOSFET due to its relatively high intrinsic gate drive resistance. On the other hand, RGD utilizes an inductor, instead of a gate drive resistor, to eliminate driving losses [149,150]. Nonetheless, RGD has limitations in providing a substantial initial charging current, leading to the development of CSGD. CSGD is designed to deliver nearly constant current for rapid charging and discharging of the SiC MOSFET gate capacitor, thereby reducing switching losses and enabling the recovery of energy stored in the gate capacitor.

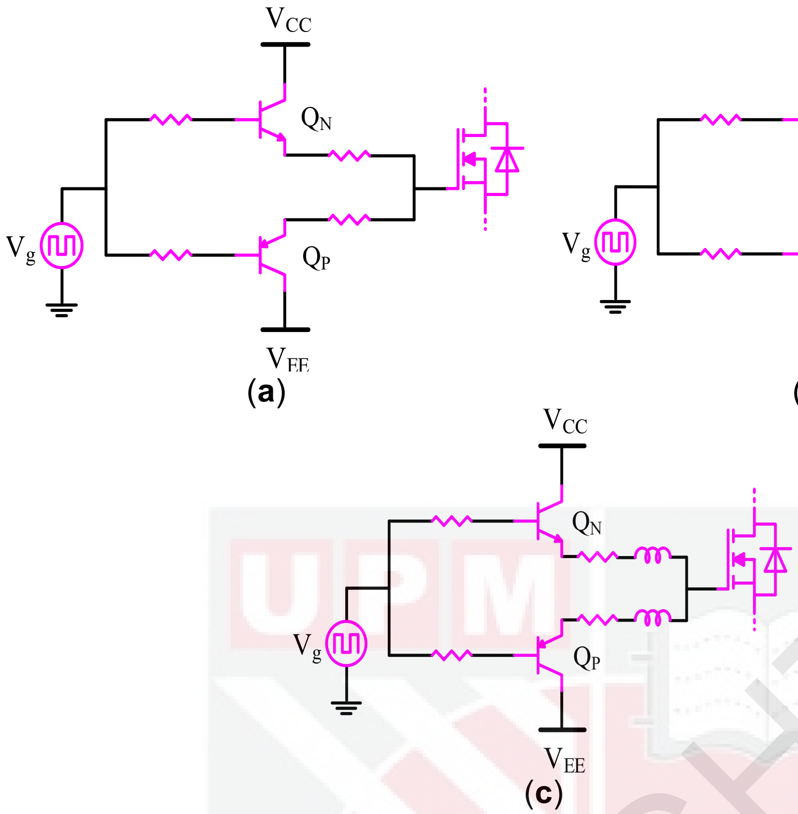

Figure 2.13 : Three Different Circuit Structures of Active Gate Drivers (a) VSGD; (b) CSGD; (c) RGD

In comparison to VSGD, CSGD appears to be a promising candidate for enhancing the switching performance of SiC MOSFET [151]. Figure 2.14 portrays the gate drive current of both VSGD and CSGD during turn-on and turn-off process. With an identical gate charge, CSGD delivers a constant current in the transient state, thereby mitigating the problem of high Miller voltage in SiC MOSFET and minimizing switching times.

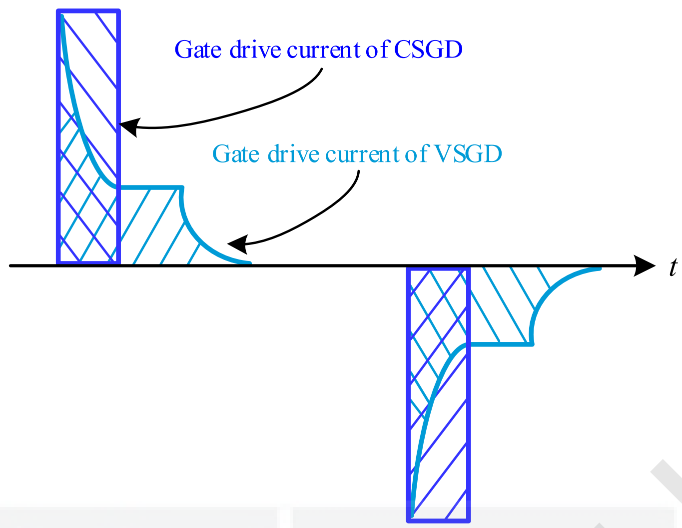

Figure 2.14 : Gate Drive Current of CSGD and VSGD

Currently, scholars and researchers have put forward their own proposals and suggestions regarding gate circuit topology, optimization design method, and controlling strategy for the CSGD of motor drive control systems [152-158]. In [152], the switching instantaneous characteristic of planar and trench SiC MOSFET is compared using both VSGD and CSGD. [153] discusses three gate drive circuit topologies - voltage source, continuous or discontinuous current source - from the perspective of power consumption and switching losses. The evaluation indicators for switching loss between CSGD and VSGD are studied in [154]. In [155], a half bridge of CSGD is proposed for hard switching of high-power electronic devices (such as SCT3022AL). [156] presents a CSGD for gallium nitride (GaN) used in high voltage applications such as electric vehicles and battery energy storage systems. A novel CSGD that addresses the voltage balance problem of series-connected GaN HEMT is introduced in [157]. Moreover, the utilization of CSGD to improve EMC performance has also been studied in [158].

However, considering parasitic parameters, the high frequency switching speed of SiC MOSFET can lead to high di/dt and dv/dt, resulting in overshoot and oscillatory in the voltage (V_{ds}) and current (I_{d}) waveforms, which also renders the motor drive control system utilizing SiC MOSFET vulnerable to EMI. In addition, if driving SiC MOSFET by lower switch frequency with additional buffer and absorption circuits can reduce the EMI effect but at the cost of increased switching losses and decreased overall system efficiency [159-161]. Specifically, during full load conditions in a power converter, both switching losses and conduction losses of SiC MOSFET become dominant, whereas under light or no-load conditions, driving losses represent a larger proportion of the total loss [162-164]. Therefore, it is imperative to adopt an optimized and balanced active gate driver between switching losses, conduction losses and driving losses.

2.5 Bidirectional Buck–Boost Converter

DC–DC converters can be categorized into two types: non-isolated topologies and isolated topologies with intermediate transformers, each having their own set of advantages and disadvantages [165-169]. Non-isolated topologies can be further subdivided into various configurations such as Buck, Boost, Buck–Boost, Zeta, Cuk, and SEPIC from Figure 2.15 [170,171].

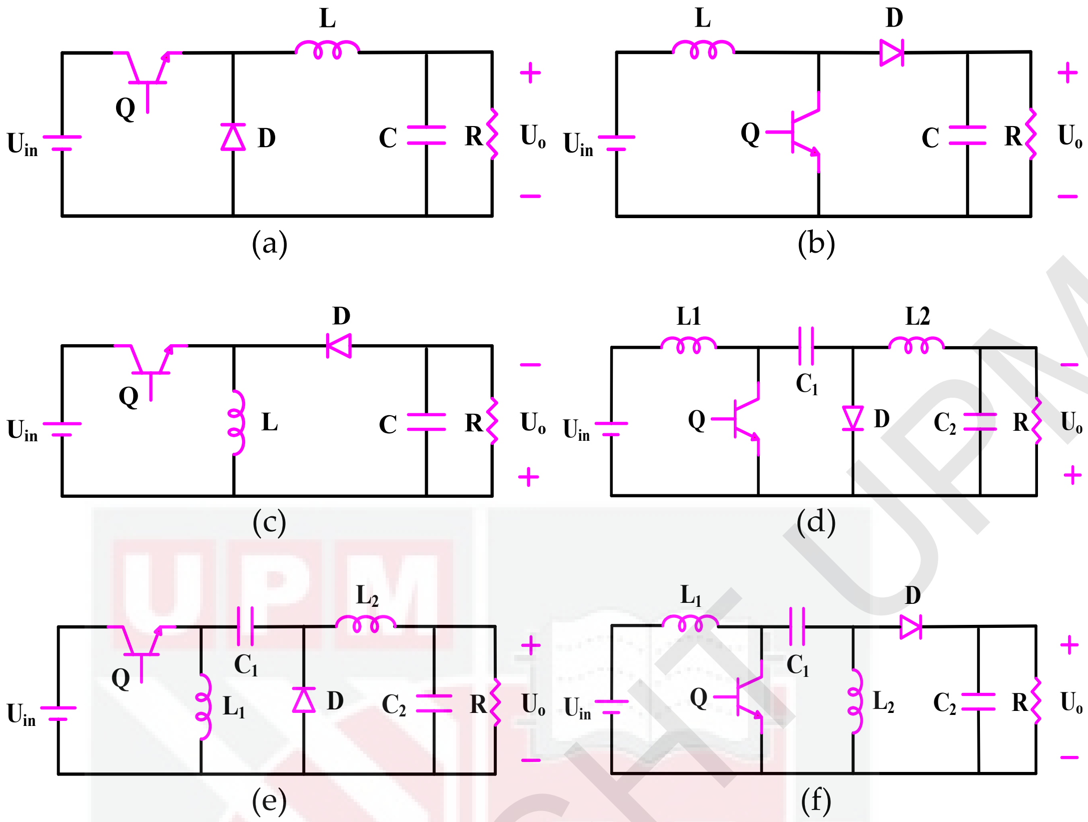

Figure 2.15 : Circuit Topology of Non-Isolated DC–DC Converter (a) Buck; (b) Boost; (c) Buck–Boost; (d) Cuk; (e) Zeta (f) SEPIC

As shown in Table 2.4, the interrelationships among six non-isolated DC–DC converters can be obtained [172-175]:

a. The Buck converter exclusively step-down voltage, whereas the Boost converter solely step-up voltage. Conversely, the Buck–Boost converter, Cuk converter, Zeta converter, and SEPIC converter possess the capability to both step up and step-down voltage.

b. The Buck converter, Boost converter, Zeta converter, and SEPIC converter exhibit the same polarity for both output and input voltage. In contrast, the Buck–Boost converter and Cuk converter have opposite polarities between their output and input voltages.

c. The power device voltage stress differs among various types of converters. For the Buck converter, it matches the input voltage. In the case of the Boost converter, it corresponds to the output voltage.

On the other hand, for the Buck–Boost converter, Cuk converter, Zeta converter, and SEPIC converter, the power device voltage stress is the combined value of both the input and output voltages.

d. The circuit topologies of the Buck converter, Boost converter, and Buck–Boost converter is characterized by their simplicity, employing only one inductor and one capacitor. In contrast, the Cuk converter, Zeta converter, and SEPIC converter exhibit relatively more complex circuit topologies, incorporating two inductors and two capacitors. It is worth noting that the middle capacitor in these converters experiences higher charging and discharging currents. Therefore, it is advisable to choose a capacitor with lower equivalent series resistance (ESR) for improved performance.

Table 2.4 : Comparisons among Six Non-Isolated DC–DC Converters

Circuit Topology	**Voltage Transfer Ratio**	**Output Voltage Polarity**	**Power Device Voltage Stress**	**Circuit Complexity**
Buck	$\frac{U_o}{U_{in}} = D_y$	positive	U_{in}	low
Boost	$\frac{U_o}{U_{in}} = \frac{1}{1 - D_y}$	positive	U_o	low
Buck–Boost	$\frac{U_o}{U_{in}} = \frac{D_y}{1 - D_y}$	negative	$U_{in} + U_o$	low
Cuk	$\frac{U_o}{U_{in}} = \frac{D_y}{1 - D_y}$	negative	$U_{in} + U_o$	high
Zeta	$\frac{U_o}{U_{in}} = \frac{D_y}{1 - D_y}$	positive	$U_{in} + U_o$	high
SEPIC	$\frac{U_o}{U_{in}} = \frac{D_y}{1 - D_y}$	positive	$U_{in} + U_o$	high

Figure 2.16 illustrates several isolated topologies, namely forward, flyback, half bridge, and full bridge configurations [176-178].

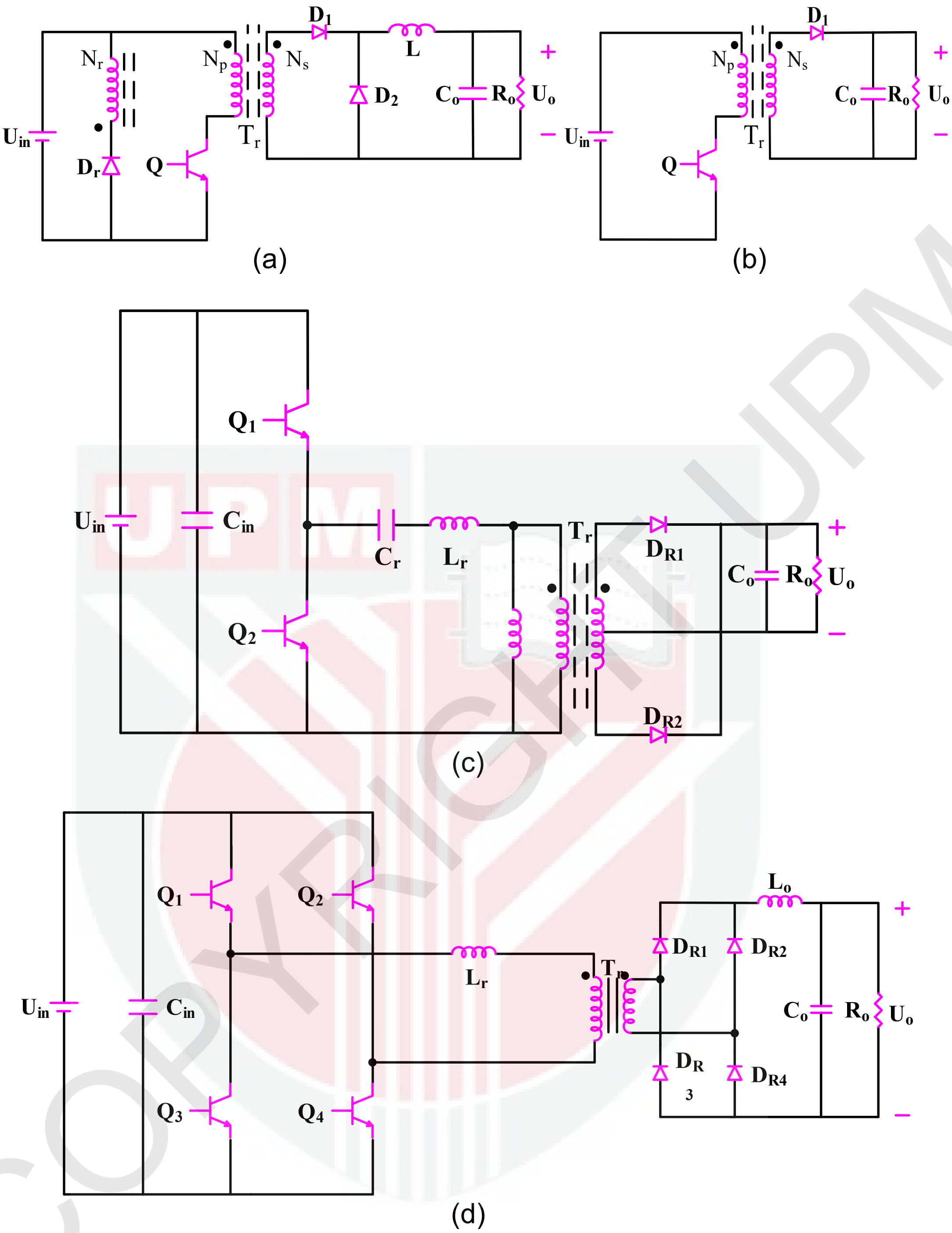

Figure 2.16 : Circuit Topology of Isolated DC–DC Converter (a) Forward; (b) Flyback; (c) Half Bridge; (d) Full Bridge

The NEEVs adopt a bidirectional DC–DC converter, which can reduce the power battery pack voltage level, improve the safety of the whole EVs, and cut costs of the battery management system (BMS); the voltage decoupling of the battery pack can input and output the most suitable and stable electrical energy according to the drive motor operating conditions, which is conducive to decrease the volume and weight of the drive motor. In addition, when the drive motor fails, the bidirectional DC–DC converter can also effectively block high voltage that may be generated from the direct current bus at the end of three phase inverter bridge, so as not to be directly introduced into the battery pack to cause potential risks, thereby improving the safety and reliability of the system [179-184].

Figure 2.17 depicts the circuit structure of the non-isolated bidirectional Buck–Boost converter, which serves as the fundamental topology for bidirectional DC-DC converters [185-188]. This topology comprises two switches, one inductor, and two capacitors.

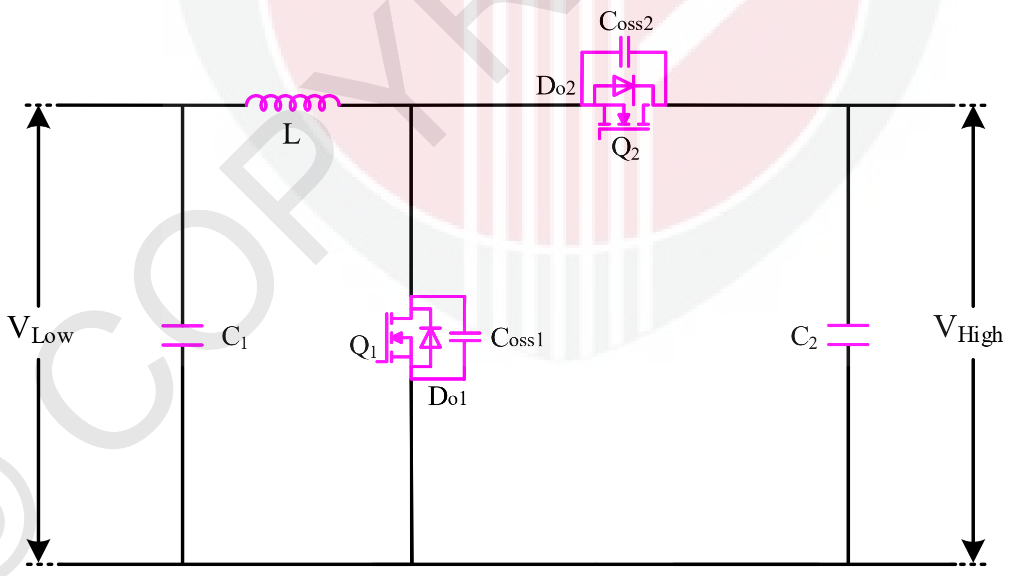

Figure 2.17 : Circuit Topology of Non-Isolated Bidirectional Buck–Boost Converter

Among the traditional bidirectional–DC/DC converter, the bidirectional Buck–Boost converter is the most widely used in NEEVs. To solve the problems, several new circuit topologies and control strategies have been introduced to improve the performance of the Buck–Boost converters for NEEVs, some excellent research on this topic have been conducted as shown in [189–195]. In [189], the working of Buck–Boost converter as a power factor correction controller applicable for battery charging in electric vehicles application, also satisfies the harmonic compliance of source current in accordance with the IEEE519 recommendations. A charger of a three-port structure [190] is realized with level-3 charging capability using a current source converter frontend together with an input filter, a polarity inversion module, and a differentially connected dual inverter drive. Additionally, due to the limited range of a single charge, charging NEEVs is one major barrier. Thus, this research [191] analyzed a dual input Buck–Boost converter (DIBBC) and proposed charging of battery pack by solar photovoltaic (PV) and dynamic wireless power transfer (WPT). In [192], a bidirectional multi-level diode-clamped Buck–Boost converter is proposed, and GaN HEMT switching devices are used to deal with both concerns about low efficiency and power density in the NEEVs application. A series of integrated equalizers based on joint Buck–Boost and switched-capacitor converters are proposed in [193] for balancing the voltages of series-connected battery packs. All these equalizers realize the any-cells-to-any-cells (AC2AC) equalization mode without increasing the count of MOSFETs and drivers. The work [194] explores the use of dual-carrier switching modulation schemes for the bidirectional Buck–Boost converters. The Buck–Boost scheme is utilized as the power converter topology to interface a storage system to a DC-link in electrical vehicles (EVs) and hybrid electric vehicles (HEVs). This research [195] proposes an input-parallel output-series (IPOS) connected bidirectional Buck–Boost converter is introduced that can dynamically vary the DC-link voltage of an electric vehicle power train.

2.6 Permanent Magnet Materials and Motor

In the 21st century's new stage of industrial development, achieving the seamless integration of manufacturing and modern science and technology is imperative. This integration aims to enhance innovation, interconnectedness, informatization, and intelligence in industrial development, thereby emphasizing the significance of high-end equipment manufacturing as a priority. Motor, serving as vital components for converting electrical energy into mechanical energy, hold extensive applications in the manufacturing industry and play a pivotal role in electromechanical energy conversion.

Motors can be macroscopically classified into alternating current (AC) motors and direct current (DC) motors based on their power supply types [196,197]. In the mid-20th century, DC motors were widely adopted in various industrial sectors due to their ease of speed regulation. However, the presence of commutators and brushes in DC motors posed maintenance challenges, resulting in poor reliability and impeding further development. Conversely, AC motors have increasingly attracted scholars' attention since the 1980s. Notably, unlike DC motors, AC motors do not necessitate complex structures such as commutators and brushes, and they are easy to manufacture, cost-effective, and exhibit superior system reliability. Consequently, AC motors have rapidly developed and found extensive applications across modern industrial domains.

The development of permanent magnet motors is intricately linked to advancements in permanent magnet materials [198–200]. During the period from the 1930s to the 1950s, successive emergence of aluminum-nickel-cobalt (Al-Ni-Co) and ferrite permanent magnets facilitated the introduction of various micro permanent magnet motors. However, the limited magnetic energy product of these materials hindered the progress of permanent magnet motors. In 1967, samarium-cobalt (Sm-Co) permanent magnets were introduced, followed by neodymium-iron-boron (Nd-Fe-B) permanent magnets in 1983. These new materials demonstrated remarkable magnetic properties, resulting in significant improvements in power density, torque density, and efficiency of the motors. Consequently, permanent magnet motors became actively researched, developed, and produced domain within the motor industry. The fundamental theory, analysis methods, and design techniques for permanent magnet motors experienced rapid advancement, culminating in the establishment of a comprehensive theoretical framework by the end of the 20th century.

2.6.1 Permanent Magnet Materials

The magnetic field is the medium for the motor to realize electromechanical energy conversion. In early motor designs, permanent magnets were utilized to establish the necessary magnetic field. However, these magnets were made from natural magnet ore and exhibited limited magnetic performance, resulting in larger motor volumes and subpar performance. In 1845, the Wheatstone general electromagnet in England replaced the use of permanent magnets and introduced the self-excited electric excitation generator in 1857, marking the advent of a new era in electric excitation [201]. This excitation mode enables the production of a sufficiently strong magnetic field, leading to smaller, lightweight motors with excellent performance. Consequently, theoretical research and development in electric excitation motors have progressed rapidly, while the application of permanent magnet materials in motors remains relatively limited.

Rare earth permanent magnets are magnetic materials that incorporate rare earth elements such as lanthanum (La), cerium (Ce), praseodymium (Pr), neodymium (Nd), promethium (Pm), samarium (Sm), europium (Eu), gadolinium (Gd), terbium (Tb), dysprosium (Dy), holmium (Ho), erbium (Er), thulium (Tm), ytterbium (Yb), lutetium (Lu), scandium (Sc), and yttrium (Y). After World War II, advancements in rare earth element separation and low-temperature technologies allowed for the investigation of their properties at low temperatures. It was observed that most rare earth elements exhibited strong magnetism at lower temperatures but were unsuitable as permanent magnetic materials due to their Curie temperature being below room temperature. Researchers then explored the potential of integrating rare earth elements with the Al-Ni-Co alloy, known for its strong magnetism at room temperature, to enhance the magnetic properties of rare earth elements under these conditions [202–204]. These materials differ in composition, preparation processes, magnetic properties, stability, economy, and mechanical characteristics, resulting in distinct processing methods and applications.

The emergence of Al-Ni-Co permanent magnet materials in the 1930s revitalized the field of permanent magnet motors. Substantial advancements have since been made over nearly 90 years in the fundamental theory, design, and manufacturing technology of these motors. These impressive developments can be attributed to the ongoing improvement in the performance of permanent magnet materials. The evolution of permanent magnet materials has progressed through different stages, encompassing carbon steel, Al-Ni-Co alloy, ferrite, and rare-earth magnets.

Permanent magnet materials play a crucial role as magnetic functional materials by establishing a constant magnetic field without requiring external energy after saturation by an external magnetic field. These materials are employed in permanent magnet motors to generate their magnetic fields. The power output of these motors spans a wide range, from a few milliwatts to several thousand kilowatts. They find applications in diverse domains, including toy motors, industrial motors, and large-scale permanent magnet motors for ship traction. The utilization of permanent magnet motors extends to various aspects of daily life, the national economy, transportation, national defense, aviation, aerospace, and more. Notably, the introduction of first, second, and third generation rare earth permanent magnet materials has provided a solid foundation for enhancing and rapidly advancing the performance of permanent magnet motors.

2.6.2 PMSM

Barlow invented the PMSM in 1831, which employs permanent magnet excitation to generate a permanent magnetic field after magnetization and exhibit exceptional excitation performance. The PMSM has a straightforward structure, operates reliably as an AC motor, and offers excellent speed regulation performance similar to a DC motor without requiring an excitation winding, electric brush, commutator, or collector ring. The PMSM consists of two primary components: the stator, made up of silicon steel sheets, a motor shell, an end cover, and a symmetrical distribution of three-phase windings, and the rotor, comprising permanent magnetic steel, a yoke, and a rotor iron core. By utilizing a three-phase inverter, the PMSM generates a space rotating magnetic field inside the stator winding at an angular velocity of electrical frequency, resulting in the generation of electromagnetic torque when interacting with the permanent magnet of the rotor, leading to motor rotation [205]. The PMSM exhibits several outstanding characteristics, which can be summarized as follows:

a. Compact and lightweight design coupled with low noise levels due to its simple structure.

b. Utilization of a permanent magnet for excitation, resulting in minimal excitation losses and high operational efficiency.

c. Remarkable static and dynamic response performance, characterized by low rotating inertia, high starting electromagnetic torque, and excellent overall response capabilities.

Two general types of PMSM can be distinguished based on the installation positions of the permanent magnets on the rotor: the surface permanent magnet synchronous motor (SPMSM) and the interior permanent magnet synchronous motor (IPMSM), as shown in Figure 2.18. The SPMSM, also referred to as the non-salient pole synchronous motor, has a rotor with surface-mounted permanent magnets, resulting in a symmetrical magnetic circuit in both the direct and quadrature axes that ensures equal d and q inductances and facilitates optimal design. In contrast, the IPMSM, also known as the salient pole synchronous motor, embeds permanent magnets within its rotor iron core and generates additional reluctance electromagnetic torque due to its asymmetric rotor magnetic circuit and high power density. This design makes the IPMSM suitable for high-speed motor applications and provides a wide field weakening range.

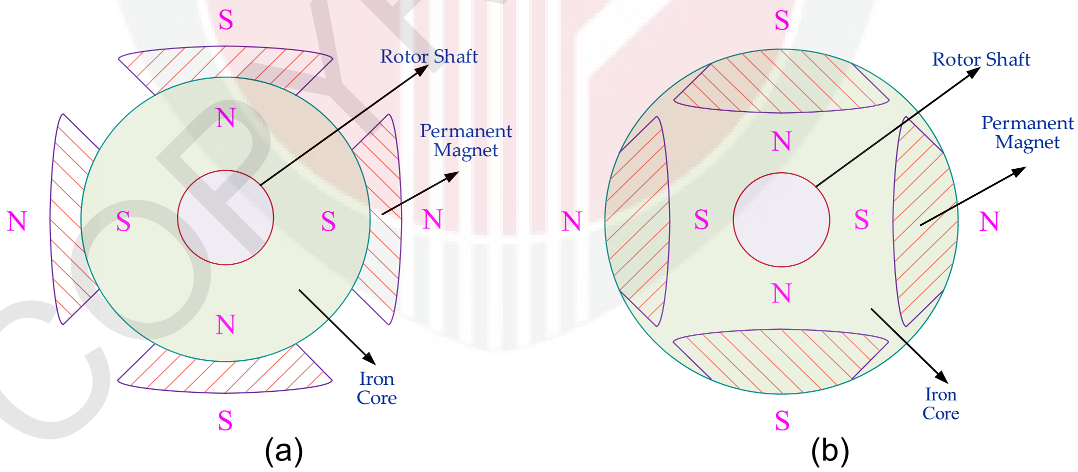

Figure 2.18 : Classification and Structure of the PMSM: (a) SPMSM; (b) IPMSM

The different rotor structures lead to variations in magnetic circuits and performance characteristics between SPMSM and IPMSM. Specifically, the

IPMSM exhibits higher efficiency but also greater cogging electromagnetic torque ripples and lower losses at high temperatures. However, note that the IPMSM may experience increased eddy current losses in both the stator and rotor due to high-frequency harmonics. Although the SPMSM can deliver power supply and electromagnetic torque similar to the IPMSM under similar high flux linkage density conditions, it tends to have higher iron losses under light loads. In the non-weakening field mode, the SPMSM typically exhibits a higher power factor compared to the IPMSM. For the purposes of this study, SPMSM has been selected as the controlled object.

Since the advent of the 21st century, there has been an increasing demand for high-performance motors. PMSM have experienced notable advancements owing to their outstanding attributes encompassing high power density, efficiency, power factor, and control performance. Consequently, PMSM has emerged as a vibrant domain within the realm of research and development for permanent magnet motors. Its applications are extensive, ranging from industrial and agricultural production to national defense, aerospace, robotics, new energy, and electric vehicles.

The utilization of PMSM is progressively expanding in high-performance applications due to advancements in product development and engineering. As a result, the demand for enhanced performance parameters such as reduced torque fluctuation, vibration, noise, and improved working reliability has also increased. Nevertheless, the limited research conducted on the common challenges encountered by permanent magnet motors is becoming more evident, thus imposing limitations on the development of high-performance permanent magnet motors.

2.7 Model Predictive Control

The late 20th century witnessed significant advancements in PMSM with a permanent magnet rotor, owing to the development of high-performance Nd-Fe-B and other permanent magnet materials. Unlike AC motors, PMSMs eliminate the need for a commutator and brush and employ a permanent magnet for rotor excitation instead. This design offers various advantages such as high reliability, simple structure, compact size, wide speed range, high power density, and high efficiency. Consequently, researchers both internally and externally have devoted considerable attention to the control methods for driving PMSM. Furthermore, the rapid progress in power electronics technology has facilitated the widespread adoption of PMSM control systems, enabling their extensive utilization in aviation, spaceflight, communications, and transportation sectors.

The advancement of power electronics and motor control technology has led to significant progress in both fields. In the realm of PMSM, various control methods, such as vector control (also known as field-oriented control, FOC, and DTC, have gained popularity in industrial applications. FOC, originally proposed and employed in AC motor speed control during the 1870s, draws inspiration from the control mode of DC motors. It decomposes the stator current into direct-axis and quadrature-axis components, effectively decoupling them to simulate the excitation current and armature current found in DC motors. By independently controlling the currents on the A-axis and D-axis, FOC achieves magnetic flux and torque control, thus enabling precise motor control [206–210]. While FOC offers high control accuracy and steady-state performance through its double closed-loop control structure, it exhibits slightly slower dynamic response. Subsequently, FOC was adapted for speed control in PMSMs, significantly contributing to the advancement of PMSM control technology. It has now become one of the most widely utilized control technologies in the industrial sector. Over a decade later, researchers introduced a new motor control technology known as DTC. Unlike FOC, DTC employs a hysteresis comparator to regulate motor torque based on the relationship between flux linkage and torque. Its structure and algorithm are simpler compared to FOC as it does not involve coordinate transformation and dynamic solution processes, thereby achieving favorable dynamic performance. However, DTC does exhibit larger torque ripple during the control process and its steady-state performance is not as robust as FOC [211,212].

Due to the strong coupling and nonlinearity inherent in PMSM control systems, the aforementioned methods may not satisfy the control demands of high-performance scenarios. To address this issue, advanced control strategies have been proposed and implemented in high-performance PMSM drive systems based on FOC and DTC. These advanced strategies include sliding mode control, auto-disturbance rejection control, self-adaptive control, fuzzy control, and model predictive control [213–215].

MPC involves predicting the future motor state using the discrete model of the inverter and motor, along with the current motor state. An optimal voltage vector is then selected based on a pre-defined evaluation index and the predicted value. MPC offers benefits such as rapid dynamic response, robust online optimization, simple structure, and constraint integration. However, complex models necessitate extensive calculations for accurate future state prediction. Initially, limited microprocessor computational capabilities restricted MPC development. Nevertheless, advancements in chip manufacturing have significantly boosted microprocessor computing power and storage capacity, enabling the full utilization of MPC's advantages. As a result, MPC has gained prominence as a research area in the past decade, attracting global scholarly exploration of its application in PMSM drive control [216–221].

As a model predictive optimization control strategy, MPC has three main components: a prediction model, rolling optimization, and feedback correction. First, according to the discrete mathematical model of the controlled object, the state quantity in the future time is predicted at the current moment of the system. Then, the predicted value and given value are brought into the cost function, and, using cost function optimization, the optimal combination of switches is selected to act on the controlled object and finally update the system state. MPC can also be referred to as receding horizon control because an MPC system continuously detects new values and repeats such processes in each control cycle. A block diagram of the model predictive control algorithm is shown in Figure 2.19.

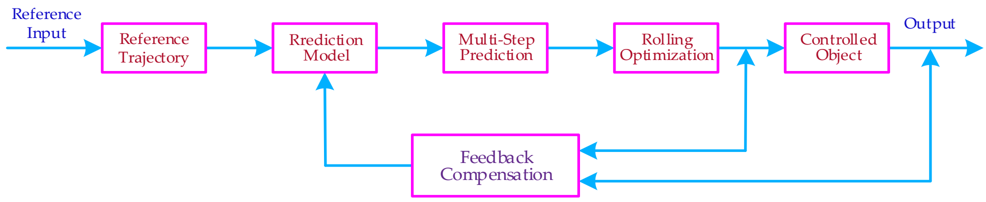

Figure 2.19 : Block Diagram of the MPC Algorithm

Figure 2.20 shows the working principle of MPC. The future state of the system in the predetermined time period is obtained by using the sampled measured values and the effective data before the time to predict the system's mathematical model. According to the principle of minimizing the cost function, the operation modes are optimally sequenced, and the first operation mode in the sequence is applied to the system to achieve optimal control. Due to the system collecting relevant data in each control cycle, the whole prediction process is executed, and rolling optimization is continuously carried out to ensure accurate outputs.

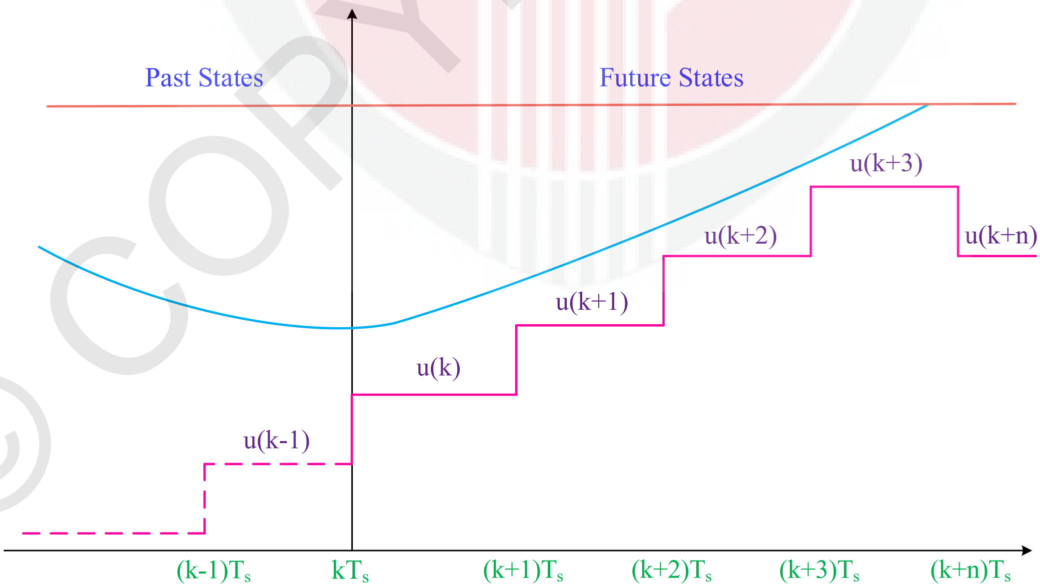

Figure 2.20 : Working Principle of Model Predictive Control

MPC has several advantages:

a. Applied to a multi-variable control system.
b. Constraints are used to optimize the controller, which is simple and easy to design.
c. High flexibility to optimize solutions for specific application areas.

MPC can be divided into two categories based on control objectives: model predictive current control (MPCC) and model predictive torque control (MPTC). MPCC focuses on controlling current by constructing a cost function to evaluate the performance of each voltage vector. The objective is to select the optimal voltage vector that minimizes motor current ripple [222–229]. On the other hand, MPTC considers both torque and flux linkage in its cost function [230–234]. However, since these parameters have different dimensions, appropriate weight coefficients must be designed based on specific control requirements to achieve desired control effects. Currently, there is no established theory for calculating the weight coefficient between torque and flux linkage. Therefore, a large number of experiments are typically conducted to derive optimal weight coefficients, resulting in a complex design process. In practical applications, weight coefficients are often chosen based on control performance requirements and experimental conditions.

Due to the differences in voltage-vector control sets, MPC can be divided into continuous control set model predictive control (CCS-MPC) and finite control set model predictive control (FCS-MPC). In the CCS-MPC, the controller output is a continuous reference signal, which is converted into an appropriate action using a modulator [235–238]. FCS-MPC makes use of the limited switching states in three-phase inverters to enumerate the corresponding conditions in all switching states. Once the optimal switching states are found, the corresponding driving signals are output immediately and held fixed during each switching cycle. FCS-MPC controls the electromagnetic torque, stator flux linkage, and stator current at the same time [239–247]. In addition, because of the different optimal control objectives, there are two main categories of important branches for FCS-MPC in the motor field: finite control set model predictive torque control (FCS-MPTC) and finite control set model predictive current control (FCS-MPCC) [248–252].

In PMSM drive control system, the inverter generates the basic voltage vector as the direct control target for the motor. Traditional MPC involves incorporating each basic voltage vector into the PMSM prediction model to obtain prediction variables (current, torque, etc.). The cost function is then calculated to evaluate the effect of each basic voltage vector, selecting the optimal voltage vector and applying it to the motor. As the basic voltage vectors generated by the two-level inverter are limited (two zero vectors and six non-zero vectors), this method is referred to as single vector model predictive control (SV-MPC). SV-MPC experiences tracking errors between the selected optimal voltage vector and the expected reference voltage, affecting the steady-state control performance of PMSM [253–255]. Enhancing the system's control frequency to reduce control intervals and achieve more precise results is an effective approach to enhance PMSM's steady-state control performance. However, this method requires high-performance digital processors and may pose challenges to implement complex control algorithms.

To address this issue, scholars have proposed multi-vector MPC to increase the number of basic voltage vectors applied to the motor within a control cycle. Multi-vector MPC can be categorized into double vector model predictive control (DV-MPC) [256,257] and three vector model predictive control (TV-MPC) [258,259]. In DV-MPC, two basic voltage vectors are applied to the motor in one control cycle, with the combined duration covering the entire control cycle. Compared to traditional SV-MPC, DV-MPC offers more flexibility in voltage vector selection and allocation of action time, resulting in more accurate output voltage vectors through individual action time calculations. DV-MPC significantly reduces the error between the expected reference voltage vector and the output voltage vector, decreases current and torque ripple, and improves the steady-state performance of the control system. On the other hand, TV-MPC utilizes two effective vectors and one zero vector to synthesize the final output voltage, enabling accurate tracking of the reference voltage within the modulation range. Consequently, TV-MPC exhibits significantly smaller current and torque ripple compared to SV-MPC and DV-MPC, leading to optimal steady-state performance.

MPC can be categorized into two types based on prediction range: single-step model predictive control (SS-MPC) and multi-step model predictive control (MS-MPC). The increase in the number of voltage vectors enhances steady-state performance but also introduces computational burden and higher switching frequency to the inverter. This creates a contradiction between the steady-state control performance of AC motor MPC and the inverter's switching frequency. It is worth noting that MS-MPC can effectively solve the contradiction between steady-state control performance and switching frequency. MS-MPC involves iterative calculations using SS-MPC to predict the system state multiple times within the prediction range. To achieve the optimal voltage vector for multiple future prediction times, MS-MPC considers the system state at all sampling times within the prediction range when constructing the cost function. As a result, MS-MPC improves steady state performance and reduces switching frequency. However, MS-MPC's use of discrete prediction models leads to complex mathematical calculations, resulting in exponential increase in computational complexity compared to SS-MPC. In practical systems, excessive calculation time may exceed the designated control cycle, significantly impacting control performance. Thus, MS-MPC methods require high-performance hardware processors, posing computational burden concerns. Despite its superior control performance, applying MS-MPC with multiple prediction layers in actual motor drives is currently challenging. Moreover, MS-MPC faces additional obstacles such as unclear theoretical guidance for weight coefficients design, simplified computational complexity, and lack of fixed switching frequency [260–263].

MPC is a widely researched and applied component in various fields, and its performance indicators, particularly those related to intensity and reliability, have garnered significant attention from specialists, scholars, and engineering technicians globally. Their studies and contributions have spanned different aspects [264-277]: a prediction-error-driven position estimation method based on current prediction errors of finite control set model predictive control for the position-sensorless control of a PMSM [264]; a modulated model predictive current controller for PMSM [265]; the use of disturbance observations to improve MPC [266–268]; model predictive control and iterative learning control to not only speed up system response time but also effectively reduce speed ripples [269]; switching sequence model predictive direct torque control for IPMSMs for NEEVs in switch open-circuit fault-tolerant mode [270]; a cascaded variable rate sliding mode speed controller for model predictive current control [271]; a cascade-free modulated predictive direct speed control scheme for PMSM drives to further enhance steady-state performance on the basis of a simple control structure [272]; better quality currents and electromagnetic torque ripples in dual-vector model predictive current control [273]; ultra-local model-free predictive current control, which does not involve any motor parameters based on nonlinear disturbance compensation [274]; a data-driven, real-time-capable, recursive least-squares estimation method for the current control of a PMSM [275]; a discrete duty-cycle control strategy to reduce both the electromagnetic torque and flux ripples that appear in model predictive torque control [276]; and discrete space vector modulation to achieve flux-linkage and electromagnetic torque ripple reduction in finite set model predictive torque control [277].

Driving PMSM plays a crucial role in the electric drive control systems of NEEVs, with high-performance motors significantly improving durability and mileage. Among the options, the PMSM is favored for its precise control, wide speed range, high density, smooth electromagnetic torque ripples, and low noise levels. However, the PMSM faces challenges in complex working conditions, making it imperative to optimize its control methodology. MPC is an advanced optimal control technology that utilizes system models to predict future changes in control variables and select optimal operations based on predetermined criteria. By setting appropriate criteria, MPC can flexibly control key parameters such as motor torque ripple, switching frequency, power loss, and maximum output current to achieve multi-objective optimal control. Compared to traditional motor control methods, MPC is intuitive, adaptable to specific control fields and objectives, and can be easily modified.

2.8 Electromagnetic Interference and Compatibility

Against this background of traditional fossil energy shortage crisis and sustainable green development road [278,279], it is encouraging that the new NEEVs have been rapidly popularized worldwide due to their inherent advantages of zero harmful gas emissions, low energy consumption and non-pollution, high efficiency and use more environmentally friendly electric energy as power sources [280–283]. Compared with conventional engine ICE, the NEEVs have more electronic and electrical equipment, including power battery pack, inverters, traction electromotors, controllers, busbar cable, as shown in Figure 2.21 [284,285].

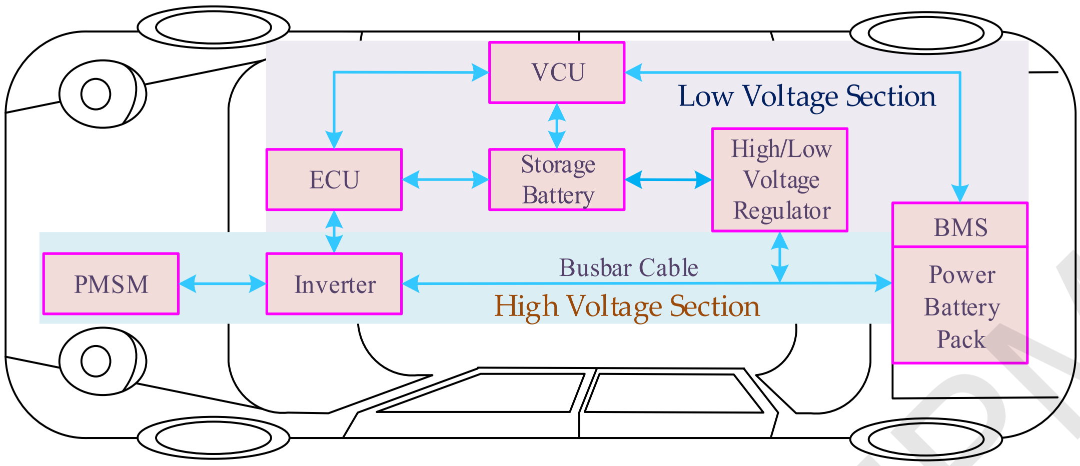

Figure 2.21 : Main Electrical Components of NEEVs

Obviously, the BMS communicate with vehicle control unit (VCU) to adjust the high direct voltage and current from power battery pack, the VCU establish a bidirectional data interchange channel through the controller area network (CAN) bus [286,287], and then the electronic control unit (ECU) send pulse width modulation (PWM) signal to drive the power switches silicon carbide metal oxide semiconductor field effect transistor (SiC MOSFET) in the inverter to turn on and off, thereby achieving permanent magnet synchronous motor (PMSM) speed control [288–290]. In actual operation, these high voltage, high current, and high power electrical components will produce EMI. To make matters even worse, the on-board electronic devices with high sensitivity, such as BMS, VCU, and ECU, are more susceptible to EMI.

In actual operation, these high voltage, high current, and high power electrical components will produce EMI. To make matters even worse, the on-board electronic devices with high sensitivity, such as BMS, VCU, and ECU, are more susceptible to EMI, which is directly related to the safety, reliability, and comfort of NEEVs [291]. Therefore, the internal electromagnetic environment is more complex, and EMC is also facing greater challenge and opportunities for NEEVs. which should attract more attention and further discussion [292,293].

It is particularly worrying that the high-speed switching actions of SiC MOSFET in motor drive control system can interact with the parasitic resistors, capacitors, and inductors from system circuit, resulting in surge voltage and ringing effect, which can lead to undesired and still worrisome EMI problems. In [294,295], the major high frequency EMI source of the SiC MOSFET is the changes from high voltage and current (dv/dt and di/dt) conversion, SiC MOSFET produce higher spectra amplitude Insulated Gate Bipolar Transistor (IGBT) in the 2MHz-50MHz frequency range. EMI has great potential to cause performance degradation, increased failure and shorten service life of NEEVs [296]. This has brought an important concern into consideration: EMC. In 1833, the English physicist and chemist Faraday discovered electromagnetic induction (1791-1867). EMC originated in the 19th century. EMC performance refers to the abilities of a device or system to function properly in its electromagnetic environment and it also would not constitute unsustainable electromagnetic disturbance to anything in the environment [297]. To cut it short, the most EMI in motor drive control system comes from:

a. High dv/dt and di/dt.
b. Impedance characteristics of resistors, capacitors, and inductors change in the high frequency range.
c. PWM contains rich voltage and current switching harmonics.

EMC testing is all about standards in Figure 2.22. Whether people are developing 5G products, automotive equipment, military equipment or something as simple as an ordinary table lamp, the device must meet the requirements set by standardization organizations shown Table 2.5 such as International Electrotechnical Commission (IEC), International Special Committee on Radio Interference (CISPR), international Standardization Organization (ISO), Institute of Electrical and Electronic Engineers (IEEE), Comite Europeen de Normalisation Electrotechnique (CENELEC), European Telecommunication Standards Institute (ETSI), Federal Communications Commission (FCC), American National Standards Institute (ANSI), Radio Technical Commission for Aeronautics (RTCA) or the Military Standards (MIL-STD) committee.

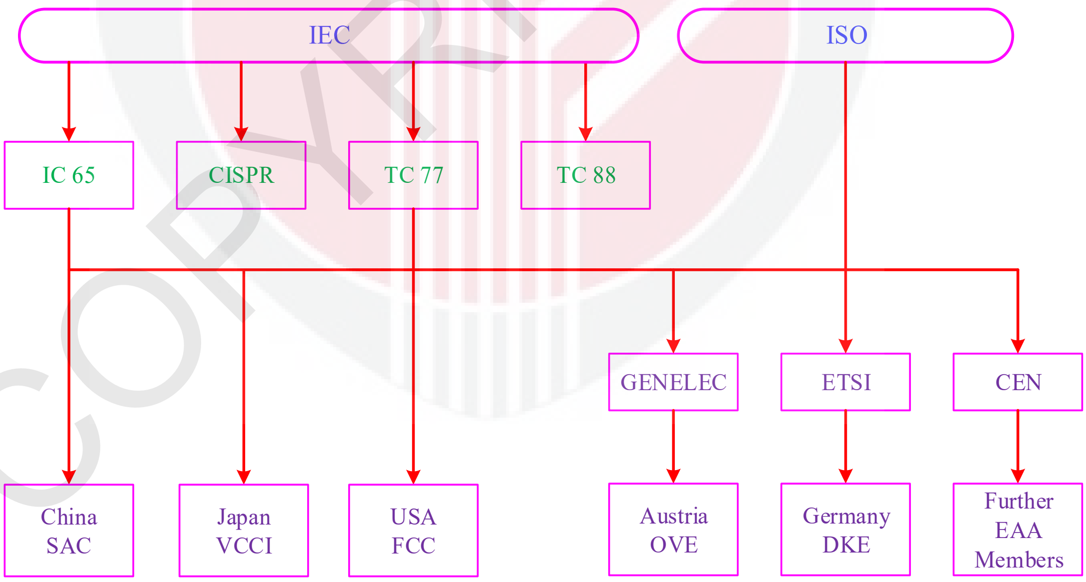

Figure 2.22 : EMC Standardization Organizations Committee

Table 2.5 : Commercial EMC Standards

Commercial Standards	CISPR	CENELEC (Europe)	FCC (USA)	METI (Japan)
Industrial, scientific medical equipment	11	EN 55011	Part 18, C	J55011
Vehicles, boats and internal combustion engines	12/25	EN 55012 EN 55025	SAEJ551 J1113	JASO D001-82
Electrical devices, household appliances and tools	14-1	EN 55014-1	NULL	J55014-1
Electrical lighting	15	EN 55015	NULL	J55015
Multimedia equipment	32	EN 55032	Part 15, B	J55032
Military equipment	MIL-STD-461			
Aviation	DO-160			

The serious EMI problems of motor drive control system are characterized by high noise amplitude, complex coupling, multipath, which are closely related to working conditions [298]. EMI can be divided into conducted EMI and radiated EMI, and CM interference and DM interference are two differential conducted form of the conducted EMI according to their own propagation path and coupling channel [299,300]. In addition, the generated CM and DM interference will form a small loop or wire antenna through busbar cable, which can cause radiated EMI to other systems or devices [301]. However, without EMC design and correction, the EMI can hardly meet the standard limit requirements (150 kHz to 30 MHz in CISPR 25). Therefore, the suppression of EMI from motor drive control system is increasingly receiving attention from both academia and the industry [302,303].

Motors that operate with a variable frequency drive (VFD) are more susceptible to bearing failure. In standard generated sine waves, the voltage is balanced; this means that the amplitudes of the wave form on both the positive and negative sides are equal. In PWM (pulse wave modulated) generated sine waves, produced by VFD's, the voltages are not balanced. This imbalance can cause voltage potential in the motor structure, leading to voltage passing between the rotor and stator to ground through the motor bearings causing damage as shown in Figure 2.23.

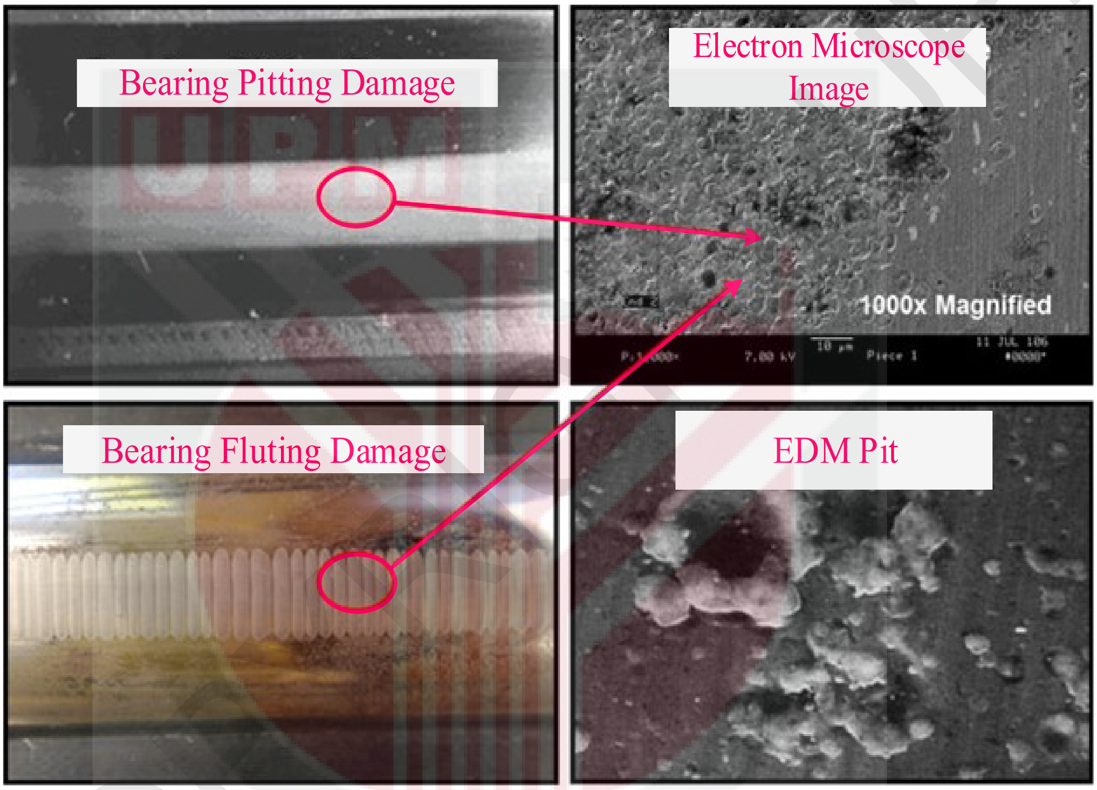

Figure 2.23 : Serious Bearing Damage Accidents

The CM voltage has several negative effects, such as bearing corrosion, localized insulation breakdown of motor winding, and EMI. The electric corrosion of the bearing is attributed to the CM voltage of frequency converter through the distributed capacitance inside the motor acting on the shaft.

When the shaft voltage is low, the insulating effect of the lubricating oil film prevents bearing current by withstanding the voltage without breakdown. However, a high shaft voltage or unstable oil film during motor start-up can puncture the lubricating oil film, causing spark discharge and heat generation that degrades the oil performance. The resulting high temperature creates grooves on the bearing's inner ring, outer ring, or ball, while prolonged discharge corrodes the bearing raceway, increasing surface roughness and yielding electric corrosion traces, as depicted in Figure 2.24. Uneven raceways are more susceptible to breakdown than flat raceways, doubling the degree of electrical corrosion, and large grooves elevate motor vibration and noise. Failure to promptly address these issues significantly diminishes bearing reliability and may lead to irreparable damage.

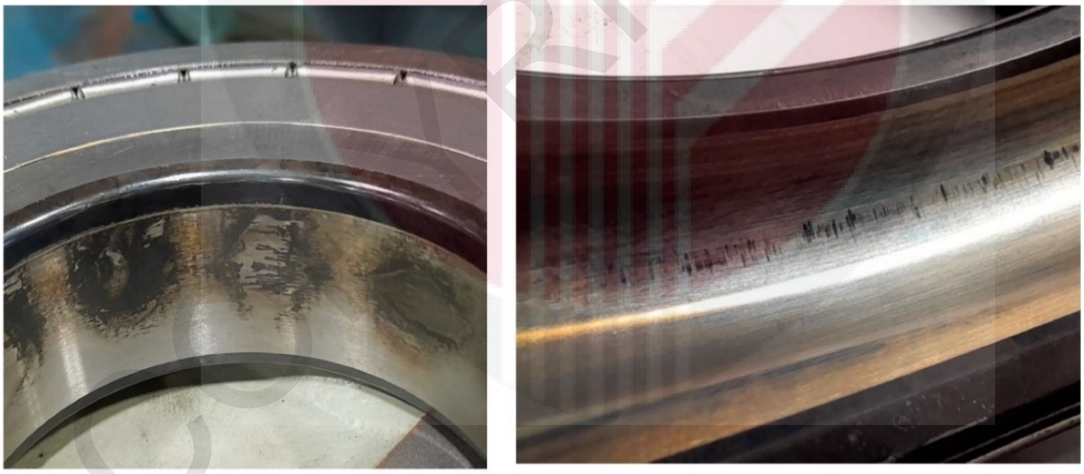

Figure 2.24 : Phenomenon of Electric Erosion on Motor Bearings

At present, the EMI of motor drive control system, the scholars and researchers have focused on three aspects: mechanism analysis, modeling and suppression measures [304–311]. In [304], this research introduces the EMC problems and investigates the EMI mechanism of motor driving systems, charging systems and other low voltage systems. The EMI of power components in NEEVs motor drive control system is studied in [305], including its propagation path and the method of interference measurement. [306] proposes a general device-based CM model that is able to describe propagating mechanism in the system. In this research [307], a high-frequency model is proposed to predict the system-level conducted EMI. A conducted emission model with lumped and finite element parameter circuit based electromagnetic simulation is presented in [308]. This work [309] describes a complete equivalent circuit model, the CM conducted emissions can be predicted and evaluated during the design phase for performance optimization purpose. [310] presents modified single stage and multistage three EMI filters to offer the same CM and DM attenuation performances for SiC inverter switching at 200 kHz. Two EMI filter design methods for high voltage DC ports of NEEVs motor controllers are proposed in [311].

Figure 2.25 illustrates the structure of the insulated end cover. An insulating gasket is positioned between the end cover and the end cover bushing, and the assembly is secured with bolts. The bolts are covered with insulating sleeves, and additional insulating gaskets are placed between the bolts and the end cover to maintain insulation. The insulated end cover introduces an insulating layer into the bearing current circuit, thereby reducing the shaft voltage carried by the oil film.

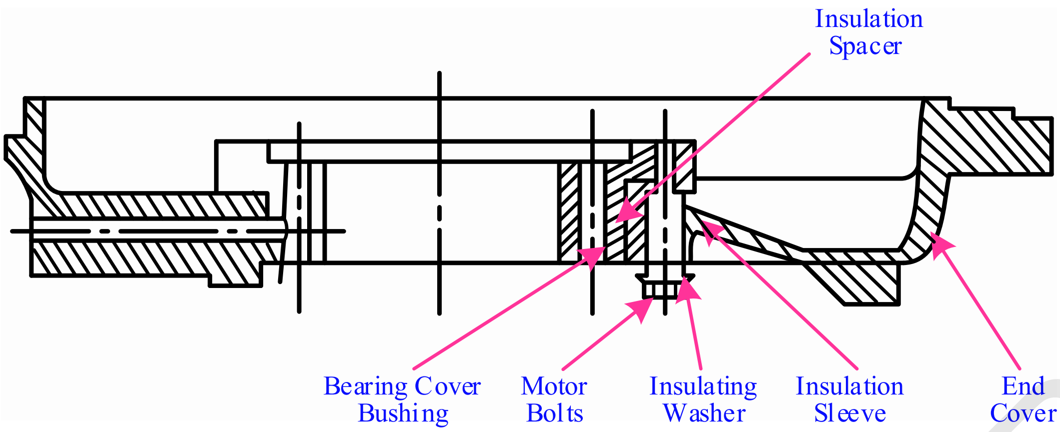

Figure 2.25 : Structure of Insulated end Cover

2.9 Research Gaps

SiC MOSFET, as a new and widely used power device, offers faster switching speeds and lower switching losses. The gate drive circuit, acting as an amplifier, connects the signal controller to the SiC MOSFET. Due to the unique characteristics of SiC MOSFET, designing an effective gate drive circuit presents several challenges. Despite numerous studies on gate drive circuits for SiC MOSFET, their application in NEEVs remains a critical area of focus.

To address the high driving loss caused by the gate resistance in traditional SiC MOSFET gate drive circuits, a more efficient, stable, and reliable active gate drive circuit is needed. This circuit should recycle the energy stored in the SiC MOSFET' parasitic capacitance, reducing driving loss and enhancing switching frequency, thereby facilitating the broader adoption of SiC MOSFET in NEEVS. Literature reviews indicate that energy recovery or reuse from the power supply can minimize driving loss and increase the switching speed of SiC MOSFET.

To address these challenges and fully exploit the performance of SiC MOSFET, a specialized gate drive circuit is essential, rather than relying on traditional designs. Developing an appropriate gate drive circuit is a critical research focus for optimizing SiC MOSFET performance in NEEVs. As previously discussed, enhancing the switching speed of SiC MOSFET is challenging due to factors such as substantial internal gate resistance, high Miller voltage, and limited gate-source voltage ratings. Additionally, ensuring the stability and reliability of the gate drive circuit is crucial for the long-term safe operation of SiC MOSFET. Thus, studying dedicated gate drive circuits for SiC MOSFET in NEEVs is of significant importance.

Environmental pollution and energy shortages have posed significant challenges to traditional ICE vehicles. The development of NEEVs offers a promising solution to address fossil energy depletion and mitigate air pollution. In NEEVs electrical propulsion system, the bidirectional DC–DC converter, as the power transmission unit of the power battery pack, plays a crucial role in energy distribution and management, which outputs electrical energy during driving and recovers braking electrical energy during deceleration, requiring bidirectional energy flow. Thus, research on the circuit structure and control methods of bidirectional DC–DC converters with a wide input range and high power transmission is of great significance.

Through comparative analysis of various isolated and non-isolated DC–DC converter circuit topologies reveals that the bidirectional Buck/Boost converter offers advantages such as fewer power devices, lower electrical stress, higher energy transfer efficiency, and simpler control, making it well-suited for the technical requirements of this research. When the NEEVs are running normally, the bidirectional Buck–Boost converter plays an important role as the core factor of electrical energy flow regulation and management between the power battery pack and motor drive inverter within the high voltage direct current bus, and transform voltage from two conversion directions, so that the motor drive system is always working in the optimal rate zone. In the process of starting or accelerating, the electrical energy flows forward to ensure the motor inverter drive performance; during braking or decelerating, the electrical energy flows back to effectively recover the excess electrical energy. The performance of the bidirectional Buck–Boost converter determines the power output and cruising range of the NEEVs, which directly has a deep impact on the performance, quality, and user experience.

The output power of the traditional bidirectional Buck–Boost circuit is constrained by a single power device, limiting its suitability for high-power applications. Therefore, improvements are needed to reduce output voltage ripples and increase power transmission, while ensuring high power, efficiency, and density to meet the demands of NEEVs.

PMSM offer significant advantages, including high reliability, compact size, low noise, strong overload capacity, and high power density, making them ideal for the electromotor of NEEVs. As PMSM must adapt to various driving conditions, the demand for accuracy, speed, and stability are increasing. Traditional control strategies are inadequate to meet these requirements.

Among advanced control technologies, MPC has gained attention for excellent dynamic performance, optimizing multiple control variables simultaneously, ensuring both steady-state performance and high-speed dynamics. Thus, applying MPC to PMSM drive control systems holds great potential.

Due to the complex and dynamic operating environment of NEEVs, PMSM are vulnerable to disturbances from various external factors, which can compromise control accuracy. MPC is highly sensitive to system parameters, and disturbances can degrade or even disrupt system performance. Therefore, enhancing MPC to improve robustness against interference is essential for ensuring reliable performance under diverse conditions. The traditional MPTC strategy, which uses a single voltage vector per control cycle, limits control accuracy and involves a complex process for designing weight coefficients in the cost function. Novel MPTC strategies are needed to enhance control precision and further optimize PMSM performance. Advancing MPC for PMSM is crucial for high-performance motor control applications.

MPTC, as one of the FCS-MPTC, incorporates motor torque and flux linkage amplitude into the cost function. However, due to their differing magnitudes, evaluating the control variable error is challenging. To address this, a weighting factor is used to balance the two control objectives, but the nonlinear relationship between electromagnetic torque and flux linkage complicates the design of an appropriate coefficient. Traditionally, the MPTC assigns a weight to the flux linkage amplitude term, with the initial coefficient set as the ratio of rated electromagnetic torque to rated flux linkage. Final selection of the weight coefficient, however, requires extensive simulations and experiments. Additionally, the traditional MPTC applies only one voltage vector per control cycle, limiting the control accuracy of electromagnetic torque and flux linkage, and resulting in significant pulsations. The online prediction and optimization of all voltage vectors within each control cycle further increases the computational load, burdening the processor.

Traditional FCS-MPTC uses a single basic voltage vector per control cycle, causing system state variables to oscillate around reference values. Recent research has shifted towards using multiple voltage vectors to synthesize the reference voltage, becoming a key area of focus. Efficiently generating the optimal continuous reference voltage vector to enhance PMSM drive control is a critical challenge in MPC. This research aims to propose an advanced FCS-MPTC control strategy, which is significant for improving PMSM drive control system performance in NEEVs.

As awareness of environmental protection and energy issues grows, the development of NEEVs is essential for promoting sustainability, energy conservation, industrial advancement, and reducing energy dependence, making it a critical trend for long-term development. Unlike traditional ICE vehicles, NEEVs are powered by power battery pack that transfer electrical energy to the PMSM through motor drive control system. NEEVs incorporate numerous power and electronic components, including high-voltage batteries, DC/DC converters, DC/AC inverters, electromotors, and high-voltage busbar cables, generating significant EMI. As a result, ensuring EMC has become a crucial challenge in the application of NEEVs.

The motor drive control of NEEVs relies on numerous electronic components. ring operation, voltage and current fluctuations, along with factors like power device switching and changes in PMSM speed or torque, induce alterations in the electromagnetic field. For instance, the high dv/dt and di/dt switching characteristics of power devices create high-frequency interference, while PMSM speed and torque variations produce low-frequency interference. These issues present significant challenges to the EMC of the motor drive control system. Consequently, research on predicting EMI in these systems is crucial for enhancing safety and reliability.

The motor drive control system of NEEVs operates with high power, voltage, and current. While increasing the number of filtering components can effectively suppress EMI, it also introduces parasitic parameters that complicate circuit design. To address the interference source, optimization methods such as improving control strategies and switching circuits can reduce electromagnetic emission intensity. However, studies indicate these methods have limited effectiveness in EMI suppression, and optimizing switching circuits may increase energy loss. A port filter, when designed with appropriate parameters, can suppress most conducted emissions from the motor drive control system. Combining the filter with optimization of parasitic parameters and key interference circuits can achieve effective suppression.

EMC testing assesses the performance of electronic equipment in an electromagnetic environment, requiring significant amounts of time, resources, and cost. EMC simulation technology offers a systematic and effective approach to predict and address EMC in motor drive control systems. By creating an equivalent circuit model, the effects of EMI can be simulated, allowing for the prediction of system performance in various electromagnetic environments and the evaluation of reliability and safety. This enables the identification of potential EMI sources, assessing their impact, and informed design decisions to mitigate EMI risks.

The internal electromagnetic environment of NEEVs is inherently complex, presenting greater challenges and opportunities for EMC. EMI directly impacts the safety, reliability, and comfort of these vehicles. Therefore, it is imperative to prioritize and engage in further discussions regarding this matter, in order to address these issues effectively and promote the development of NEEVs. This research needs to focus on the motor drive control system to investigate the generation mechanism, propagation path, and suppression measures of EMI. An equivalent circuit model for conducted interference is developed to create a system-level simulation platform, analyze key parasitic parameters affecting conducted emissions, and implement targeted optimization strategies. EMC simulation technology can identify potential EMI issues during the product design phase, reducing failure rates and accident risks in NEEVs, while enhancing overall safety and reliability. Additionally, it lowers testing costs, reduces production costs and improves market competitiveness. The methods and insights from this research not only address EMC challenges in

NEEVs but also provide valuable references for EMC testing and evaluation in other automotive electronics.

The EMI of NEEVs motor drive control system holds significant practical research value. Given the widespread nature of EMI in these systems, predicting and simulating interference by analyzing propagation path and generation mechanisms allows for the early identification of interference frequency and intensity. This proactive approach can detect non-compliant products, implement suppression measures, reduce costly laboratory testing, improve system qualification rates, and shorten the development cycle for both motor drive control system and NEEVs. For manufacturers, predicting EMI is crucial for ensuring products meet standards and becoming an essential technical tool for NEEVs development. From an academic perspective, the research of EMI in motor drive control system integrates various fields, including circuit theory, electromagnetism, and mathematics, providing a robust platform for interdisciplinary research. Thus, analyzing EMI in motor drive control system is a critical topic in EMC, with significant research importance.

2.10 Summary

The literature review related to this research has been presented and discussed by the previous researchers. It begins with the background of NEEVs, providing an in-depth investigation into the present status, latest deployment, and future prospects in the implementation of NEEVs while introducing the subsystems and their components: electrification transportation degrees, power battery pack, electrical propulsion system. Also, it has been found that, the research and design of PMSM drive control system for NEEVs based on SiC MOSFET have some directions: active gate driver, bidirectional Buck–Boost converter, model predictive control, electromagnetic interference and compatibility discussed in this chapter. The next chapter elaborates a thorough review of the methodological aspects as well as a detailed discussion of the approaches that are employed to fulfill the research's objective.

CHAPTER 3

METHODOLOGY

3.1 Introduction

This chapter presents the methodologies used to achieve the research objectives. The second section covers the design of an active H-Bridge inverter discontinuous current source gate driver, while the third section discusses the three-phase interleaved parallel bidirectional Buck-Boost converter. Additionally, the fourth section explores the technical theories of PMSM, and the fifth proposes a three-voltage vector duty cycle optimization strategy based on finite set model predictive control. The sixth section addresses shaft voltage and bearing current of PMSM, and finally, the chapter clarifies the method for addressing electromagnetic interference and compatibility in a motor drive control system based on PMSM with SiC MOSFET.

Figure 3.1 provides an overview of the research, detailing the various phases and processes involved, which illustrates the entire methodological framework employed in the study, with the research objectives highlighted in blue rectangles and the research methods outlined in brown rectangles. This chapter aims to elucidate the overall approach utilized from the project's inception to its successful completion. Consequently, the methodological steps must be carefully designed to align with the objectives outlined in Chapter 1.

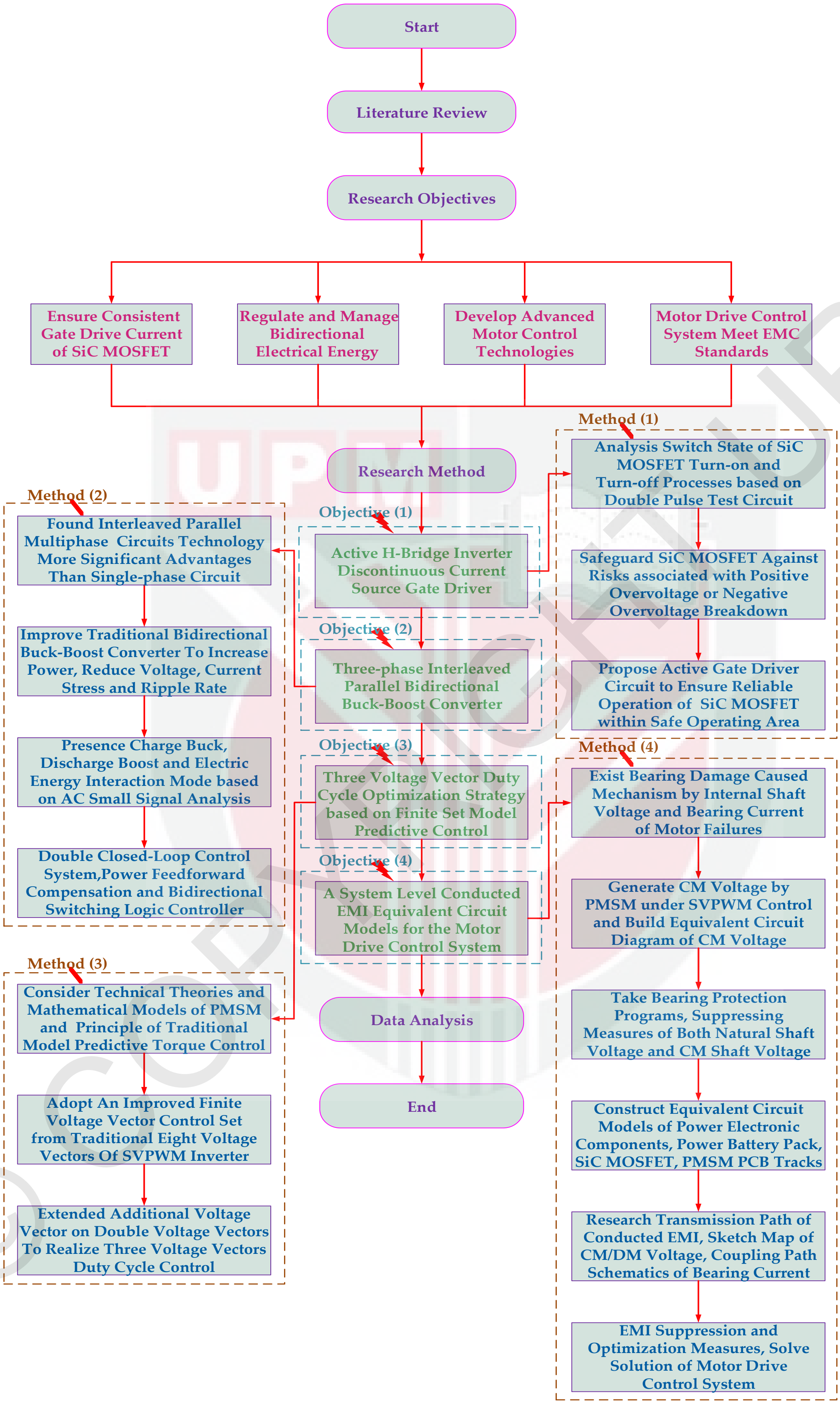

Figure 3.1 : Methodology Flowchart of the Research Process

3.2 Active H-Bridge Inverter Discontinuous Current Source Gate Driver

In recent years, the third-generation semiconductor materials have significant advantages in band gap, electric breakdown field, saturated electron drift velocity, thermal conductivity and radiation resistance, which further meet the new requirements of high temperature, high power, high voltage, high frequency in modern electronic technology field. SiC MOSFET have faster switching speed, smaller losses, and high temperature working tolerance, which can reduce the size and volume of passive components (such as heat sinks, inductors, capacitors) to achieve higher power density and efficiency. Therefore, SiC MOSFET has been widely predicted to be superior to that IGBT as power switch devices, which provides a promising solution for the motor drive control system in NEEVs.

3.2.1 Switch State Analysis Based on Double Pulse Test Circuit

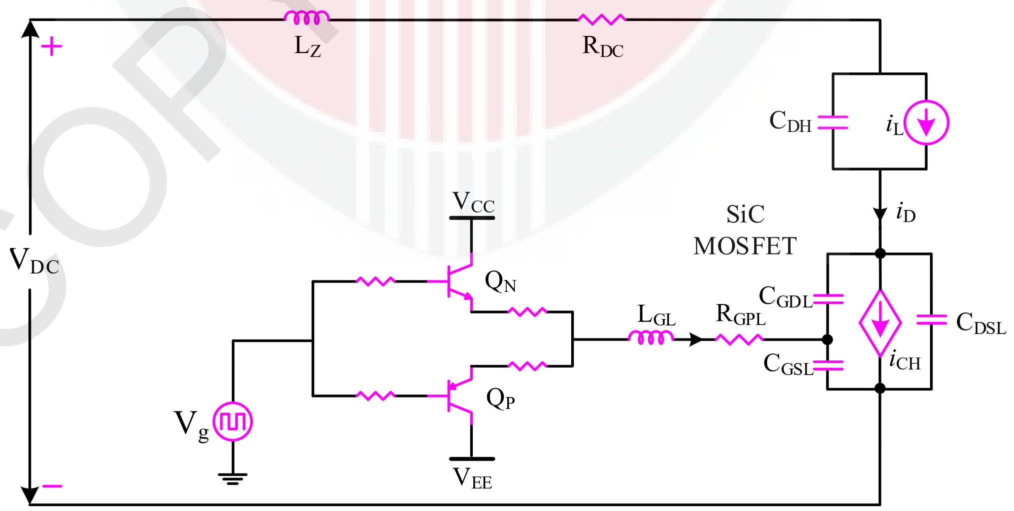

Figure 3.2 : Double Pulse Test Circuit with Parasitic Parameters

Figure 3.2 showcases the double pulse test circuit with gate driver, which is employed for the switch state analysis of the SiC MOSFET turn-on and turn-off processes as well as the generation mechanism of voltage and current waveform oscillation. In this circuit, V_{DC} represents the DC input voltage for power supply, while R_{DC} and L_Z denote the parasitic resistance and inductance between the SiC MOSFET device module and the DC bus, respectively. Additionally, C_{GDL} , C_{GSL} , and C_{DSL} represent the capacitance between the three interelectrode of the SiC MOSFET device module, while L_{GL} signifies the parasitic inductance between the SiC MOSFET device module and the gate drive circuit. Furthermore, R_{GPL} indicate the gate resistance between the SiC MOSFET device module and the external gate drive circuit.

3.2.2 SiC MOSFET Switching Process Characteristics

The turn-on and turn-off processes of SiC MOSFET can be divided into four stages. First, take the conduction process as an example.

3.2.2.1 SiC MOSFET Turn-On Process

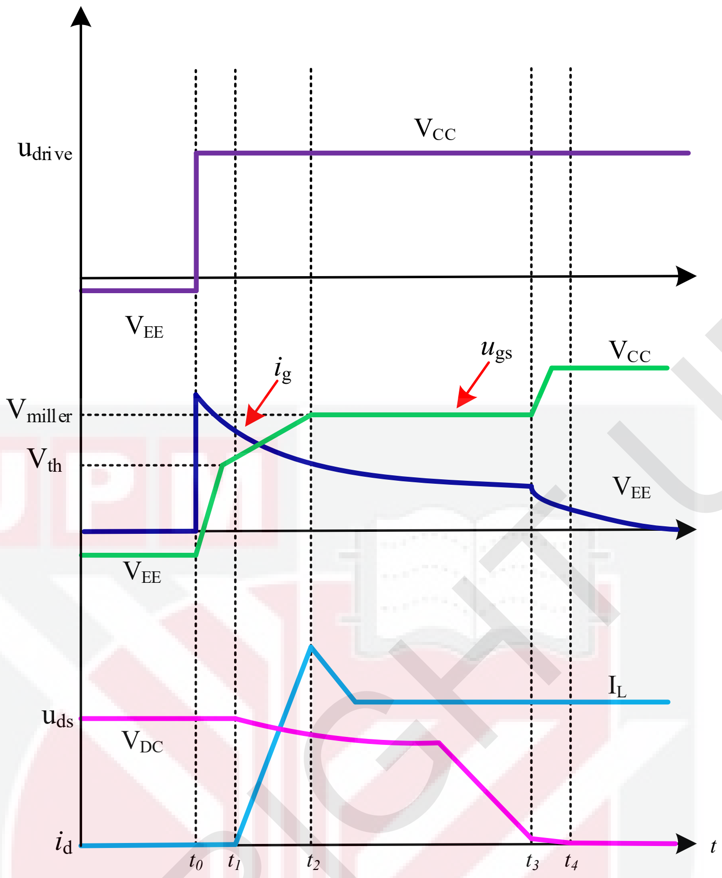

Figure 3.3 : Turn-on process of SiC MOSFET

[t_0~t_1]: Turn-on delay stage. A transition occurs in the driving voltage from a negative driving voltage V_{EE} to a positive driving voltage V_{CC}. The driving power supply charges the input capacitor $C_{iss} = C_{gs} + C_{gd}$ of the SiC MOSFET through the driving resistor R_g. It is important to note that, at this point, the SiC MOSFET remains in the off state, and the current path can be observed in Figure 3.3. As the charging process advances, the voltage u_{gs} continues to increase:

$$u_{gs}(t) = V_{EE} + (V_{CC} - V_{EE})\left[1 - e^{-(t-t_g)i\omega t/\tau W_i}\right] \quad (3.1)$$

Upon the attainment of the threshold voltage V_{th} by the voltage u_{gs}, the initial stage terminates, and the duration t_{don} of the turn-on delay stage can be expressed using Equation 3.2:

$$t_{don} = t_1 - t_0 = \tau_{iss1} \times \ln\left(\frac{V_{CC} - V_{EE}}{V_{CC} - V_{th}}\right) \tag{3.2}$$

Equation 3.2 demonstrates that the duration t_{don} of the turn-on delay stage can be reduced by decreasing the external drive resistance R_g or increasing the positive driving voltage V_{CC}. Moreover, injecting additional drive current facilitates an accelerated charging process, thereby shortening the turn-on delay stage time.

[t_1~t_2]: Current rise stage. The voltage u_{gs} exceeds the threshold voltage V_{th}, resulting in an increase of the drain current i_d from zero. This can be mathematically expressed as:

$$i_d = g_m \times \left[u_{gs}(t) - V_{th}\right] \tag{3.3}$$

During this stage, the driving power supply continues to charge the input capacitor C_{iss}, causing the voltage u_{gs} to exponentially increase. As the drain current i_d reaches the load current I_L, the voltage u_{gs} equates to the Miller level $\mathrm{V_{miller}}$. The duration t_r of the current rise stage can be expressed as:

$$t_r = t_2 - t_1 = \tau_{gs} \times \ln\left(\frac{V_{CC} - V_{th}}{V_{CC} - \mathrm{V_{miller}}}\right) \tag{3.4}$$

The current rate of change of i_d can be expressed as:

$$\frac{di_d}{dt} = g_m \times \frac{du_{gs}}{dt} = g_m \times \frac{i_g}{C_{iss}} \tag{3.5}$$

During the turn-on process, when i_d exceeds I_L, the charging current of the junction capacitor and the drain current i_d collaborate to generate the peak current I_{dpeak}:

$$I_{\text{dpeak}} \approx I_L + \sqrt{Q_n \times \frac{di_d}{dt}} \tag{3.6}$$

Once the turn-on current reaches its peak value, the interaction between the parasitic inductance, parasitic capacitance, and equivalent resistance in the power supply loop causes i_d to gradually return to its steady-state value via second-order damping oscillation. The oscillation frequency f_{on} and damping coefficient ξ_{ond} can be calculated using Equation 3.7 and Equation 3.8, respectively:

$$f_{on} \approx \frac{1}{2\pi\sqrt{L_{eq}C_{eq}}} \tag{3.7}$$

$$\xi_{ond} = \frac{R_{eq}}{2}\sqrt{\frac{C_{eq}}{L_{eq}}} \tag{3.8}$$

By combining Equation 3.5 and Equation 3.6, it is evident that reducing the i_g during the current rise stage can suppress the I_{dpeak} during turn-on process. Conversely, from Equation 3.7 and Equation 3.8, it is apparent that the oscillation frequency of i_d solely relies on the parasitic parameters of the SiC MOSFET device and power loop. Despite R_{eq} being small and the damping coefficient relatively low, the switching oscillation of the SiC MOSFET device is inevitable. However, the current amplitude and oscillation time are proportional to the current peak value. Consequently, reducing the turn-on process I_{dpeak} can decrease the amplitude and duration of oscillation, leading to reduced high-frequency EMI emissions.

[t_2~t_3]: Voltage drop stage. The drain current i_d returns to I_L after oscillation following the attainment of I_{dpeak}. Simultaneously, the gate-source voltage u_{gs} remains constant at the Miller level $\mathrm{V}_{\mathrm{miller}}$, giving rise to what is known as the Miller platform. During this stage, the gate current i_g remains steady as the Miller capacitor C_{gd} charges. The expression for i_g can be given as:

$$i_g = \frac{V_{CC} - \mathrm{V}_{\mathrm{miller}}}{R_g} \tag{3.9}$$

The voltage change rate of v_{ds} during the voltage drop stage can be mathematically expressed as:

$$\frac{d\mathrm{u}_{\mathrm{ds}}}{dt} = -\frac{i_g}{C_{gd}} \tag{3.10}$$

The duration of the voltage drop stage, denoted as t_{fu}, can be expressed as:

$$t_{fu} = t_3 - t_2 \approx \frac{C_{gd}(\mathrm{V}_{\mathrm{dc}} - \mathrm{u}_{\mathrm{ds}})}{I} \tag{3.11}$$

By examining Equation 3.11, it becomes evident that both the duration of the voltage drop stage, and the switching loss can be decreased by increasing the driving current.

[t_3~t_4]: Saturated conduction stage. The driving power supply actively charges both the gate-source capacitance C_{gs} and the gate-drain capacitance C_{gd} until the gate-source voltage u_{gs} reaches the positive driving voltage V_{CC}. It is worth noting that increasing the driving current can effectively shorten the duration of saturated conduction and expedite the turn-on process of the SiC MOSFET.

3.2.2.2 SiC MOSFET Turn-Off Process

The turn-off process, in contrast, can be divided into four distinct stages: the turn-off delay stage (t_5~t_6), the voltage rising stage (t_6~t_7), the current drop stage (t_7~t_8), and the closing stage (t_8~t_9) as depicted in Figure 3.4.

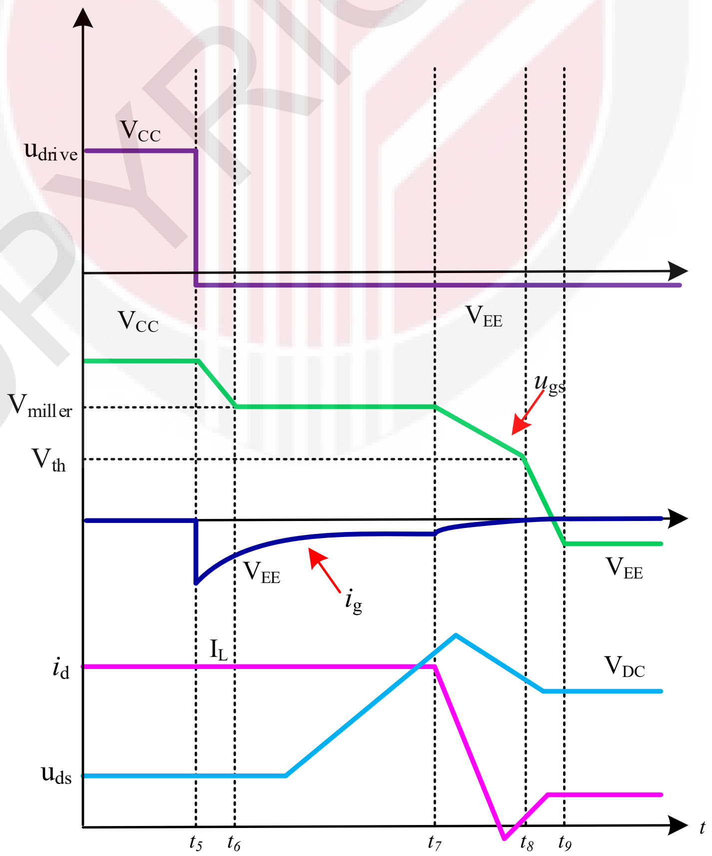

Figure 3.4 : Turn-off Process of SiC MOSFET

When u_{ds} rises to the bus voltage V_{dc}, i_d begins to drop. Due to the influence of parasitic inductance in the power supply loop, the overvoltage peak V_{dspeak} occurs when SiC MOSFET is turned off.

When the drain-source voltage u_{ds} reaches the bus voltage V_{dc}, the drain current i_d starts to decrease. However, due to the presence of parasitic inductance in the power supply loop, an overvoltage peak V_{dspeak} occurs when the SiC MOSFET is turned off:

$$V_{dspeak} = \mathrm{V_{dc}} + L_{loop}\frac{dI_d}{dt} \tag{3.12}$$

Equation 3.7 and Equation 3.8 can still be employed to describe the oscillation frequency and damping coefficient of u_{ds} during turn-off process, but the equivalent capacitance is now $C_{eq} = C_{ds} + C_{gd}$, while the equivalent inductance remains L_{loop}. The current rate of change can still be described by Equation 3.5. Thus, during the current falling stage, decreasing the driving current can effectively attenuate overvoltage occurrences during turn-off process, diminish the amplitude of voltage oscillation, and expedite the oscillation process.

The turn-off process, the voltage rising stage, and the turn-off end stage can be equivalently represented as an RC discharge process. Adding a discharge path in these stages facilitates the rapid discharge of the gate capacitor, thereby expediting the turn-off process and reducing turn-off losses.

3.2.3 Active Gate Driver for SiC MOSFET

To safeguard the SiC MOSFET against the risks associated with positive overvoltage or negative overvoltage breakdown, it is imperative to provide an ample voltage margin for crosstalk compensation. The principle underlying crosstalk elimination can be summarized as follows:

a. During the occurrence of a positive spike in the gate signal, it is necessary to establish a suitably negative gate-source voltage in order to rapidly deactivate the SiC MOSFET and prevent the occurrence of false triggering events associated with positive overvoltage or negative overvoltage breakdown.

b. Following the period of a positive spike in the gate signal, it is essential to promptly raise the gate-source voltage to the zero level to facilitate conduction and prevent the risk of negative overvoltage breakdown.

c. The proposed gate driver circuit should fulfill this objective without the need for additional control signals, while also maintaining simplicity and cost-effectiveness.

To fully exploit the exceptional performance of SiC MOSFET, crosstalk in the three-phase leg must be suppressed in the PMSM drive control system. Currently, effective crosstalk mitigation strategies can be classified into the following four categories:

a. Reducing gate resistance or increasing the gate-source capacitance. However, decreasing the gate resistance can lead to an increase in dv/dt and may result in spikes and oscillation in the switching waveform due to the presence of parasitic parameters in the circuit. Typically, the turn-off resistance is lower than the turn-on resistance, and a capacitor connected in parallel with the turn-off resistance can mitigate the positive spike of the gate-source voltage. Nevertheless, the introduction of additional capacitance prolongs the turn-off process delay time. The capacitor is only connected in parallel with the gate-source when crosstalk occurs, effectively reducing the delay time. However, this approach solely suppresses the positive spike of the gate-source voltage.

b. Raising the negative gate bias voltage. This approach can regulate the positive peak value of the gate-source, but it can also exacerbate the negative overvoltage stress on the gate-source. The datasheet indicates that the optimal negative bias voltage for SiC MOSFET is –5V, and its maximum negative voltage tolerance is approximately –10V, which offers a narrow range for voltage adjustment. Consequently, when negative stray gate voltage emerges, exceeding the maximum negative voltage is likely to occur, elevating the electrical stress on the SiC MOSFET.

c. Using an active Miller clamp is a viable solution. This method involves the inclusion of an additional transistor between the gate and source terminals. This transistor is activated to create a short circuit in the gate-source region when the gate voltage of the affected SiC MOSFET surpasses the clamping threshold voltage. The technology has been successfully commercialized and is widely employed in gate drive integrated circuit (IC). However, in practical applications, the presence of parasitic parameters in the circuit introduces a coupling effect between the gate loop and the power loop. As a result, during fast-switching transients of the SiC MOSFET, the gate voltage may experience violent oscillations, leading to inaccuracies in detecting the true gate-source voltage. Therefore, the effectiveness of the active Miller clamp method may be compromised. The specific implementation of the three aforementioned methods for mitigating crosstalk is illustrated in Figure 3.5, depicting the corresponding concrete electrical circuit.

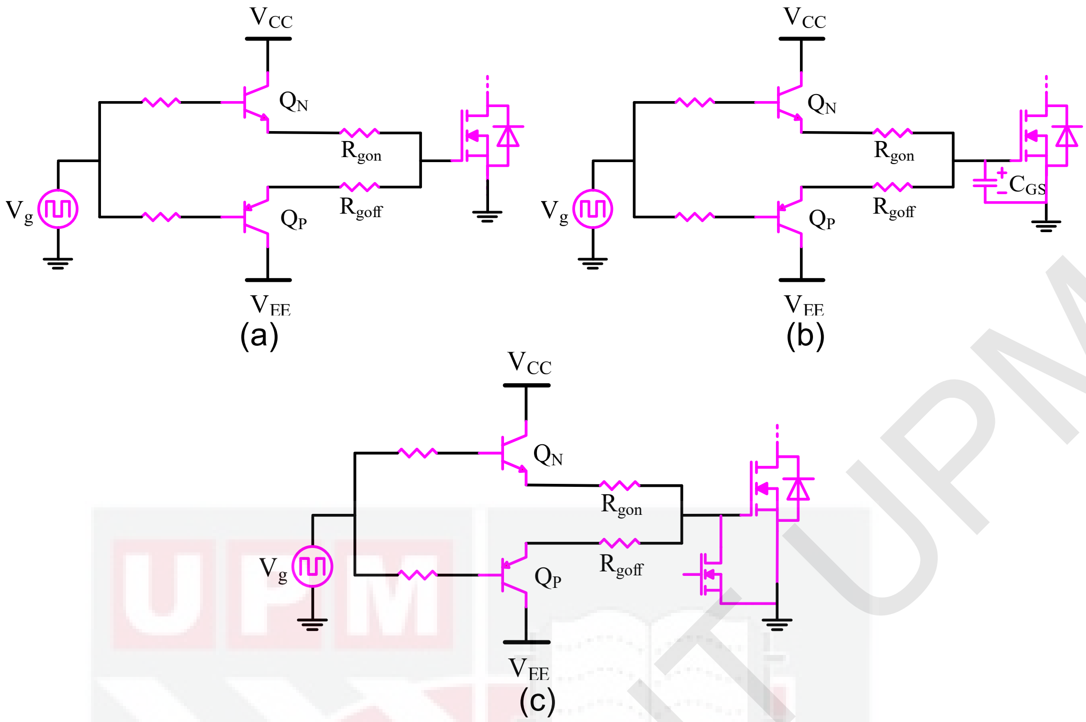

Figure 3.5 : Concrete Measures to Reduce the Crosstalk (a) Reducing the Gate Resistance or Increasing the Gate-Source Capacitance; (b) Raising the Negative Gate Bias Voltage; (c) Using Active Miller Clamp

d. Adding a multi-level gate voltage. This approach involves the integration of auxiliary circuits in the gate-source loop to regulate the gate voltage level during the switching transient process of SiC MOSFET. The primary objective is to prevent false triggering of positive overvoltage or negative overvoltage breakdown. Figure 3.6 illustrates the implementation of gate driver IC and peripheral auxiliary circuits (transistors, diodes, resistors, capacitors) to generate multi-level gate voltage, which can effectively alleviate crosstalk issues. However, implementing this technique requires the control of auxiliary switches, which significantly increases the complexity of control.

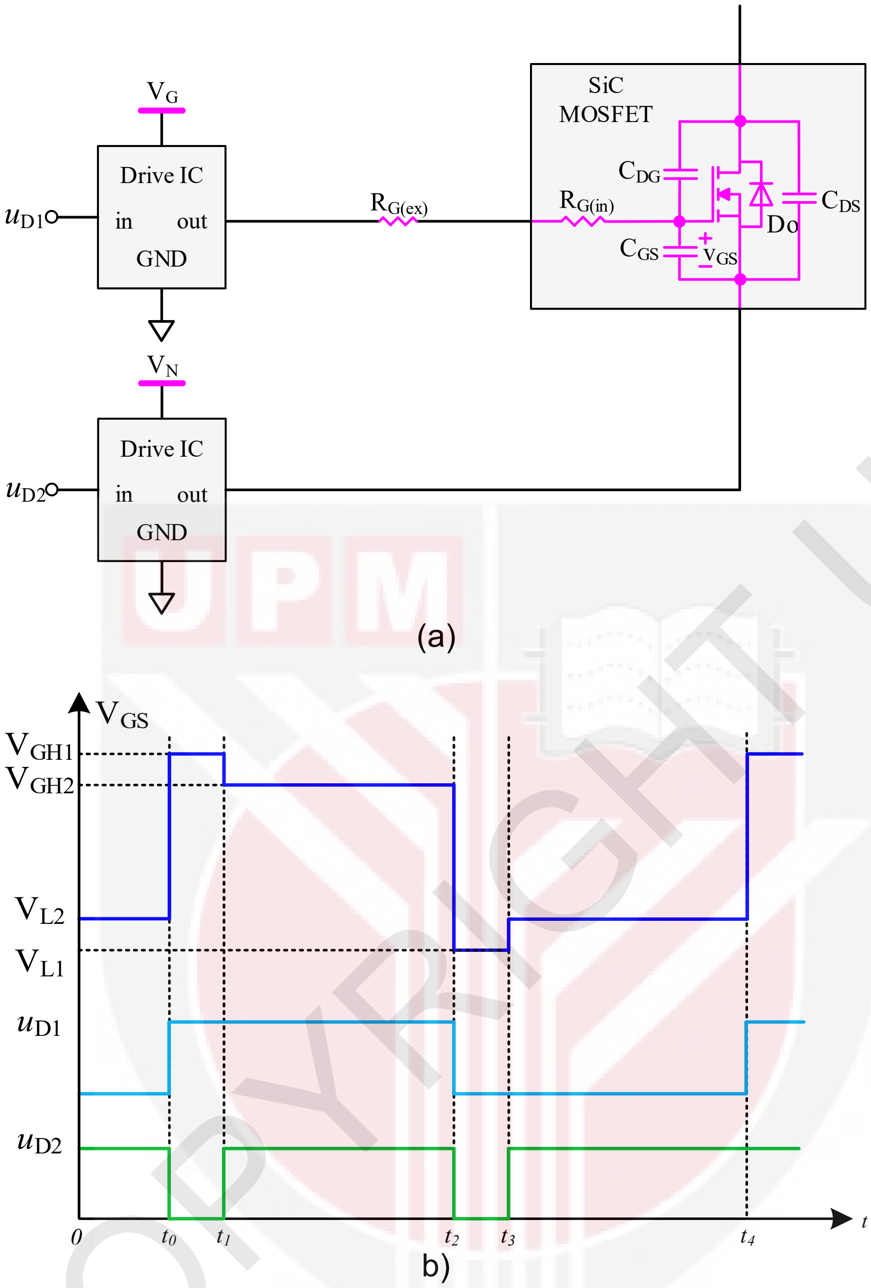

Figure 3.6 : Adding Multi-Level Gate Voltage (a) Circuit Topology; (b) Key Waveform

The performance of SiC MOSFET is contingent upon its electrical parameters and gate driver configuration. The primary responsibility of the gate driver is to guarantee the reliable operation of the SiC MOSFET within its safe operating area (SOA) throughout whole lifespan. An appropriate gate driver circuit should encompass the following considerations:

a. Applying a sufficiently high positive gate bias voltage is essential for minimizing the turn-on resistance $R_{GS(on)}$ of the SiC MOSFET.

b. Employing a suitably low negative gate bias voltage level serves to enhance noise immunity by mitigating the possibility of triggering the gate threshold voltage.

c. Selecting a driver that offers a low impedance path from the gate side, thereby preventing the generation of hazardous voltage spikes on the gate due to I_{DG} caused by dv/dt. Utilizing separate turn-on resistance $R_{g(on)}$ and turn-off resistance $R_{g(off)}$ may prove beneficial in achieving the desired switching on and off speed. Each independent gate resistance for SiC MOSFET facilitates noise reduction.

d. To enhance the performance and reliability of the gate drive circuit, it is recommended to position additional Zener diodes or snubber capacitors in close proximity to the gate-source pins.

e. Incorporating decoupling capacitors serves to bypass power supply voltage noise to the ground, thereby enhancing the gate drive circuit's performance and reliability.

f. The adoption of a Kelvin connection is necessary due to the significant impact of the gate-source inductance, which is a key contributing factor to the generation of high levels of ringing resulting from high current voltage swing rates.

g. Minimizing the gate loop inductance is achieved by reducing the length of the PCB layout.

h. To mitigate the influence of high dv/dt noise from switch nodes on gate signals, it is advisable to prevent the overlapping of power and signal routes.

3.2.4 H-Bridge Inverter Discontinuous Current Source Gate Driver

As previously discussed, enhancing the switching speed of SiC MOSFET is challenging due to factors such as substantial internal gate resistance, high Miller voltage, and limited gate-source voltage ratings. To address problem, this research presents a solution in the form of a discontinuous current source gate driver circuit (CSGD). This circuit comprises a voltage source, H-bridge inverter, and input inductor. Experimental results affirm the feasibility and effectiveness of this approach.

The circuit topology of the discontinuous CSGD is depicted in Figure 3.7. It consists of an H-bridge inverter comprising four controllable SiC MOSFET, denoted as $S_1 \sim S_4$, including their respective body diodes. Additionally, VCC serves as a low voltage power supply providing the driving voltage, while L_r functions as a current source inductor. The core concept behind this design is to generate positive and negative current pulses that are applied to the gate-source capacitor (C_{gs}) during each switch transient. These pulses cause the gate voltage to rise and fall correspondingly, enabling the SiC MOSFET to initiate conduction and turn off effectively with a nearly constant driving current.

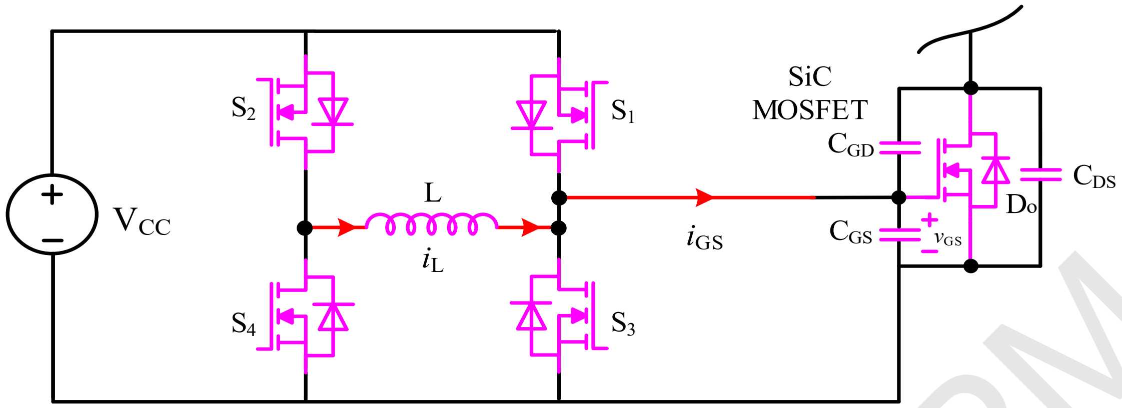

Figure 3.7 : Circuit Topology of H-Bridge Inverter Discontinuous CSGD

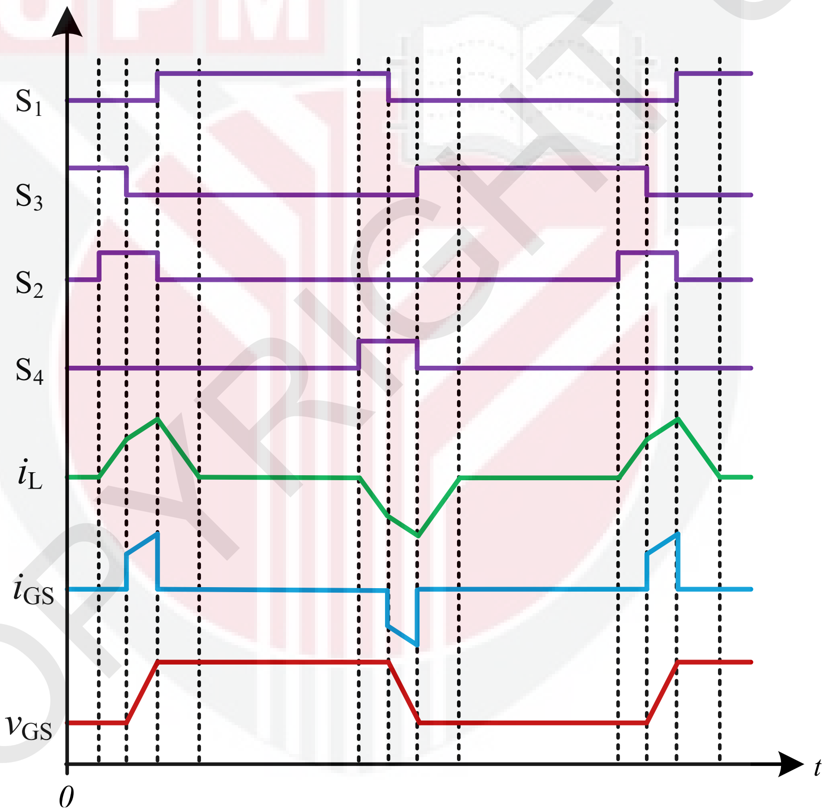

Figure 3.8 : Key Waveforms the Proposed Discontinuous CSGD

The operation stages of four drive switches S_1, S_2, S_3, S_4, discontinuous inductor current i_L, gate drive current i_{GS} and gate to source voltage v_{GS} are illustrated in Figure 3.8.

3.2.5 Reflections and Concepts on Intelligent Gate Drivers

The primary function of conventional gate driver is to amplify the control signal applied to the SiC MOSFET, offer signal isolation, and safeguard the SiC MOSFET during fault conditions. However, intelligent gate drivers go beyond these functions by enhancing switching performance and protection capabilities. The integration of SiC MOSFET with intelligent gate drivers presents an opportunity to enhance the performance of future power converters. Figure 3.9 introduces several novel concepts of intelligent gate drivers.

a. Optimization of Switch Performance

Conventional gate drivers employ $R_{g(on)}$ and $R_{g(off)}$ resistors to apply turn on and off voltages to SiC MOSFET. Conversely, intelligent gate drivers utilize current controlled gate source circuits or gate array resistors as control variables, which can be modified based on measurement results to regulate switching behavior. The implementation of intelligent gate drivers enables the online optimization of significant parameters such as dead time, di/dt, dv/dt, overvoltage, switch loss, and EMI.

b. Monitoring and Protection

To facilitate monitoring and protection, intelligent gate drivers require access to real-time information on the electrical parameters and performance of SiC MOSFET. This can be accomplished through the monitoring of primary equipment voltage and current. A suitable circuit can be employed to measure the voltage and current on both the gate side and current side. As the operating temperature significantly affects the performance and parameters of SiC MOSFET, current intelligent power module (IPM) integrates an on-chip temperature sensor to measure the junction temperature of SiC MOSFET. However, obtaining an accurate junction temperature reading for traditional discrete SiC MOSFET remains challenging, and it is typically estimated using housing temperature and electrical measurements.

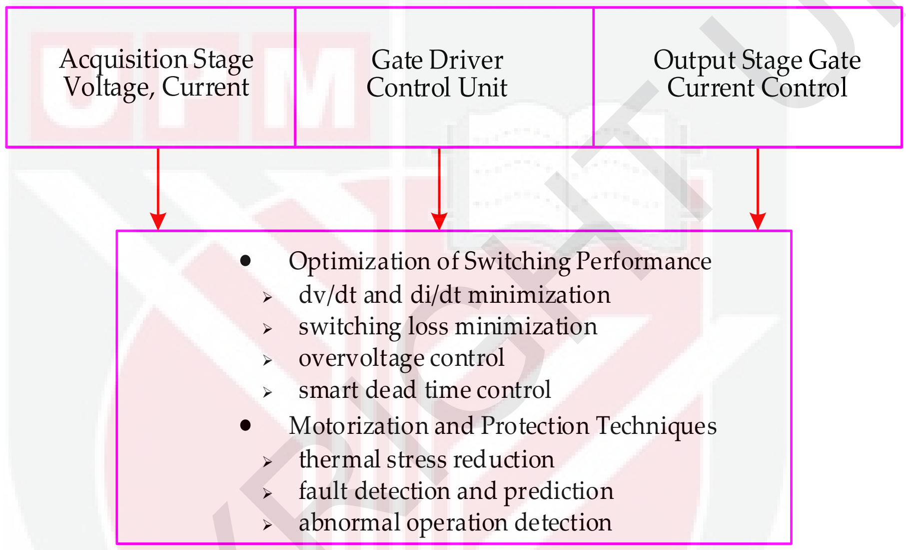

Figure 3.9 : Concept and Function of Intelligent Gate Driver

Switching behavior optimization necessitates the real-time monitoring of the switching waveform and speed of SiC MOSFET, which typically operate within the microsecond range. These places elevated demands on sensing circuitry, whereby the sampling of voltage and current signals is required to occur within nanoseconds. Unfortunately, conventional sensors cannot provide GHz bandwidth range, with the parallel coaxial resistor being the only exception. However, due to its large size, integrating it into a commercial gate driver circuit is infeasible. Consequently, current measurement based intelligent gate drivers' operation for SiC MOSFET is unviable, and voltage measurement must serve as the basis for the intelligent gate drive algorithm. Furthermore, voltage measurement must be performed within the GHz bandwidth. Given that commercial power electronics transformers operate within the kHz range, methods such as high-speed Analog-to-Digital (ADC) converter circuit must be considered.

Moreover, the intelligent gate drive algorithm needs to be compatible with the GHz bandwidth range. The higher switching speed necessitates enhanced capabilities for the control processor, thus warranting the utilization of high-speed microprocessors such as digital signal processor (DSP) and field programmable gate array (FPGA). Closed-loop control, due to its requirement for multiple GHz bandwidths, is not an appropriate solution. Therefore, the development of novel control technologies is imperative in addressing this limitation.

3.3 Three Phase Interleaved Parallel Bidirectional Buck–Boost Converter

In large power applications of the NEEVs, the requirements for power switching devices, rectifier diodes, filter capacitors, energy storage inductors, and other parts (active and passive) are becoming much higher than before, which leads to difficulties in circuit design. From the above Section 2.5 literature review, it can be found that the interleaved parallel multiphase identical circuits technology is widely used in low voltage and high current with large power supply occasions, which has more significant advantages than single-phase circuit [312,313]:

a. Each phase circuit only shares part of the power capacity, reducing the voltage and current stress of electronic switch devices.

b. Improve reliability, even if there are problems in one phase circuit, other phase circuits can still work normally.

c. High-efficiency range of the circuit can be widened by switching phase mode under different power levels.

d. Interleaved parallel technology can improve the equivalent switching frequency of the whole system, depress current ripple, and help to reduce the volume and weight of the filter.

Therefore, in order to effectively increase power and reduce voltage and current stress of electronic components, improve the inherent high ripple rate disadvantage of the traditional bidirectional Buck–Boost converter, a three-phase interleaved parallel bidirectional Buck–Boost (TPIPBi-Buck–Boost) converter is analyzed, and designed in this research, study circuit topology and control strategy, which has very important theoretical research value and broad practical application prospects. In recent years, it is also the hot spot of the energy management system in NEEVs.

3.3.1 Principal Configuration and Operation State in TPIPBi-Buck–Boost Converter

As shown in Figure 3.10, the TPIPBi-Buck–Boost converter, which integrates three same topological structures, V_{Boost} is the high-voltage side of the direct current bus, V_{Buck} is the low-voltage side of the power battery pack, Q_1 to Q_6 are the SiC MOSFET while D_{o1} to D_{o6} and C_{oss1} to C_{oss6} are their parasitic antiparallel diodes and block capacitors, L_1 to L_3 is the energy storage inductors, R_1 to R_2 and C_1 to C_2 are the load resistors and filter capacitors of input and output, respectively. Q_1, Q_2, Q_3, Q_4, Q_5, and Q_6 are connected in series on three-phase inverter bridge, the upper and lower power switches adopt pulse width modulation (PWM) phase shift interleaved complementary control method, and the phase angle of the drive signal differs by 2π/3 = 120° in turn (regardless of dead time).

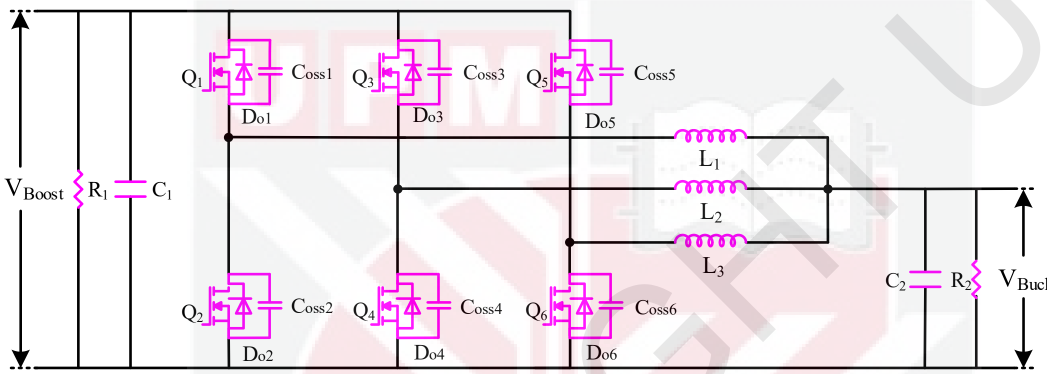

Figure 3.10 : Proposed TPIPBi-Buck–Boost Converter

Based on the above analysis, the TPIPBi-Buck–Boost converter has three operating modes:

a. Charge Buck mode, the battery pack stores the feedback electric energy from the motor drive inverter in the direct current bus through the Boost–Buck converter.

b. Discharge Boost mode, the battery pack release the inner electric energy for direct current bus through the Buck–Boost converter to maintain voltage stability.

c. Electric energy interaction mode, when the NEEVs run normally, transmit and exchange bidirectional electric energy in real time between the power battery pack and direct current bus, so that the Buck and Boost mode can always switch quickly to prevent overcharge or over-discharge of the battery pack.

In order to clarify the operation modes of the TPIPBi-Buck–Boost converter, the battery pack is equivalent to the direct current power supply, and its internal resistance and voltage equalization between single modules are ignored. Some assumptions are summarized as follows:

a. The electrical components and parameters of each phase circuit are the same, and the circulating current loss is not considered.

b. The switch drive signal of each phase shift circuit is strictly conducted, and the phase-to-phase current is equal without offset.

c. The converter is in a stable state, and the inductance works in continuous conduction mode (CCM), regardless of non-ideal saturation conditions.

3.3.1.1 Charge Buck Mode of TPIPBi-Buck–Boost Converter

The switching cycle of the TPIPBi-Buck–Boost converter in charge Buck mode can be dived into eight stages, corresponding to the eight equivalent circuits shown in Figure 3.11. The operation stages are described as follows:

Stage 1 (Figure 3.11a): Q_1, Q_3, and Q_5 are turned off, at the same time, D_{o2}, D_{o4}, and D_{o6} conduct naturally, while high voltage side V_{Boost} stores L_1, L_2 and L_3 are transmitting electrical energy to the low voltage side V_{Buck}. The voltage drops of the L_1 to L_3 and current of the C_2 are given as follows:

$$
\begin{cases}
L_1 \dfrac{di_{L_1}}{dt} = -V_{Buck} \\
L_2 \dfrac{di_{L_2}}{dt} = -V_{Buck} \\
L_3 \dfrac{di_{L_3}}{dt} = -V_{Buck} \\
C_2 \dfrac{dV_{Buck}}{dt} = i_{L_1} + i_{L_2} + i_{L_3} - \dfrac{V_{Buck}}{R_2}
\end{cases}
\tag{3.13}
$$

Stage 2 (Figure 3.11b): Q_1 turn on, Q_3 and Q_5 are turned off, at the same time, D_{o4} and D_{o6} conduct naturally, D_{o2} is off, while high voltage side V_{Boost} stores L_1 together with L_2 and L_3 are transmitting electrical energy to the low voltage side V_{Buck}. The voltage drops of the L_1 to L_3 and current of the C_2 are given as follows:

$$
\begin{cases}
L_1 \dfrac{di_{L_1}}{dt} = V_{Boost} - V_{Buck} \\
L_2 \dfrac{di_{L_2}}{dt} = -V_{Buck} \\
L_3 \dfrac{di_{L_3}}{dt} = -V_{Buck} \\
C_2 \dfrac{dV_{Buck}}{dt} = i_{L_1} + i_{L_2} + i_{L_3} - \dfrac{V_{Buck}}{R_2}
\end{cases}
\tag{3.14}
$$

Stage 3 (Figure 3.11c): Q_3 turn on, Q_1 and Q_5 are turned off, at the same time, D_{o2} and D_{o6} conduct naturally, D_{o4} is off, while high voltage side V_{Boost} stores L_2 together with L_1 and L_3 are transmitting electrical energy to the low voltage side V_{Buck}. The voltage drops of the L_1 to L_3 and current of the C_2 are given as follows:

$$\begin{cases} L_1 \dfrac{di_{L_1}}{dt} = -V_{Buck} \\ L_2 \dfrac{di_{L_2}}{dt} = V_{Boost} - V_{Buck} \\ L_3 \dfrac{di_{L_3}}{dt} = -V_{Buck} \\ C_2 \dfrac{dV_{Buck}}{dt} = i_{L_1} + i_{L_2} + i_{L_3} - \dfrac{V_{Buck}}{R_2} \end{cases} \tag{3.15}$$

Stage 4 (Figure 3.11d): Q_5 turn on, Q_1 and Q_3 are turned off, at the same time, D_{o2} and D_{o4} conduct naturally, D_{o6} is off, while high voltage side V_{Boost} stores L_3 together with L_1 and L_2 are transmitting electrical energy to the low voltage side V_{Buck}. The voltage drops of the L_1 to L_3 and current of the C_2 are given as follows:

$$\begin{cases} L_1 \dfrac{di_{L_1}}{dt} = -V_{Buck} \\ L_2 \dfrac{di_{L_2}}{dt} = -V_{Buck} \\ L_3 \dfrac{di_{L_3}}{dt} = V_{Boost} - V_{Buck} \\ C_2 \dfrac{dV_{Buck}}{dt} = i_{L_1} + i_{L_2} + i_{L_3} - \dfrac{V_{Buck}}{R_2} \end{cases} \tag{3.16}$$

Stage 5 (Figure 3.11e): Q_1 and Q_3 turn on, Q_5 is turned off, at the same time, D_{o6} conducts naturally, D_{o2} and D_{o4} are off, while high voltage side V_{Boost} stores L_1 and L_2 together with L_3 are transmitting electrical energy to the low voltage side V_{Buck}. The voltage drops of the L_1 to L_3 and current of the C_2 are given as follows:

$$\begin{cases} L_1 \dfrac{di_{L_1}}{dt} = V_{Boost} - V_{Buck} \\ L_2 \dfrac{di_{L_2}}{dt} = V_{Boost} - V_{Buck} \\ L_3 \dfrac{di_{L_3}}{dt} = -V_{Buck} \\ C_2 \dfrac{dV_{Buck}}{dt} = i_{L_1} + i_{L_2} + i_{L_3} - \dfrac{V_{Buck}}{R_2} \end{cases} \tag{3.17}$$

Stage 6 (Figure 3.11f): Q_1 and Q_5 turn on, Q_3 is turned off, at the same time, D_{o4} conducts naturally, D_{o2} and D_{o6} are off, while high voltage side V_{Boost} stores L_1 and L_3 together with L_2 are transmitting electrical energy to the low voltage side V_{Buck}. The voltage drops of the L_1 to L_3 and current of the C_2 are given as follows:

$$\begin{cases} L_1 \dfrac{di_{L_1}}{dt} = V_{Boost} - V_{Buck} \\ L_2 \dfrac{di_{L_2}}{dt} = -V_{Buck} \\ L_3 \dfrac{di_{L_3}}{dt} = V_{Boost} - V_{Buck} \\ C_2 \dfrac{dV_{Buck}}{dt} = i_{L_1} + i_{L_2} + i_{L_3} - \dfrac{V_{Buck}}{R_2} \end{cases} \tag{3.18}$$

Stage 7 (Figure 3.11g): Q_3 and Q_5 turn on, Q_1 is turned off, at the same time, D_{o2} conducts naturally, D_{o4} and D_{o6} are off, while high voltage side V_{Boost} stores L_2 and L_3 together with L_1 are transmitting electrical energy to the low voltage side V_{Buck}. The voltage drops of the L_1 to L_3 and current of the C_2 are given as follows:

$$
\begin{cases}
L_1 \dfrac{di_{L_1}}{dt} = -V_{Buck} \\
L_2 \dfrac{di_{L_2}}{dt} = V_{Boost} - V_{Buck} \\
L_3 \dfrac{di_{L_3}}{dt} = V_{Boost} - V_{Buck} \\
C_2 \dfrac{dV_{Buck}}{dt} = i_{L_1} + i_{L_2} + i_{L_3} - \dfrac{V_{Buck}}{R_2}
\end{cases}
\tag{3.19}
$$

Stage 8 (Figure 3.11h): Q_1, Q_3 and Q_5 turn on, at the same time, D_{o2}, D_{o4} and D_{o6} are off, while high voltage side V_{Boost} stores L_1, L_2 and L_3 are transmitting electrical energy to the low voltage side V_{Buck}. The voltage drops of the L_1 to L_3 and current of the C_2 are given as follows:

$$
\begin{cases}
L_1 \dfrac{di_{L_1}}{dt} = V_{Boost} - V_{Buck} \\
L_2 \dfrac{di_{L_2}}{dt} = V_{Boost} - V_{Buck} \\
L_3 \dfrac{di_{L_3}}{dt} = V_{Boost} - V_{Buck} \\
C_2 \dfrac{dV_{Buck}}{dt} = i_{L_1} + i_{L_2} + i_{L_3} - \dfrac{V_{Buck}}{R_2}
\end{cases}
\tag{3.20}
$$

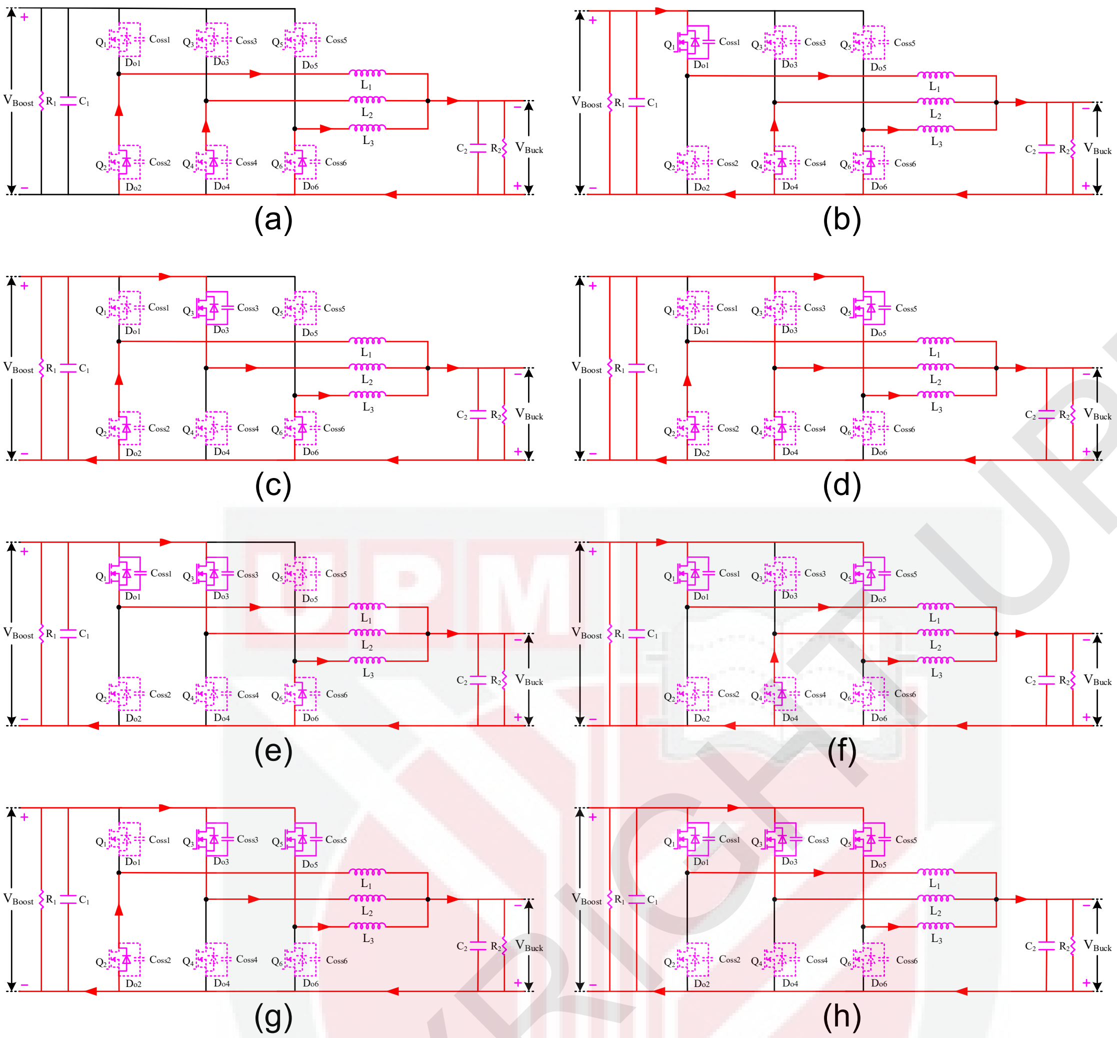

Figure 3.11 : Equivalent Circuits in Charge Buck Mode: (a) Stage 1; (b) Stage 2; (c) Stage 3; (d) Stage 4; (e) Stage 5; (f) Stage 6; (g) Stage 7; (h) Stage 8

The key waveforms of the charge Buck mode of TPIPBi-Buck–Boost converter are shown in Figure 3.12. In each switching cycle, Table 3.1 depicts that they can be divided into three cases:

Table 3.1 : Define Stages of Charge Buck Mode under Duty Ratio

Duty Ratio	Charge Buck Mode
0<d≤1/3	stages 1,2,3,4
1/3<d≤2/3	stages 2,3,4,5,6,7
2/3<d<1	stages 5,6,7,8

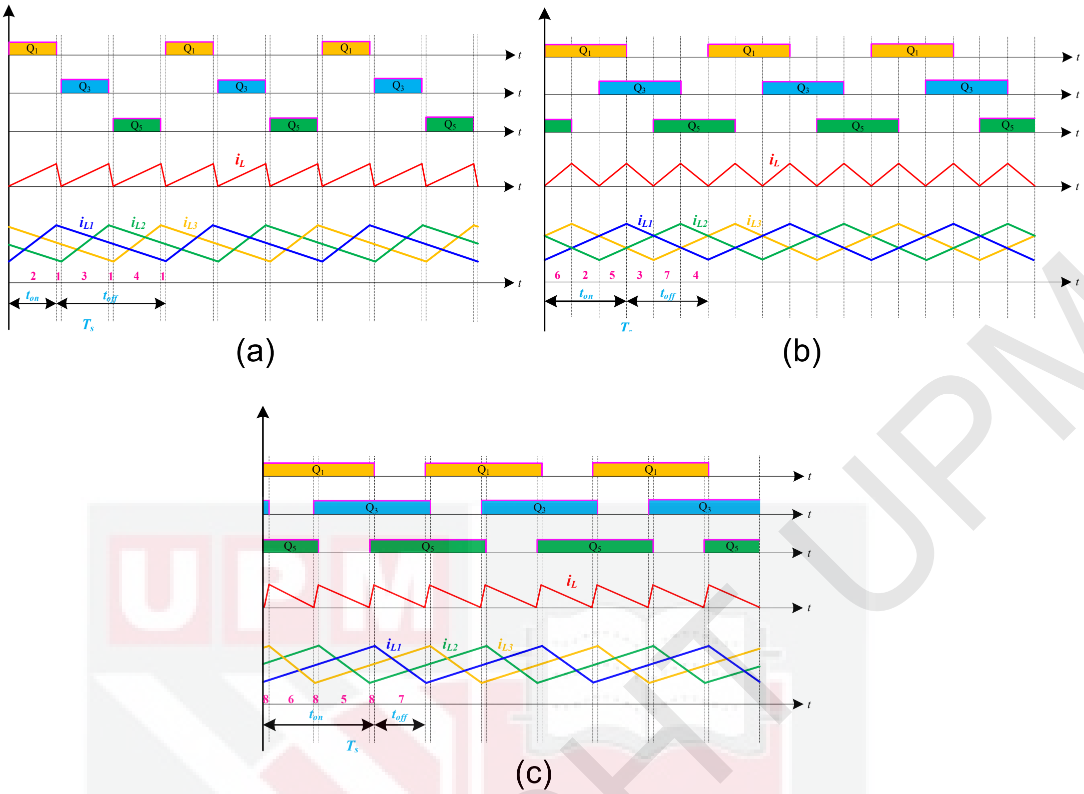

Figure 3.12 : Key Waveforms the Charge Buck Mode: (a) 0 < d ≤ 1/3; (b) 1/3 < d ≤ 2/3; (c) 2/3 < d < 1

3.3.1.2 Discharge Boost Mode of TPIPBi-Buck–Boost Converter

The switching cycle in discharge Boost mode of the TPIPBi-Buck–Boost converter can be divided into eight stages in a similar way, corresponding to the eight equivalent circuits shown in Figure 3.13. The operation stages are also described as follows:

Stage 1 (Figure 3.13a): Q_2, Q_4 and Q_6 are turned off, at the same time, D_{o1}, D_{o3} and D_{o5} conduct naturally, while low voltage side V_{Buck} stores L_1, L_2 and L_3 are transmitting electrical energy to the high voltage side V_{Boost}. The voltage drops of the L_1 to L_3 and current of the C_1 are given as follows:

$$
\begin{cases}
L_1 \dfrac{di_{L_1}}{dt} = V_{Buck} - V_{Boost} \\
L_2 \dfrac{di_{L_2}}{dt} = V_{Buck} - V_{Boost} \\
L_3 \dfrac{di_{L_3}}{dt} = V_{Buck} - V_{Boost} \\
C_1 \dfrac{dV_{Boost}}{dt} = i_{L_1} + i_{L_2} + i_{L_3} - \dfrac{V_{Boost}}{R_1}
\end{cases}
\tag{3.21}
$$

Stage 2 (Figure 3.13b): Q_2 turn on, Q_4 and Q_6 are turned off, at the same time, D_{o3} and D_{o5} conduct naturally, D_{o1} is off, while low voltage side V_{Buck} stores L_1 together with L_2 and L_3 are transmitting electrical energy to the high voltage side V_{Boost}. The voltage drops of the L_1 to L_3 and current of the C_1 are given as follows:

$$
\begin{cases}
L_1 \dfrac{di_{L_1}}{dt} = V_{Buck} \\
L_2 \dfrac{di_{L_2}}{dt} = V_{Buck} - V_{Boost} \\
L_3 \dfrac{di_{L_3}}{dt} = V_{Buck} - V_{Boost} \\
C_1 \dfrac{dV_{Boost}}{dt} = i_{L_2} + i_{L_3} - \dfrac{V_{Boost}}{R_1}
\end{cases}
\tag{3.22}
$$

Stage 3 (Figure 3.13c): Q_4 turn on, Q_2 and Q_6 are turned off, at the same time, D_{o1} and D_{o5} conduct naturally, D_{o3} is off, while low voltage side V_{Buck} stores L_2 together with L_1 and L_3 are transmitting electrical energy to the high voltage side V_{Boost}. The voltage drops of the L_1 to L_3 and current of the C_1 are given as follows:

$$
\begin{cases}
L_1 \dfrac{di_{L_1}}{dt} = V_{Buck} - V_{Boost} \\
L_2 \dfrac{di_{L_2}}{dt} = V_{Buck} \\
L_3 \dfrac{di_{L_3}}{dt} = V_{Buck} - V_{Boost} \\
C_1 \dfrac{dV_{Boost}}{dt} = i_{L_1} + i_{L_3} - \dfrac{V_{Boost}}{R_1}
\end{cases}
\tag{3.23}
$$

Stage 4 (Figure 3.13d): Q_6 turn on, Q_2 and Q_4 are turned off, at the same time, D_{o1} and D_{o3} conduct naturally, D_{o5} is off, while low voltage side V_{Buck} stores L_3 together with L_1 and L_2 are transmitting electrical energy to the high voltage side V_{Boost}. The voltage drops of the L_1 to L_3 and current of the C_1 are given as follows:

$$
\begin{cases}
L_1 \dfrac{di_{L_1}}{dt} = V_{Buck} - V_{Boost} \\
L_2 \dfrac{di_{L_2}}{dt} = V_{Buck} - V_{Boost} \\
L_3 \dfrac{di_{L_3}}{dt} = V_{Buck} \\
C_1 \dfrac{dV_{Boost}}{dt} = i_{L_1} + i_{L_2} - \dfrac{V_{Boost}}{R_2}
\end{cases}
\tag{3.24}
$$

Stage 5 (Figure 3.13e): Q_2 and Q_4 turn on, Q_6 is turned off, at the same time, D_{o5} conducts naturally, D_{o1} and D_{o3} are off, while low voltage side V_{Buck} stores L_1 and L_2 together with L_3 are transmitting electrical energy to the high voltage side V_{Boost}. The voltage drops of the L_1 to L_3 and current of the C_1 are given as follows:

$$
\begin{cases}
L_1 \dfrac{di_{L_1}}{dt} = V_{Buck} \\
L_2 \dfrac{di_{L_2}}{dt} = V_{Buck} \\
L_3 \dfrac{di_{L_3}}{dt} = V_{Buck} - V_{Boost} \\
C_1 \dfrac{dV_{Boost}}{dt} = i_{L_3} - \dfrac{V_{Boost}}{R_1}
\end{cases} \tag{3.25}
$$

Stage 6 (Figure 3.13f): Q_2 and Q_6 turn on, Q_4 is turned off, at the same time, D_{o3} conducts naturally, D_{o1} and D_{o5} are off, while low voltage side V_{Buck} stores L_1 and L_3 together with L_2 are transmitting electrical energy to the high voltage side V_{Boost}. The voltage drops of the L_1 to L_3 and current of the C_1 are given as follows:

$$
\begin{cases}
L_1 \dfrac{di_{L_1}}{dt} = V_{Buck} \\
L_2 \dfrac{di_{L_2}}{dt} = V_{Buck} - V_{Boost} \\
L_3 \dfrac{di_{L_3}}{dt} = V_{Buck} \\
C_1 \dfrac{dV_{Boost}}{dt} = i_{L_2} - \dfrac{V_{Boost}}{R_1}
\end{cases} \tag{3.26}
$$

Stage 7 (Figure 3.13g): Q_4 and Q_6 turn on, Q_2 is turned off, at the same time, D_{o1} conducts naturally, D_{o3} and D_{o5} are off, while low voltage side V_{Buck} stores L_2 and L_3 together with L_1 are transmitting electrical energy to the high voltage side V_{Boost}. The voltage drops of the L_1 to L_3 and current of the C_1 are given as follows:

$$\begin{cases} L_1 \dfrac{di_{L_1}}{dt} = V_{Buck} - V_{Boost} \\ L_2 \dfrac{di_{L_2}}{dt} = V_{Buck} \\ L_3 \dfrac{di_{L_3}}{dt} = V_{Buck} \\ C_1 \dfrac{dV_{Boost}}{dt} = i_{L_1} - \dfrac{V_{Boost}}{R_1} \end{cases} \tag{3.27}$$

Stage 8 (Figure 3.13h): Q_2, Q_4 and Q_6 turn on, at the same time, D_{o1}, D_{o3} and D_{o5} are off, while low voltage side V_{Buck} stores L_1, L_2 and L_3 are transmitting electrical energy to the high voltage side V_{Boost}. The voltage drops of the L_1 to L_3 and current of the C_1 are given as follows:

$$\begin{cases} L_1 \dfrac{di_{L_1}}{dt} = V_{Buck} \\ L_2 \dfrac{di_{L_2}}{dt} = V_{Buck} \\ L_3 \dfrac{di_{L_3}}{dt} = V_{Buck} \\ C_1 \dfrac{dV_{Boost}}{dt} = -\dfrac{V_{Boost}}{R_1} \end{cases} \tag{3.28}$$

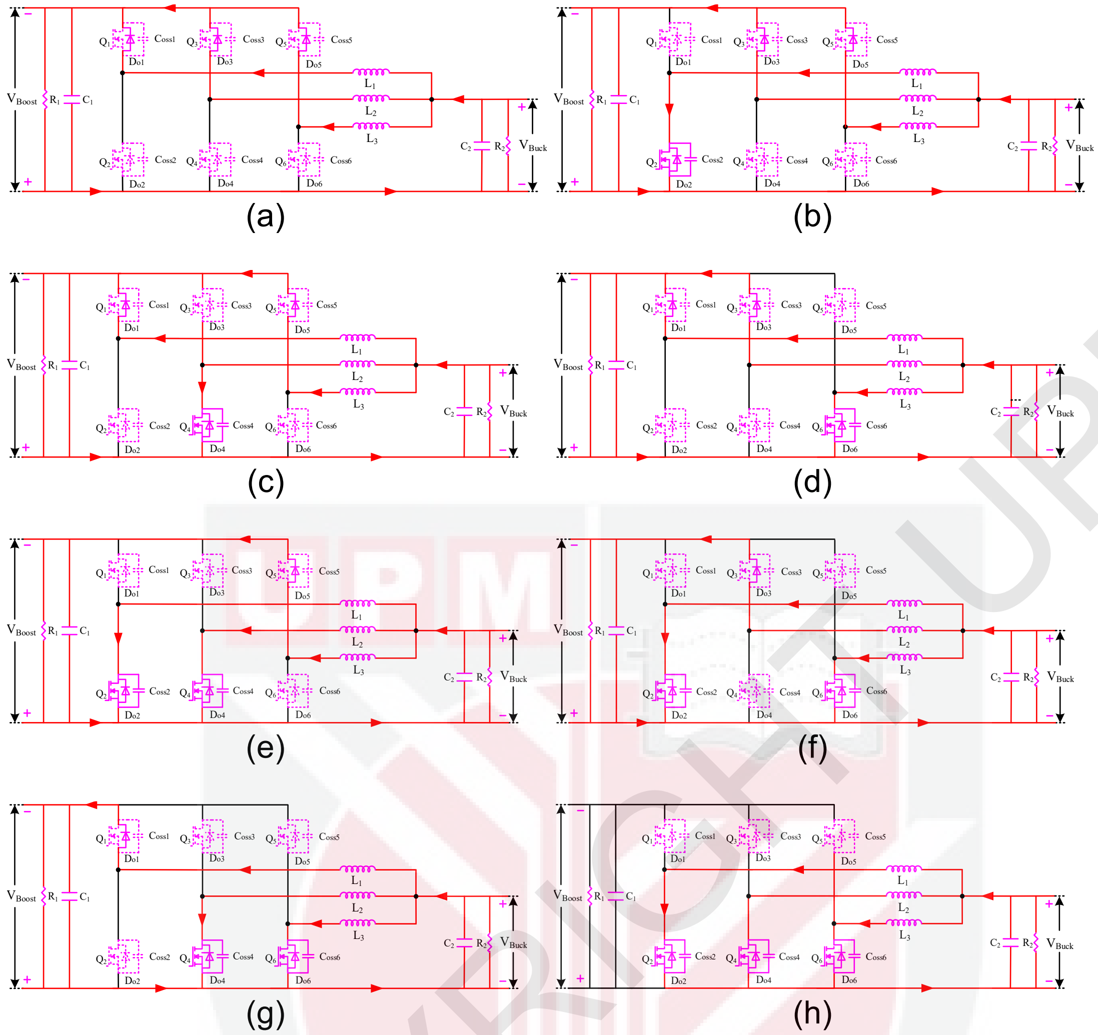

Figure 3.13 : Equivalent Circuits in Discharge Boost Mode: (a) Stage 1; (b) Stage 2; (c) Stage 3; (d) Stage 4; (e) Stage 5; (f) Stage 6; (g) Stage 7; (h) Stage 8

The key waveforms of the charge Boost mode of TPIPBi-Buck–Boost converter are shown in Figure 3.14. In each switching cycle, Table 3.2 depicts that they can be divided into three cases:

Table 3.2 : Define Stages of Discharge Boost Mode under Duty Ratio

Duty Ratio	Charge Boost Mode
0<d≤1/3	stages 1,2,3,4
1/3<d≤2/3	stages 2,3,4,5,6,7
2/3<d<1	stages 5,6,7,8

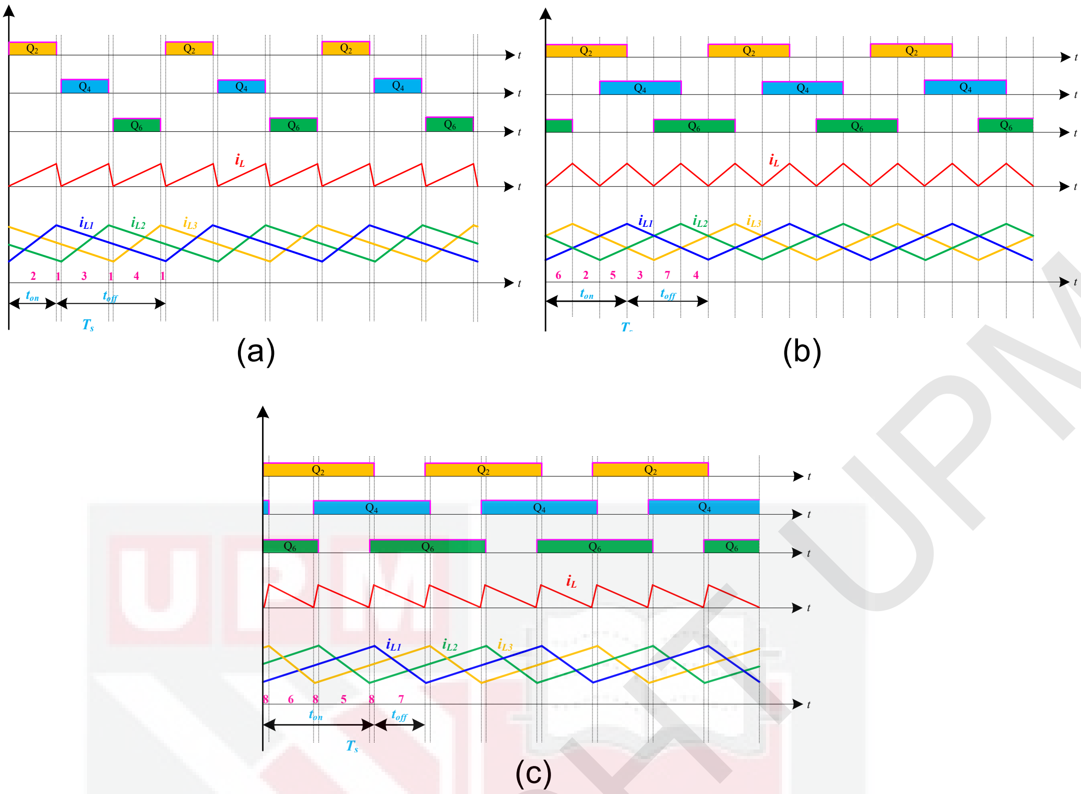

Figure 3.14 : Key Waveforms the Discharge Boost Mode: (a) 0 < d ≤ 1/3; (b) 1/3 < d ≤ 2/3; (c) 2/3 < d < 1

3.3.1.3 Electrical Energy Interaction Mode

The previous theoretical analysis proves that the TPIPBi-Buck–Boost converter not only achieves charge Buck and discharge Boost mode, but also has the ability of real-time bidirectional electrical energy exchange when the entire system is working properly.

As shown in Figure 3.15, in the electrical energy interaction mode, when the EVs run normally, the battery pack and direct current bus transmit real-time bidirectional electrical energy exchange, so that the TPIPBi-Buck–Boost converter can switch between charge Buck mode and discharge Boost mode quickly, smoothly and flexibly, to prevent overcharge or over discharge of the battery pack. In addition, this electrical energy interaction mode is not fundamentally different from the working conditions of Buck and Boost conversion of normal circuits. The drive angle of the power switches Q_1 to Q_6 are phase-shifted by 120° and independent of each other, which avoids the discontinuous current conduction of the energy storage inductors L_1 to L_3 when the light load, poor current stability, and large instantaneous inrush current when the modes are switching. In this mode, regardless of whether charge Buck mode and discharge Boost mode is implemented, the duty cycle of Q_1, Q_2, Q_3, or Q_4, Q_5, Q_6 are correspondingly close to 0. Both the low voltage side V_{Buck} and high voltage side V_{Boost} of the TPIPBi-Buck–Boost converter is kept constant and energy exchange is realized, to hold the voltage stability of the battery pack and the direct current bus in all circumstances.

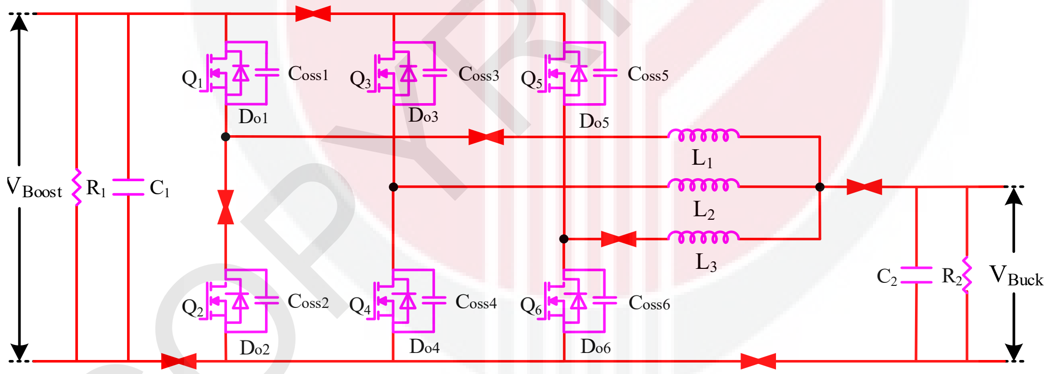

Figure 3.15 : Equivalent Circuits in Electrical Energy Interaction Mode

3.3.2 Mathematical Model of TPIPBi-Buck–Boost Converter

The TPIPBi-Buck–Boost converter is a nonlinear, strongly coupled multivariable system, and it is necessary to solve mathematical equations to obtain the relationship among variables in the circuits [314,315].

Section 3.2.2 puts forward the AC small signal equivalent circuit model based on the non-ideal electronic components and supplies by using the basic modeling method for the proposed TPIPBi-Buck–Boost converter in Section 2. The transfer functions of voltage and current double closed control loop in charge buck and discharge Boost mode are viewed, which lay the foundations for the digital control strategy in Section 4. In a modeled and analyzed process, the TPIPBi-Buck–Boost converter in CCM is to reduce the voltage and current ripple because of increasing the power.

3.3.2.1 Charge Buck Mode Based on AC Small Signal Analysis

In the charge Buck mode of the TPIPBi-Buck–Boost converter, Q_1, Q_3 and Q_5 turn on, the voltage drops of the L_1 to L_3 are given as follows:

$$\begin{cases} v_{L_1}(t) = L_1 \dfrac{di_{L_1}(t)}{dt} = v_{Boost}(t) - v_{Buck}(t) \\ v_{L_2}(t) = L_2 \dfrac{di_{L_2}(t)}{dt} = v_{Boost}(t) - v_{Buck}(t) \\ v_{L_3}(t) = L_3 \dfrac{di_{L_3}(t)}{dt} = v_{Boost}(t) - v_{Buck}(t) \end{cases} \tag{3.29}$$

Q_1, Q_3 and Q_5 are turned off, the voltage drops of the L_1 to L_3 are given as follows:

$$\begin{cases} v_{L_1}(t) = L_1 \dfrac{di_{L_1}}{dt} = -v_{Buck}(t) \\ v_{L_2}(t) = L_2 \dfrac{di_{L_2}}{dt} = -v_{Buck}(t) \\ v_{L_3}(t) = L_3 \dfrac{di_{L_3}}{dt} = -v_{Buck}(t) \end{cases} \tag{3.30}$$

In order to eliminate the influence of switching ripple, when the TPIPBi-Buck–Boost converter needs to satisfy the small ripple assumption $f_t \ll f_s$ and the low frequency assumption $f_g \ll f_s$ (turnover frequency f_t, switching frequency f_s, and AC small signal frequency f_g), the input voltage $v_{Boost}(t)$ and the output voltage $v_{Buck}(t)$ are continuous and change little in one switching cycle T_s, so they can be approximately equivalent to the average value, namely:

$$\begin{cases} v_{Boost}(t) \approx \langle v_{Boost}(t) \rangle_{T_s} \\ v_{Buck}(t) \approx \langle v_{Buck}(t) \rangle_{T_s} \end{cases} \tag{3.31}$$

According to Equation 3.30 and Equation 3.31, the average voltages of the L_1 to L_3 in T_s are, respectively:

$$\begin{cases} \langle v_{L_1}(t) \rangle_{T_s} = \dfrac{1}{T_s}\left[\displaystyle\int_0^{d_1T_s} v_{L_1}(t)\,dt + \int_{d_1T_s}^{T_s} v_{L_1}(t)\,dt\right] = d_1 \langle v_{Boost}(t) \rangle_{T_s} - \langle v_{Buck}(\\ \langle v_{L_2}(t) \rangle_{T_s} = \dfrac{1}{T_s}\left[\displaystyle\int_0^{d_3T_s} v_{L_2}(t)\,dt + \int_{d_3T_s}^{T_s} v_{L_2}(t)\,dt\right] = d_3 \langle v_{Boost}(t) \rangle_{T_s} - \langle v_{Buck}(\\ \langle v_{L_3}(t) \rangle_{T_s} = \dfrac{1}{T_s}\left[\displaystyle\int_0^{d_5T_s} v_{L_3}(t)\,dt + \int_{d_5T_s}^{T_s} v_{L_3}(t)\,dt\right] = d_5 \langle v_{Boost}(t) \rangle_{T_s} - \langle v_{Buck}(\end{cases} \tag{3.32}$$

Averaging characteristic of the energy storage inductors L_1 to L_3:

$$\begin{cases} \langle v_{L_1}(t) \rangle_{T_s} = L_1 \dfrac{d\langle i_{L_1}(t) \rangle_{T_s}}{dt} \\ \langle v_{L_2}(t) \rangle_{T_s} = L_2 \dfrac{d\langle i_{L_2}(t) \rangle_{T_s}}{dt} \\ \langle v_{L_3}(t) \rangle_{T_s} = L_3 \dfrac{d\langle i_{L_3}(t) \rangle_{T_s}}{dt} \end{cases} \tag{3.33}$$

Substituting Equation 3.32 into Equation 3.33 yields:

$$\begin{cases} L_1 \dfrac{d\langle i_{L_1}(t)\rangle_{T_s}}{dt} = d_1'\langle v_{Boost}(t)\rangle_{T_s} - \langle v_{Buck}(t)\rangle_{T_s} \\ L_2 \dfrac{d\langle i_{L_2}(t)\rangle_{T_s}}{dt} = d_3'\langle v_{Boost}(t)\rangle_{T_s} - \langle v_{Buck}(t)\rangle_{T_s} \\ L_3 \dfrac{d\langle i_{L_3}(t)\rangle_{T_s}}{dt} = d_5'\langle v_{Boost}(t)\rangle_{T_s} - \langle v_{Buck}(t)\rangle_{T_s} \end{cases} \tag{3.34}$$

where $d_i' = 1 - d_i (i = 1,3,5)$, according to Kirchhoff's Law, the average current of the capacitor C_2 in T_s is:

$$\begin{aligned} \langle i_{C_2}(t)\rangle_{T_s} &= C_2 \frac{d\langle v_{Boost}(t)\rangle_{T_s}}{dt} \\ &= d_1'\langle i_{L_1}(t)\rangle_{T_s} + d_3'\langle i_{L_2}(t)\rangle_{T_s} + d_5'\langle i_{L_3}(t)\rangle_{T_s} - \frac{\langle v_{Buck}(t)\rangle_{T_s}}{R_2} \end{aligned} \tag{3.35}$$

So far, the relationship between the voltage and current of the TPIPBi-Buck–Boost converter in charge Buck mode has been established, but Equation 3.34 and Equation 3.35 are a set of nonlinear equations, and each variable contains direct current and low frequency small signal components. An approximate analytical method can be used to solve the nonlinear equations, that is, to find the static operating point and perform linearization processing to separate the direct current component and the AC small signal component. In order to ensure that the linearization of the TPIPBi-Buck–Boost converter at the static operating point does not cause large errors, the small signal assumption must be satisfied:

$$\begin{cases} \hat{x}(t) \ll |X(t)| \\ \mathrm{x}(t) \approx \langle \mathrm{x}(t)\rangle_{T_s} \end{cases} \tag{3.36}$$

where $\hat{x}(t)$ is the AC component magnitude of each variable, $|X|$ is the corresponding direct current component. For the average $\langle \mathrm{x}(t) \rangle_{T_s}$ of $x(t)$ in T_s, it can be decomposed into the sum of the direct current component X and the AC small signal component $\hat{x}(t)$, that is:

$$\langle \mathrm{x}(t) \rangle_{T_s} = X + \hat{x}(t) \tag{3.37}$$

Thus, the assumption is

$$\begin{cases} \langle v_{Buck}(t) \rangle_{T_s} = V_{Buck} + \hat{v}_{Buck}(t) \\ \langle v_{Boost}(t) \rangle_{T_s} = V_{Boost} + \hat{v}_{Boost}(t) \\ \langle i_{L_1}(t) \rangle_{T_s} = I_{L_3} + \hat{\imath}_{L_1}(t) \\ \langle i_{L_2}(t) \rangle_{T_s} = I_{L_3} + \hat{\imath}_{L_2}(t) \\ \langle i_{L_3}(t) \rangle_{T_s} = I_{L_3} + \hat{\imath}_{L_3}(t) \end{cases} \tag{3.38}$$

Substituting Equation 3.38 into Equation 3.35 yields:

$$\begin{cases} L_1 \dfrac{d\left[I_{L_1} + \hat{\imath}_{L_1}(t)\right]}{dt} = \left[D_1 + \hat{d}_1(t)\right]\left[V_{Boost} + \hat{v}_{Boost}(t)\right] - \left[V_{Buck} - \hat{v}_{Buck}(t)\right] \\ L_2 \dfrac{d\left[I_{L_2} + \hat{\imath}_{L_2}(t)\right]}{dt} = \left[D_3 + \hat{d}_3(t)\right]\left[V_{Boost} + \hat{v}_{Boost}(t)\right] - \left[V_{Buck} - \hat{v}_{Buck}(t)\right] \\ L_3 \dfrac{d\langle I_{L_3} + \hat{\imath}_{L_3}(t)\rangle}{dt} = \left[D_5 + \hat{d}_5(t)\right]\left[V_{Boost} + \hat{v}_{Boost}(t)\right] - \left[V_{Buck} - \hat{v}_{Buck}(t)\right] \end{cases} \tag{3.39}$$

Finishing Equation 3.39, and can be obtained by ignoring the second order minute term:

$$\begin{cases} L_1 \dfrac{d\hat{\imath}_{L_1}(t)}{dt} = D_1 \hat{v}_{Boost}(t) + V_{Boost} \hat{d}_1(t) - \hat{v}_{Buck}(t) \\ L_2 \dfrac{d\hat{\imath}_{L_2}(t)}{dt} = D_3 \hat{v}_{Boost}(t) + V_{Boost} \hat{d}_3(t) - \hat{v}_{Buck}(t) \\ L_3 \dfrac{d\hat{\imath}_{L_3}(t)}{dt} = D_5 \hat{v}_{Boost}(t) + V_{Boost} \hat{d}_5(t) - \hat{v}_{Buck}(t) \end{cases} \tag{3.40}$$

Similarly, substituting Equation 3.38 into Equation 3.37 yields:

$$C_2 \frac{dV_{Buck}(t)}{dt} = d_1' \hat{\imath}_{L_1}(t) - I_{L_1}\hat{d}_1(t) + d_3' \hat{\imath}_{L_2}(t) - I_{L_2}\hat{d}_3(t) + d_5' \hat{\imath}_{L_3}(t) - I_{L_3}\hat{d}_5(t) - \frac{\hat{v}_{Boost}(t)}{R_1} \tag{3.41}$$

According to Equation 3.40 and Equation 3.41, the AC small signal equivalent circuit model of the TPIPBi-Buck–Boost Converter in charge Buck mode can be established, as illustrated in Figure 3.16.

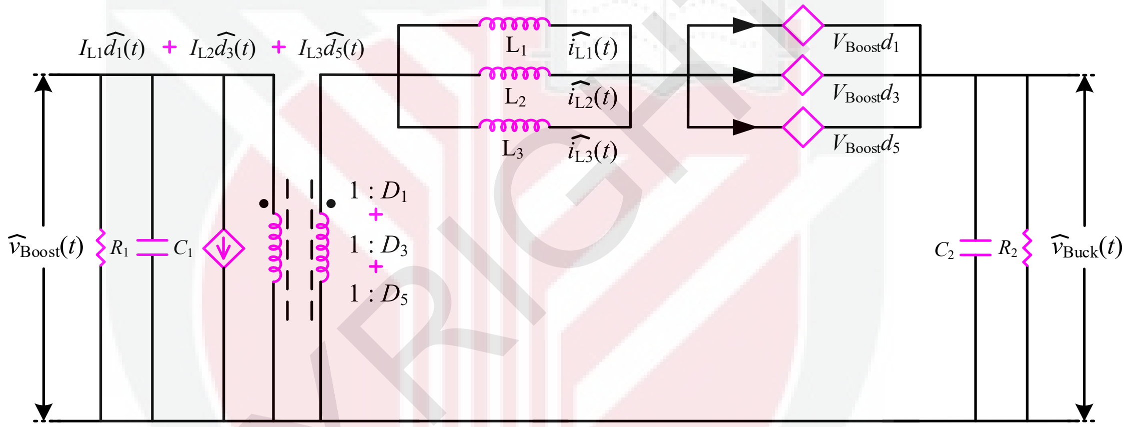

Figure 3.16 : Charge Buck Mode Based on AC Small Signal Analysis

If the TPIPBi-Buck–Boost converter is in ideal conditions, the three-phase circuit parameters are completely consistent:

$$\begin{cases} L_1 = L_2 = L_3 = L \\ I_{L_1} = I_{L_1} = I_{L_1} = I_L \\ d_1 = d_2 = d_3 = d \end{cases} \tag{3.42}$$

The frequency domain equation after Laplace transform of Equation 3.40 and Equation 3.41 is:

$$
\begin{cases} Ls\hat{\imath}_L(s) = D\hat{v}_{Boost}(s) + V_{Boost}\hat{d}(s) - \hat{v}_{Buck}(s) \\ Cs\hat{v}_{Buck}(s) = 3\hat{\imath}_L(s) - \dfrac{\hat{v}_{Buck}(s)}{R_2} \end{cases} \tag{3.43}
$$

To calculate the AC small signal equivalent circuit model of the TPIPBi-Buck–Boost converter in charge Buck mode, to control the low voltage side V_{Buck}, make $\hat{v}_{Boost}(s) = 0$, and substitute into Equation 3.43, and the controlled $G_{id}(s)$ of the current inner loop can be obtained through a series of simplified calculations, that is, the transfer function from $d(s)$ to $i_L(s)$ is:

$$
G_{id}(s) = \left.\frac{\hat{\imath}_L(s)}{\hat{d}(s)}\right|_{\hat{v}_{Boost}(s)=0} = \frac{V_{Boost}C_2 s + \dfrac{V_{Boost}}{R_2}}{LC_2 s^2 + \dfrac{Ls}{R_2} + 3} \tag{3.44}
$$

The transfer function from $d(s)$ to $V_{Boost}(s)$ is:

$$
\left.\frac{\hat{V}_{Buck}(s)}{\hat{d}(s)}\right|_{\hat{v}_{Boost}(s)=0} = \frac{3V_{Boost}}{LCs^2 + \dfrac{Ls}{R_2} + 3} \tag{3.45}
$$

The voltage loop controlled $G_{vi}(s)$, that is, the transfer function from $i_L(s)$ to $V_{Boost}(s)$ is:

$$
\begin{aligned} G_{vi}(s) &= \left.\frac{\hat{v}_{Buck}(s)}{\hat{\imath}_L(s)}\right|_{\hat{v}_{Boost}(s)=0} = \left.\frac{\hat{v}_{Buck}(s)}{\hat{d}(s)}\right|_{\hat{v}_{Boost}(s)=0} \left.\frac{\hat{d}(s)}{\hat{\imath}_L(s)}\right|_{\hat{v}_{Boost}(s)=0} \\ &= \frac{3}{C_2 s + \dfrac{1}{R_2}} \end{aligned} \tag{3.46}
$$

3.3.2.2 Discharge Boost Mode Based on AC Small Signal Analysis

From the modeling of charge Buck mode in the previous section, it can be seen that there is a dual relationship between charge Buck mode and discharge boost mode of TPIPBi-Buck–Boost Converter. Similarly, in discharge Boost mode, Q_2, Q_4 and Q_5 turn on, the voltage drops of the L_1 to L_3 are given as follows:

$$\begin{cases} v_{L_1}(t) = L_1 \dfrac{di_{L_1}}{dt} = v_{Buck}(t) \\ v_{L_2}(t) = L_2 \dfrac{di_{L_2}}{dt} = v_{Buck}(t) \\ v_{L_3}(t) = L_3 \dfrac{di_{L_3}}{dt} = v_{Buck}(t) \end{cases} \tag{3.47}$$

Q_2, Q_4 and Q_6 are turned off, the voltage drops of the L_1 to L_3 are given as follows:

$$\begin{cases} v_{L_1}(t) = L_1 \dfrac{di_{L_1}}{dt} = v_{Buck}(t) - v_{Boost}(t) \\ v_{L_2}(t) = L_2 \dfrac{di_{L_2}}{dt} = v_{Buck}(t) - v_{Boost}(t) \\ v_{L_3}(t) = L_3 \dfrac{di_{L_3}}{dt} = v_{Buck}(t) - v_{Boost}(t) \end{cases} \tag{3.48}$$

According to Equation 3.47 and Equation 3.48, the average voltages of the L_1 to L_3 in T_s are, respectively:

$$\begin{cases} \langle v_{L_1}(t)\rangle_{T_s} = \dfrac{1}{T_s}\left[\displaystyle\int_{0}^{d_2T_s} v_{L_1}(t)\,dt + \int_{d_2T_s}^{T_s} v_{L_1}(t)\,dt\right] = \langle v_{Buck}(t)\rangle_{T_s} - (1-d_2)\langle v \\ \langle v_{L_2}(t)\rangle_{T_s} = \dfrac{1}{T_s}\left[\displaystyle\int_{0}^{d_4T_s} v_{L_2}(t)\,dt + \int_{d_4T_s}^{T_s} v_{L_2}(t)\,dt\right] = \langle v_{Buck}(t)\rangle_{T_s} - (1-d_4)\langle v \\ \langle v_{L_3}(t)\rangle_{T_s} = \dfrac{1}{T_s}\left[\displaystyle\int_{0}^{d_6T_s} v_{L_3}(t)\,dt + \int_{d_6T_s}^{T_s} v_{L_3}(t)\,dt\right] = \langle v_{Buck}(t)\rangle_{T_s} - (1-d_6)\langle v \end{cases} \quad (3.49)$$

After averaging the inductance characteristic:

$$\begin{cases} \langle v_{L_1}(t)\rangle_{T_s} = L_1\dfrac{d\langle i_{L_1}(t)\rangle_{T_s}}{dt} \\ \langle v_{L_2}(t)\rangle_{T_s} = L_2\dfrac{d\langle i_{L_2}(t)\rangle_{T_s}}{dt} \\ \langle v_{L_3}(t)\rangle_{T_s} = L_3\dfrac{d\langle i_{L_3}(t)\rangle_{T_s}}{dt} \end{cases} \quad (3.50)$$

Substituting Equation 3.50 into Equation 3.49 yields:

$$\begin{cases} L_1\dfrac{d\langle i_{L_1}(t)\rangle_{T_s}}{dt} = \langle v_{Boost}(t)\rangle_{T_s} - d_2'\langle v_{Buck}(t)\rangle_{T_s} \\ L_2\dfrac{d\langle i_{L_2}(t)\rangle_{T_s}}{dt} = \langle v_{Boost}(t)\rangle_{T_s} - d_4'\langle v_{Buck}(t)\rangle_{T_s} \\ L_3\dfrac{d\langle i_{L_3}(t)\rangle_{T_s}}{dt} = \langle v_{Boost}(t)\rangle_{T_s} - d_6'\langle v_{Buck}(t)\rangle_{T_s} \end{cases} \quad (3.51)$$

where $d_i' = 1 - d_i (i = 2, 4, 6)$, according to Kirchhoff's Law, the average current of the capacitor C_1 in T_s is:

$$\begin{aligned} \langle i_{C_1}(t)\rangle_{T_s} &= C_1\frac{d\langle v_{Boost}(t)\rangle_{T_s}}{dt} \\ &= d_2'\langle i_{L_1}(t)\rangle_{T_s} + d_4'\langle i_{L_2}(t)\rangle_{T_s} + d_6'\langle i_{L_3}(t)\rangle_{T_s} - \frac{\langle v_{Boost}(t)\rangle_{T_s}}{R_1} \end{aligned} \quad (3.52)$$

Substituting Equation 3.38 into Equation 3.51 yields:

$$\begin{cases} L_1 \dfrac{d\langle I_{L_1} + \hat{\imath}_{L_1}(t)\rangle}{dt} = [V_{Buck} + \hat{v}_{Buck}(t)] - \left[d_2' - \hat{d}_2(t)\right][V_{Boost} + \hat{v}_{Boost}(t)] \\ L_2 \dfrac{d\langle I_{L_2} + \hat{\imath}_{L_2}(t)\rangle}{dt} = [V_{Buck} + \hat{v}_{Buck}(t)] - \left[d_4' - \hat{d}_4(t)\right][V_{Boost} + \hat{v}_{Boost}(t)] \\ L_3 \dfrac{d\langle I_{L_3} + \hat{\imath}_{L_3}(t)\rangle}{dt} = [V_{Buck} + \hat{v}_{Buck}(t)] - \left[d_6' - \hat{d}_6(t)\right][V_{Boost} + \hat{v}_{Boost}(t)] \end{cases} \tag{3.53}$$

Finishing Equation 3.53, and can be obtained by ignoring the second order minute term:

$$\begin{cases} L_1 \dfrac{d\hat{\imath}_{L_1}(t)}{dt} = \hat{v}_{Buck}(t) + d_2'\hat{v}_{Boost}(t) + V_{Boost}\hat{d}_2(t) \\ L_2 \dfrac{d\hat{\imath}_{L_2}(t)}{dt} = \hat{v}_{Buck}(t) + d_4'\hat{v}_{Boost}(t) + V_{Boost}\hat{d}_4(t) \\ L_3 \dfrac{d\hat{\imath}_{L_3}(t)}{dt} = \hat{v}_{Buck}(t) + d_6'\hat{v}_{Boost}(t) + V_{Boost}\hat{d}_6(t) \end{cases} \tag{3.54}$$

Similarly, substitute Equation 3.38 into Equation 3.52 yields:

$$\begin{aligned} C_2 \frac{dv_{Boost}(t)}{dt} &= d_2'\hat{\imath}_{L_1}(t) - I_{L_1}\hat{d}_2(t) + d_4'\hat{\imath}_{L_2}(t) - I_{L_2}\hat{d}_4(t) + d_6'\hat{\imath}_{L_3}(t) \\ &\quad - I_{L_3}\hat{d}_6(t) - \frac{\hat{v}_{Boost}(t)}{R_1} \end{aligned} \tag{3.55}$$

According to Equation 3.54 and Equation 3.55, the AC small signal equivalent circuit model of the TPIPBi-Buck–Boost Converter in discharge Boost mode can be established, as illustrated in the Figure 3.17.

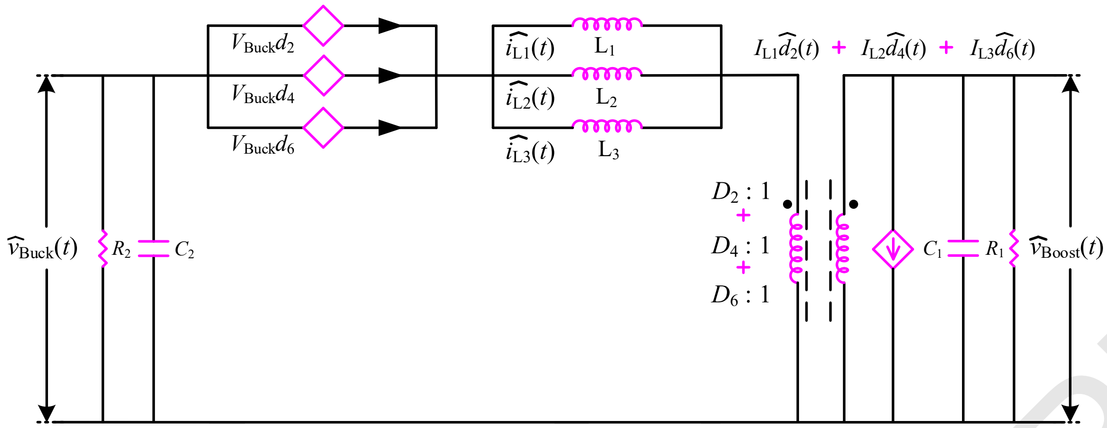

Figure 3.17 : Discharge Boost Mode Based on AC Small Signal Analysis

If the TPIPBi-Buck–Boost converter is in ideal conditions, the three-phase circuit parameters are completely consistent:

$$\begin{cases} L_1 = L_2 = L_3 = L \\ I_{L_1} = I_{L_2} = I_{L_3} = I_L \\ d_2 = d_4 = d_6 = d \end{cases} \tag{3.56}$$

The frequency domain equation after Laplace transform of Equation 3.55 and Equation 3.56 are:

$$\begin{cases} Ls\hat{\imath}_L(s) = \hat{v}_{Buck}(s) - D'\hat{v}_{Boost}(s) - V_{Boost}\hat{d}(s) \\ Cs\hat{v}_{Boost}(s) = 3D'\hat{\imath}_L(s) - 3I_L\hat{d}(s) - \dfrac{\hat{v}_{Boost}(s)}{R_1} \end{cases} \tag{3.57}$$

To calculate the AC small signal equivalent circuit model of the TPIPBi-Buck–Boost converter in discharge Buck mode, to control the high voltage side V_{Boost} make $\hat{v}_{Buck}(s) = 0$, and substitute into Equation 3.57, and the controlled $G_{id}(s)$ of the current inner loop can be obtained through a series of simplified calculations, that is, the transfer function from $d(s)$ to $i_L(s)$ is:

$$G_{id}(s) = \left.\frac{\hat{i}_L(s)}{\hat{d}(s)}\right|_{\hat{v}_{Buck}=0} = \frac{V_{Boost}C_1 s + \frac{2V_{Boost}}{R_1}}{LC_1 s^2 + \frac{Ls}{R_1} + 3D'^2} \tag{3.58}$$

The transfer function from $V_{Boost}(s)$ to $d(s)$ is:

$$\left.\frac{\hat{v}_{Boost}(s)}{\hat{d}(s)}\right|_{\hat{v}_{Buck}=0} = \frac{3D' - \frac{Ls}{RD'}}{LC_1 s^2 + \frac{Ls}{R_1} + 3D'^2} \tag{3.59}$$

The voltage loop controlled $G_{vi}(s)$, that is, the transfer function from $i_L(s)$ to $V_{Boost}(s)$ is:

$$\begin{aligned} G_{vi}(s) = \left.\frac{\hat{v}_{Boost}(s)}{\hat{i}_L(s)}\right|_{\hat{v}_{Buck}=0} &= \left.\frac{\hat{v}_{Boost}(s)}{\hat{d}(s)}\right|_{\hat{v}_{Buck}=0} \left.\frac{\hat{d}(s)}{\hat{i}_L(s)}\right|_{\hat{v}_{Buck}=0} \\ &= \frac{3D'^2 R_1 - Ls}{C_1 R_1 D' s + 2D'} \end{aligned} \tag{3.60}$$

3.3.3 Digital Implementation for TPIPBi-Buck–Boost Converter with Infineon

The analysis and design of the control method determine the performance of the TPIPBi-Buck–Boost converter, which is the focus and difficulty of the whole system. In order to improve the stability and dynamic response of the new NEEVs, Section 3.3.3 will combine the open loop derivation results based on the AC small signal model in Section 3.3.2, and purposefully carry out the optimal design of the double closed-loop control system with XDPTM Digital Power Controllers by Infineon Technologies AG, which also provides an important theoretical basis for the concrete realization methods of hardware and software.

3.3.3.1 Analysis and Design of Double Closed-Loop Control System

According to the actual application requirements, in the process of frequent starting, acceleration, deceleration, and braking of the drive motor, the voltage, and current of the direct current bus are constantly changing in a wide range. For the TPIPBi-Buck–Boost converter with different power flow directions, the transfer functions are also very different, and stable and accurate control is relatively difficult.

In view of the specific requirements of the above problems, a double closed-loop control strategy is considered in Figure 3.18, in which the voltage loop is used as the outer loop and the current loop as the inner loop, which not only enhances the system stability, but also improves the dynamic response. Analyzing the TPIPBi-Buck–Boost converter circuit topology, low voltage side V_{Buck} and high voltage side V_{Boost}, a novel control strategy is adopted to place the controlled voltage and current at different sides, it not only achieves that the direct current bus voltage is controlled in the forward direction, and the reverse charging current of the battery pack is well controlled.

In the digital signal control system, the direct bus voltage and the energy storage inductor current are simultaneously sampled in one sampling period, converted into digital signals by A/D, digitally filtered, and subtracted from the corresponding offset to obtain the digital signal. The high side voltage terminal command is given by the Infineon XDPP1100-Q040, and compared with the voltage sampling value to obtain the voltage error signal, the output value obtains the current given signal through the PID regulator, and the current given signal is compared with the current sampling value to obtain the current error signal, the output value of the PWM register is output through the PID regulator, so as to achieve the purpose of controlling the high side voltage output and low side current.

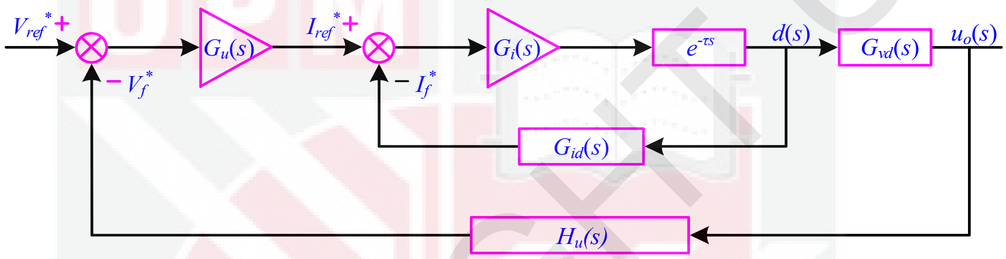

Figure 3.18 : Block Diagram of Double Closed-Loop Control System

Where $G_u(s)$ is the voltage loop correction network transfer function, $G_i(s)$ is the current loop correction network transfer function, $e^{-\tau s}$ is the delay caused by digital sampling, calculation and update of the duty cycle, $G_{id}(s)$ is the transfer function of duty cycle $\hat{d}$ to the inductive current, $G_{vd}(s)$ is the transfer function of duty cycle $\hat{d}$ to the input and output voltage, $H_u(s)$ is the transfer function for voltage sampling.

3.3.3.2 Current inner Loop Compensation Controller

In Figure 3.19, the current inner loop is designed with a PI controller. Since the delay segment does not change the system gain, only changes the phase, and is not considered, for the time being, the open loop transfer function of the current inner loop can be expressed as:

$$G_{i_o}(s) = \frac{\hat{V}_{Buck}(s)}{d'^2(s)} \frac{K_{ip}s + K_{ii}}{s} \frac{V_{Boost}C_2 s + \frac{V_{Boost}}{R_2}}{LC_2 s^2 + \frac{Ls}{R_2} + 3} \tag{3.61}$$

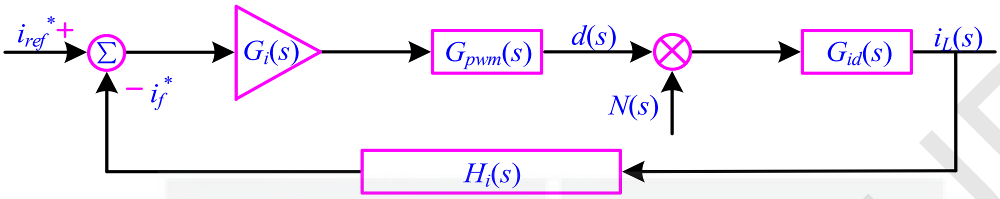

Figure 3.19 : Block Diagram of Current Inner Loop Compensation Controller

The closed-loop transfer function of the current inner loop:

$$G_i'(s) = K \frac{(K_{ip}s + K_{ii})\left(V_{Boost}C_2 s + \frac{V_{Boost}}{R_2}\right)}{K_1 s^3 + K_2 s^2 + K_3 s^1 + K_4 s^0} \tag{3.62}$$

where $K = \frac{\hat{V}_{Buck}}{d'^2}$, $K_1 = \frac{C_2 L}{d'^2}$, $K_2 = \frac{L}{R_2 d'^2} + \frac{K_{ip}}{C_2}$, $K_3 = K_{ii}C_2 + \frac{2K_{ip}}{R_2} + 1$, $K_3 = \frac{2K_{ip}}{R_2}$.

From the analysis of Equation 3.62, it can be known that K_1 is much smaller than the other coefficients and the s^3 is negligible:

$$(K_{ip}s + K_{ii})\left(V_{Boost}C_2 s + \frac{V_{Boost}}{R_2}\right) = K_1 s^3 + K_2 s^2 + K_3 s^1 + K_4 s^0 \tag{3.63}$$

Therefore, $G_{i_{open\_loop}}(s) \cong K$ in Equation 6.62, the current inner loop is equivalent to a proportional segment. In the system, the delay segment can be equivalent to a first-order inertial segment, and the influence of the pole can be offset by the PI parameter of the current inner loop.

3.3.3.3 Voltage Outer Loop Compensation Controller

For the TPIPBi-Buck–Boost converter with insufficient phase and amplitude margins in open loop state, and the right half plane zero-point problem, it needs to be corrected accordingly. The double pole and double zero compensation network are usually selected to achieve closed-loop control to meet the stability requirements.

In digital power supply, PID correction is usually chosen, which is essentially an active lag-ahead correction whose transfer function can be expressed as:

$$G_{pid}(s) = K_p\left(1 + \frac{1}{\tau_i} + \frac{\tau_i}{1 + \frac{\tau_d}{N}s}\right) = K_1\left[\frac{K_2 s^2 + K_3 s^1 + s^0}{s(K_4 s + 1)}\right] \tag{3.64}$$

where $K_1 = \frac{K_p}{\tau_i}$, $K_2 = \frac{\tau_i \tau_d}{1+\frac{1}{N}}$, $K_3 = \tau_i + \frac{\tau_d}{N}$, $K_4 = \frac{\tau_d}{N}$, τ_i and τ_d are, respectively, integral and differential time constants, $N \geqq 10$.

In the Figure 3.20, $G_i'(s)$ is a closed-loop transfer function of the voltage outer loop, and $G_i'(s)$ can be equivalent to a proportional segment, which makes it relatively convenient to design the voltage outer loop compensator.

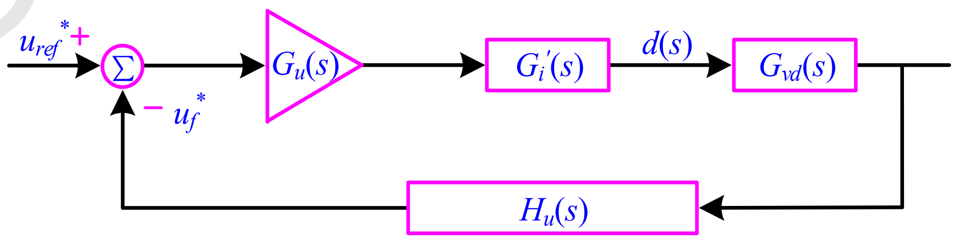

Figure 3.20 : Block Diagram of Voltage Outer Loop Compensation Controller

3.3.3.4 Power Feedforward Compensation Controller

Under the complex conditions of the NEEVs, if the power demand and load current of the drive motor suddenly drop, causing the system to provide more electrical energy than needed, and the filter capacitor on the direct current bus voltage side is charged to absorb excess energy. The direct current bus voltage fluctuates during the frequent charging and discharging process. In general, increasing the filter capacitor capacity, but enlarges the volume and cost of the system virtually. Aiming at the problem of insufficient voltage fluctuation and dynamic response under transient response, a power feedforward control strategy is adopted in this research to predict the power demand trend through the electromagnetic torque of the drive motor, and eliminate voltage fluctuation, which is easy to be realized in digital control systems.

By adding an input voltage compensation segment to the system, the transient response speed caused can be increased by the input disturbance. The control block diagram is shown in Figure 3.21.

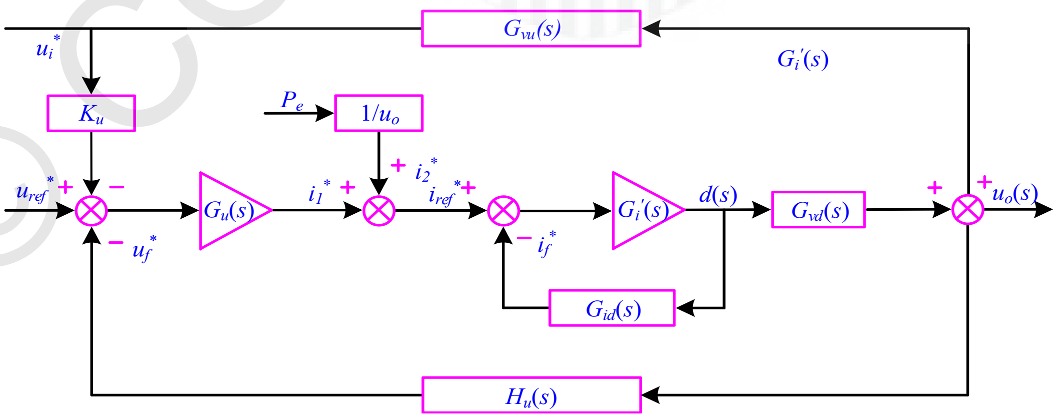

Figure 3.21 : Block Diagram of Power Feedforward Compensation Controller

$$P_e = 2\pi \frac{\gamma T_e n}{60} \tag{3.65}$$

P_e is the electromagnetic power of the permanent magnet synchronous motor, γ, T_e, n are, respectively, power factor, electromagnetic torque, and speed. The electromagnetic power P_e of the drive motor can be calculated by using Equation 3.65. When the operating condition of NEEVs, Infineon XDPP1100-Q040 issues a torque instruction through the CAN bus and subtract with the P_e. The result is divided from the bus voltage instruction, and the current instruction value i_2^* is obtained. The output i_1^* of the voltage compensation controller is added as the given instruction of the current inner loop. It allows the system to adjust the output electrical energy depending on the instruction value given by the electromagnetic power even if the voltage is still constant. Thus, the purpose of eliminating direct current bus voltage fluctuation caused by electrical energy change is achieved.

For the compensation of input voltage disturbance u_i^*, it should satisfy:

$$G_{vu}(s) = K_u G_u(s) G_i'(s) G_{vd}(s) \tag{3.66}$$

Derived from Equation 3.66, when $K_u = \frac{G_{vu}(s)}{G_u(s)G_i'(s)G_{vd}(s)}$, thus, $\frac{\hat{u}_o(s)}{\hat{u}_i(s)} = 0$, theoretically, the disturbance of the output voltage is completely unaffected by the input voltage disturbance u_i^*.

3.3.3.5 Bidirectional Switching Logic Controller

When the TPIPBi-Buck–Boost converter is in discharge Boost mode, the direct current bus voltage V_{bus} is collected to form the voltage outer loop, and after comparing with V_{bus_ref}, $i_{L\_boost\_ref}$ of the current inner loop is generated through the voltage outer loop compensator, comparing with i_{L_boost}, and the final duty cycle $d_{buck-boost}$ is produced by the current inner loop compensator. In the charge Buck mode, the battery pack voltage $V_{battery}$ is collected to form the voltage outer loop, and after comparing with $V_{battery\_ref}$, $i_{L\_buck\_ref}$ of the current inner loop is generated through the voltage outer loop compensator, comparing with i_{L_buck}, and the final duty cycle $d_{boost-buck}$ is produced by the current inner loop compensator. The driving signal is output through the Infineon Technologies AG Digital Power Controllers XDPP1100-Q040 to change the operating state. To reduce voltage and current surges, the TPIPBi-Buck–Boost converter works by soft start in electric energy interaction mode seen in Figure 3.22.

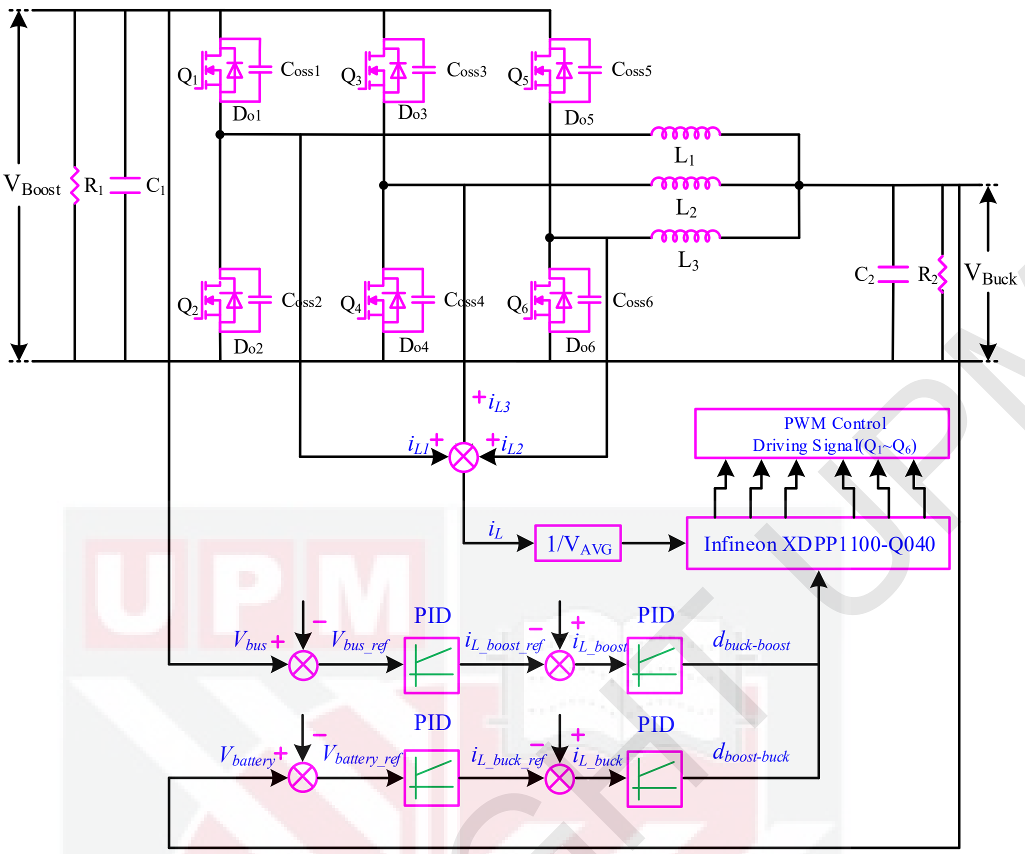

Figure 3.22 : Block Diagram of Bidirectional Switching Logic Controller with Infineon

3.4 Three Voltage Vector Duty Cycle Optimization Strategy Based on Finite Set Model Predictive Control

PMSM are widely used in NEEVs and in other fields because of their simple structure, light weight, small size, and high power density. With the continuous advancement of production technology, the requirements of accuracy, rapidity, and stability in permanent magnet synchronous motor systems have gradually increased. Among many advanced control technologies, this research proposes an optimized model predictive torque control strategy based on voltage vector expansion. This strategy involves the construction of a reference stator flux linkage vector based on the analytical relationship between electromagnetic torque, reference stator flux linkage amplitude, and rotor flux linkage and the transfer of the separate control of electromagnetic torque and flux linkage amplitude into flux linkage vector control. At the same time, the optimal duty cycle corresponding to the two adjacent extended voltage vectors and the zero vector is calculated according to geometric relationships so as to realize the three voltage vector duty cycle optimization control.

3.4.1 Brief Discussion on Principle of Model Predictive Control

Among the high-performance control methods for PMSM, MPC has garnered attention in PMSM control research due to its simple structure, straightforward implementation, and notable performance. In contrast to vector control, MPC eliminates the need for a current loop PI controller design. By leveraging the cost function, it enables the direct selection of the optimal voltage vector to act on the PMSM, resulting in improved dynamic performance. Unlike DTC, MPC utilizes real-time calculations to ensure the application of the optimal voltage vector, leading to more accurate voltage selection and enhanced steady-state performance. Furthermore, the cost function employed in MPC for optimal vector selection can be extended with control variables to achieve multi-objective control, offering greater flexibility in control structure compared to traditional vector control and DTC.

Dead-beat control (DBC) and finite control set model predictive control (FCS-MPC) are prevalent predictive control methods. DBC focuses on tracking the electromagnetic torque, stator flux linkage command, or stator current command within a single cycle. DBC utilizes the mathematical model to predict the reference voltage vector and modulates the inverter's switching signal through SVPWM, thereby exhibiting commendable dynamic and steady-state tracking performance. However, the efficacy of DBC hinges upon the accuracy of the mathematical model. Inaccurate motor model parameters or parameter variations during operation can lead to deviations between the calculated reference voltage vector and the expected value. Additionally, inherent delays in the digital control system, such as current sampling delay and duty cycle update delay, result in the reference voltage vector being calculated at one time but applied to the inverter at the subsequent time, thereby diminishing the PMSM control performance.

MPC leverages the discrete mathematical model and the discrete switching state of the inverter to optimize the cost function online, selecting the optimal voltage vector (the inverter's switching state) to be applied to the PMSM at the subsequent control time. MPC offers the advantages of a simple principle, robust nonlinear constraint capability, and favorable dynamic characteristics. Furthermore, MPC can directly output the switch state without PWM, simplifying implementation. Nonetheless, MPC encounters several challenges, including extensive computation, intricate weight coefficient design, and substantial torque, flux linkage, or current ripple. The issue of considerable computation is particularly prominent, especially when multi-step prediction is employed, leading to an exponential increase in computational load. To address this challenge, various methods have been proposed, such as the sphere decoding algorithm, binary search tree method, and voltage vector preselection method, all of which effectively reduce the computational burden.

MPC can be categorized into MPTC and MPCC based on different control variables. MPCC governs the stator current, while MPTC concurrently manages electromagnetic torque and stator flux linkage, which pertain to distinct dimensions. As a result, it is crucial to design weight coefficients in the cost function to balance the relationship between these control variables. In MPCC, the cost function pertains to the current magnitude, and as the dimensions of each current magnitude are identical, the weight coefficient design issue among these magnitudes can be circumvented. Conversely, in MPTC, the primary control variables in the cost function are electromagnetic torque and stator flux linkage, with differing dimensions. Therefore, designing the weight coefficients is necessary to achieve control balance between torque and flux linkage, and the reasonableness of this design directly impacts the control system's performance. Currently, weight coefficient design typically involves time-consuming and non-intuitive methods such as experimental or simulation-based adjustments. Moreover, the inadequate steady-state performance of the MPC method has impeded its further advancement. To enhance the steady-state performance, the DV-MPC and TV-MPC are proposed. DV-MPC operates on two vectors per cycle, effectively mitigating over-regulation and under-regulation issues associated with single-vector operation, resulting in smoother electromagnetic torque, stator flux linkage, and three-phase current. Similarly, TV-MPC's steady-state control effect, acting on three vectors per cycle, rivals that of vector control. However, employing more action vectors leads to a more intricate control structure, increased computational load, and elevated switching loss and average switching frequency.

The principal block diagram of traditional MPTC is depicted in Figure 3.23. The outer loop corresponds to speed control, with the desired electromagnetic torque achieved through PI adjustment using the variance between the desired value and the feedback speed. Subsequently, the desired stator flux linkage can be computed using maximum torque per ampere (MTPA) control. Concurrently, the control system acquires the phase current through current sampling, which is then transformed into the current $i_s(k)$ in the static coordinate system by Clarke transformation. The system predicts the current $i_s(k+1)$ at time $(k+1)$ by leveraging the voltage value and electrical angular velocity. Substituting seven fundamental voltage vectors (treating two zero vectors as one) successively into the prediction equation for electromagnetic torque and stator flux linkage yields the predictions for electromagnetic torque $T_e(k+1)$ and stator flux linkage $\psi_s(k+1)$ at the subsequent time step. These predicted torque and flux linkage values are then utilized in the cost function, and the cost function's value is evaluated. The basic voltage vector yielding the minimum cost function value is chosen as the optimal voltage vector at the next time step.

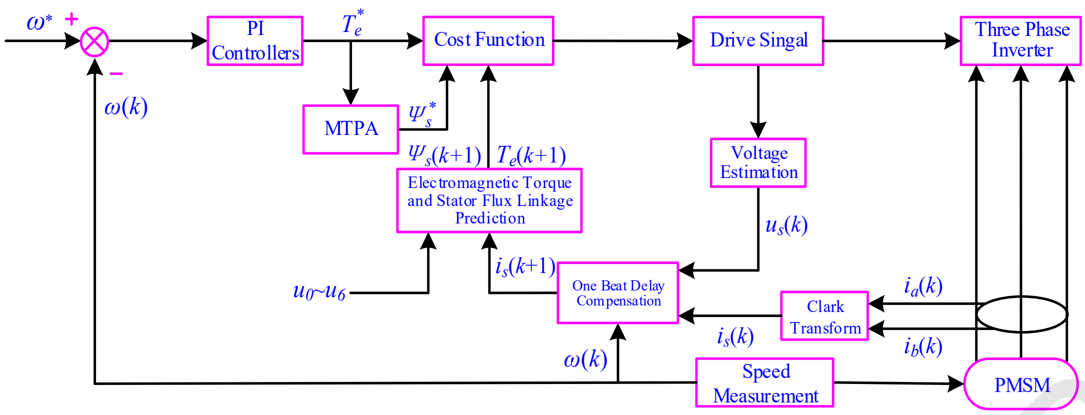

Figure 3.23 : Principal Block Diagram of Traditional MPTC

Similar to MPCC, the practical implementation of MPTC involves digital control systems that necessitate sampling, logical calculations, and algorithmic execution to realize the control algorithm. Consequently, the optimal voltage vector selected at time k only influences PMSM at time $k+1$, introducing a one-step delay that significantly affects the system's control performance, albeit being unavoidable. Particularly, at lower sampling frequencies, this one-step delay exerts a more pronounced impact on the control system, underscoring the need for compensation.

Utilizing the mathematical model of PMSM, the flux linkage equation is integrated into the voltage equation, and subsequently discretized to derive the current prediction model.

$$i_s(k+1) = i_s(k) + \frac{T_s}{L_s}\left[u_s(k) - Ri_s(k) - j\omega\Psi_f e^{j\theta}\right] \qquad (3.67)$$

Where, $i_s = \begin{pmatrix} i_\alpha \\ i_\beta \end{pmatrix}$, $u_s = \begin{pmatrix} u_\alpha \\ u_\beta \end{pmatrix}$. Equation 3.67 reveals that the sampling current $i_s(k+1)$ at $k+1$ can be forecasted based on the sampling current $i_s(k)$ at k and the optimal basic voltage vector $u_s(k)$, thus facilitating one-step delay compensation. Nonetheless, the accuracy of this prediction approach is relatively limited. To enhance the precision of current prediction, the Euler formula with prediction and correction functions is employed:

$$\begin{cases} i_p(k+1) = i_s(k) + \frac{T_s}{L_s}\left[u_s(k) - Ri_s(k) - j\omega\Psi_f e^{j\theta}\right] \\ i_s(k+1) = i_p(k+1) - \frac{T_s R}{2L_s}\left[i_p(k+1) - i_s(k)\right] \end{cases} \tag{3.68}$$

Where, $i_p(k+1)$ represents the predicted value, while $i_s(k+1)$ denotes the corrected value. Building upon the current prediction derived from Equation 3.68, the electromagnetic torque and flux linkage for the subsequent control cycle can be further predicted by integrating the motor flux equation and electromagnetic torque equation. The specific prediction equation is as follows:

$$\begin{cases} \Psi_\alpha = L_d i_\alpha + \Psi_f \cos\theta \\ \Psi_\beta = L_q i_\beta + \Psi_f \sin\theta \end{cases} \tag{3.69}$$

$$T_e = \frac{3}{2}p\left(\Psi_\alpha i_\beta - \Psi_\beta i_\alpha\right) \tag{3.70}$$

3.4.2 Three Voltage Vector Duty Cycle Optimization

In order to apply MPC in the motor driving systems of NEEVs, it is necessary to build a mathematical description of the prediction model for the PMSM. A discrete time model needs to include all of the control variables and predict them. The forward Euler formula can be expressed as:

$$\frac{dx}{dt} = \frac{x(K+1) - x(k)}{T_s} \tag{3.71}$$

where T_s is the sampling period, K is the current time, and $x(K+1)$ is the predictive value at the next time.

In the d and q rotating coordinate system, discretizing the voltage expressions for the PMSM by the forward Euler formula, the current prediction model can be written as follows:

$$\begin{cases} i_d(K+1) = i_d(k) + \dfrac{1}{L_d}\left[-R_s i_d(k) + \omega_e L_q i_d(k) + u_d(k)\right] T_s \\ i_q(K+1) = i_q(k) + \dfrac{1}{L_q}\left[-R_s i_q(k) + \omega_e L_d i_q(k) + u_q(k) - \omega_e \Psi_f\right] T_s \end{cases} \tag{3.72}$$

Discretizing the flux linkage expressions of the PMSM by the forward Euler formula, the flux linkage prediction models are:

$$\begin{cases} \Psi_d(K+1) = T_s\left[u_d(k) - R_s i_d(k) + \omega_e \Psi_q(k)\right] + \omega_e \Psi_d(k) \\ \Psi_q(K+1) = T_s\left[u_q(k) - R_s i_q(k) + \omega_e \Psi_d(k)\right] + \omega_e \Psi_q(k) \end{cases} \tag{3.73}$$

Substituting Equation 3.72 and Equation 3.73 for electromagnetic torque expressions yields:

$$\left\{ T_e(K+1) = \frac{3}{2} p i_q(k+1)\left[i_d(k+1)\left(L_d - L_q\right) + \Psi_f\right] \right. \tag{3.74}$$

Therefore, Equation 3.72, Equation 3.73 and Equation 3.74 are the important components and theoretical fundaments of the mathematical model for predictive control with the PMSM.

3.4.2.1 Alternative Voltage Vector Extension

In traditional MPTC, eight basic voltage vectors generated by a three-phase inverter are directly used as inputs to the MPTC controller to predict the current, electromagnetic torque, and flux linkage. Rolling optimization of the prediction results is carried out according to the cost function, so that the voltage vector with the smallest cost function acts on the motor system. Since the selection of voltage vectors is limited to the eight basic voltage vectors, they usually have high electromagnetic torque and flux linkage pulsations. In addition, the traditional MPTC needs to optimize the prediction of each voltage vector in a control cycle, which increases the computational burden.

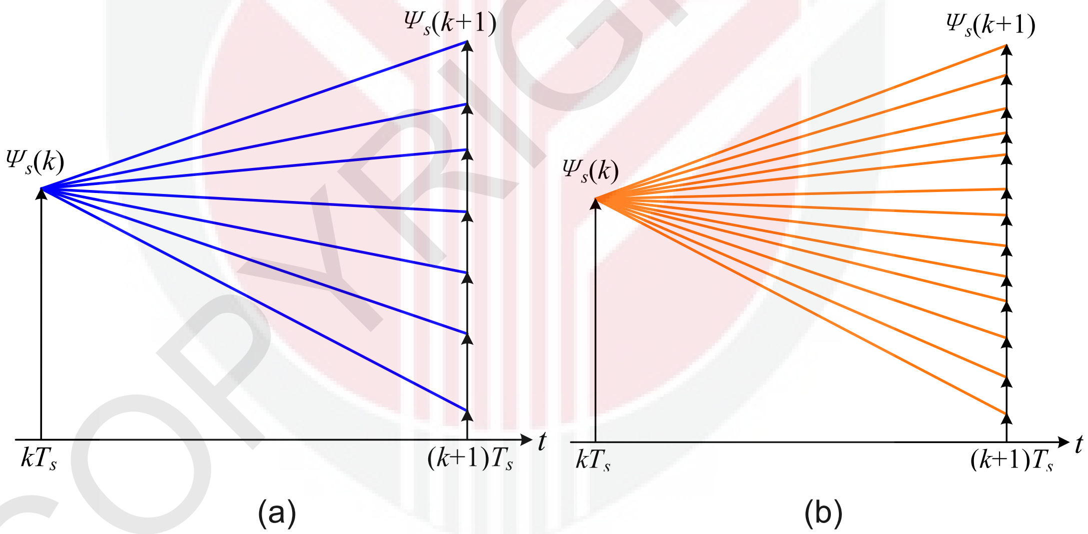

Figure 3.24 : Different Predictions of the Stator Flux Linkage Vector: (a) before; (b) after

To improve the selection accuracy, an improved finite voltage vector control set is adopted based on the traditional eight voltage vectors. At the same time, in order to make full use of the flux linkage vector control algorithm, the traditional finite control set is optimized to allow more choice regarding the numbers and phase angles of alternative voltage vectors, and a filter for predicting flux linkage vectors can be obtained, which enables the cost function to select a voltage vector with less electromagnetic torque and flux linkage error for more effective control. Furthermore, the electromagnetic torque and flux linkage pulsations can be reduced by increasing the virtual voltage vector. As shown in Figure 3.24, increase in the different voltage vectors makes the prediction result of the flux linkage vector more refined, and the cost function can select the predictive flux linkage vector with less error.

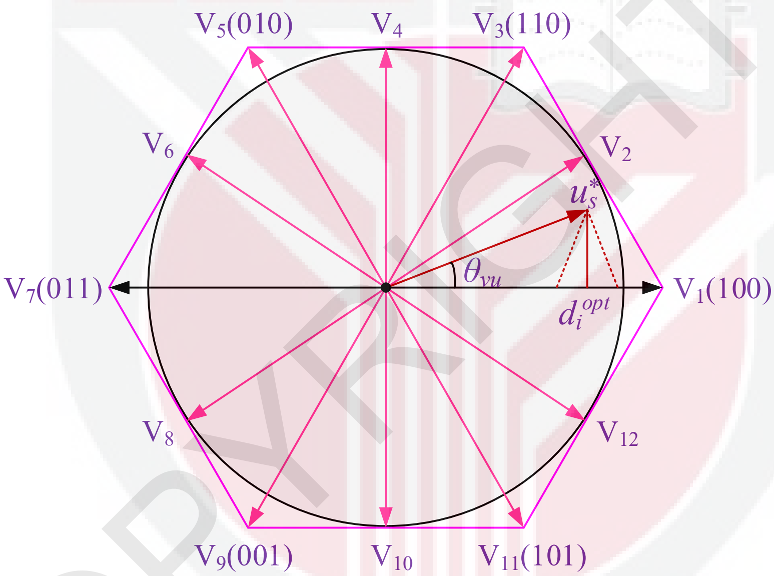

Figure 3.25 : Extended Voltage Vector Control Set

The specific improvement methods are as follows: the two-level three-phase voltage source inverter can only produce eight switch states, according to the arrangement and combination, corresponding to six non-zero vectors and two zero vectors. In order to improve the accuracy of MPTC, six virtual voltage vectors are added to the traditional basic voltage vectors, which are half of the two adjacent synthesized voltage vectors, and the amplitude is 0.866 times that of the basic voltage vector. In this way, the number of alternative effective voltage vectors is changed from 6 to 12. The extended voltage vector control sets $V_1 \cdots V_{12}$ are defined in Figure 3.25.

According to traditional MPTC, fourteen extended voltage vectors are substituted into each control cycle for prediction, and screening through the cost function will greatly increase the algorithm's calculational burden for the microprocessor, reducing the operating efficiency. Therefore, this research makes further improvements while extending the voltage vector screening range.

The extended voltage vectors V_1-V_{12} are shown in Figure 3.25. Two adjacent extended basic voltage vectors can be determined at the spatial position of the reference voltage vector in the spatial sector, such that they are close to the actual reference stator flux linkage vector, reducing the number of alternative voltage vectors to two adjacent extended voltage vectors. In traditional MPTC, an optimal voltage vector is selected based on the cost function and acts throughout the whole system. There are only eight basic voltage vectors, and the design of weight coefficients is cumbersome. The optimized FCS-MPTC strategy realizes the duty cycle control of multiple voltage vectors based on the reference voltage vector. Applying multiple voltage vectors to the SPMSM not only eliminates the weight coefficient design process, but also effectively balances the electromagnetic torque and flux linkage pulsations.

3.4.2.2 Double Voltage Vector Duty Cycle Control

The extended voltage vector V_i and the zero-voltage vector V_0 are combined to form a candidate voltage vector. By adjusting the duty cycle of the extended voltage vector V_i, the candidate stator voltage vector $u_s^{\cdot}$ can be expressed as:

$$u_s^{\cdot} = \frac{t_{vi}}{T_s} V_i = d_i V_i + (1 - d_i) V_0 \tag{3.75}$$

where t_{vi} is the action time and d_i is the duty cycle.

In order to evaluate the influence of the combined candidate voltage vectors on the stator flux linkage vectors, Equation 3.76 is used to replace the traditional cost function in MPTC; it only contains the flux linkage vectors and includes no design for the weight factor:

$$g = |\Psi_s^* - \Psi_s(k+2)| \tag{3.76}$$

The new stator flux linkage vector cost function incorporates the actual amplitude of the electromagnetic torque and flux linkage, including the corresponding reference values. The candidate voltage vectors obtained from Equation 3.74 are used to predict the stator flux linkage vector $\Psi_s(k+2)$ at $(k+2)T_s$ by means of Equation 3.72, which is carried into Equation 3.76:

$$\begin{aligned} g = |\Psi_s^* - \Psi_s(k+2)| &= |\Psi_s^* + T_s R_s i_s(k+1) - T_s d_i V_i - \Psi_s(k+1)| \\ &= T_s |u_s^* - d_i V_i| \end{aligned} \tag{3.77}$$

It can be seen from Equation 3.77 that in order to minimize the cost function, it is necessary for the difference vector between the candidate voltage vector and the reference voltage vector to be perpendicular to the extended voltage vector when the cost function is the smallest. The optimal duty cycle of the extended voltage vector can be expressed as:

$$d_i^{opt} = \frac{|u_s^*| \cos\theta_{vu}}{|V_i|} = \frac{|\Psi_s^* - \Psi_s(k+1) + T_s R_s i_s(k+1)| \cos\theta_{vu}}{|V_i| T_s} \tag{3.78}$$

where d_i^{opt} is the duty cycle of the extended voltage vector and θ_{vu} is the included angle between the extended voltage vector and the reference voltage vector. Bringing the optimal duty cycle derived from Equation 3.78 into Equation 3.77 and selecting the extended voltage vector, which minimizes the cost function and the corresponding optimal duty cycle from the two adjacent extended voltage vectors of the reference voltage vector, acts on the system to achieve double-vector control.

3.4.2.3 Three Voltage Vector Duty Cycle Control

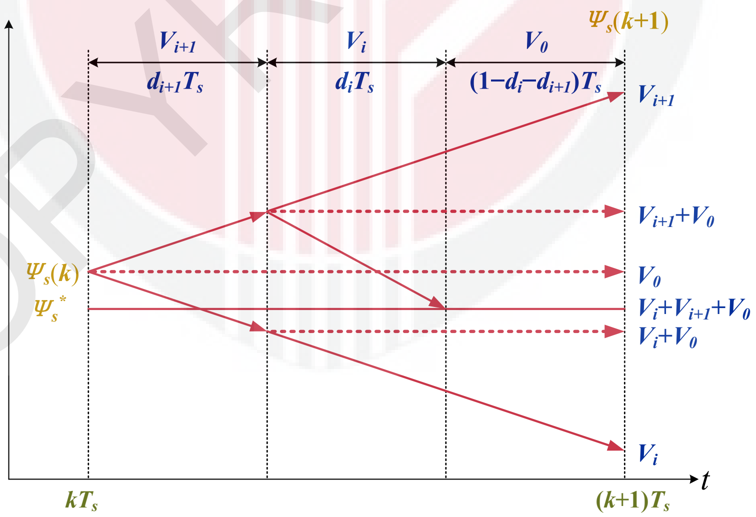

Figure 3.26 : Schematic View of the Different Voltage Vectors on the Stator Flux Linkage Vectors

Based on the reference stator voltage vectors obtained in the double voltage vector duty cycle control above, by filtering out the two adjacent extended voltage vectors to reduce two vector numbers, the duty cycle is introduced with zero vectors to obtain the voltage vectors for different amplitudes. The optimal voltage vector and its duty cycle are selected to act on the motor system by using the new stator flux linkage vector cost function. Therefore, the control precision of the electromagnetic torque and flux linkage is effectively improved. The effects of different voltage vector combinations on the pulsations of the stator flux linkage vectors are shown in Figure 3.27. It can be seen from Figure 3.26 that the tracking control of the stator flux vector can be achieved by optimally allocating the duty cycles of the different voltage vectors.

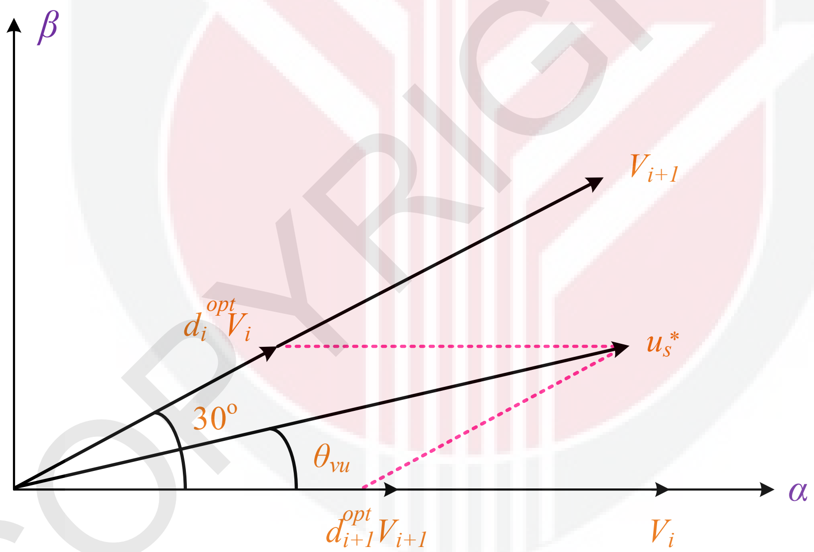

Figure 3.27 : Diagrammatic Sketch of Three Voltage Vectors Used to Synthesize a Reference Vector

On the basis of the double voltage vector duty cycle control, an additional effective voltage vector is added, that is, two adjacent extended voltage vectors and zero vectors are used to construct a reference voltage vector to realize the duty cycle control of three voltage vectors. By adjusting the operating times of the three voltage vectors in one control cycle, the synthetic candidate voltage vectors are coincident with the reference voltage vectors, thus achieving more accurate control. The principle of using three voltage vectors to synthesize a reference voltage vector is shown in Figure 3.26.

$$u_s^* = d_i V_i + d_{i+1} V_{i+1} + (1 - d_i - d_{i+1}) V_0 \tag{3.79}$$

where V_i is the extended voltage vector and d_{i+1} is duty cycle of V_i.

Similarly, in order to evaluate the influence of the combined candidate voltage vectors on the stator flux linkage vectors through three voltage vector duty cycle control, as expressed in Equation 3.76, the candidate voltage vector obtained from Equation 3.79 is used to predict the stator flux linkage vector $\Psi_s(k+2)$ at $(k+2)T_s$, which is carried into Equation 3.80 to obtain:

$$\begin{aligned} \mathrm{g} &= |\Psi_s^* - \Psi_s(k+2)| \\ &= |\Psi_s^* + T_s R_s i_s(k+1) - T_s d_i V_i - T_s d_{i+1} V_{i+1} - \Psi_s(k+1)| \\ &= T_s |u_s^* - d_i V_i - d_{i+1} V_{i+1}| \end{aligned} \tag{3.80}$$

In order to optimize the cost function of the stator flux linkage vectors, the reference voltage vector and candidate voltage vector of the three voltage vector combination are equal, and the optimal duty cycle of two adjacent extended voltage vectors can be obtained according to the parallelogram vector combination method. Using the triangle sine theorem from geometric relationships:

$$\frac{d_i^{opt}|V_i|}{sin(\pi/6-\theta_{vu})}=\frac{d_{i+1}^{opt}|V_{i+1}|}{sin(\theta_{vu})}=\frac{|u_s^*|}{sin(5\pi/6)} \tag{3.81}$$

The optimal duty cycle of two adjacent extended voltage vectors can be derived from Equation 3.81:

$$d_i^{opt}=\frac{|u_s^*|\,sin(\pi/6-\theta_{vu})}{|V_i|\,sin(5\pi/6)}=\frac{2|u_s^*|\,sin(\pi/6-\theta_{vu})}{|V_i|} \tag{3.82}$$

$$d_{i+1}^{opt}=\frac{|u_s^*|\,sin(\theta_{vu})}{|V_{i+1}|\,sin(5\pi/6)}=\frac{2|u_s^*|\,sin(\theta_{vu})}{|V_{i+1}|} \tag{3.83}$$

Based on two adjacent extended basic voltage vectors and their corresponding optimal duty cycle, two effective and zero vectors are combined to achieve duty cycle control. The control effectiveness of the combinational voltage vectors with the duty cycle is fully considered, ensuring that the added voltage vector follows the reference voltage vectors and achieves the deadbeat control of the stator flux linkage vector according to its reference value, effectively improving the control accuracy of the electromagnetic torque and stator flux linkage. A block diagram of FCS-MPTC is presented in Figure 3.28.

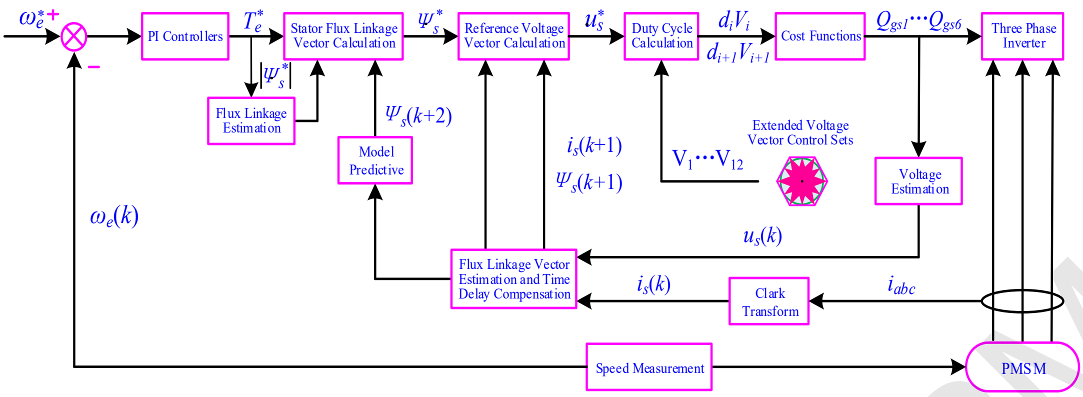

Figure 3.28 : Block Diagram of the Optimization Strategy for FCS-MPTC

The PMSM is driven by a three-phase inverter module, and the reference rotor electrical angular velocity ω_e^* compares with the rotor electrical angular velocity $\omega_e(k)$ obtained from speed measurement. After the PI controller, the reference electromagnetic torque T_e^* , the reference stator flux linkage amplitude $|\Psi_s^*|$, and the stator flux linkage vector $\Psi_s(K+2)$ are included in a stator flux linkage vector calculation. The reference stator flux linkage vector Ψ_s^* , the stator flux linkage vector $\Psi_s(k+1)$, and the stator current vector $i_s(k+1)$ are incorporated into a reference stator voltage vector u_s^* by flux linkage vector estimation and time-delay compensation (through conversion of the three-phase current i_{abc} to the stator current vector $i_s(k)$ of the α and β static coordinate system after Clarke transformation, with the stator voltage vector $u_s(k)$ from the voltage estimation). Based on the extended voltage vector control sets $V_1 \cdots V_{12}$, the drive signals $Q_{gs1} \cdots Q_{gs6}$ are generated from the cost functions $d_i V_i$ and $d_{i+1} V_{i+1}$. All that has been described above is indispensable for the PMSM to work well.

3.5 Shaft Voltage and Bearing Current of PMSM

Statistically, 41% of motor failures result from bearing damage. The causes of bearing failure encompass shaft voltage, load mutation, load vibration, overload, bearing pollution, overheating, insufficient or invalid lubricating oil, misaligned installation, looseness, and improper maintenance. This section primarily discusses the causes, hazards, and solutions for internal shaft voltage in motors.

3.5.1 Generation Mechanism

The causes of shaft voltage can be classified into five main categories:

a. Unipolar Effect of Axial Flux

In electrically excited synchronous motors there exist various circuits, such as collector ring devices and rotor winding ends, surround the rotating shaft. The design should ensure that the magnetomotive force generated by these circuits offsets each other. Improper design or short circuiting of the rotor winding between turns can lead to unbalanced magnetomotive forces and result in axial remanence. Moreover, abnormal conditions such as generator short circuiting can magnetize the shaft, bearing bush, casing, and other devices, retaining residual magnetism. The resulting magnetic field lines flow through the bearing bush, generating shaft voltage as the main shaft rotates. This shaft voltage, produced by the monopole effect of axial flux, comprises a DC component that varies with the load.

b. Generator Static Excitation System

In the static excitation system of electrically excited synchronous motors, the rectifier introduces high-amplitude voltage pulses into the rotor winding, generating shaft voltage on the shaft through the distributed capacitance between the rotor winding and the shaft.

c. Electrostatic Charge Accumulation

In a turbine generator, water molecules in the steam collide with and create friction on the turbine generator blades, resulting in the generation of electrostatic charge on the high-speed rotating turbine generator rotor. The accumulation of this electrostatic charge causes shaft voltage.

d. Unbalanced Magnetic Circuit

Rotor eccentricity, sector structure, fractional slot structure, three-phase winding imbalance, three-phase power supply voltage imbalance, winding turn short circuit due to motor manufacturing deviation, bearing wear, and other factors result in magnetic circuit imbalance. This imbalance generates an alternating net magnetic flux around the shaft, inducing inherent shaft voltage.

e. CM Voltage of Three-Phase Inverter

In conventional PWM control, the three-phase output voltage of the frequency converter exhibits a 120° phase angle difference, but the sum of the three-phase output voltage is non-zero, resulting in a stepped zero sequence voltage known as the CM voltage. The alternating frequency corresponds to the switching frequency of the frequency converter. Due to distributed capacitors in the motor, the CM voltage traverses various circuits between the coil and rotor, the coil and stator core, and the coil and casing, ultimately leading to the application of CM shaft voltage on the bearing.

In the early stages of permanent magnet motor development, limited single machine power, low speeds, and an integer number of slots per pole resulted in either negligible or no shaft voltage production, leading to minimal associated harm.

In the 1980s, the advent of high-performance permanent magnet materials propelled the research, development, and utilization of permanent magnet motors into a new era of rapid advancement. This period witnessed continuous increases in the capacity and speed of single-machine permanent magnet motors. Inverter-powered permanent magnet motors experienced substantial growth, leading to an increasingly significant impact of shaft voltage. For instance, high-power line-start PMSM commonly exhibit elevated inherent shaft voltage due to rotor eccentricity and machining deviation. Meanwhile, CM shaft voltage presents a prevalent issue in small power inverter fed PMSM, necessitating the implementation of corresponding measures to mitigate bearing damage caused by shaft voltage.

The line-start PMSM is powered directly by the grid, resulting in only inherent shaft voltage. Conversely, the PMSM fed by a frequency converter exhibits both inherent shaft voltage and CM shaft voltage. The generation mechanism and characteristics of these two types of shaft voltage are elaborated below.

3.5.1.1 Inherent Shaft Voltage

In a permanent magnet motor, the permanent magnetic field and armature reaction magnetic field can both generate inherent shaft voltage:

a. Inherent Shaft Voltage of Permanent Magnetic Field

As previously discussed, motor manufacturing deviations such as rotor eccentricity, sector structure, fractional slot stator structure, and bearing wear can lead to asymmetry in the motor's magnetic circuit. The resulting shaft voltage generated by the interaction between the permanent magnet and the asymmetric stator magnetic circuit structure is referred to as the inherent shaft voltage of the permanent magnetic field.

b. Inherent Shaft Voltage of Armature Reaction Magnetic Field

In the case of a SPMSM with a uniform air gap and integral slot winding, along with the application of symmetrical or asymmetrical three-phase current, the inherent shaft voltage of the armature reaction magnetic field will not be generated. Conversely, in fractional slot winding PMSM, the application of symmetrical or asymmetrical three-phase current typically leads to the generation of inherent shaft voltage from the armature reaction magnetic field. Additionally, the inherent shaft voltage of the armature reaction magnetic field is also alternating, and the path of shaft current generated by the armature reaction magnetic field aligns with that of the permanent magnet magnetic field.

3.5.1.2 CM Shaft Voltage

The voltage between the neutral point and the reference ground of the motor denotes the CM voltage. When PMSM is powered by symmetrical sine wave three-phase voltage, the CM voltage remains at zero. However, when a frequency converter is employed for power supply, the three-phase voltage is comprised of a series of pulses, resulting in the CM voltage no longer being zero but an alternating voltage made up of pulses, as illustrated in Figure 3.29. This CM voltage establishes a circuit through the distributed capacitance and bearing capacitance across the stator, rotor, winding, and permanent magnet, thereby giving rise to bearing current. Based on different flow paths, three types of bearing current are generated by the CM voltage shaft voltage

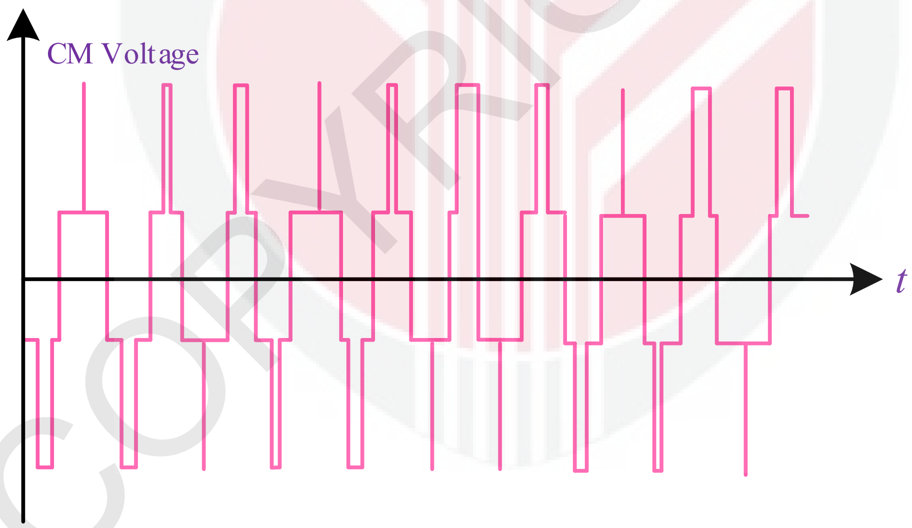

Figure 3.29 : Generated CM Voltage Waveform by PWM

a. Capacitive Discharge Current

The CM voltage results in shaft voltage through the distributed capacitance among the stator winding, stator core, and rotor. If the bearing oil film breaks down, high frequency bearing current is produced, following the path: stator winding→rotor→shaft→end caps at both ends→motor shell→ground wires→frequency converter. Typically, the shaft is grounded by a brush or protective ring to protect the bearing.

b. Rotation Shaft Grounding Current

The CM voltage generates high-frequency leakage current that flows to the casing through the capacitance between the stator winding and the stator core. This current must be returned to the frequency converter. The majority of it returns to the frequency converter through the casing ground wire, bypassing the bearing and therefore having no impact on it. However, any return circuit carries impedance, resulting in the shell potential being higher than ground. When the motor shaft is connected to a gearbox or other transmission machinery that is firmly grounded and has a similar potential to the frequency converter housing through a metal coupling, the bearing will experience an elevated voltage level. In the event of a breakdown in the bearing oil film, a portion of the current will flow through the bearing, shaft, and transmission machinery before returning to the frequency converter. If the rotating shaft lacks direct contact with ground level, part of the current will flow through the bearings of the gearbox or load machinery, causing damage to these bearings prior to the motor bearings.

c. High Frequency Circulating Bearing Current

As previously discussed, the CM voltage produces high-frequency leakage current that flows to the stator core and casing through the capacitance between the stator winding and stator core. Consequently, the high-frequency current entering the stator winding from the frequency converter is greater than the high-frequency current flowing back to the frequency converter from the stator winding, leading to a non-zero axial current in the winding. This axial current generates high-frequency alternating magnetic flux, resulting in high-frequency shaft voltage following the same path as the inherent shaft voltage. In the event of a breakdown in the bearing oil film, high frequency circulating current will flow through the bearing.

3.5.1.3 CM Voltage Equivalent Circuit

The distributed capacitance between the stator core, rotor core, stator winding, permanent magnet, and bearing capacitance collectively form a circuit, giving the CM shaft voltage.

The CM voltage represents the zero-sequence component, leading to the need for the PMSM to be treated as an equivalent zero sequence circuit during CM voltage analysis. In PMSM, in addition to winding resistance and inductance, distributed capacitance is also present. From a capacitive perspective, the PMSM comprises four electrodes: stator core (including shell), rotor core (including shaft), permanent magnet, and stator winding. Distributed capacitance exists between these electrodes, and the bearing is considered as a capacitance prior to breakdown. Considering the structure of the PMSM, the distributed capacitance, zero sequence resistance, zero sequence inductance, and inverter are combined to form the CM equivalent circuit of the motor frequency converter system, as illustrated in Figure 3.30.

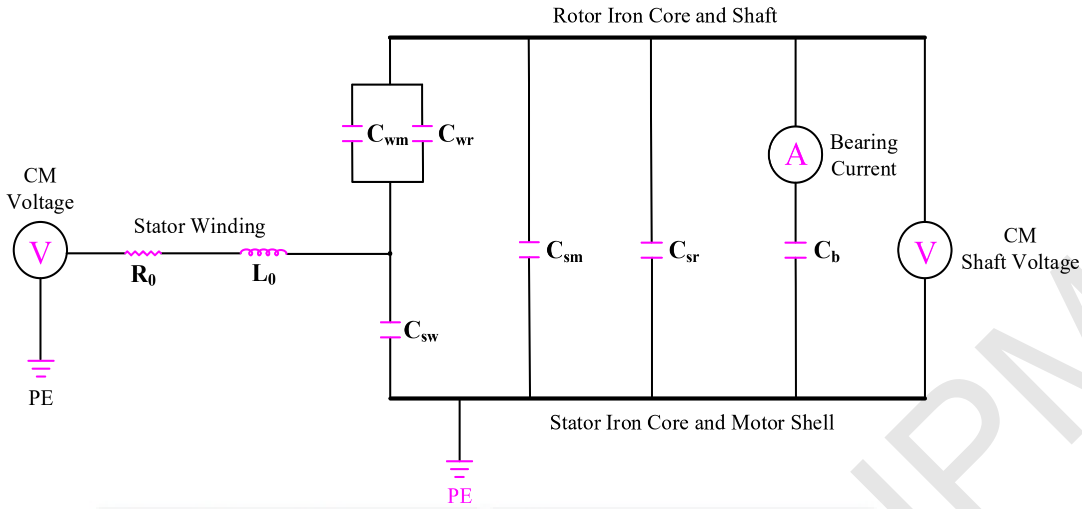

Figure 3.30 : Equivalent Circuit Diagram of CM Voltage

Where, R_0 represents the winding zero sequence resistance, equal to 1/3 of the phase winding resistance, while L_0 denotes the winding zero sequence inductance, equivalent to 1/3 of the phase winding inductance. Additionally, C_b stands for the bearing capacitance, C_{sw} is the capacitance between the winding and the stator core, C_{wm} represents the capacitance between the winding and the permanent magnet, C_{wr} signifies the capacitance between the winding and the rotor core, C_{sm} denotes the capacitance between the stator core and the permanent magnet, and C_{sr} indicates the capacitance between the stator core and the rotor core.

3.5.2 Suppressing Measures

The PMSM, as an advanced motor type, plays a critical role in modern industry. Implementing effective protective measures and strategies is essential for ensuring its optimal and efficient operation.

3.5.2.1 Bearing Protection Measures

When the shaft voltage is insufficient to damage the bearing, protective measures cannot be implemented. However, when the shaft voltage is high enough to puncture the bearing oil film, mitigation measures must be employed. These measures include reducing the shaft voltage, minimizing the voltage borne by the bearing oil film, and directly grounding the shaft voltage. Methods for reducing the voltage borne by the bearing oil film primarily involve using insulated bearings and insulated end caps. Directly grounding the shaft voltage entails installing a grounding brush on the shaft. These methods are briefly outlined below:

a. Insulated Bearing

An insulated bearing is characterized by its insulating properties, which are achieved through the application of a specialized process to coat the outer or inner ring with an insulating material, or by utilizing ceramic rolling elements.

b. Insulated Bearing Housing

The inner hole and end face of the insulated bearing housing are coated with a layer of insulating material of specific hardness, serving the same function as the insulated bearing.

c. Grounding Brush

Grounding brushes are installed at one or both ends of the shaft. However, this method is susceptible to reduced reliability due to exposure to environmental dust and oil stains, necessitating regular maintenance.

d. Grounding Protection Ring

The grounding protection ring consists of a grounding ring with numerous fixed conductive fibers. When secured to the end cover with screws, the conductive fibers make substantial contact with the shaft, ensuring effective conduction between the shaft and the end cover, and direct grounding of the shaft voltage. Its function parallels that of a grounding brush, while boasting heightened reliability.

The shaft grounding ring, located near either end of the shaft refers to Figure 3.31, utilizes carbon fiber brushes to establish contact with the shaft, providing a direct path to ground for the current flowing through the shaft. This redirection of current prevents it from passing through the bearings, thus mitigating bearing failure resulting from unbalanced PWM waves.

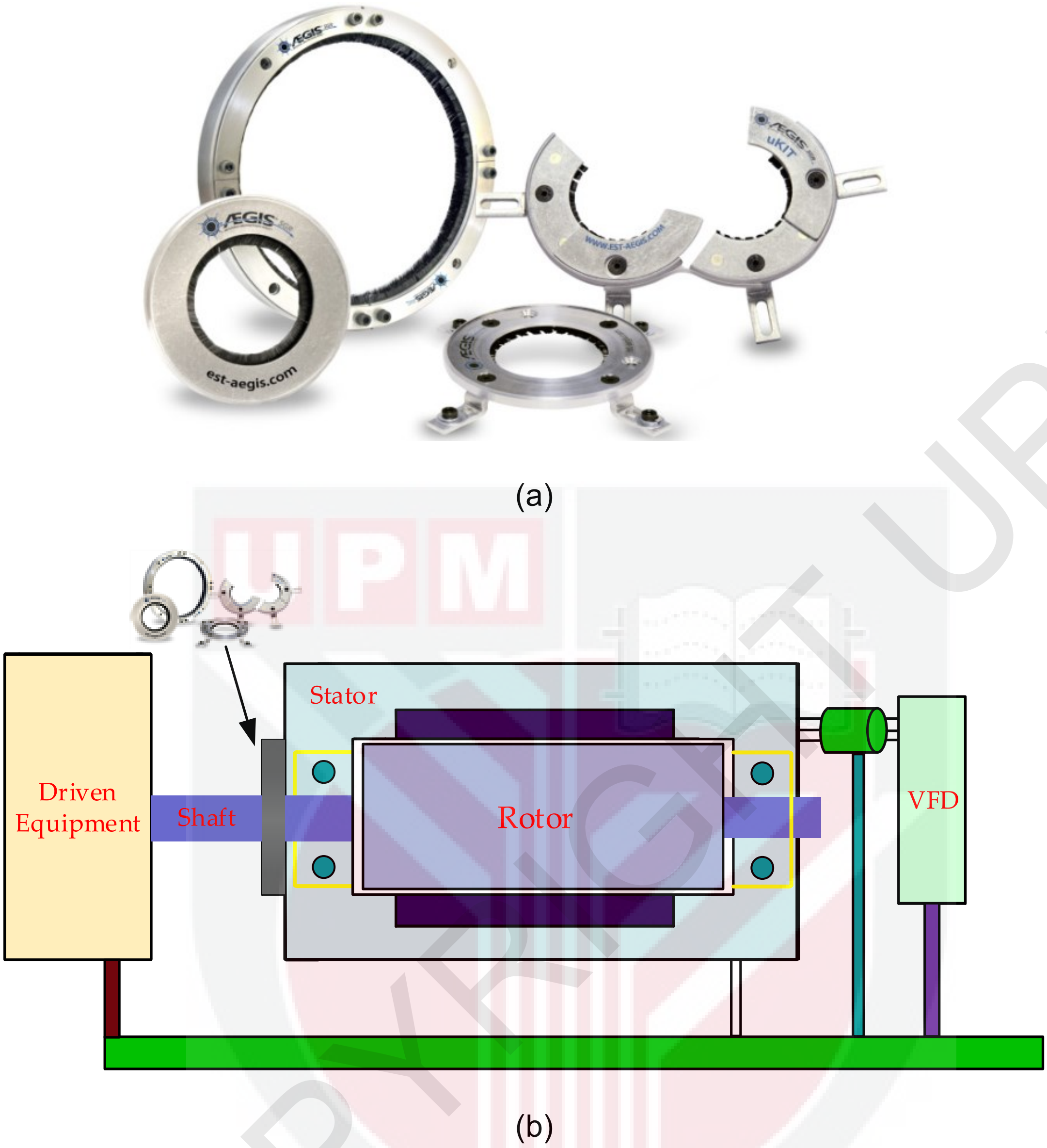

Figure 3.31 : Physical Map of Grounding Protection Ring: (a) Contour Structure; (b) Installation Location

There are several designs of shaft grounding rings. While they provide the same protection, each of them offers unique mounting options specific for need:

a. Split Rings

Split rings come in two pieces allowing for insulation on a motor shaft that it still connected to the driven equipment without removing the pulley or coupling. These rings can either be mounted with screws, clips or with conductive epoxy.

b. Solid Rings

These rings are installed flush with the motor using conductive epoxy, clips, stand-off brackets or bolt through. The Epoxy takes 10 minutes to dry after installation. This line (method of installation) of rings is often installed when motors are in a shop for repair or in the field prior to installation on the driven equipment.

c. Press Fit

Rings can be press fit installed if the motor is in a shop. The motor end bracket is bored out to a 0.0005"-0.0015" interference fit.

Insulated bearings, insulated bearing chambers and insulated end cover are suitable for weakening the inherent shaft voltage and not suitable for common mode shaft voltage. The grounding brush and grounding protection ring are suitable for the weakening of common mode shaft voltage and not suitable for the inherent shaft voltage.

3.5.2.2 Suppressing Measures of CM Voltage

As is mentioned above, shaft voltage and bearing current can cause significant damage to the PMSM, and some Suppressing Measures need to be taken to decrease CM voltage.

a. Active and Passive Filter

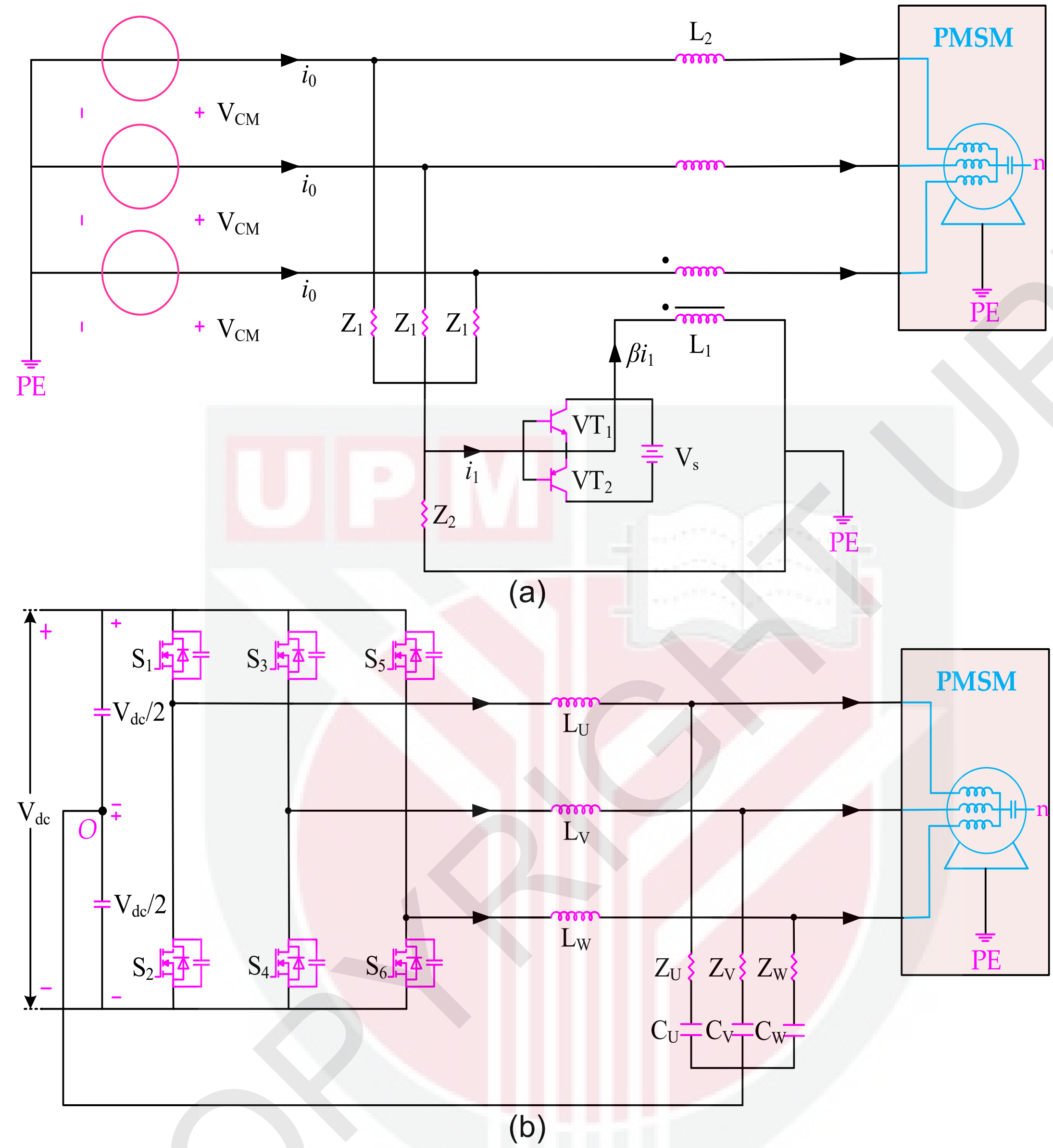

Figure 3.32 : Variable Frequency Motor Drive Control System with Suppressing Measures (a) Active Filter; (b) Passive Filter

Figure 3.32(a) depicts a variable frequency motor drive system featuring a source filter. The active power filter comprises voltage detection, push-pull circuit, and CM transformer circuit. V_{CM} and i_0 denote common mode voltage and common mode current, respectively. Z_1 and Z_2 represent CM voltage detection circuits comprising passive devices. Upon detecting the CM voltage, the detection circuit generates control current. The push-pull circuit amplifies the control current and applies it to the transformer to produce a voltage with equivalent amplitude but opposite polarity to the CM voltage, thereby counteracting the CM voltage at the inverter output.

Figure 3.32(b) illustrates the variable frequency motor drive system with a passive filter, where an RLC passive filter is inserted between the frequency converter and the motor, with the common end of the filter connected to the midpoint of the DC bus.

b. Multilevel Inverters

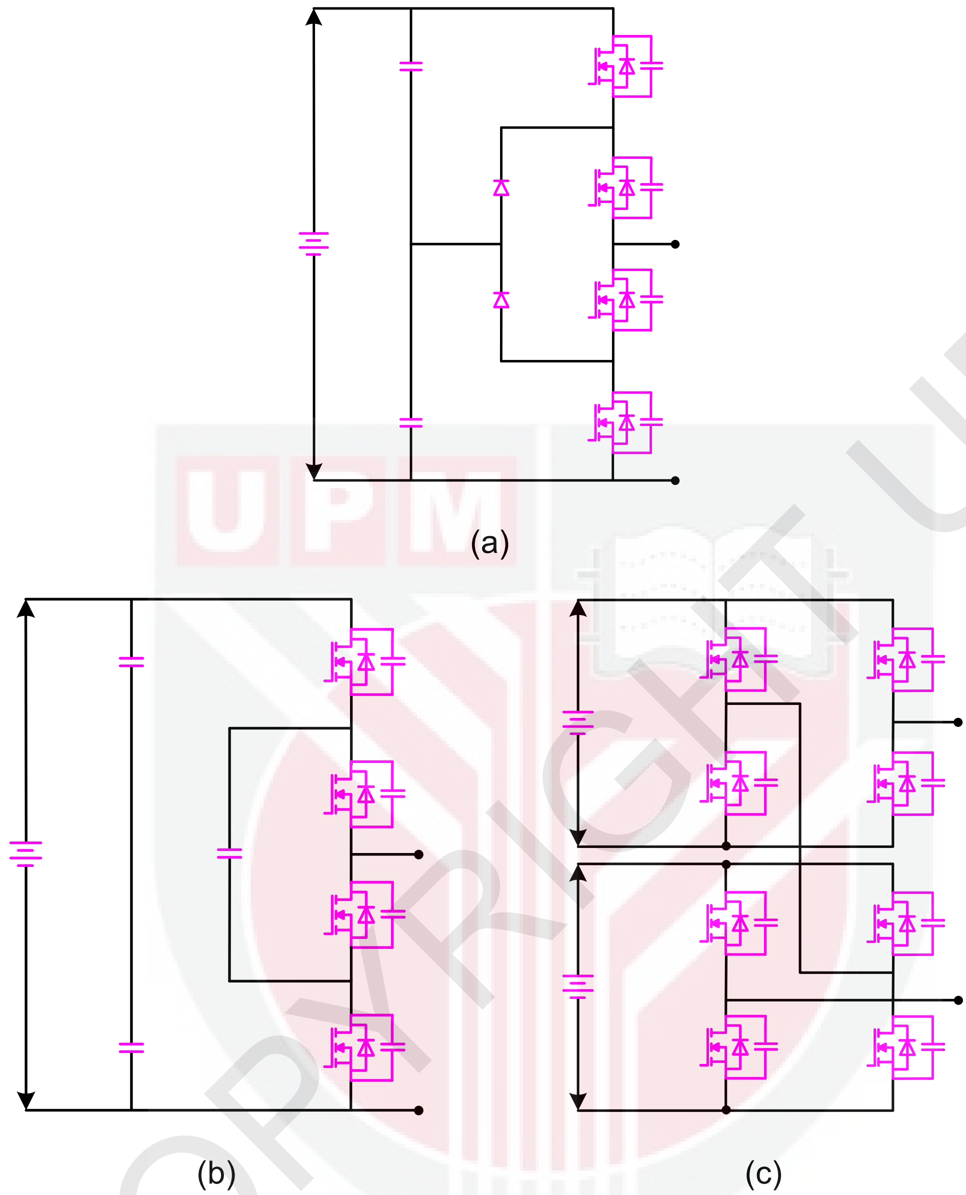

Figure 3.33 : Multilevel Inverters: (a) NPC (b) FC (c) CHB

Multilevel inverters have gained significant attention in the research community due to their application in high voltage and large power conversion scenarios. The exploration of circuit topologies and PWM control methods for multilevel inverters has emerged as a prominent area of investigation. In comparison to the conventional two-level inverters, the multilevel inverters offer several advantages such as reduced voltage stress on SiC MOSFET, lower THD, and EMI. These desirable features make multilevel inverters well-suited for motor drive control systems, which can be categorized into three main configurations: neutral point clamped (NPC), flying capacitor (FC), and cascaded H-bridge (CHB), as illustrated in Figure 3.33.

3.6 EMI Harm and Protection about Motor Drive Control System Based on PMSM with SiC MOSFET

The wide band gap SiC MOSFET and PMSM become advantageous source for NEEVs, leading to EMI problems, which make the motor drive control system difficult to EMC standards. In this research, the generation mechanism, propagation path and test infrastructure of EMI are explained, and a system level conducted EMI equivalent circuit models for the motor drive control system is proposed, which includes power battery pack, busbar cable, LISN, three phase inverter, and PMSM. On this foundation, the principles of suppression and optimization EMI noise are discussed.

3.6.1 EMI Testing Fundamentals

Section 2.8 introduces conducted EMI testing principles, techniques and equipment to lay the foundation of simulate and experiment.

3.6.1.1 LISN and EMI Receiver

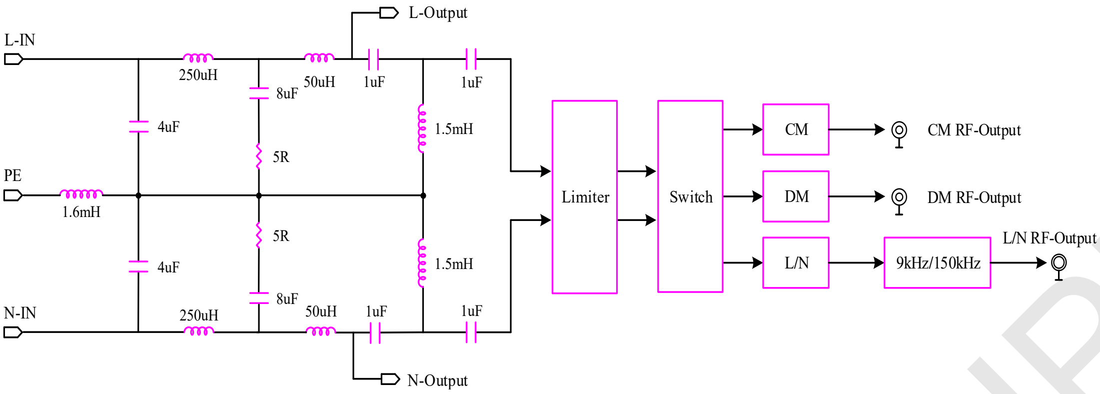

Figure 3.34 : LISN Internal Detailed Circuit Schematic

Conducted EMI propagates to other components or whole system through the busbar cable, which can be measured by voltage or current method. Generally speaking, the line impedance stability network (LISN) is a low pass filter connected between the device under test (DUT) and power supply lines, as shown in Figure 3.34. The LISN is used as EMI testing setup for two purposes: the first function is to block and transfer high frequency electrical noise pollution from external grid system; another function is to provide test ports and interfaces for spectrum analyzers or EMI receivers.

The measurement frequency range of LISN is 150 kHz and 30 MHz for motor drive control system, the measuring point resistance and inductance are 5Ω and 250uH respectively between each input power line and the common ground, so as to ensure the consistency of the measured data results in different test sites. The impedance characteristics curve of LISN are given in Figure 3.35.

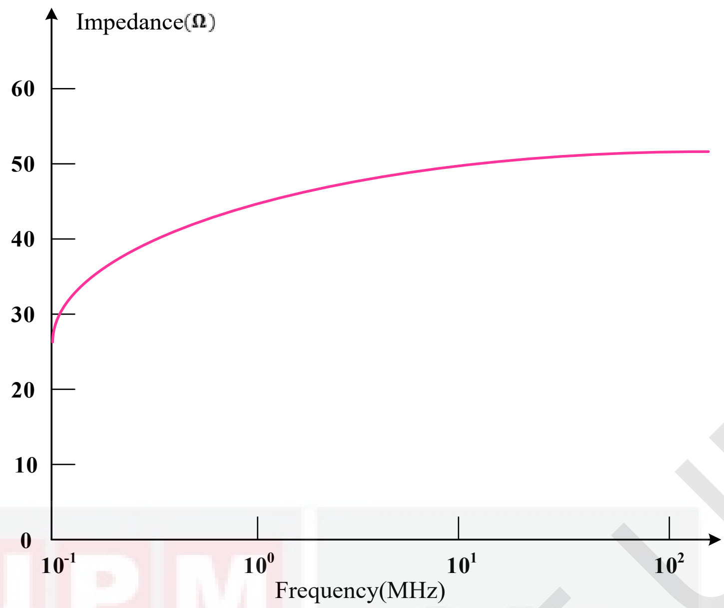

Figure 3.35 : LISN Impedance Curve

The normal workflow of EMI receiver is indicated in Figure 3.36. The RF input signal measured by LISN is first passed through attenuator and preselector and enlarged by high frequency amplifier. Then, the preprocessed signal mixes with the local oscillator and enters an intermediate frequency filter, the attenuator and amplifier ensure that only the intermediate frequency signal passes through them. After that, the peak, RMS, average or quasi peak of the intermediate frequency signal can be obtained by choosing different detector circuits. Finally, these values are selected by low frequency amplifier, filter and analog to digital (A/D) conversion to display the spectrum curve on the screen.

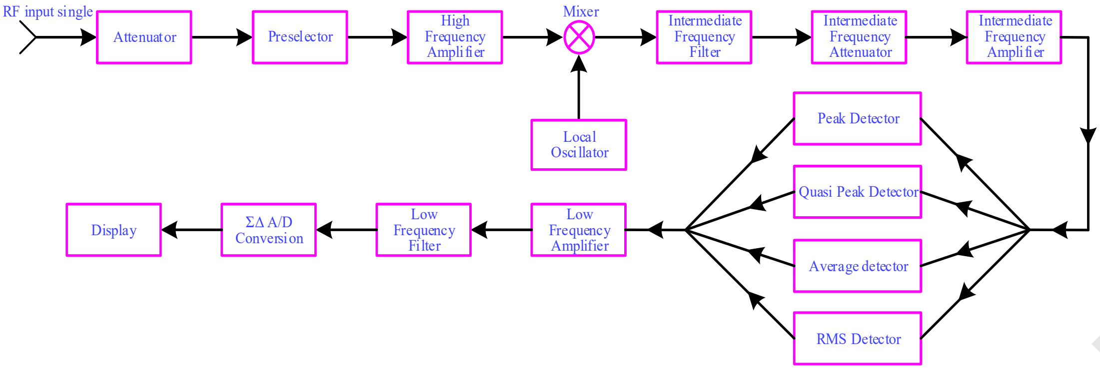

Figure 3.36 : EMI Receiver Block Diagram

3.6.1.2 Test Platform

The LISN, EMI receiver, DUT are placed on a metal ground plane seen in Figure 3.37.

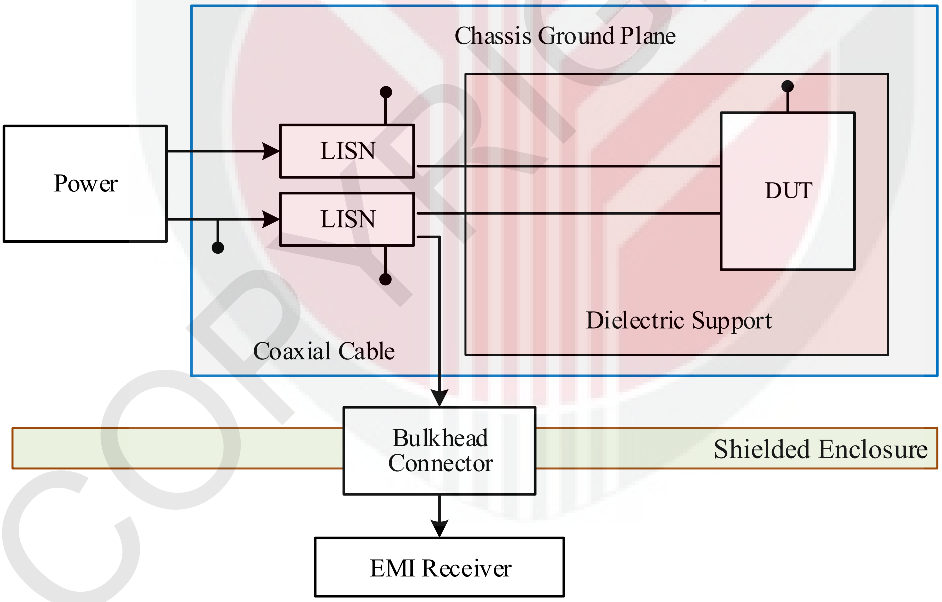

Figure 3.37 : EMI Test Environment

3.6.1.3 Conducted CM and DM Interference

The conductive EMI noise voltage is decomposed into CM and DM voltage. The CM noise is the average voltage V_{CM} and the DM noise is the difference voltage V_{DM} of two LISN resistors:

$$V_{CM} = (V_u + V_d)/2 \tag{3.84}$$

$$V_{DM} = V_u - V_d \tag{3.85}$$

where V_u and V_d are the voltage noise signals measured across the upward and downward LISN respectively.

The conductive EMI noise currents are also defined into CM and DM currents. CM currents flow through the phase and neutral conductors and take ground wire as the return path whereas differential mode currents flow between neutral and phase conductors. The phase noise currents I_P and neutral noise currents I_N can be rewritten as:

$$I_{CM} = (I_P + I_N)/2 \tag{3.86}$$

$$I_{DM} = (I_P - I_N)/2 \tag{3.87}$$

Where I_{CM} and I_{DM} are CM and DM currents respectively depicted in Figure 3.38. I_P and I_N represent the current flowing in phase and neutral lines.

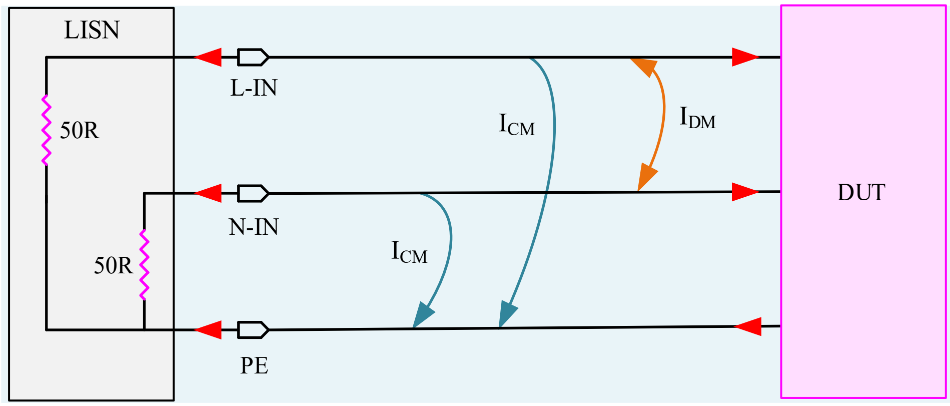

Figure 3.38 : CM and DM Flowing Paths

3.6.2 EMI Modeling of Motor Drive Control System

In the past, EMI modeling was considered difficult and impractical because it required detailed parameters that could not be predicted until the printed circuit board (PCB) layout was completed. Section 3.6.2 establishes and analyzes the EMI system level equivalent circuit model, which follows the top-down process and can be changed with the project progress to improve fidelity.

3.6.2.1 Equivalent Circuit Models of Power Electronic Components

The EMI of the motor drive control system is fundamentally caused by its own power electronics components. Therefore, it is necessary to establish an effective and accurate equivalent circuit model, such as resistor, capacitor, busbar cable, power battery pack, SiC MOSFET, PMSM, and PCB wiring.

a. Electric Capacitor Models

As Figure 3.39 shows Capacitance C is the ideal capacitor, and R_p is the insulation resistance corresponding to the direct leakage current. Heat dissipation within the plates, terminals and all conducting parts are represented by R_s and it is known as the equivalent series resistance (ESR). L stands for the total inductance of the leads and plates as the equivalent series inductance (ESL).

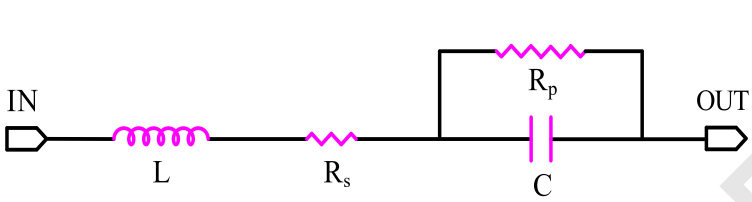

Figure 3.39 : Equivalent Circuit Model of an Electric Capacitor

b. Busbar Cable

Busbar cables, found in power distribution systems, are distributed elements whose lengths may by far exceed the operating wavelength in Figure 3.40. They can be modeled as multi-conductor transmission lines, where many frequency-dependent characteristics including per unit length parameters, skin and proximity effect, dielectric losses, and transmission line propagation, reflections, and delay need to be appropriately accounted.

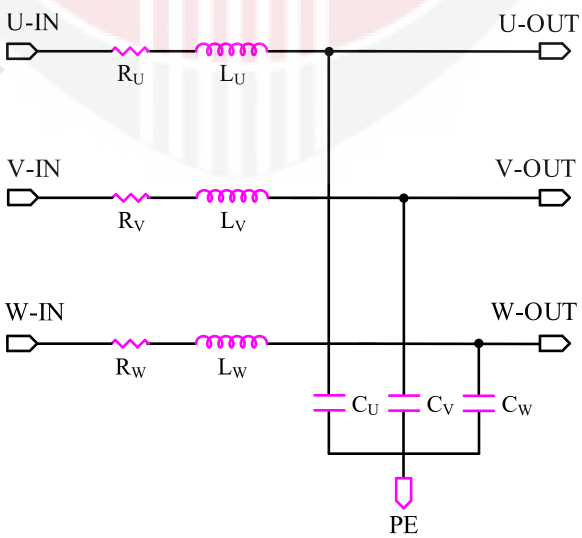

Figure 3.40 : Equivalent Circuit for Modeling a Long Three Phase Busbar Cable

Therefore, the main purpose of modeling the busbar cable is to determine the resistance R, inductance L and the capacitance C per unit length cable.

First, calculate the resistance R:

$$R = \rho/s = \rho/\pi r_1^2 \tag{3.88}$$

Where, ρ is the resistivity of materials, s is the cross-sectional area, r_1 is the cross-section radius.

Next, calculate the inductance L. The cable has an inner conductor and an outer conductor, also called shielding layer. So L consists of the inner self-inductance L_i and the outer self-inductance L_e in Figure 3.41.

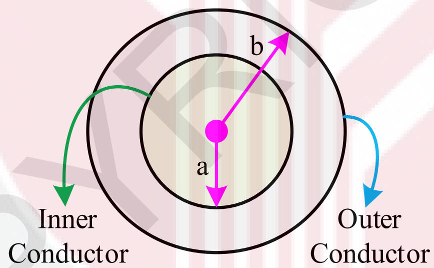

Figure 3.41 : Busbar Cable Self-Inductance Diagram

According to the transmission line theory, internal self-inductance per meter L_i is:

$$L_i = \mu_0/8\pi \tag{3.89}$$

μ_0 is the permeability of vacuum. The value of the outside self-inductance per meter is:

$$L_e = (\mu_0/2\pi)\, ln\, b/a \tag{3.90}$$

So, the value of the self-inductance per meter of the cable L is:

$$L = L_i + L_e = \mu_0/8\pi + (\mu_0/2\pi)\, ln\, b/a \tag{3.91}$$

At last, calculate the capacitance between the shielding layer and the unit length cable C.

According to transmission line theory, the expression of C is:

$$C = \int_V E \cdot D\, dv / U_1 U_2 \tag{3.92}$$

Where U_1 is the inner conductor to ground voltage, and U_2 is the shielding layer to ground voltage. They are all fixed values. E is electric field intensity, D is the electric displacement.

c. Power Battery Pack

In the market, in order to extend the driving mileage of NEEVs, a large number of low voltage single cell are required to be connected into high-voltage power battery pack. The equivalent circuit model is shown in Figure 3.42.

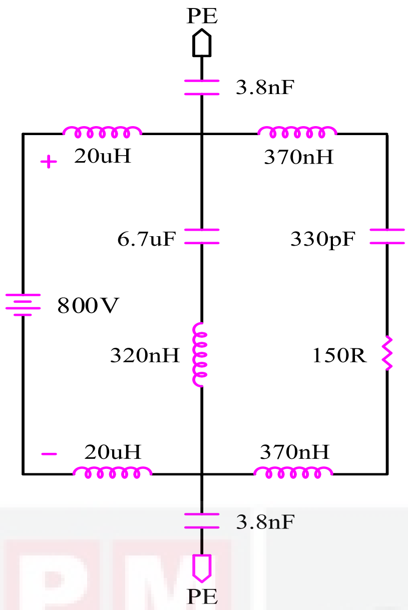

Figure 3.42 : Equivalent Circuit Model of Power Battery Pack

d. SiC MOSFET

For SiC MOSFET, parasitic capacitance and inductance need to be considered for more accurate modeling. As shown in Figure 3.43, the turn on resistance R_G, C_{GD} and C_{GS} are parasitic capacitances between the grid and drain respectively from the manufacturer datasheet. The C_{DS} is both parasitic capacitance from the drain to the source and the junction capacitance of the antiparallel diode. L_G, L_D, and L_S are parasitic inductances of drain, source and gate, as well as packaging pins. C_{p1} and C_{p2} are the parasitic capacitance between the power module and the metal substrate.

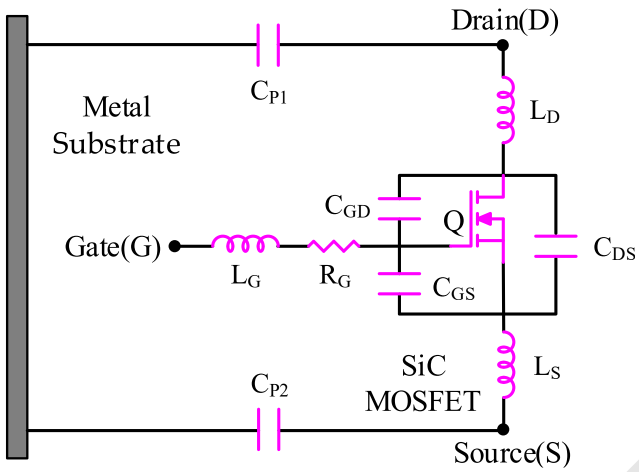

Figure 3.43 : SiC MOSFET Equivalent Circuit Model with Parasitic Parameters

e. PMSM

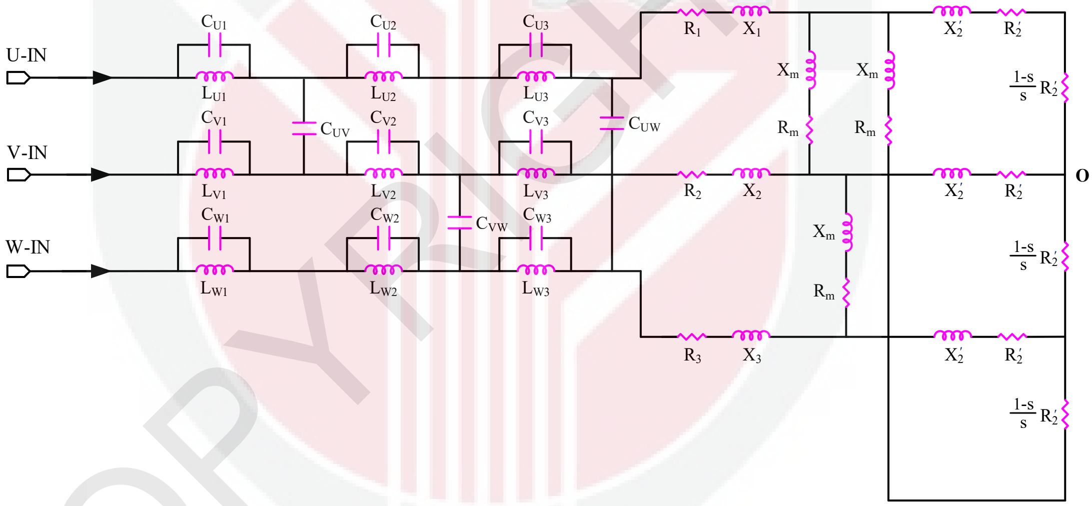

Figure 3.44 : Coupled Three Phase RLC Equivalent Circuit Model of PMSM

PMSM can be as the most complex electrical parts in the motor drive control system. And it is impossible to know the whole parameter details in practice, the physical modeling method of the motor is usually not applicable. The PMSM is a low frequency induction device and modeled by a three phase linear RLC circuit in Figure 3.44.

f. PCB Tracks

The influence of PCB tracks interconnect design is sometimes overlooked in EMC research and analysis. When extracting the parasitic parameters of PCB tracks, only the parasitic resistance and inductance are considered because the parasitic capacitance is very small. For example, PCB tracks L and N can be regarded as two conductors. The equivalent circuit model is shown in Figure 3.45, where R_1 and L_1 are the resistance and self-inductance of track L, R_2 and L_2 are the resistance and self-inductance of track N, and K_{L-N} is the mutual inductance between the two tracks.

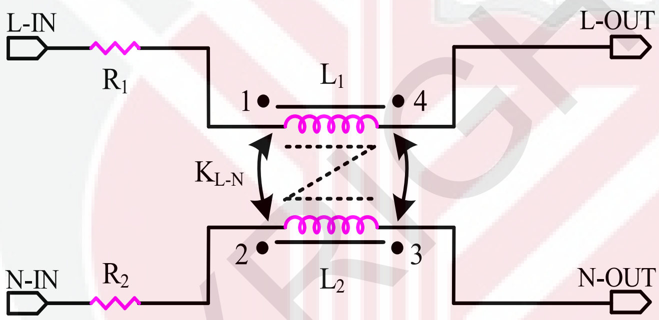

Figure 3.45 : HF Equivalent Circuit Model of the PCB Tracks L and N

It can be seen from Table 3.3 that with the increase of frequency, self-inductance and mutual inductance values hardly change, while resistance changes greatly and provide some useful experiences and lessons for ultra-high frequency motor drive control system.

Table 3.3 : HF Parasitic Parameters of PCB Tracks L and N

frequency	R_1(mΩ)	R_2(mΩ)	L_1(nH)	L_2 (nH)	M_{12} (nH)
f=150kHz	13.33	12.91	32.92	34.95	6.48
f=10MHz	14.36	13.89	32.81	34.83	6.41
f=30MHz	21.05	20.91	31.70	33.71	6.16

3.6.2.2 Equivalent Circuit Models of Motor Drive Control System

Figure 3.46 represents the system level equivalent circuit models of motor drive control system, including power battery pack, LISN, three phase inverter, busbar cable and PMSM. The spectrum of EMI source is distributed in the frequency range from 150kHz to 30MHz. Therefore, the parasitic parameters must be considered to research and analysis the transmission path of conducted EMI.

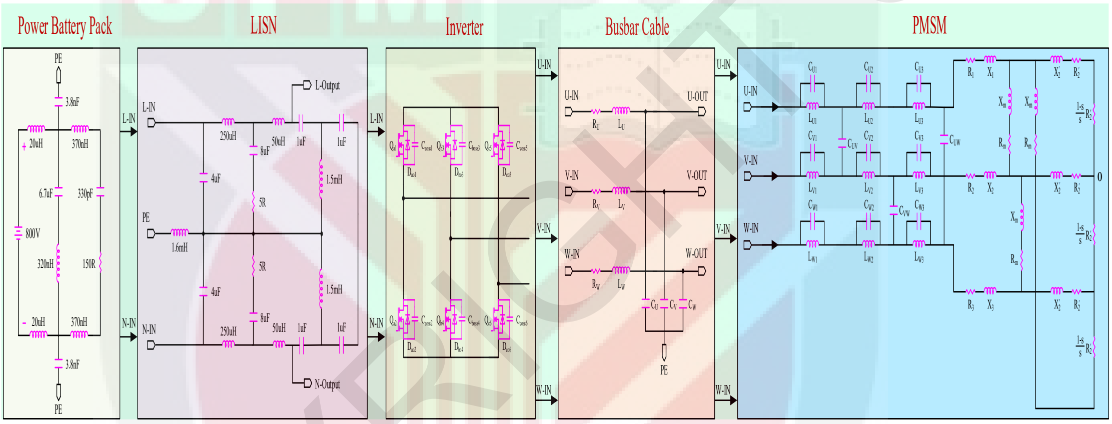

Figure 3.46 : System Level Equivalent Circuit Models of Motor Drive Control System

3.6.3 EMI Affects of High Switching Frequency for Motor Drive Control System

While fast switching SiC MOFET presents both exciting opportunities and significant technical challenges in motor drive control systems. Figure 3.47 illustrates that the utilization of SVPWM in a three-phase inverter driving a PMSM results in asymmetrical instantaneous voltages, leading to a high frequency CM voltage that adversely affects the windings, stator, and rotor of the motor. This high frequency CM voltage further impacts the stray and parasitic capacitances, resulting in the generation of high amplitude and frequency CM current. More importantly, the CM current has a detrimental effect on motor bearings, significantly reducing the operation life span of frequency conversion motors.

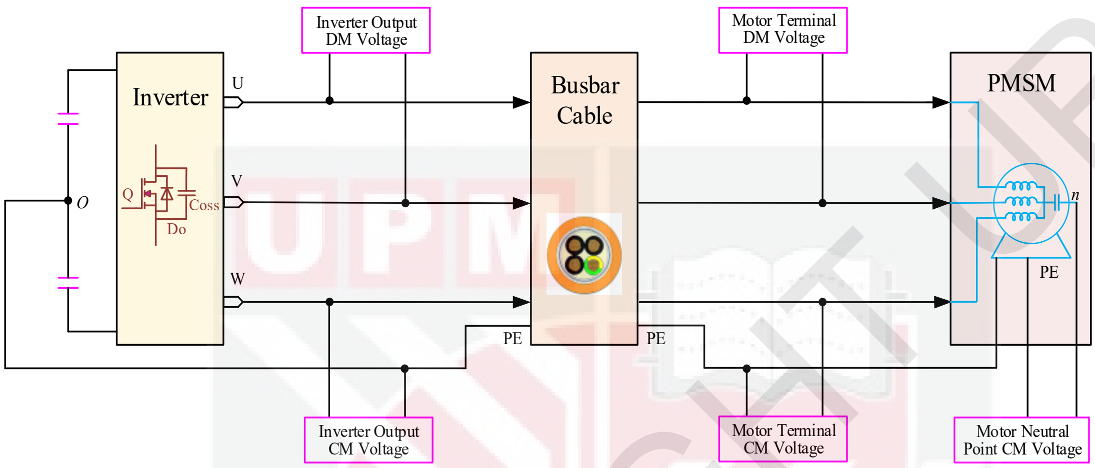

Figure 3.47 : Sketch Map of CM/DM Voltage in Motor Drive Control System

3.6.3.1 Failure Mechanism of Motor Insulation

In a voltage source inverter motor drive control system, the output pulses during fast turn-on and turn-off of SiC MOSFET can cause an increase in overvoltage levels at the motor terminals and stator neutral, referred to as the reflected wave. This overvoltage is characterized by CM (phase-to-ground) motor-terminal overvoltage, DM (phase-to-phase) motor-terminal overvoltage, and CM stator-neutral overvoltage (motor-neutral-to-ground), and is influenced by factors such as the busbar cable length, the impedance mismatch between the busbar cable and the motor, and the rise and fall times of the inverter output voltage. In addition, the overvoltage occurs at the motor side and the overcurrent also exists at the inverter side. Overvoltage leads to partial discharge (PD) onset, which can accelerate motor winding insulation degradation, increase stress on bearings, and result in premature failure. At the same time, overvoltage creates EMI problems, while overcurrent impacts the switching characteristics of electric power equipment.

3.6.3.2 Damage of Shaft Voltage and Bearing Current

In motor drive control systems, the switching operations of power electronic devices may give rise to high-frequency leakage currents of up to 10MHz. These leakage currents can inadvertently impact circuit breakers and initiate trip faults, in addition, it is highly likely that they are highly likely to flow through the motor bearings and cause serious damage. There are three main bearing current phenomena: bearing discharge current, capacitive bearing current, and induced (or circulating) bearing current. Bearing discharge currents are caused by breakthroughs of the bearing grease, resulting in the discharge of the bearing capacitance. These discharge currents circulate solely within the motor and cannot be measured externally, flowing through both bearings and the capacitance between the rotor and stator. Capacitive bearing currents are generated when CM voltage is applied to the motor, with a portion of the CM voltage also being applied to the bearings due to the parasitic capacitance of the motor. Similar to the bearing discharge current, the induced bearing current circulates inside the motor and cannot be measured externally.

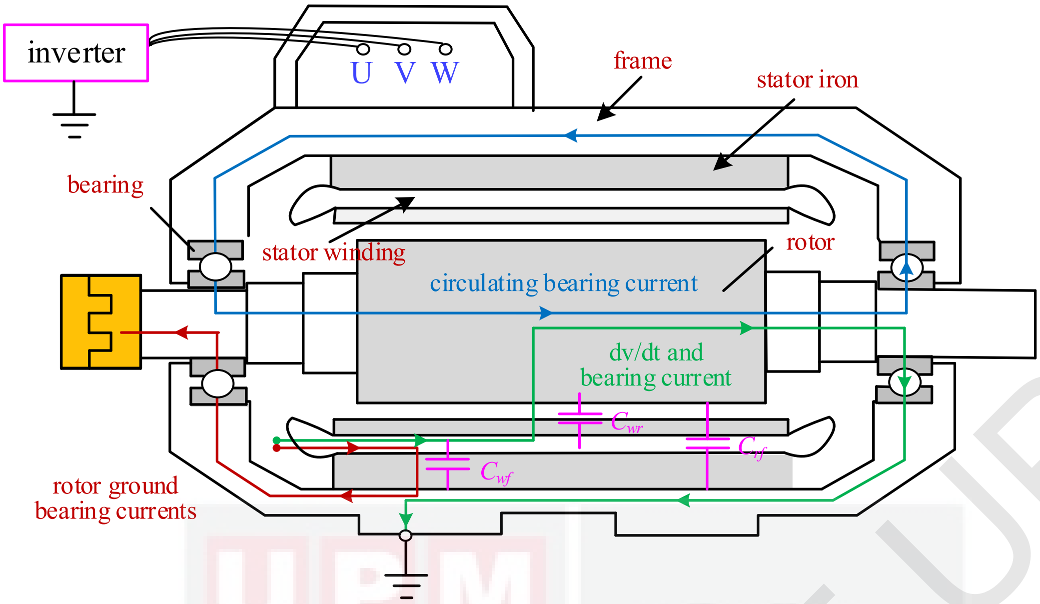

Figure 3.48 : Coupling Path Schematics of Bearing Current

The high CM voltage is produced through the PWM operation of the inverter, exerting an influence on the capacitive coupling paths formed by three primary stray capacitors within the motor. These capacitors include the capacitance between the stator winding and frame (C_{wf}), the capacitance between the rotor and frame (C_{rf}), and the capacitance between the stator winding and rotor (C_{wr}). As a result of this coupling, a bearing voltage (V_b) is generated. The coupling paths are illustrated in Figure 3.48.

Shaft voltage encompasses the voltage that arises at the two bearing ends of the motor or between the motor rotor shaft and the bearings during motor operation. Normally, when the shaft voltage remains low, the lubricating oil film between the motor rotor shaft and the bearing functions as an effective insulator. However, if the shaft voltage exceeds to a certain threshold duo to external factors, the lubricating oil film will be penetrated, leading to discharge and the creation of a bearing current circuit. This bearing current not only disrupts the stability of the lubricating oil film but also gradually deteriorates the quality of the cooling and lubricating oil. Additionally, as the bearing current passes through the metal contact point between the bearing and the shaft, it generates intense heat instantaneously, resulting in localized bearing melting. The melted bearing alloy then splashes under rolling pressure, causing the formation of small pits and burnouts on the inner surface of the bearing. Ultimately, accelerated mechanical wear occurs, leading to bearing damage, while severe cases may result in bearing shell burnouts, accidents, and enforced shutdowns.

As the voltage arcs between the bearings and the housing, it leaves microscopic weld splatters. These splatters make the bearings' rolling elements; ball or roller, and internal raceways rough; which could lead to the bearing failure.

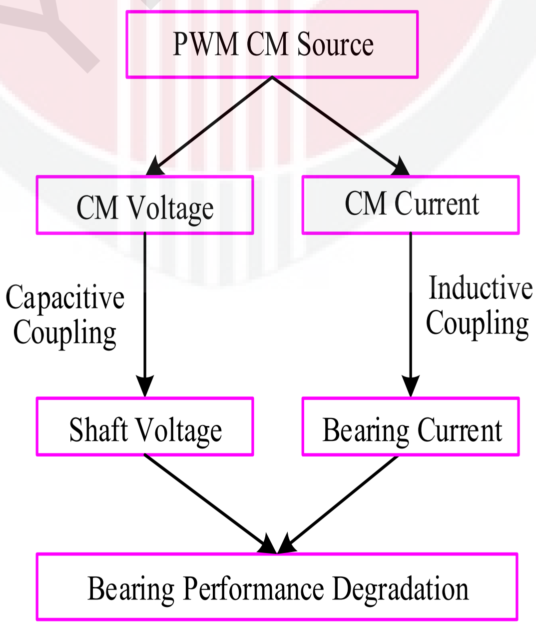

Figure 3.49 : Causal Chain of Bearing Damage

Figure 3.49 illustrates the generation of high-frequency CM voltage and current by the PWM CM source. These CM signals, upon passing through coupling capacitors and inductors, give rise to shaft voltage and bearing current. Consequently, this phenomenon results in degradation of bearing performance.

3.6.4 EMI Suppression Discussion of Motor Drive Control System

Section 3.6.4 introduces the conducted EMI model of motor drive control system in NEEVS to better understand how generates and propagates paths and predict noise levels. However, due to EMC standards, the conducted EMI needs to be limited. In order to improve the conducting of EMI, it is usually necessary to consider three aspects: suppressing interference source, optimizing propagation path and improving equipment immunity.

3.6.4.1 EMI Suppression and Optimization Measures

At the moment, as for the motor drive control system, specific measures mainly include electromagnetic shielding grounding, installation filters, advanced PWM strategies, and redesigning the system structure and layout.

a. Electromagnetic Shielding

Electromagnetic waves are the main mode of electromagnetic energy transmission. Electromagnetic shielding is a shell made of soft magnetic metal material that almost surrounds the equipment to prevent external electromagnetic fields effect. The inverter can be shielded as a whole and has a sound grounding.

b. Filter

Electromagnetic shields are usually used to prevent radiation EMI. And for conduction EMI, filtering is the most effective measure of protection. Adding filters is a convenient solution, including passive and active EMI filters. However, due to the limited bandwidth of integrated operational amplifiers in active EMI filters, it is difficult to suppress EMI effectively in a wide frequency range. Because of relatively simple structure, effective frequency bandwidth and large noise attenuation, passive EMI filter is the most widely used to suppress EMI in motor drive control system.

The EMI filter mismatched impedance usually has a better performance. According to the filter mismatch principle: inductor L is regarded as a high resistance element; capacitor C is a low resistance element. If the output load is inductive high resistance, the output filter is capacitive low resistance; and the output load is capacitive low resistance, the output filter load is inductive high resistance, as shown in Figure 3.50.

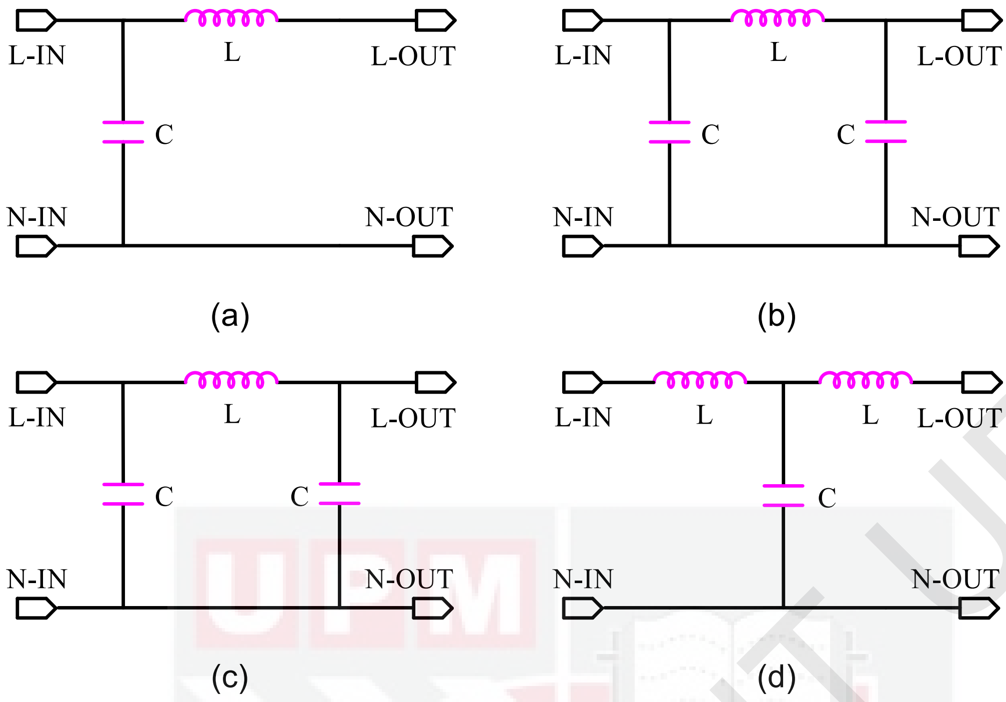

Figure 3.50 : Impedance Mismatch of Passive EMI Filters

The CM and DM passive EMI filter are now mainly applicable to the motor drive control system. When the CM component of a signal tries to go through the choke, it will meet a high impedance, due to the inductance created by the magnetization of the core and the coils. In opposition to the CM behavior, the DM component of the signal will see almost no impedance in the choke, this phenomenon could be explained with the magnetic field compensation inside the core. If the core is not magnetized, then no inductance will appear in the line. The two and three phase common mode busbar cable chokes of Würth Elektronik Group are widely used in conduction EMI filtering circuits because of their high impedance parameters, high power density and diverse magnetic cores in Figure 3.51.

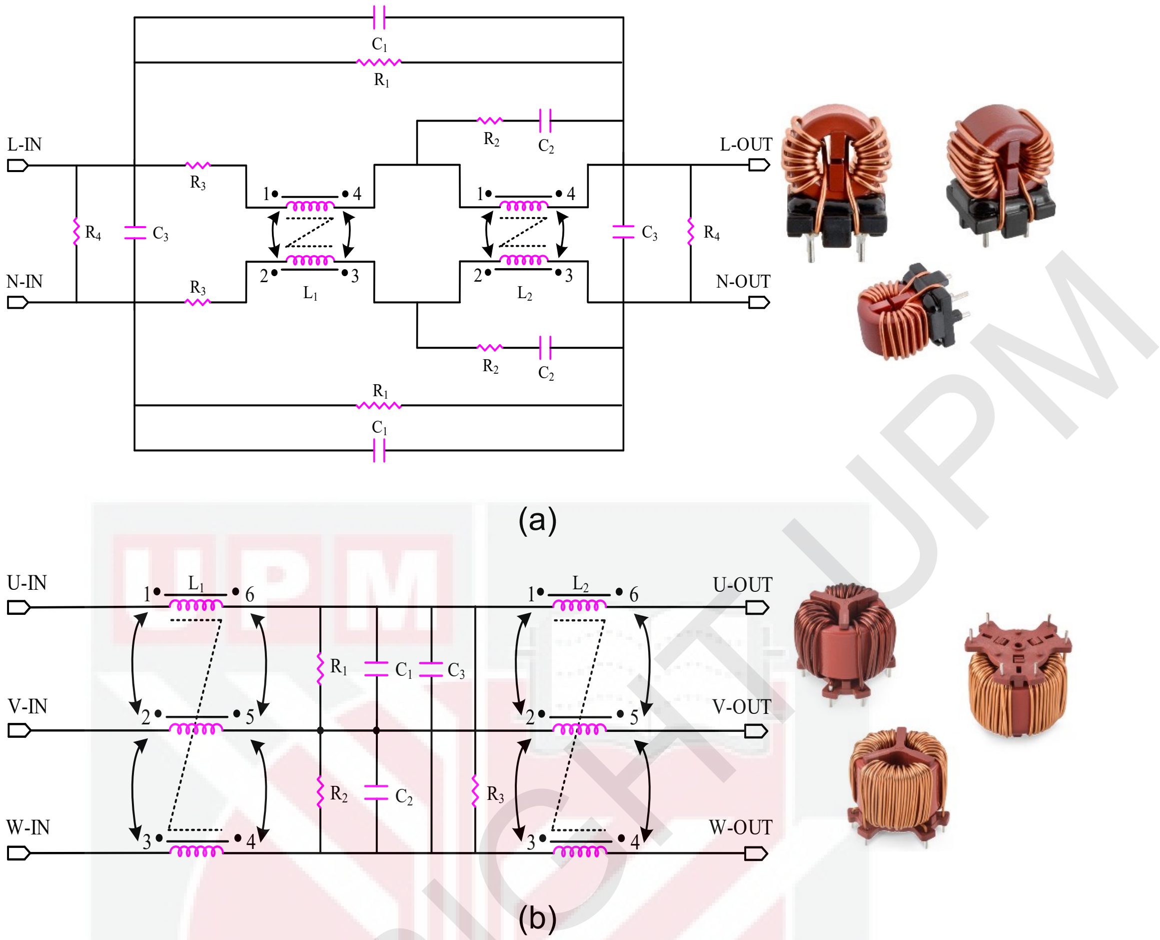

Figure 3.51 : CM busbar Cable Choke and Physical Picture (a) Two Phase (b) Three Phase

c. Advanced PWM Strategies

The angular frequency of the EMI spectrum is determined by the duty cycle and switching frequency of the PWM waveform. According to the different frequency, it can be divided into constant switching frequency PWM (CSFPWM) and variable switching frequency (VSFPWM): random switching frequency PWM(RSFPWM), period switching frequency PWM(PSFPWM), and model prediction switching frequency PWM(MPSFPWM). By using VSFPWM, the output voltage and current concentrated harmonic of inverter in low frequency range are expanded to a wider band, which has lower EMI peak value. As shown in Figure 3.52, the ordinate axis is harmonic amplitude, and f on abscissa axis is carrier frequency.

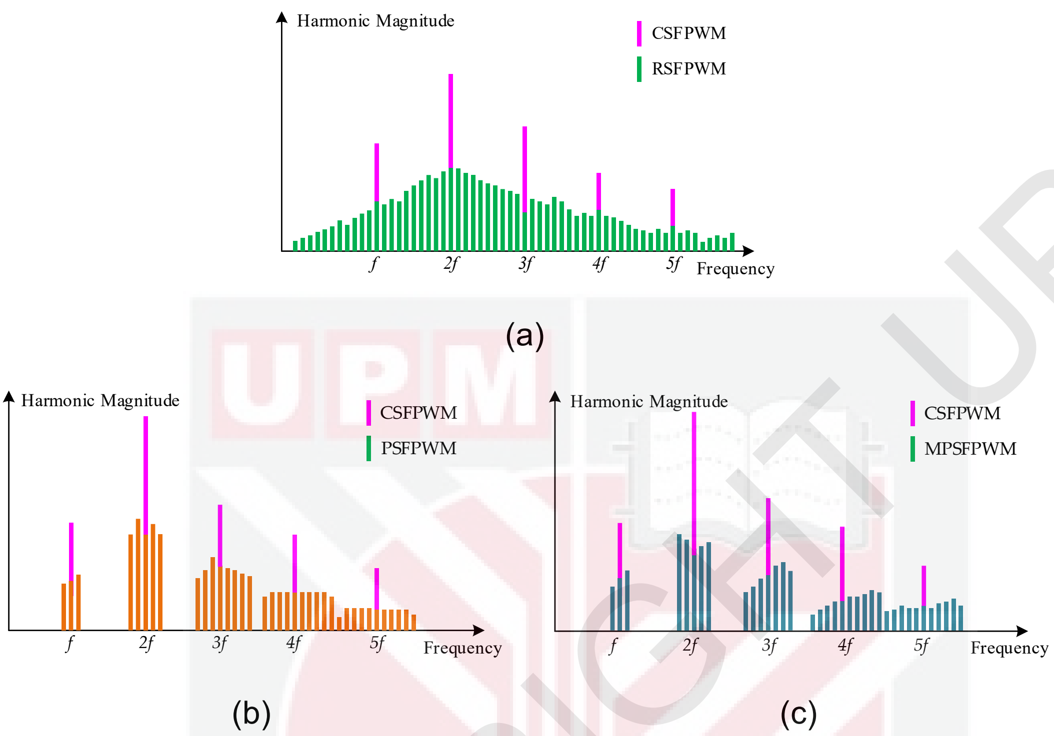

Figure 3.52 : Harmonic Magnitude of VSFPWM and CSFPWM (a) RSFPWM; (b) PSFPWM; (c) MPSFPWM

d. Complex Inverter Circuit Topologies

EMI always exists in the motor drive control system based on three-phase two-level inverter. To further minimize EMI, some improved inverter circuit topologies have been proposed, such as three level inverter, and double parallel inverter as shown in Figure 3.53. Multistage inverters have smaller dv/dt, which can reduce the inverter output voltage and current harmonics. Unfortunately, more complex inverter circuit topologies have higher hardware costs and control complexity and reduce the power density of the system.

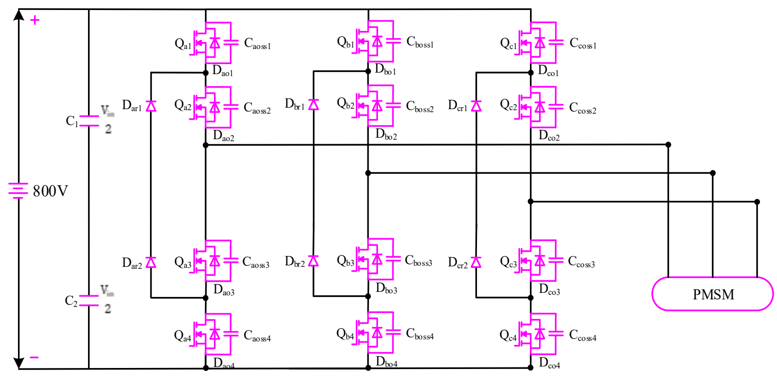

(a)

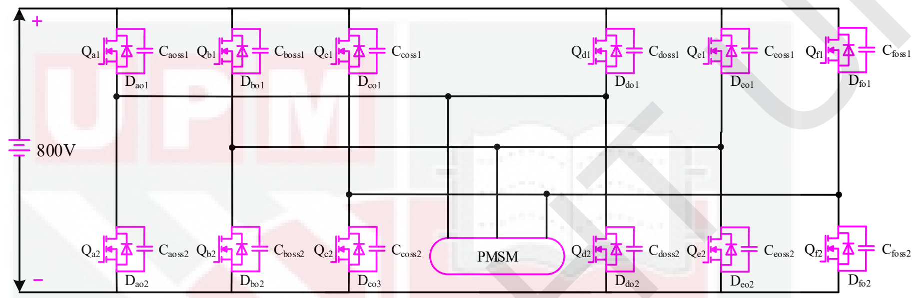

(b)

Figure 3.53 : Complex Inverter Circuit Topologies (a) Three Level Inverter; (b) Double Parallel Inverter

3.6.4.2 EMI Solve Solution of Motor Drive Control System

In order to suppress the conducted EMI noise of the motor drive control system, passive filters with high insertion loss, wide frequency band and strong currents are usually installed on the power battery pack, bus cables, three phase inverters and the motors, as shown in Figure 3.54.

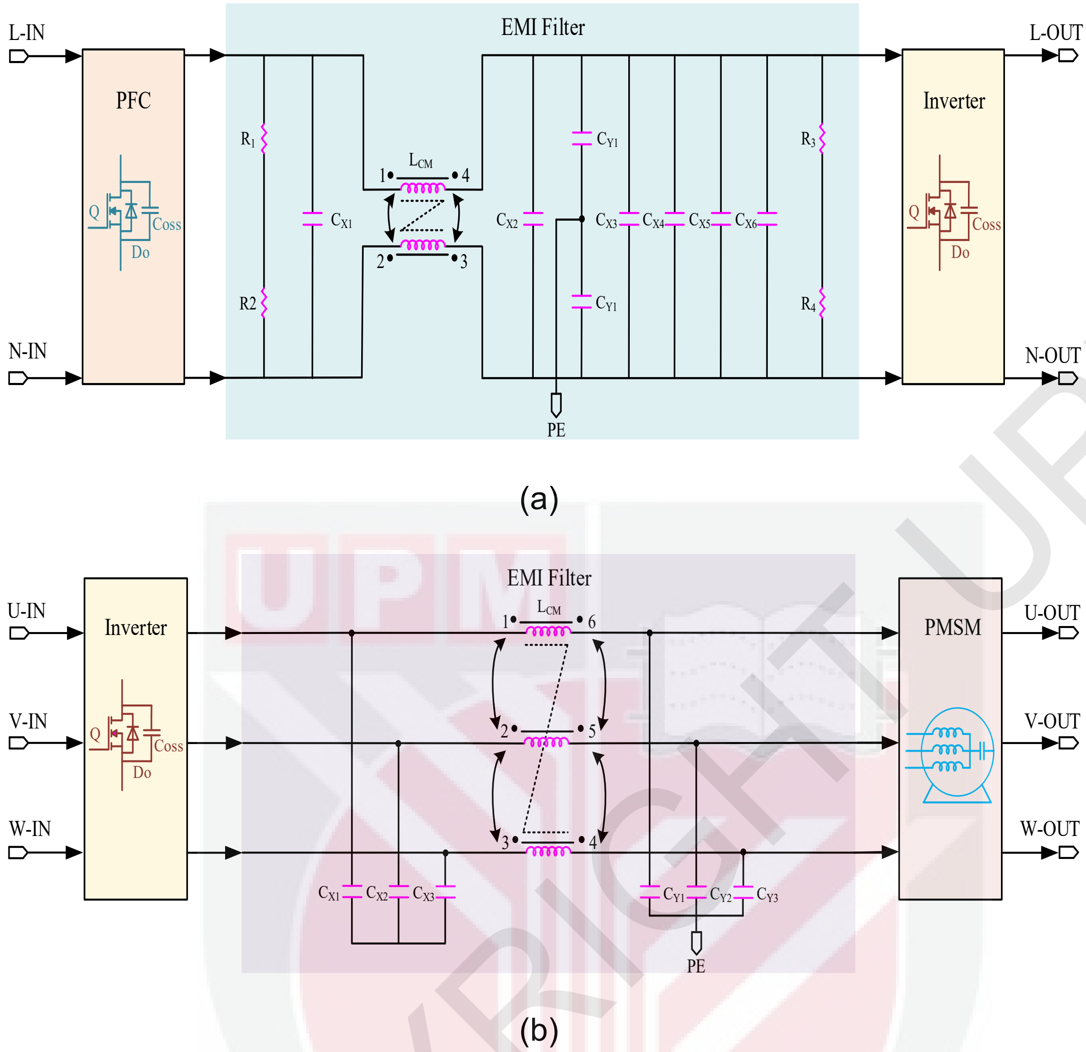

Figure 3.54 : CM and DM Passive EMI Filter (a) between Power Battery Back to Inverter; (b) between Inverter to PMSM

The parasitic parameters coupling to ground and shielding from the busbar cables and PMSM are the main cause of CM current in the motor drive control system. The high frequency current produces DM noise. After accurately capturing CM and DM effects, the EMC filters can be calculated to meet EMC standards.

3.6.5 Summary

As a summary, this chapter discusses strategies and methodology used. Detailed discussion is emphasized on the procedure of conducting the study and the research framework as the direction of this study. This chapter discusses the research and design of PMSM drive control system for NEEVs based on SiC MOSFET. The developed study designs consisted of the active H-bridge inverter discontinuous current source gate driver for SiC MOSFET, three phase interleaved parallel bidirectional Buck–Boost converter, three voltage vector duty cycle optimization strategy based on finite set model predictive control, shaft voltage and bearing current of PMSM, and EMI harm and protection measures about motor drive control system. The next chapters cover the results of the proposed research objectives.

CHAPTER 4

RESULTS AND DISCUSSIONS

4.1 Introduction

This chapter presents and discusses the specific results of the study, which involve the achievement of the main objectives of this research through experimentation. The chapter provides detailed discussions and observations on the experimental results, including the design and performance of an active H-Bridge inverter discontinuous current source gate driver, a three-phase interleaved parallel bidirectional Buck–Boost converter, a voltage vector duty cycle optimization strategy based on finite set model predictive control, and measures for suppressing electromagnetic interference in a motor drive control system based on PMSM with SiC MOSFET.

4.2 Active H-Bridge Inverter Discontinuous Current Source Gate Driver

As previously discussed, enhancing the switching speed of SiC MOSFET is challenging due to factors such as substantial internal gate resistance, high Miller voltage, and limited gate-source voltage ratings. To address problems, this research presents a solution in the form of a discontinuous CSGD circuit. This circuit comprises a voltage source, H-bridge inverter, and input inductor. Experimental results affirm the feasibility and effectiveness of this approach.

To further substantiate the efficacy of the proposed discontinuous CSGD and facilitate a comparison with the conventional VSGD, extensive data regarding the main parameters and waveforms of the SiC MOSFET power module throughout the turn-on and turn-off processes are obtained, as illustrated in Figure 4.1 and Figure 4.2.

Figure 4.1 presents the waveforms captured during the turn-on process for both the conventional VSGD and the proposed discontinuous CSGD, obtained via a double pulse test. Under dynamic testing, the discontinuous CSGD has lower turn-on loss, smaller delays, and shorter rise time on the SiC MOSFET compared to conventional VSGD.

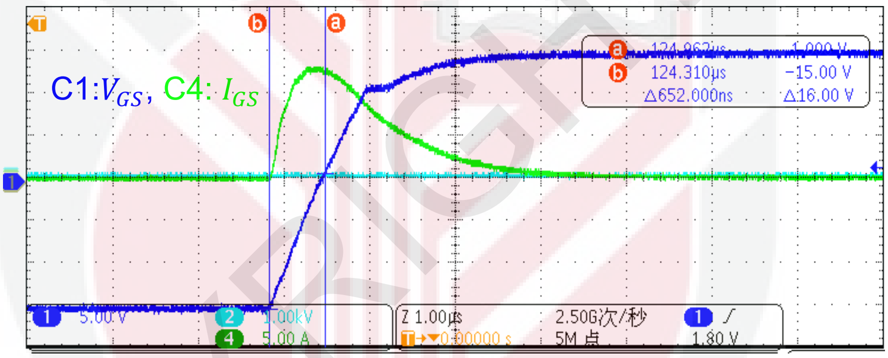

(a)

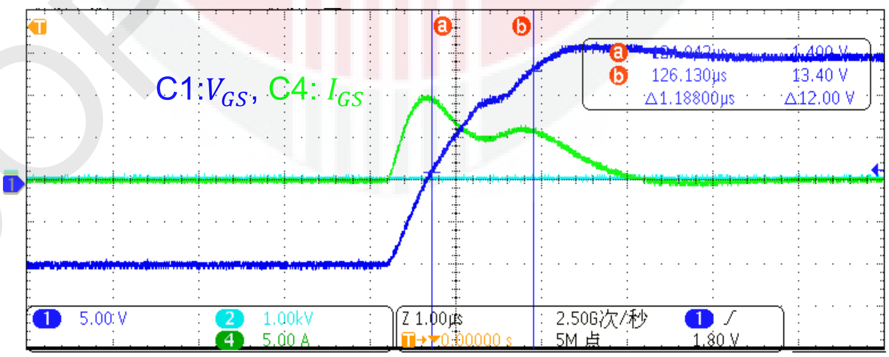

(b)

Figure 4.1 : Turn-On Process (a) Conventional VSGD; (b) Discontinuous CSGD

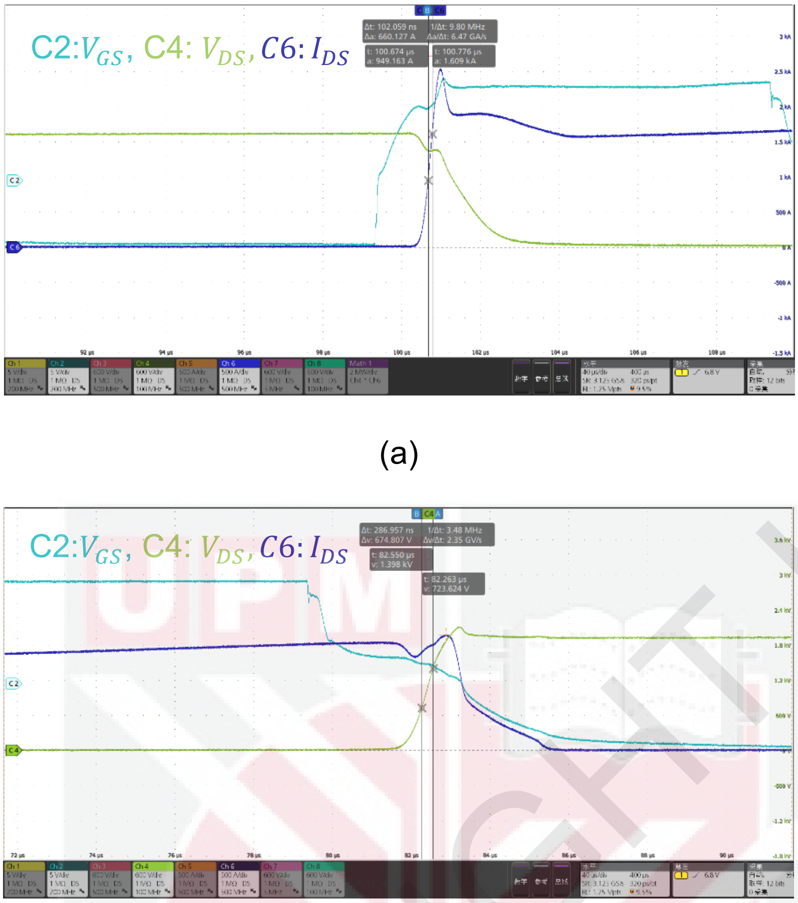

(a)

(b)

Figure 4.2 : Switching Waveform of Discontinuous CSGD (a) Turn-On Process; (b) Turn-Off Process

Table 4.1 demonstrates that the discontinuous CSGD exhibits lower turn-on loss and delay time during dynamic testing. However, it also yields a higher di/dt, leading to increased peak stress on the SiC MOSFET in comparison to the conventional VSGD.

Table 4.1 : Experimental Parameters Discontinuous CSGD and Conventional VSGD

Testing condition i_{GS}: 13A	Item	E_{on}: mJ	T_{don}: ms	T_r: ms	di/dt: kA/ms	I_{rrm}: A	V_{rrm}: V
V_{dc}: 1050V	CSGD	57.98	422	103.5	6.10	608	1361
I_{dc}: 600A	VSGD	129.73	497	153.8	4.07	469	1180

The turn on process under varying load currents is tested using the proposed discontinuous CSGD, depicted in Figure 4.3.

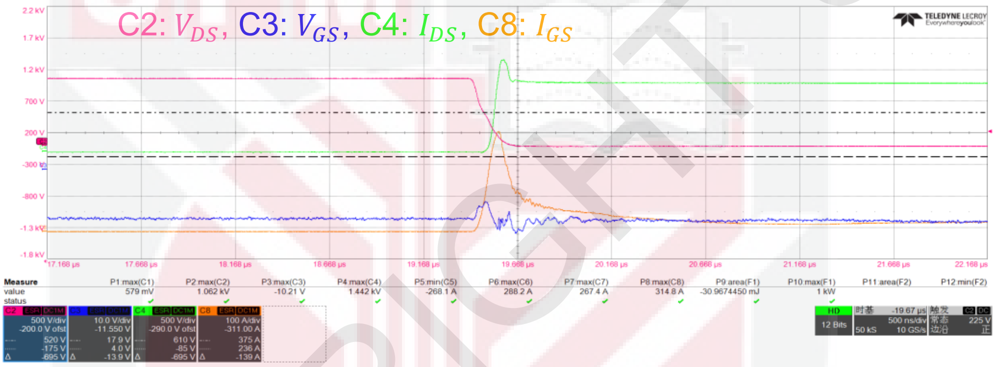

(a)

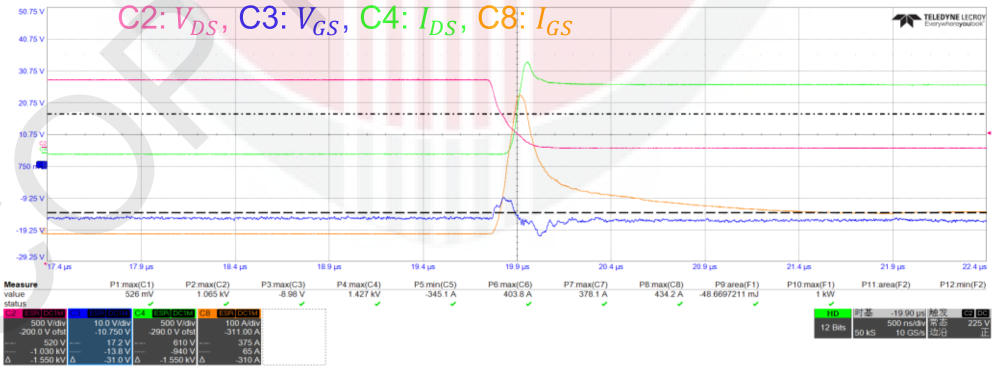

(b)

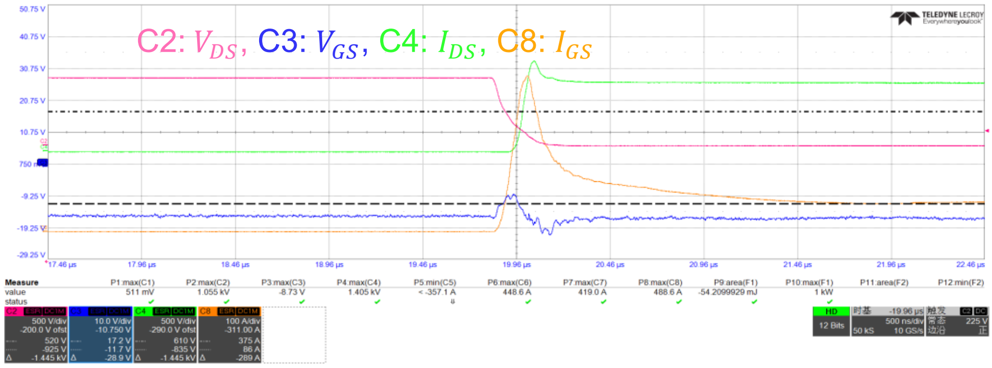

(c)

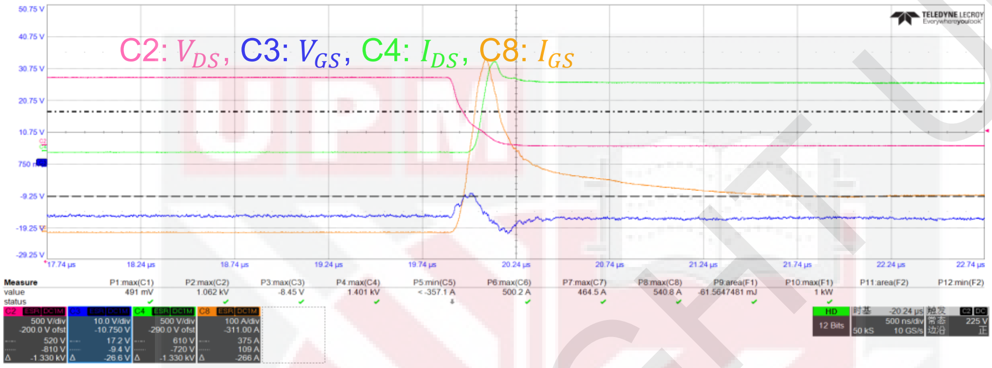

(d)

Figure 4.3 : Turn-On Process under Different Load Currents (a) 30A; (b) 60A; (c) 90A; (d) 120A

4.3 Model Control and Digital Implementation of the Three Phase Interleaved Parallel Bidirectional Buck–Boost Converter

To further verify the proposed circuit topologies and control strategy given in the previous sections, a prototype of TPIPBi-Buck–Boost converter was built and tested in Infineon laboratory. Figures 4.4 to 4.6 show the experimental waveforms, and then Infineon Technologies AG Digital Power Controllers XDPP1100-Q040 support full digital implementation. The TPIPBi-Buck–Boost converter has several operating modes and stages, charge Buck mode, discharge Boost mode, and electric energy interaction mode. The input voltage was supplied from the battery pack, and the converter output was accessed by the DC electronic load. In addition, for the sake of simplicity, only some typical experimental results are selected.

Figure 4.4(a) shows the start-up transients, it can be seen that the system has extremely high stability, fast dynamic response, and almost no overshoot of the output voltage. Figure 4.4(b) presents the experiment waveforms of Q_2 drive pulse signal $(2\text{: } \mathrm{V_{GS2}})$, voltage across $(1\text{: } \mathrm{V_{DS2}})$ in discharge Boost mode, and Q_3 drive pulse signal $(4\text{: } \mathrm{V_{GS3}})$, voltage across $(3\text{: } \mathrm{V_{DS3}})$ in charge Buck mode. There are no significant voltage spikes on the power switches Q_2 and Q_3, which signify the ZVS turn on completely before the drain to source voltage decreases above zero and turn off at an exceptionally low current. Therefore, the high frequency switching losses become negligible. All thanks to the Infineon's CoolSiC™ MOSFET and EiceDRIVER™ Gate Driver ICs are built on a state-of-the-art trench semiconductor process optimized to allow for both the lowest losses in the application and the highest reliability in operation: part count reduction, improved efficiency, space, and weight savings.

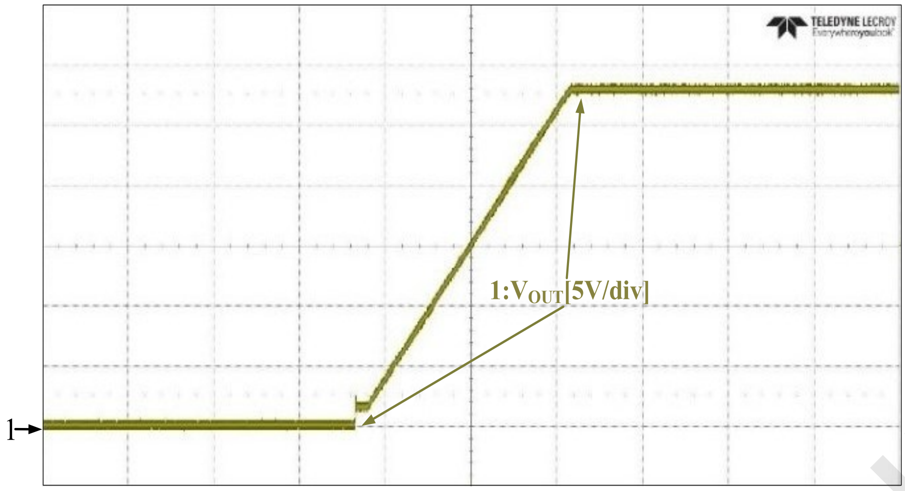

(a)

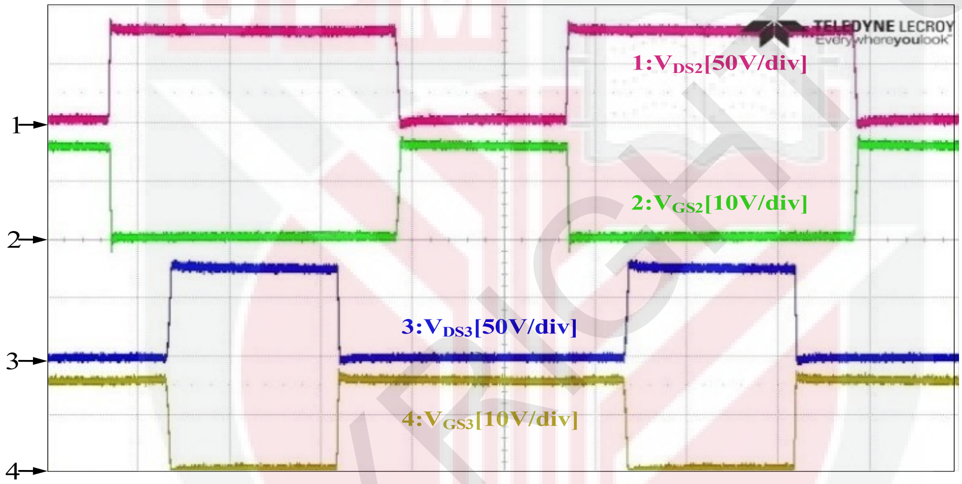

(b)

Figure 4.4 : (a) start-Up Transients; (b) $1{:}\,V_{DS2}, 2{:}\,V_{GS2}$ in Discharge Boost Mode, and $3{:}\,V_{DS3}, 4{:}\,V_{GS3}$ in Charge Buck Mode

Figure 4.5 gives the dynamic test results, in the proposed converter, due to the double closed-loop control system, voltage outer loop and current inner loop compensation controller can keep the output voltage and current stable, so as to achieve the power balance of the system.

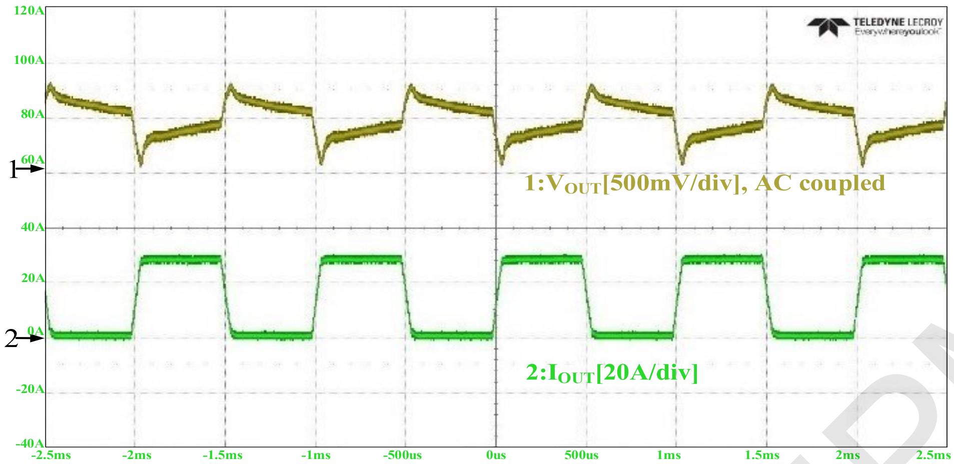

(a)

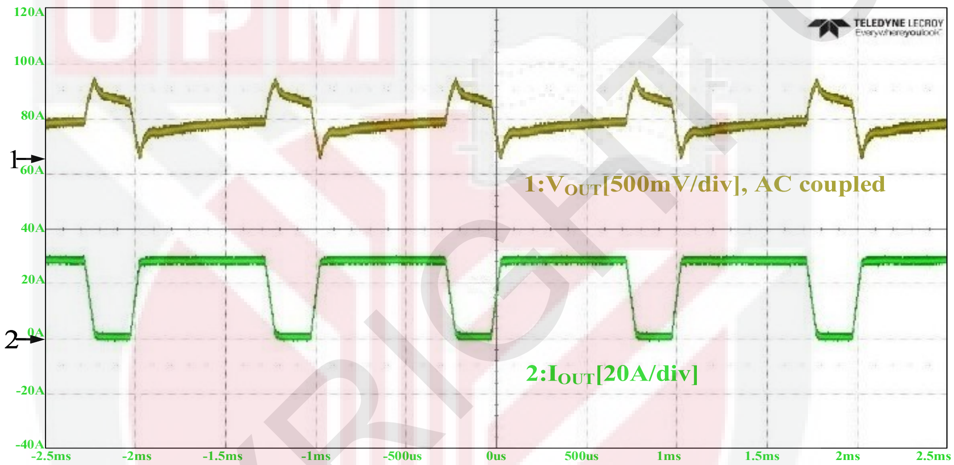

(b)

Figure 4.5 : V_{OUT}, I_{OUT} in Double Closed-Loop Control System

To verify the correctness of the power feedforward compensation controller, now through the load characteristic change experiment, increase and decrease the input voltage, respectively, and observe the change in the output voltage and the response speed. Figure 4.6 show the V_{OUT}, I_{OUT} response of start-up and close-down, and the output voltage fluctuates within a small range. After a short period of adjustment, the output voltage remains unchanged and reaches a stable state again, which almost becomes a step response, which further proves the feasibility of the control system.

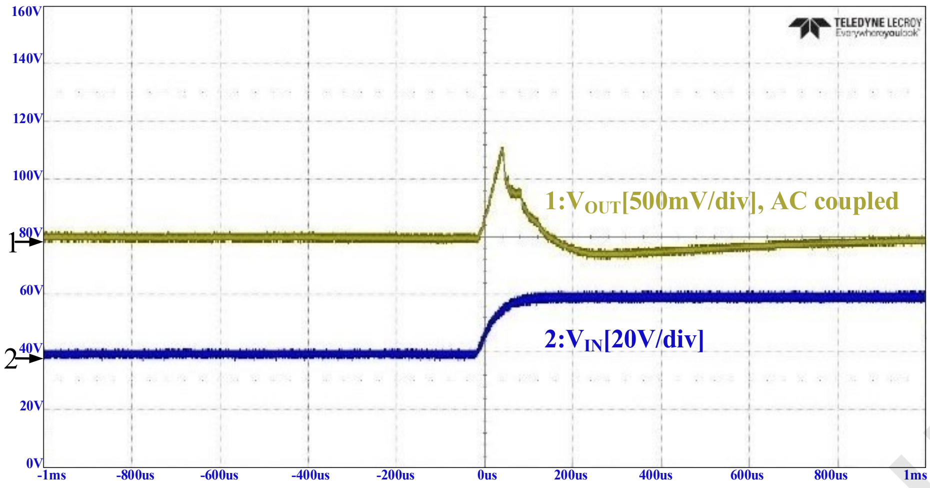

(a)

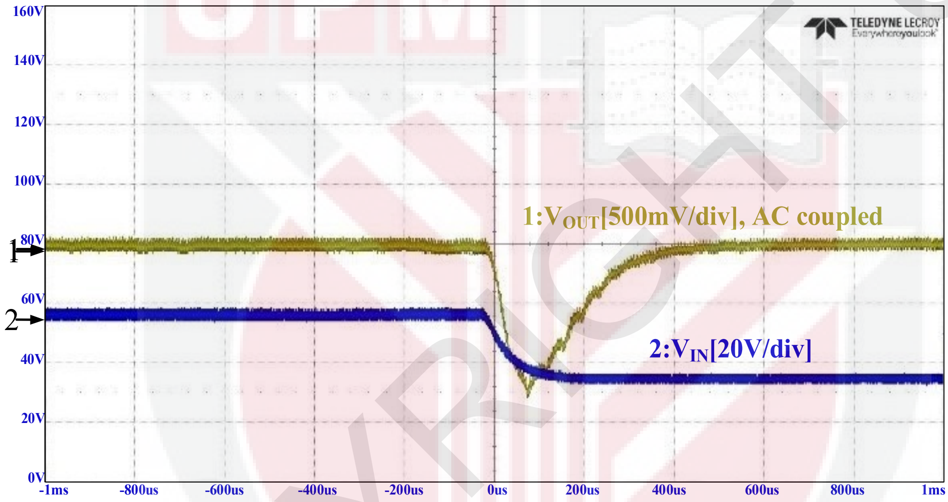

(b)

Figure 4.6 : V_{OUT}, I_{OUT} Response of Start-Up and Close-Down in Power Feedforward Compensation Controller

In the full load range, Figure 4.7 presents the output periodic and random deviation (PARD) ripple is within 20mV.

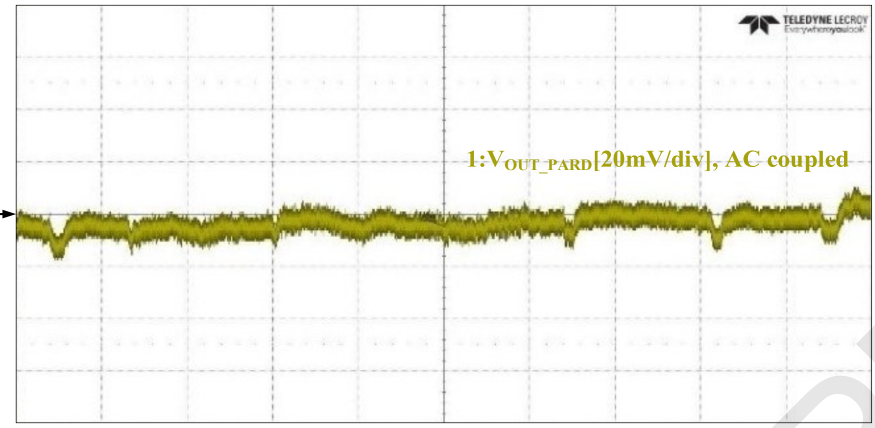

(a)

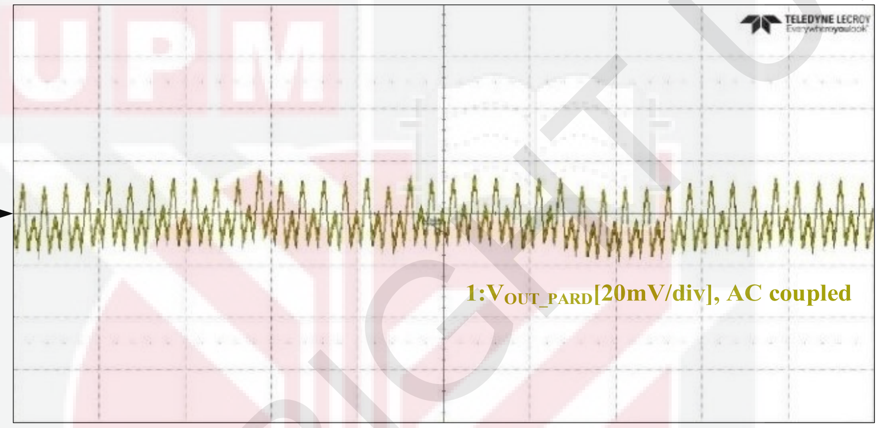

(b)

Figure 4.7 : Steady-State Experimental Waveforms of Voltage Ripples in Different Output Power

The efficiency curve of the system with different current levels is shown in Figure 4.8. The experimental result is obtained from Power Analyzer YOKOGAWA WT1800. When the input voltage is 36V, the output voltage is 28V, the output current is 20A, and the efficiency can reach nearly 98%.

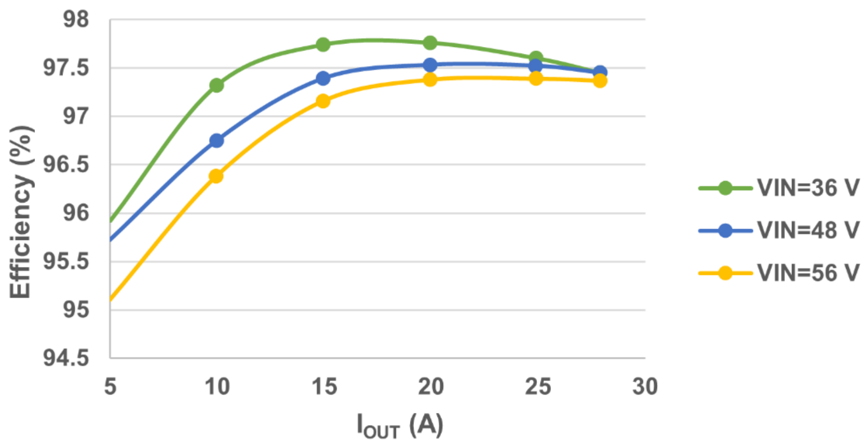

Figure 4.8 : Efficiency Curve of Prototype

4.4 Expanded Three Voltage Vector Duty Cycle Optimization Model Predictive Torque Control

In order to eliminate the weight coefficient of the cost function in traditional MPTC, this research proposes an expanded three voltage vector duty cycle optimization model predictive torque control strategy. In order to verify the practicability of the proposed method, a PMSM platform based on Infineon's DSP+FPGA has been developed. The experimental results show that the recommended solution could effectively further enhance and improve control-system performance and energy efficiency.

In order to validate the previous analysis and the proposed FCS-MPTC methods experimentally, a three-phase SPMSM drive platform was developed under Infineon's laboratory conditions to evaluate the effectiveness of the three voltage vector duty cycle optimization strategy based on finite set model predictive control with respect to both steady-state and dynamic performance.

In the experiment, the magnetic powder brake was used as a load for the SPMSM. The direct current bus supply voltage was 300V, the control frequency was 10kHz, and the sampling period was 200μs. The voltage and current waveforms were directly observed by means of an oscilloscope. The d-q-axis current, rotating speed, electromagnetic torque, and other analog quantities were obtained through the A/D conversion chip. The whole system includes a hardware circuit and a software program: a three-phase inverter module, a drive isolation circuit, a direct current bus voltage sampling circuit, a phase current sampling circuit, a temperature sampling circuit, and an auxiliary power-supply circuit.

Figure 4.9(a) shows the experimental waveforms of the drive voltage $3{:}V_{GS}$, the voltage across $1{:}V_{DS}$, and the arm current $2{:}I$ of the three-phase inverter bridge; Figure 4.9(b) depicts the primary voltage $1{:}V$ and the current $2{:}I$ of the main transformer. Figure 4.9(c) shows the drive voltage $3{:}V_{GS}$, the voltage across $1{:}V_{DS}$, and the primary side current $2{:}I$ of the auxiliary switch. The waveform in Figure 4.9(d) presents the primary voltage $1{:}V$ and the current $2{:}I$ of the auxiliary transformer.

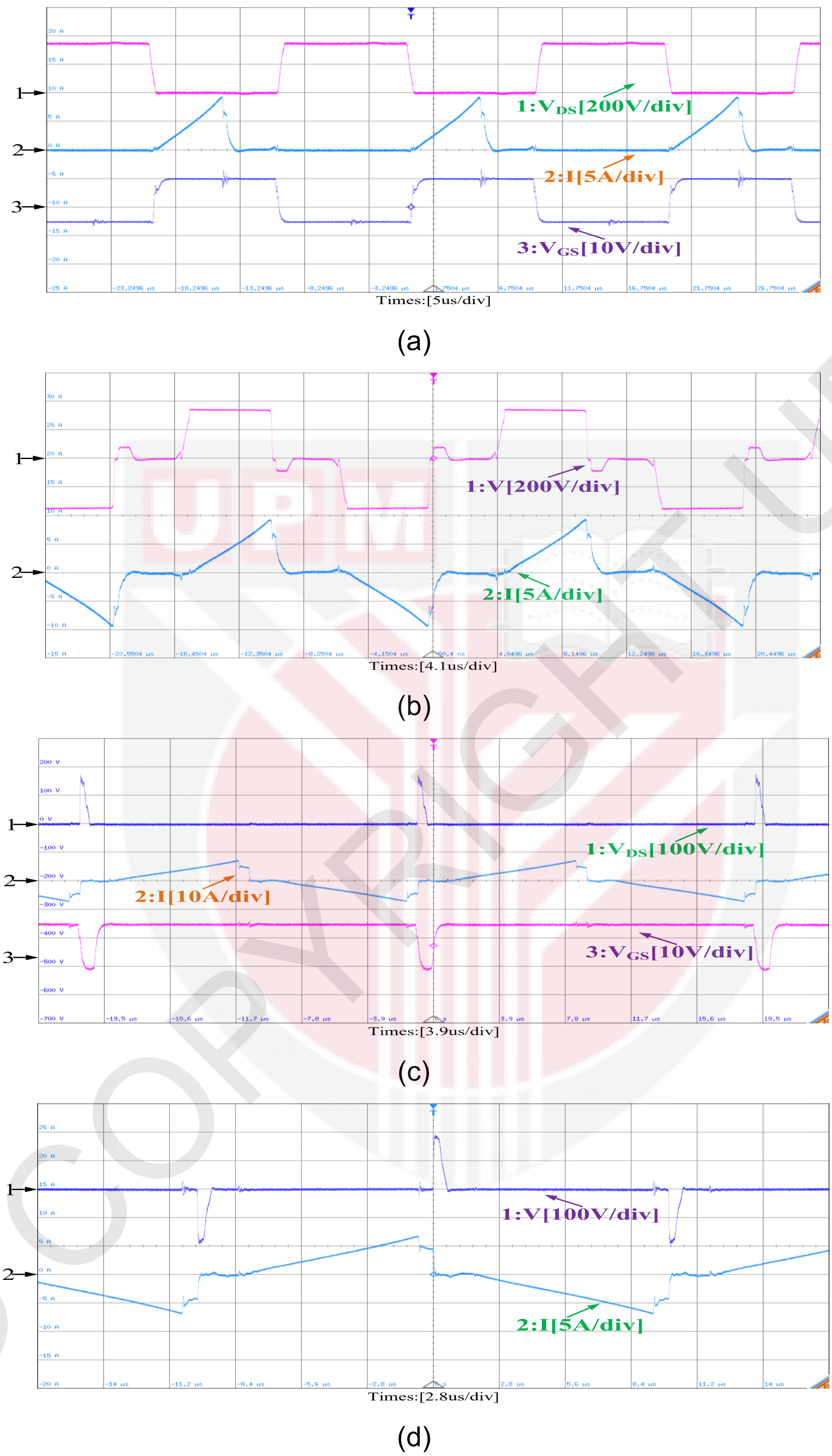

Figure 4.9 : Experimental Waveforms: (a) Three-Phase Inverter Bridge; (b) Primary Side of the Main Transformer; (c) Auxiliary Switch; (d) Auxiliary Transformer

A. Case 1: Steady-State Performance Under Different Speeds and Loads

In order to study the influence of rotating speed on steady-state performance under different speeds and loads, experimental waveforms for the d-q-axis current at 300rpm and 500rpm with 2N/m load torque can be seen in Figure 4.10. As the speed increases, unstable torque current is generated due to the distortion of stator current, resulting in significant torque fluctuations and an increase in pulsating current on both the d and q axes.

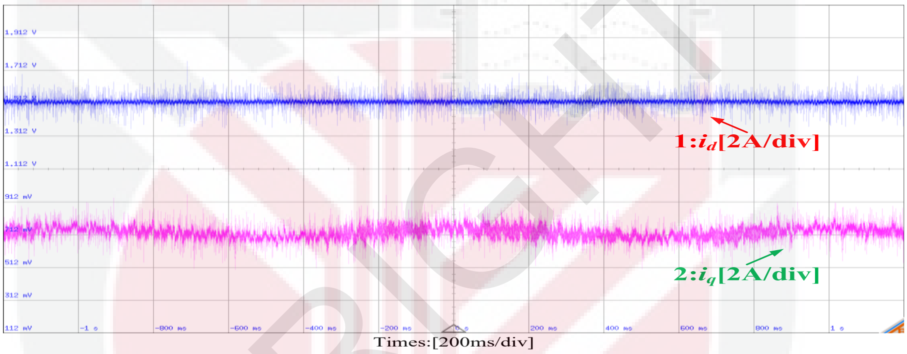

(a)

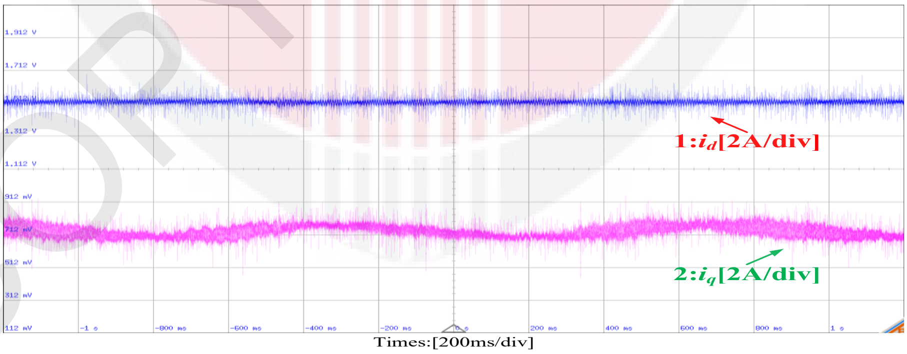

(b)

Figure 4.10 : Steady-State Experimental Waveforms of the d-q-axis Current: (a) 300rpm at 2N/m; (b) 500 rpm at 2N/m

B. Case 2: Dynamic Performance Evaluation with Sudden Speeding Up and Down

Figure 4.11(a) shows that under 500rpm with 2N/m load torque, it accelerates 300rpm from a steady state of about 100ms and decelerates from 300rpm to 200rpm after 40ms. The performance following the change in the given speed is better, and the q-axis current can change rapidly. Figure 4.11(b) shows the experimental waveform of the current loop following performance. Since the sampling period is 100μs, the feedback q-axis current is stepped. The given q-axis current starts at 10 A, the actual q-axis current reaches 10 A after three sampling cycles of about 300μs. It can be seen that the current loop of the three voltage vector duty cycle optimization strategy has better dynamic performance.

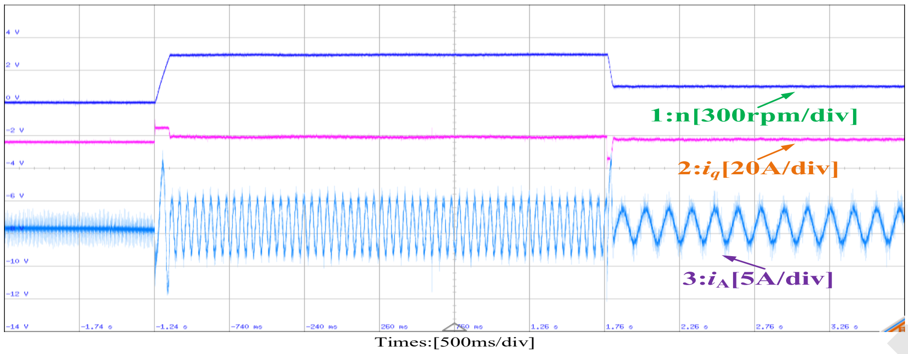

(a)

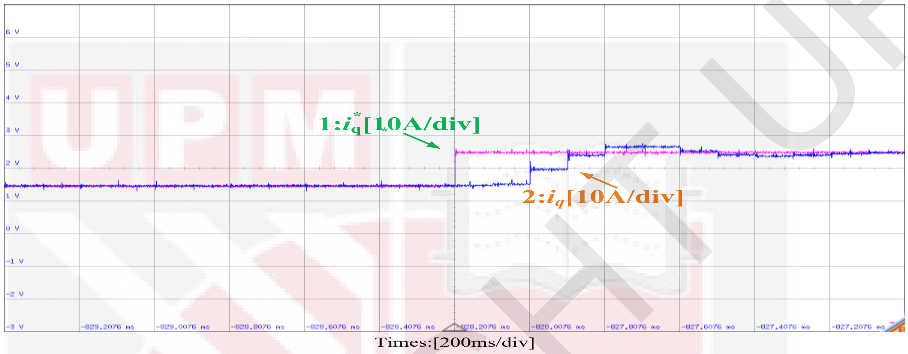

(b)

Figure 4.11 : Dynamic Performance Evaluation: (a) Acceleration and Deceleration At 500r/Min with 2N/M; (B) Current Loop Following Performance

4.5 Suppression and Optimization Measures about Motor Drive Control System

In this section, a system level equivalent circuit model of motor drive control system based on PMSM with SiC MOSFET for NEEVs is established through circuit simulation software SIMetrix/SIMPLIS, which is used to simulate conduct EMI noise effectively. According to EMC Standards, the conducted EMC noise is measured in laboratory, and the comparison between simulation and experimental results was analyzed.

The EM5040B is a (50uH+5Ω) ||50ΩV LISN depicted in Figure 4.12, which can maintain a stable impedance between the tested equipment's terminal and the reference ground within the 9kHz to 30MHz radio frequency range. It effectively isolates extraneous signals from the grid within the measuring circuit and exclusively couples the interference voltage of the tested equipment to the measuring EMI receiver's input. EM5040B's overall performance complies with the CISPR16-1-2:2006 standard, enabling the measurement of conducted disturbance voltage in single-phase equipment. Its standard BNC output interface and 50Ω output impedance are compatible with receivers, spectrum analyzer, and other measuring equipment from various manufacturers. Additionally, the EM5040B features an artificial hand function for simulating handheld device measurements and can measure CM and DM interference, providing targeted guidance for rectifying EMC issues, particularly in EMI filter testing.

Figure 4.12 : LISN EM5040B (9kHz/150kHz-30MHz, 16A, with CM/DM)

EM5080B is a fully digital pre-certified receiver operating in the time domain and complies with the CISPR16-1-1 standard as depicted in Figure 4.13. It utilizes a real-time analysis technology platform to perform high-speed FFT analysis and calculation of broadband signals, leveraging the powerful supercomputing capabilities of a PC platform. With a real-time bandwidth of up to 10MHz, it enables rapid electromagnetic disturbance measurement. EM5080B receiver offers fast scanning speed, high precision, and excellent stability.

Figure 4.13 : EMI Receiver EM5080B 9KHz~1GHz

The conduction testing platform integrates the LISN EM5040B and EMI Receiver EM5080B, illustrated Figure 4.14 and Table 4.2. These products conform to international standards, resulting in significant ground leakage current. Inadequate grounding may lead to serious electric shock or injury.

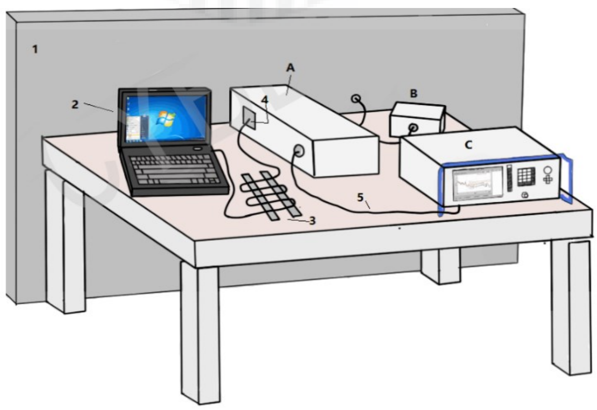

Figure 4.14 : Conducted EMI Testing Platform
Therefore, users are obligated to:

a. Ensure proper grounding of the instrument, with grounding points located on the side and back.

b. Isolation transformers must be installed to provide dual assurance.

c. Do not open the casing or wiring during operation and avoid use in areas containing flammable or explosive materials. Ensure the instrument's surface is dry and clean before use.

d. Ensure the product is operated within the specified voltage and current range.

Table 4.2 : Important Component Parts of Conducted EMI Testing Platform

Item	Description
1	exceed 2m×2m metal plate
2	EUT
3	Power supply line folding method
4	power supply of EUT
5	Output shield wire
A	LISN
B	isolation transformer
C	EMI receiver

a. Test Arrangement

The Experimental equipment is composed of two LISN, EMI receiver, power battery pack, long four core shielded busbar cables, three phase inverter, PMSM and dynamometer machine. Under normal circumstances, the EMI receiver can measure the conductive interference voltage of the positive and negative power lines within a frequency range of 150kHz to 30MHz by LISN.

The six SiC MOSFET drive voltage signal with 10KHz switching frequency under SVPWM control algorithm and three phase winding current are given in

Figure 4.15 by SIMetrix/SIMPLIS. The switching speed of the SiC MOSFET can be flexibly regulated with the changing of external $R_{G(on)}$ and $R_{G(off)}$ gate resistor.

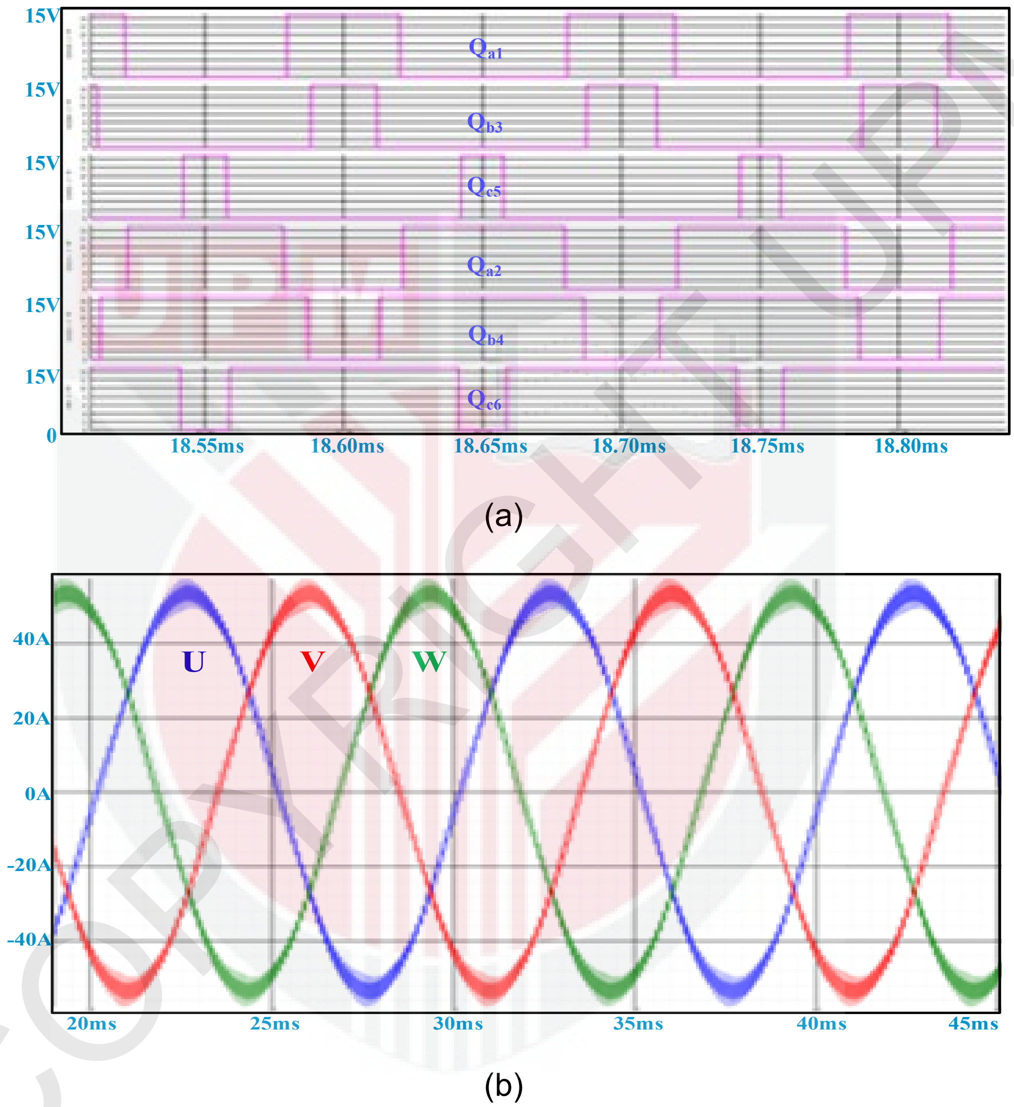

Figure 4.15 : SVPWM Control PMSM by SIMetrix/SIMPLIS (a) Drive Voltage Signal; (b) Three Phase Winding Current

b. Switching Frequency

Figure 4.16 shows the CM and DM voltage noise spectra curve in different switching frequencies. It can be observed that the CM voltage noise source makes up the majority in the low frequency range, while the CM and DM are nearly equal in the high frequency range. The reason is that the noise source in the low frequency range is determined by the PWM modulation method, while the high frequency range is caused by the turn on and off behavior and parasitic parameters of SiC MOSFET. Obviously, the lower switching frequencies can effectively suppress conducted EMC noise in motor drive control system. However, due to the increase in size and volume of passive components, the lower switching frequencies cannot ensure higher power density. In order to balance the power density between conducted EMC noise and motor drive control system, it is necessary to optimize the switching frequency.

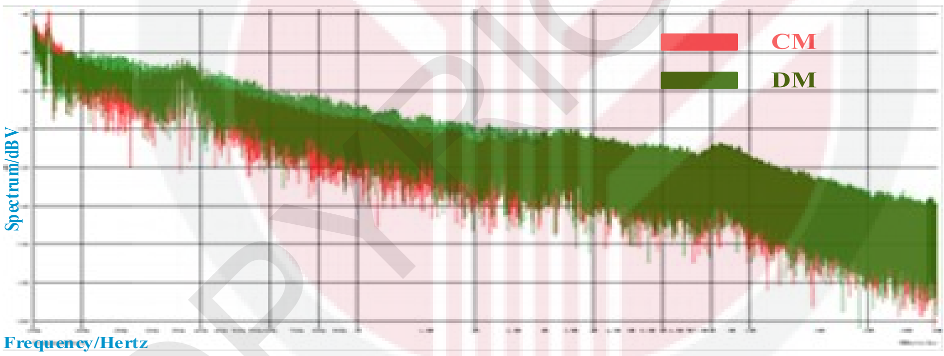

(a)

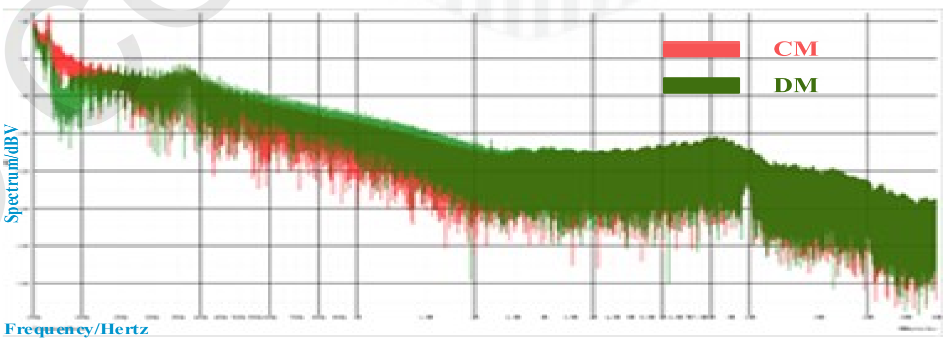

(b)

Figure 4.16 : CM and DM Voltage Noise Spectra Curve in Switching Frequency (a) 10KHz; (b) 20KHz

c. Load Power

Figure 4.17 compares the spectrum curves of CM and DM noise under different load power conditions. It can be found that the CM noise varies little with the load power in the low frequency range, while the DM noise is more than the great. The level of CM noise and DM noise at heavy load power is significantly higher than that at light load power.

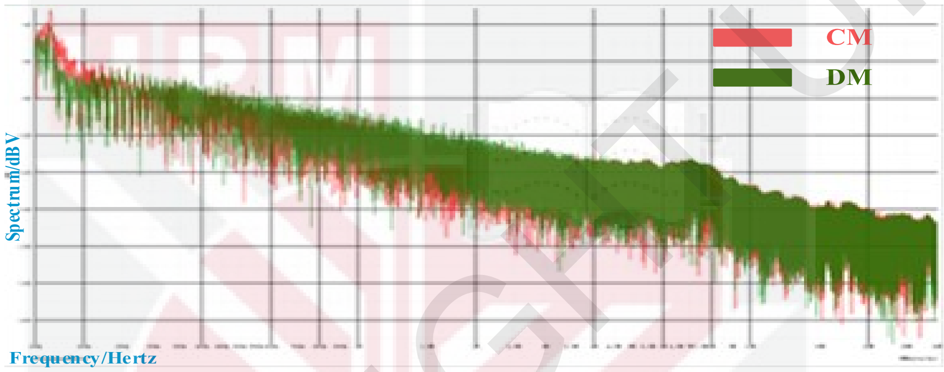

(a)

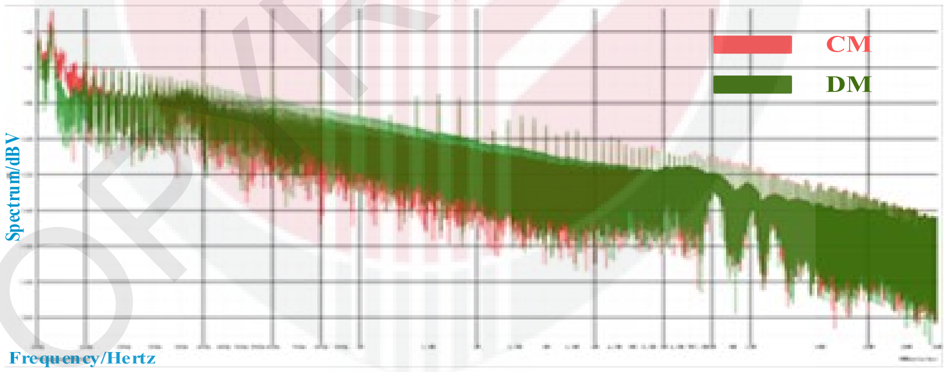

(b)

Figure 4.17 : CM and DM Voltage Noise Spectra Curve in Load Power (a) Light; (b) Heavy

d. EMI Filter

Figure 4.18 proves the total EMI noise spectrum curves obtained by simulation and experiment. Figure 4-20 show that before adding the CM and DM passive

EMI filters, the conducted EMI voltage amplitude of the motor drive control system peaks near 60dBμV, exceeding EMI standard limits. After applying the filter, the peak is reduced by approximately 20dBμV to 40dBμV in the 150kHz to 30MHz range, significantly reducing overall noise levels. The EMI voltage peak and high-frequency band are notably reduced, with stable results and minimal fluctuations. These improvements meet EMI standard limits, confirming the effectiveness of the suppression scheme and validating the theoretical analysis.

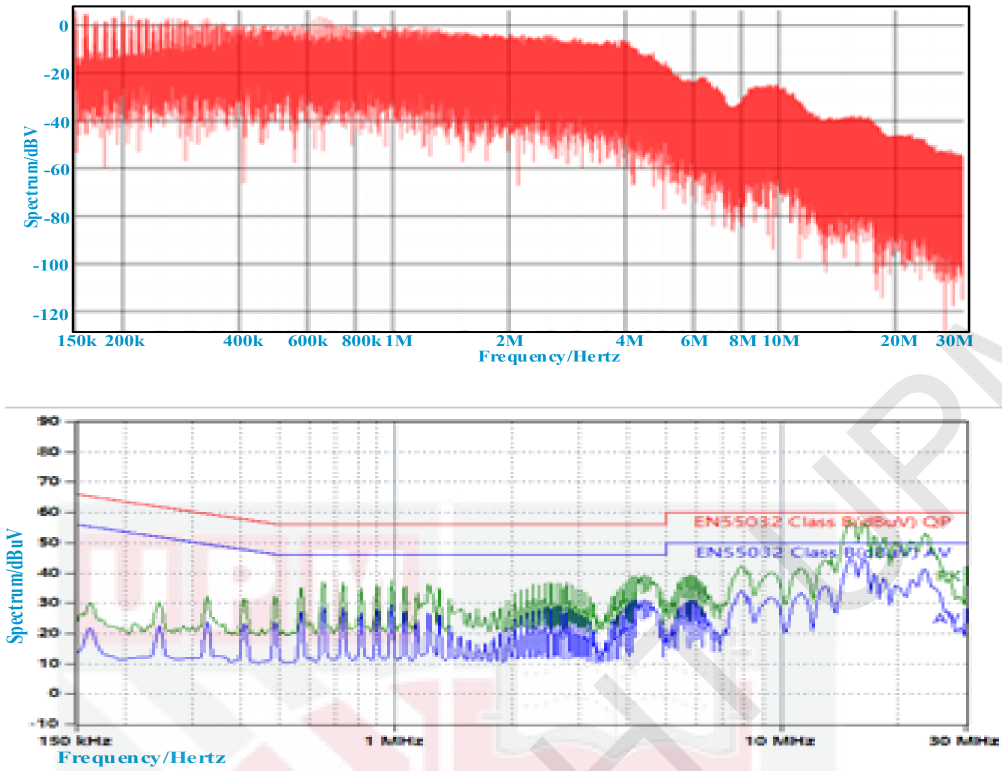

(a)

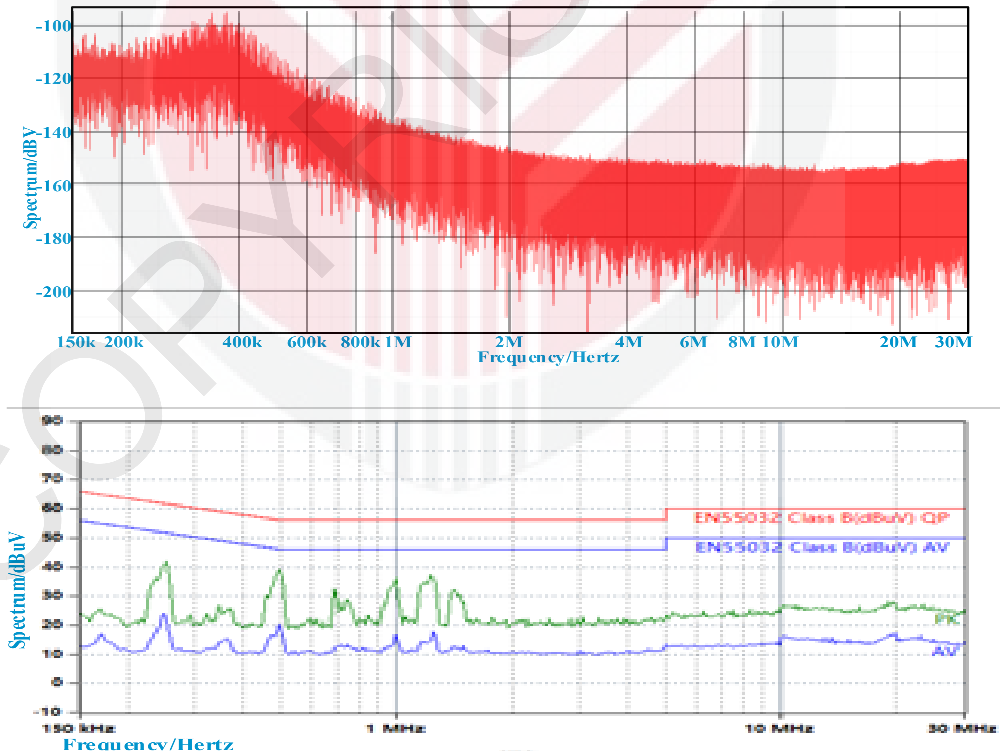

(b)

Figure 4.18 : Total EMI Noise Spectrum Curves for Using EMI Filter (a) before No; (b) after Have

The experimental results demonstrate that adding CM and DM passive EMI filters effectively suppresses the conducted EMI noise in the motor drive control system, reducing radiation interference. Thus, the theoretical approach proposed in this research provides valuable guidance for the forward design of EMC.

4.6 Summary

This chapter provides a comprehensive summary of the simulation and experimental results obtained in the research. The findings from both simulations and experiments were thoroughly discussed to fulfill the objectives of the research. The results clearly demonstrate the effectiveness of the proposed research and design of a PMSM drive control system for NEEVs based on SiC MOSFET.

The SiC MOSFET, as a representative of third-generation wide band gap materials, is widely utilized in motor drive control systems. The use of a three-phase converter with SVPWM to drive PMSM based on SiC MOSFET power devices, operating at high switching frequencies, presents a challenge due to the potential for significant EMI resulting from higher dv/dt and di/dt. To mitigate voltage and current overshoot and oscillation during SiC MOSFET turn on and off process, this research proposes a novel active H-bridge inverter discontinuous CSGD, which ensures a constant gate drive current throughout the turn on and off periods for motor drive control system in NEEVs, offering advantageous features of simplicity and cost-effectiveness. Furthermore, it significantly minimizes SiC MOSFET switching loss, thereby effectively controlling dv/dt and di/dt. The active H-bridge inverter discontinuous CSGD approach offers a new perspective for operating SiC MOSFET at high switching frequencies, with significant theoretical and practical implications. The feasibility and advantages of active H-bridge inverter discontinuous CSGD were confirmed by theoretical analyses and experiment results.

This research presents a TPIPBi-Buck–Boost converter, which is the core factor of electrical energy flow regulation and management between the battery pack and motor drive inverter within the high voltage direct current bus and converts the voltage from two directions. The principal configuration and operating states of the TPIPBi-Buck–Boost converter is determined, and the characteristic waveforms are shown in charge Buck, discharge Boost, and electric energy interaction modes. The mathematical model based on AC small signal is presented and provides theoretical fundaments of the digital implementation in double closed-loop control system, current inner loop compensation controller, voltage outer loop compensation controller, power feedforward compensation controller and power feedforward compensation controller. The XDPTM Digital Power Controllers XDPP1100-Q040 of Infineon Technologies AG is a highly integrated and fully programmable controller offering optimized solutions, which feature optimized power processing blocks and pre-programmed peripherals to enhance the performance of the converter, reduce external components and minimize firmware development effort. The performance of the converter in steady-state and during mode transition is verified by a hardware prototype in laboratory. Therefore, it is foreseeable that this paper could assist with the energy storage management applications of NEEVs.

With the continuous advancement of production technology, the requirements of accuracy, rapidity, and stability in permanent magnet synchronous motor systems have gradually increased. Among many advanced control technologies, this research has proposed an optimized expanded three voltage vector duty cycle optimization MPTC method based on voltage vector expansion. This strategy involves the construction of a reference stator flux linkage vector based on the analytical relationship among electromagnetic torque, reference stator flux linkage amplitude, and rotor flux linkage to convert the separate control of electromagnetic torque and flux linkage amplitude into flux linkage vector control, thereby avoiding the cumbersome design of weighting coefficients. On the basis of delay compensation, the reference voltage vector is calculated online according to the deadbeat control principle. Simultaneously, the voltage vector control set is extended, two adjacent voltage vectors are determined according to the spatial position of the reference voltage vector, and the optimal duty cycle corresponding to the two adjacent voltage vectors and the zero vector is calculated according to geometric relationships, so as to realize the three voltage vector duty cycle control. It eliminates the weight coefficient of the cost function in traditional MPTC and further enhances system performance. Based on the software and hardware implementation scheme, a PMSM drive control platform with Infineon's DSP+FPGA was built to conduct experimental research on different control strategies, and the feasibility and effectiveness of the proposed strategy have been verified with experimental results.

The SiC MOSFET and PMSM can significantly improve efficiency, performance, and power density, making high speed motor controllers possible. However, more serious EMI noise has also emerged. Therefore, it is necessary to conduct mechanism modeling, simulation and experimental verification to study conducted EMI of the motor drive control system. This research takes the system level equivalent circuit model as the research and analysis object. which is composed of power battery pack, busbar cable, LISN, three phase inverter, PMSM and other power electronic components. This modeling method can not only establish EMI sources, CM and DM propagation paths, but also simulate control strategies and operating conditions. Simulation and experimental results indicate the feasibility of the scheme. This research has made an outstanding contribution in predicting the conducted EMI noise during the initial design phase, which can avoid additional printed circuit board (PCB) updating. The study can provide a reliable theoretical basis and guiding methodology for accurate modeling and effective suppression of EMI.

Overall, the experimental results validate the effectiveness of the proposed research objectives in enhancing motor drive control system performance and energy efficiency for NEEVs.

CHAPTER 5

CONCLUSION AND RECOMMENDATIONS

5.1 Conclusions

In recent years, the consumption of conventional energy sources has surged. Rising fuel costs and environmental concerns have prompted the development of the NEEVs. There are four objectives that have been set for the research as stated in Chapter 1. All the objectives of this research were fulfilled. as follows:

a. This research introduces a novel CSGD approach that maintains a constant gate drive current during both turn-on and turn-off periods for motor drive control systems in NEEVs, offering simplicity and cost-effectiveness. The circuit includes a voltage source, H-bridge inverter, and input inductor, significantly reducing SiC MOSFET switching losses and managing dv/dt and di/dt effectively. The discontinuous CSGD method offers new insights into operating SiC MOSFET at high switching frequencies, with notable theoretical and practical benefits. The method's feasibility and advantages have been confirmed through theoretical analysis and experimental results.

b. This research proposes and analyzes the TPIPBi-Buck–Boost converter for new energy electric vehicles. It regulates electrical energy flow between the battery pack and motor drive inverter within the high-voltage DC bus, converting voltage bidirectionally. During start-up or acceleration, energy flows forward to support motor inverter performance, while during braking or deceleration, it flows in reverse to recover excess energy. The converter decouples the battery pack voltage to provide stable energy based on motor conditions. Additionally, it blocks high voltage from the DC bus during motor failure, enhancing the safety and reliability of NEEVs.

c. This research proposes an optimized FCS-MPTC method using voltage vector expansion. It constructs a reference stator flux linkage vector based on the relationships between electromagnetic torque, flux linkage amplitude, and rotor flux linkage, converting separate controls into unified flux linkage vector control. Delay compensation is incorporated, with online calculation of the reference voltage vector using deadbeat control principles. The method extends the voltage vector control set, determines adjacent voltage vectors based on the reference vector's spatial position, and calculates the optimal duty cycles for these vectors and the zero vector, thereby eliminating the weight coefficient from traditional MPTC and enhancing system performance. Experimental validation using Infineon’s DSP + FPGA confirms the feasibility and effectiveness of the proposed strategy.

d. This research focuses on a system-level equivalent circuit model comprising the power battery pack, busbar cable, LISN, three-phase inverter, PMSM, and other power electronic components. This approach establishes EMI sources, CM and DM propagation paths, and simulates control strategies and operating conditions. Simulation and experimental results confirm the scheme's feasibility. The research significantly aids in predicting conducted EMI noise during the initial design phase, reducing the need for PCB updates. It provides a reliable theoretical foundation and methodology for accurate modeling and effective EMI suppression.

5.2 Recommendations for Future Research

This research aims to propose a development blueprint for NEEVs. The enabling technologies and future prospects are briefly introduced as follows:

a. Power Battery Pack: Exploration will focus on lithium-ion, lithium-metal (such as solid-state), and post-lithium technologies. Alternatives to conventional batteries, such as move-and-charge and wireless power systems, will be investigated. Data-driven electrothermal models are promising for real-time state prediction, health diagnosis, and charging control, while future high-energy batteries will integrate with information and internet technologies.

b. Electrical Propulsion System: The main challenge is enhancing vehicle efficiency by reducing parasitic losses in electric drive units and advancing electric mechanical drives, including transmissions and direct drive motors.

c. Moreover, successful growth of NEEVs depends on establishing international standards, universal infrastructures, and user-friendly software. Technologies like 5G, big data, AI, cloud computing, and blockchain are expected to support smart and green NEEVs.

REFERENCES

[1] C. W. Su, L. D. Pang, M. Qin, O. R. Lobont, and M. Umar, “The spillover effects among fossil fuel, renewables and carbon markets: Evidence under the dual dilemma of climate change and energy crises,” Energy, vol. 274, pp. 273042023, 2023.

[2] R. K. Shrestha, P. A. Jacinthe, R. Lal, K. Lorenz, M. P. Singh, S. M. Demyan, W. Ren, and L. E. Lindsey, “Biochar and greenhouse gas emissions: Comment on ‘Biochar as a negative emission technology: A synthesis of field research on greenhouse gas emissions,” J. Environ. Qual., vol. 52, no. 6, pp. 1062–1062, 2023.

[3] L. Domaracká, M. Taušová, K. Čulková, P. Tauš, and P. Gomboš, “Development of Greenhouse Gas Emission and Evaluation of Carbon Resource Use in Chosen EU Countries,” Energies, vol. 16, no. 3, pp. 1254, 2023.

[4] L. P. Huang, X. Y. Geng, and J. X. Liu, “Study on the Spatial Differences, Dynamic Evolution and Convergence of Global Carbon Dioxide Emissions,” Sustainability, vol. 15, no. 6, pp. 5329, 2023.

[5] T. M. Andrews, N. P. Simpson, K. J. Mach, and C. H. Trisos, “Risk from responses to a changing climate,” Clim. Risk Manage., vol. 39, pp. 100487, 2023

[6] S. A. Hussain, F. Razi, K. Hewage, and R. Sadiq, “The perspective of energy poverty and 1st energy crisis of green transition,” Energy, vol. 275, pp.127487, 2023.

[7] A. A. Nassani, Z. Yousaf, M. Radulescu, D. Balsalobre-Lorente, H. Hussain, and M. Haffar, “Green Innovation through Green and Blue Infrastructure Development: Investigation of Pollution Reduction and Green Technology in Emerging Economy,” Energies. vol. 16, no. 4, pp. 1944, 2023.

[8] H. Z. Qi, X. C. Huang, M. Sheeraz, “Green financing for renewable energy development: Driving the attainment of zero-emission targets,” Renewable Energy, vol. 213, pp. 30–37, 2023.

[9] R. Y. Zhong, W. Z. Wu, M. W. Akbar, and Z. Zia, “How environmental protection activities and industrial revolution contributes in the nexus of energy security and environmental sustainability?” Environ. Sci. Pollut. Res., vol. 30, no. 47, pp. 104620–104632, 2023.

[10] C. B. Zhang, X. Zhao, R. Sacchi, and F.Q. You, “Trade-off between critical metal requirement and transportation decarbonization in automotive electrification,” Nat. Commun. , vol.14, no.1, pp.1616, 2023.

[11] C. C. Chan, W. Han, H. L. Tian, Y. B. Liu, T. L. Ma, and C. Q. Jiang, “Automotive revolution and carbon neutrality,” Front. Energy, vol. 17, no. 6, pp. 693–703, 2023.

[12] D. N. Lucsko, and M. N. Eisler, “Age of Auto Electric: Environment, Energy, and the Quest for the Sustainable Car,” IEEE Technol. Soc. Mag., vol. 42, no. 3, pp. 22–24, 2023.

[13] X. L. Tian, E. O. D. Waygood, C.J. An, Z.K. Chen, H. Peng, “Achieving urban net-zero targets through regionalized electric bus penetration and energy transition,” Transp. Res. Part D Transp. Environ., vol. 120, pp. 103797, 2023.

[14] G. Rohith, K. B. Devika, P. P. Menon, and S. C. Subramanian, “Sustainable Heavy Goods Vehicle Electrification Strategies for Long-Haul Road Freight Transportation,” IEEE Access, vol. 11, pp. 26459–26470, 2023.

[15] R. J. Chen, and Y. P. Zhang, “Assessing freight structure and its effect on transport CO2 emissions: heterogeneous and mediating effect analysis,” Environ. Sci. Pollut. Res., vol. 30, no. 14, pp. 42034–42055, 2023.

[16] P. Z. Cui, J. F. Zhang, Y. Y. Liu, Y. R. Zhou, Z. Y. Zhu, J. Gao, Y. L. Wang, “Comprehensive analysis of clean fuel vehicle life cycle environment under multiple fuel scenarios,” Energy, vol. 275, no. 127466, 2023.

[17] A. Galati, N. Adamashvili, and M. Crescimanno, “A feasibility analysis on adopting electric vehicles in the short food supply chain based on GHG emissions and economic costs estimations,” Sustainable Prod. Consumption, vol. 36, pp. 49–61, 2023.

[18] M. Tarafdar-Hagh, K. Taghizad-Tavana, M. Ghanbari-Ghalehjoughi, S. Nojavan, P. Jafari, and A. M. Shotorbani, “Optimizing Electric Vehicle Operations for a Smart Environment: A Comprehensive Review,” Energies, vol. 16, no. 11, pp. 4302, 2023.

[19] J. M. D. Coey, “Perspective and Prospects for Rare Earth Permanent Magnets,” Engineering, vol. 6, no. 2, pp. 119–131, 2020.

[20] A. Rahman, R. Dutta, G. Chu, D. Xiao, V. K. Thippiripati, and M. F. Rahman, “Open-Winding Permanent Magnet Synchronous Generator for Renewable Energy–A Review,” Energies, vol. 16, no. 14, pp. 5268, 2023.

[21] B.J. Baliga, “Silicon Carbide Power Devices: Progress and Future Outlook,” IEEE J. Emerging Sel. Top. Power Electron., vol.11, no. 3, pp. 2400–2411, 2023.

[22] A. Ghezelbash, V. Khaligh, S. H. Fahimifard, and J. J. Liu, “A Comparative Perspective of the Effects of CO2 and Non-CO2 Greenhouse Gas Emissions on Global Solar, Wind, and Geothermal Energy Investment,” Energies, vol. 16, no. 7, pp. 3025, 2023.

[23] K. M. Dittmer, E. Wollenberg, M. Cohen, and C. Egler, “How good is the data for tracking countries’ agricultural greenhouse gas emissions? Making use of multiple national greenhouse gas inventories,” Front. Sustain. Food Syst., vol. 7, pp. 1156822, 2023.

[24] X. Zhang, and J. R. Li, “Recovery of greenhouse gas as cleaner fossil fuel contributes to carbon neutrality,” Green Energy Environ., vol. 8, no. 2, pp. 351–353, 2022.

[25] M. Jayakumar, K. B. Gebeyehu, L. D. Abo, A. W. Tadesse, B. Vivekanandan, V. P. Sundramurthy, W. Bacha, V. Ashokkumar, and G. Baskar, “A comprehensive outlook on topical processing methods for biofuel production and its thermal applications: Current advances, sustainability and challenges,” Fuel, vol. 349, pp. 128690, 2023.

[26] M. A. Azni, R. M. Khalid, U. A. Hasran, and S. K. Kamarudin, “Review of the Effects of Fossil Fuels and the Need for a Hydrogen Fuel Cell Policy in Malaysia,” Sustainability, vol. 15, no. 5, pp. 4033, 2023.

[27] Y. R. Huang, J, Lin, Y. Y. Wang, J. Min, R. Wang, D. Jin, and B. We, “Forecast of Fossil Fuel Demand Based On Low Carbon Emissions from the Perspective of Energy,” Chem. Technol. Fuels Oils, vol. 58, no. 6, pp. 1075–1082, 2023.

[28] M. Hamurcu, and T. Eren, “Multicriteria decision making and goal programming for determination of electric automobile aimed at sustainable green environment: a case study,” Environ. Syst. Dec., vol. 43, no. 2, pp. 211–231, 2023.

[29] J. M. Lao, H. Q. Song, C. Wang, and Y. Zhou, “Research on atmospheric pollutant and greenhouse gas emission reductions of trucks by substituting fuel oil with green hydrogen: A case study,” Int. J. Hydrogen Energy, vol. 48, no. 30, pp. 11555–11566, 2023.

[30] C. Mora, D. Spirandelli, E. C. Franklin, J. Lynham, M. B. Kantar, W. Miles, C.Z. Smith, K. Freel, J. Moy, L. V. Louis, E. W. Barba, K. Bettinger, A. G. Frazier, J. F. Colburn, N. Hanasaki, E. Hawkins, Y. Hirabayashi, W. Knorr, C. M. Little, K. Emanuel, J. Sheffield, J. A. Patz, and C. L. Hunter, “Broad threat to humanity from cumulative climate hazards intensified by greenhouse gas emissions,” Nat. Clim. Change, vol. 8, no. 12, pp. 1062–1071, 2018.

[31] J. A. Patz, H. Frumkin, T. Holloway, D. J. Vimont, and A. Haines, “Climate change: challenges and opportunities for global health,” JAMA J. Am. Med. Assoc., vol. 312, no. 15, pp. 1565–1580, 2014.

[32] M. Höök, and X. Tang, “Depletion of fossil fuels and anthropogenic climate change-A review,” Energy Policy, vol. 52, pp. 797–809, 2013.

[33] J. Lelieveld, K. Klingmüller, A. Pozzer, R.T. Burnett, A. Haines, and V. Ramanathan, “Effects of fossil fuel and total anthropogenic emission removal on public health and climate,” PNAS, vol. 116, no. 15, pp. 7192–7197, 2019.

[34] F. Perera, and K. Nadeau, “Climate change, fossil-fuel pollution, and children's health,” N. Engl. J. Med., vol. 386, no. 24, pp. 2303–2314, 2022.

[35] K. L. Ebi, J. Vanos, J. W. Baldwin, J. E. Bell, D.M. Hondula, N. A. Errett, K. Hayes, C. E. Reid, S. Saha, J. Spector, and P. Berry, “Extreme weather and climate change: population health and health system implications,” Annu. Rev. Public Health, vol. 42, no. 1, pp. 293–315, 2021.

[36] S. Bilgen, “Structure and environmental impact of global energy consumption,” Renewable Sustainable Energy Rev., vol. 38, pp. 890–902, 2014.

[37] S. Fawzy, A. I. Osman, J. Doran, and D. W. Rooney, “Strategies for mitigation of climate change: a review,” Environ. Chem. Lett., vol. 18, no. 6, pp. 2069–2094, 2020.

[38] C. Zhang, G. M. Zeng, D. L. Huang, C. Lai, M. Chen, M. Cheng, W. W. Tang, L. Tang, H. R. Dong, B. B. Huang, X. F. Tan, and R. Z. Wang, “Biochar for environmental management: Mitigating greenhouse gas emissions, contaminant treatment, and potential negative impacts,” Chem. Eng. J., vol. 373, pp. 902–922, 2019.

[39] Z. F. Mi, D. B. Guan, Z. Liu, J. R. Liu, V. Viguie, N. Fromer, and Y. T. Wang, “Cities: The core of climate change mitigation,” J. Cleaner Prod., vol. 207, pp. 582–589, 2019.

[40] H. Altintas, and Y. Kassouri, “Is the environmental Kuznets Curve in Europe related to the per-capita ecological footprint or CO2 emissions?,” Ecol. Indic., vol. 113, pp. 106187, 2020.

[41] A. T. Hoang, S. Nizetic, A. I. Olcer, H. C. Ong, W. H. Chen, C. T. Chong, S. Thomas, S. A. Bandh, and X. P. Nguyen, “Impacts of COVID-19 pandemic on the global energy system and the shift progress to renewable energy: Opportunities, challenges, and policy implications,” Energy Policy., vol. 154, pp. 112322, 2021.

[42] O. Ellabban, H. Abu-Rub, and F. Blaabjerg, “Renewable energy resources: Current status, future prospects and their enabling technology,” Renewable Sustainable Energy Rev., vol. 39, pp. 748–764, 2014.

[43] U. Shahzad, “Environmental taxes, energy consumption, and environmental quality: Theoretical survey with policy implications,” Environ. Sci. Pollut. Res., vol. 27, pp. 24848–24862, 2020.

[44] X. P. Nguyen, and A. T. Hoang, “The Flywheel Energy Storage System: An Effective Solution to Accumulate Renewable Energy,” 2020 6th International Conference on Advanced Computing and Communication Systems (ICACCS), Coimbatore, India, 2020, pp. 1322–1328, 2020.

[45] H. S. Boudet, “Public perceptions of and responses to new energy technologies,” Nat. Energy, vol. 4, no. 6, pp. 446–455, 2019.

[46] Y. Van Fan, S. Perry, J. J. Klemes, and C. T. Lee, “A review on air emissions assessment: Transportation,” J. Cleaner Prod., vol. 194, pp. 673–684, 2018.

[47] A. T. Hoang, A. M. Foley, S. Nizetic, Z. H. Huang, H. C. Ong, A. I. Ölçer, V. Pham, X. P. Nguyen, “Energy-related approach for reduction of CO2 emissions: A critical strategy on the port-to-ship pathway,” J. Cleaner Prod., vol. 355, pp. 131772, 2022.

[48] A. Ghosh, “Possibilities and Challenges for the Inclusion of the Electric Vehicle (EV) to Reduce the Carbon Footprint in the Transport Sector: A Review,” Energies, vol. 13, no. 10, pp. 2602, 2020.

[49] W. J. Requia, M. Mohamed, C. D. Higgins, A. Arain, and M. Ferguson, “How clean are electric vehicles? Evidence-based review of the effects of electric mobility on air pollutants, greenhouse gas emissions and human health,” Atmos. Environ., vol. 185, no. 7, pp. 64–77, 2018.

[50] T. R. Hawkins, O. M. Gausen, and A. H. Strømman, “Environmental impacts of hybrid and electric vehicles—a review,” Int. J. Life Cycle Assess., vol. 17, no. 8, pp. 997–1014, 2012.

[51] A. K. M. R. R. Habib, and K. Butler, “Environmental and economic comparison of hydrogen fuel cell and battery electric vehicles,” Future Technology, vol. 1, no. 2, pp. 25–33, 2022.

[52] H. P. Nguyen, A. T. Hoang, A. T. Le, V. V. Pham, and V. N. Tran, “Learned experiences from the policy and roadmap of advanced countries for the strategic orientation to electric vehicles: A case study in Vietnam,” Energy Sources Part A, pp. 1–10, 2020.

[53] D. Pevec, J. Babic, and V. Podobnik, “Electric vehicles: A data science perspective review,” Electronics, vol. 8, no. 10, pp. 1190, 2019.

[54] R. R. Kumar, and K. Alok, “Adoption of electric vehicle: A literature review and prospects for sustainability,” J. Cleaner Prod., vol. 253, pp. 119911, 2020.

[55] T. Mo, Y. Li, K-t. Lau, C. K. Poon, Y. Wu, and Y. Luo, “Trends and Emerging Technologies for the Development of Electric Vehicles,” Energies, vol. 15, no. 17, pp. 6271, 2022.

[56] M. S. Hossain, L. Kumar, M. E. Assad, and R. Alayi, “Advancements and future prospects of electric vehicle technologies: A comprehensive review,” Complexity, vol. 2022, pp. 3304796, 2022.

[57] A. M. Andwari, A. Pesiridis, S. Rajoo, R. Martinez-Botas, and V. Esfahanian, “A review of battery electric vehicle technology and readiness levels,” Renewable Sustainable Energy Rev., vol. 78, pp. 414–430, 2017.

[58] S. Habib, M. M. Khan, F. Abbas, L. Sang, M. U. Shahid and H. Tang, “A comprehensive study of implemented international standards, technical challenges, impacts and prospects for electric vehicles,” IEEE Access, vol. 6, pp. 13866–13890, 2018.

[59] M. U. Cuma, and T. Koroglu, “A comprehensive review on estimation strategies used in hybrid and battery electric vehicles,” Renewable Sustainable Energy Rev., vol. 42, pp. 517–531, 2015.

[60] V. G. Bui, T. M. T. Bui, A. T. Hoang, S. Nizetic, R. Sakthivel, V. N. Tran, V. H. Bui, D. Engel, and H. Hadiyanto, “Energy storage onboard zero-emission two-wheelers: Challenges and technical solutions,” Sustainable Energy Technol. Assess., vol. 47, pp. 101435, 2021.

[61] M. A. Hannan, M. M. Hoque, A. Mohamed, and A. Ayob, “Review of energy storage systems for electric vehicle applications: Issues and challenges,” Renewable Sustainable Energy Rev., vol. 69, pp. 771–789, 2017.

[62] M.K. Hasan, M. Mahmud, A. K. M. A. Habib, S. M. A. Motakabber, and S. Islam, “Review of electric vehicle energy storage and management system: Standards, issues, and challenges,” J. Energy Storage, vol. 41, pp. 102940, 2021.

[63] B. O. Varga, A. Sagoian, and F. Mariasiu, “Prediction of Electric Vehicle Range: A Comprehensive Review of Current Issues and Challenges,” Energies, vol. 12, no. 5, pp. 946, 2019.

[64] I. Husain, B. Ozpineci, M. S. Islam, E. Gurpinar, G. J. Su, W. S. Yu, S. Chowdhury, L. Xue, D. Rahman, and R. Sahu, “Electric Drive Technology Trends, Challenges, and Opportunities for Future Electric Vehicles,” Proc. IEEE, vol. 109, no. 6, pp. 1039–1059, 2021.

[65] S. S. Ravi, and M. Aziz, “Utilization of Electric Vehicles for Vehicle-to-Grid Services: Progress and Perspectives,” Energies, vol. 15, no. 2, pp. 589, 2022.

[66] L. Mihet-Popa, and S. Saponara, “Toward green vehicles digitalization for the next generation of connected and electrified transport systems,” Energies, vol. 11, no. 11, pp. 3124, 2018.

[67] R. Kene, T. Olwal, and B. J. van Wyk, “Sustainable electric vehicle transportation,” Sustainability, vol. 13, no. 22, pp. 12379, 2021.

[68] A. K. Gupta, A. K. Jha, S. Singh, S. N. Saha, and S. K. Singh, “A comparative review on electric vehicles and hybrid vehicles,” 2022 1st IEEE International Conference on Industrial Electronics: Developments & Applications (ICIDeA), Bhubaneswar, India, 2022, pp. 83–88, 2022.

[69] M. Ehsani, K. V. Singh, H. O. Bansal and R. T. Mehrjardi, “State of the Art and Trends in Electric and Hybrid Electric Vehicles,” Proc. IEEE, vol. 109, no. 6, pp. 967–984, 2021.

[70] M. A. Hannan, F. A. Azidin, and A. Mohamed, “Hybrid electric vehicles and their challenges: A review,” Renewable Sustainable Energy Rev., vol. 29, pp. 135–150, 2014.

[71] C. C. Chan, A. Bouscayrol and K. Chen, “Hybrid, and Fuel-Cell Vehicles: Architectures and Modeling,” IEEE Trans. Veh. Technol., vol. 59, no. 2, pp. 589–598, 2010.

[72] B. G. Pollet, I. Staffell, and J. L. Shang, “Current status of hybrid, battery and fuel cell electric vehicles: From electrochemistry to market prospects,” Electrochim. Acta, vol. 84, pp. 235–249, 2012.

[73] J. Y. Wang, H. L. Wang, and Y. Fan, “Techno-economic challenges of fuel cell commercialization,” Engineering, vol. 4, no. 3, pp. 352–360, 2018.

[74] B. G. Pollet, S. S. Kocha, and I. Staffell, “Current status of automotive fuel cells for sustainable transport,” Curr. Opin. Electrochem., vol. 16, pp. 90–95, 2019.

[75] M. Inci, M. Buyuk, M. H. Demir, and G. Ilbey, “A review and research on fuel cell electric vehicles: Topologies, power electronic converters, energy management methods, technical challenges, marketing and future aspects,” Renewable Sustainable Energy Rev., vol. 137, pp. 110648, 2021.

[76] I. S. Sorlei, N. Bizon, P. Thounthong, M. Varlam, E. Carcadea, M. Culcer, M. Iliescu, and M. Raceanu, “Fuel cell electric vehicles—A brief review of current topologies and energy management strategies,” Energies, vol. 14, no. 1, pp. 252, 2021.

[77] E. Tazelaar, B. Veenhuizen, J. Jagerman and T. Faassen, “Energy Management Strategies for fuel cell hybrid vehicles; an overview,” 2013 World Electric Vehicle Symposium and Exhibition (EVS27), Barcelona, Spain, 2013, pp. 1–12, 2013.

[78] D. Cabezuelo, J. Andreu, I. Kortabarria, I. M. de Alegría and E. Robles, “Powertrain systems of electric, hybrid and fuel-cell vehicles: State of the technology,” 2017 IEEE 26th International Symposium on Industrial Electronics (ISIE), Edinburgh, UK, 2017, pp. 1445–1450, 2017.

[79] F. Blaabjerg, H. Wang, I. Vernica, B. Liu and P. Davari, “Reliability of Power Electronic Systems for EV/HEV Applications,” Proc. IEEE, vol. 109, no. 6, pp. 1060–1076, 2021.

[80] D. G. Barroso, Y. Yang, F. A. Machado and A. Emadi, “Electrified automotive propulsion systems: State-of-the-art review,” IEEE Trans. Transp. Electrif., vol. 8, no. 2, pp. 2898–2914, 2022.

[81] K. Bhadane, P. Sanjeevikumar, B. Khan, M. Thakre, A. Ahmad, T. Jaware, D. P. Patil, and A. S. Pande, “A comprising study on modernization of electric vehicle subsystems, challenges, opportunities and strategies for its further development,” 2021 4th Biennial International Conference on Nascent Technologies in Engineering (ICNTE), NaviMumbai, India, 2021, pp. 1–9, 2021.

[82] D. D. Tran, M. Vafaeipour, M. El Baghdadi, R. Barrero, J. Van Mierlo, and O. Hegazy, “Thorough state-of-the-art analysis of electric and hybrid vehicle powertrains: Topologies and integrated energy management strategies,” Renewable Sustainable Energy Rev., vol. 119, pp. 109596, 2020.

[83] I. Banagar, A. M. Andwari, S. Mehranfar, J. Könnö, and E. Kurvinen, “Electric vehicles’ powertrain systems architectures design complexity,” Future Technology, vol. 2, no. 3, pp. 1–4, 2023.

[84] H. Dong, J. Q. Fu, Z. C. Zhao, Q. Liu, Y. Y. Li, and J. P. Liu, “A comparative study on the energy flow of a conventional gasoline-powered vehicle and a new dual clutch parallel-series plug-in hybrid electric vehicle under NEDC,” Energy Convers. Manage., vol. 218, pp. 113019, 2020.

[85] X. Q. Lu, Y. B. Wu, J. Lian, Y. Y. Zhang, C. Chen, P. S. Wang, and L. Z. Meng, “Energy management of hybrid electric vehicles: A review of energy optimization of fuel cell hybrid power system based on genetic algorithm,” Energy Convers. Manage., vol. 205, pp. 112474, 2020.

[86] R. S. Sankarkumar, and R. Natarajan, “Energy management techniques and topologies suitable for hybrid energy storage system powered electric vehicles: An overview,” Int. Trans. Electr. Energy Syst., vol. 31, no. 4, pp. e12819, 2021.

[87] S. Manzetti, and F. Mariasiu, “Electric vehicle battery technologies: From present state to future systems,” Renewable Sustainable Energy Rev., vol. 51, pp. 1004–1012, 2015.

[88] L. S. Martins, L. F. Guimaraes, A. B. Botelho, J. A. S. Tenorio, and D. C. R. Espinosa, “Electric car battery: An overview on global demand, recycling and future approaches towards sustainability,” J. Environ. Manage., vol. 295, pp. 113091, 2021.

[89] X. I. Xia, P. W. Li, “A review of the life cycle assessment of electric vehicles: Considering the influence of batteries,” Sci. Total Environ., vol. 814, pp. 152870, 2022.

[90] E. Chemali, M. Preindl, P. Malysz and A. Emadi, “Electrochemical and electrostatic energy storage and management systems for electric drive vehicles: State-of-the-art review and future trends,” IEEE J. Emerging Sel. Top. Power Electron., vol. 4, no. 3, pp. 1117–1134, 2016.

[91] A. Picatoste, D. Justel, and J. M. F. Mendoza, “Circularity and life cycle environmental impact assessment of batteries for electric vehicles: Industrial challenges, best practices and research guidelines,” Renewable Sustainable Energy Rev., vol. 169, pp. 112941, 2022.

[92] M. Subramanian, A. T. Hoang, B. Kalidasan, S. Nizetic, J. M. Solomon, D. Balasubramanian, C. Subramaniyan, G. Thenmozhi, H. Metghalchi, and X. P. Nguyen, “A technical review on composite phase change material based secondary assisted battery thermal management system for electric vehicles,” J. Cleaner Prod., vol. 322, pp. 129079, 2021.

[93] A. V. Kuppusamy, S. Bashir, S. Ramesh, S. Ramesh, and K. Ramesh, “Solar cell-integrated energy storage devices for electric vehicles: a breakthrough in the green renewable energy,” Ionics, vol. 28, no. 9, pp. 4065–4081, 2022.

[94] D. Bresser, K. Hosoi, D. Howell, H. Li, H. Zeisel, K. Amine, P. Stefano, S. Passerini,” Perspectives of automotive battery R&D in China, Germany, Japan, and the USA,” J. Power Sources, vol. 382, pp. 176-178, 2018.

[95] A. K. M. Ahasan Habib, S. M. A. Motakabber and M. I. Ibrahimy," Comparative Study of electrochemical battery for electric vehicles applications. 2019 IEEE International Conference on Power, Electrical, and Electronics and Industrial Applications (PEEIACON), Dhaka, Bangladesh 2019, pp. 43–47, 2019.

[96] W. Liu, T. Placke, and K. T. Chau, "Overview of batteries and battery management for electric vehicles," Energy Rep., vol. 8, pp. 4058–4084, 2022.

[97] G. Zhao, X. L. Wang, and M. Negnevitsky, "Connecting battery technologies for electric vehicles from battery materials to management," iScience, vol. 25, no. 2, pp. 103744, 2022.

[98] P. Asef, M. Milan, A. Lapthorn, and S. Padmanaban, "Future Trends and Aging Analysis of Battery Energy Storage Systems for Electric Vehicles," Sustainability, vol. 13, no. 24, pp. 13779, 2021.

[99] G. Zubi, R. Dufo-Lopez, M. Carvalho, and G. Pasaoglu, "The Lithium-Ion battery: State of the art and future perspectives," Renewable Sustainable Energy Rev., vol. 89, pp. 292–308, 2018.

[100] Y. Yang, E. G. Okonkwo, G. Y. Huang, S. M. Xu, W. Sun, and Y. H. He, "On the sustainability of lithium-ion battery industry–A review and perspective," Energy Storage Mater., vol. 36, pp. 186–1212, 2021.

[101] R. Wagner, N. Preschitschek, S. Passerini, J. Leker, and M. Winter, "Current research trends and prospects among the various materials and designs used in lithium-based batteries," J. Appl. Electrochem., vol. 43, pp. 481–496, 2013.

[102] J. F. Peters, M. Baumann, B. Zimmermann, J. Braun, and M. Weil, "The environmental impact of Li-Ion batteries and the role of key parameters–A review," Renewable Sustainable Energy Rev., vol. 67, pp. 491–506, 2017.

[103] A. Mauger, and C. M. Julien, "Critical review on lithium-ion batteries: are they safe? Sustainable?," Ionics, vol. 23, no. 8, pp. 1933–1947, 2017.

[104] Y. L. Ding, Z. P. Cano, A. P. Yu, J. Lu, and Z. W. Chen, "Automotive li-ion batteries: Current status and future perspectives," Electrochem. Energy Rev., vol. 2, no. 1, pp. 1–28, 2019.

[105] K. Laadjal, A. J. M. Cardoso, "Estimation of lithium-ion batteries State-condition in electric vehicle applications: Issues and state of the art," Electronics, vol. 10, no. 13, pp. 1588, 2021.

[106] F. H. Gandoman, J. Jaguemont, S. Goutam, R. Gopalakrishnan, Y. Firouz, T. Kalogiannis, N. Omar, and J. Van Mierlo, “Concept of reliability and safety assessment of lithium-ion batteries in electric vehicles: Basics, progress, and challenges,” Appl. Energy, vol. 251, pp. 113343, 2019.

[107] M. A. Hannan, M. M. Hoque, A. Hussain, Y. Yusof, and P. J. Ker, “State-of-the-art and energy management system of lithium-ion batteries in electric vehicle applications: Issues and recommendations,” IEEE ACCESS, vol. 6, pp. 19362–19378, 2018.

[108] Y. Xu, F. Liu, J. Guo, M. Li, and B. Han, “Mechanical properties and thermal runaway study of automotive lithium-ion power batteries,” Ionics, vol. 28, no. 1, pp. 107–116, 2022.

[109] A. K. M. R. R. Habib, and K. Butler, “Alternatives to lithium-ion batteries in electric vehicles,” Future Technology, vol. 1, no. 1, pp. 33–34, 2022.

[110] S. Singh, V. More and R. Batheri, “Driving Electric Vehicles into the Future with Battery Management Systems,” IEEE Eng. Manage. Rev., vol. 50, no. 3, pp. 157–161, 2022.

[111] M. S. H. Lipu, M. A. Hannan, T. F. Karim, A. Hussain, M. H. M. Saad, A. Ayob, M. S. Miah, T. M. I. Mahlia, “Intelligent algorithms and control strategies for battery management system in electric vehicles: Progress, challenges and future outlook,” J. Cleaner Prod., vol. 292, pp. 126044, 2021.

[112] M. A. Hannan, S. B. Wali, P. J. Ker, M. S. Abd Rahman, M. Mansor, V. K. Ramachandaramurthy, K. M. Muttaqi, T. M. I. Mahlia, and Z. Y. Dong, “Battery energy-storage system: A review of technologies, optimization objectives, constraints, approaches, and outstanding issues,” J. Cleaner Prod., vol. 42, pp. 103023, 2021.

[113] A. Ibrahim, and F. M. Jiang, “The electric vehicle energy management: An overview of the energy system and related modeling and simulation,” Renewable Sustainable Energy Rev., vol. 144, pp. 111049, 2021.

[114] S. Aghajan-Eshkevari, S. Azad, M. Nazari-Heris, M. T. Ameli, and S. Asadi, “Charging and discharging of electric vehicles in power systems: An updated and detailed review of methods, control structures, objectives, and optimization methodologies,” Sustainability, vol. 14, no. 4, pp. 2137, 2022.

[115] T. Muni Prakash, K. K. Vinoth, P. R. Naik, R. P. V. S. Varma, R. Supraja, and R. V. Lingadhal, “A review on optimization techniques of battery charging in electric vehicles,” 2022 2nd International Conference on Artificial Intelligence and Signal Processing (AISP), Vijayawada, India vol. 2022, pp. 1–5, 2022.

[116] R. Collin, Y. Miao, A. Yokochi, P. Enjeti, and A. von Jouanne, “Advanced electric vehicle fast-charging technologies,” Energies, vol. 12, no. 10, pp. 1839, 2019.

[117] S. Hemavathi, and A. Shinisha, “A study on trends and developments in electric vehicle charging technologies,” J. Energy Storage, vol. 52, no. c, pp. 105013, 2022.

[118] C. L. Chen, Z. B. Wei, and A. C. Knoll, “Charging optimization for li-ion battery in electric vehicles: A review,” IEEE Trans. Transp. Electrif., vol. 8, no. 3, pp. 3068–3089, 2022.

[119] M. U. Ali, A. Zafar, S. H. Nengroo, S. Hussain, M. Junaid Alvi, and H.-J. Kim, “Towards a smarter battery management system for electric vehicle applications: A critical review of lithium-ion battery state of charge estimation,” Energies, vol. 12, no. 3, pp. 446, 2019.

[120] T. Muni Prakash, K. K. Vinoth, A. Singh, R. P. V. S. Varma, R. Supraja, P. R. Naik, and R. V. Lingadhal, “A review on optimization techniques of charging the battery in EV,” 2022 Second International Conference on Artificial Intelligence and Smart Energy (ICAIS), Coimbatore, India, vol. 2022, pp. 799–804, 2022.

[121] H. P. Nguyen, A. T. Hoang, S. Nizetic, X. P. Nguyen, A. T. Le, C. N. Luong, V. D. Chu, V. Pham, “The electric propulsion system as a green solution for management strategy of CO2 emission in ocean shipping: A comprehensive review,” Int. Trans. Electr. Energy Syst., vol. 31, no. 11, pp. e12580, 2021.

[122] S. M. Cui, S. L. Han, and C. C. Chan, “Overview of multi-machine drive systems for electric and hybrid electric vehicles,” 2014 IEEE Conference and Expo Transportation Electrification Asia-Pacific (ITEC Asia-Pacific), Beijing, China, 2014, pp. 1–6, 2014.

[123] Y. Amry, E. Elbouchikhi, F. Le Gall, M. Ghogho, and S. El Hani, “Electric Vehicle Traction Drives and Charging Station Power Electronics: Current Status and Challenges,” Energies, vol. 15, no. 16, pp. 6037, 2022.

[124] I. Aghabali, J. Bauman, P. J. Kollmeyer, Y. W. Wang, B. Bilgin, and A. Emadi, “800-V Electric Vehicle Powertrains: Review and Analysis of Benefits, Challenges, and Future Trends,” IEEE Trans. Transp. Electrif., vol. 7, no. 3, pp. 927–948, 2021.

[125] I. López, E. Ibarra, A. Matallana, J. Andreu, and I. Kortabarria, “Next generation electric drives for HEV/EV propulsion systems: Technology, trends and challenges,” Renewable Sustainable Energy Rev., vol. 114, pp. 109336, 2019.

[126] S. Cai, J. L. Kirtley and C. H. T. Lee, “Critical review of direct-drive electrical machine systems for electric and hybrid electric vehicles,” IEEE Trans. Energy Convers., vol. 37, no. 4, pp. 2657–2668, 2022.

[127] M. U. Sardar, M. F. Dou, U. Saleem, M. K. Nawaz and M. Hassan, “A Scholarly Review of Methods for Design Optimization of IPM Synchronous Motors Used in Electric Vehicles,” 2022 International Conference on Emerging Trends in Electrical, Control, and Telecommunication Engineering (ETECTE), Lahore, Pakistan, vol. 2022, pp. 1–6, 2022.

[128] S. J. Rind, Y. X. Ren, Y. H. Hu, J. B. Wang, and L. Jiang, “Configurations and control of traction motors for electric vehicles: A review,” Chin. J. Electr. Eng., vol. 3, no. 3, pp. 1–17, 2017.

[129] Y. A. Alamoudi, A. Ferrah, R. Panduranga, A. Althobaiti and F. Mulolani, “State-of-the art electrical machines for modern electric vehicles,” 2019 Advances in Science and Engineering Technology International Conferences (ASET), Dubai, United Arab Emirates, vol. 2019, pp. 1–8, 2019.

[130] C. H. Liu, K. T. Chau, C. H. T. Lee and Z. X. Song, “A critical review of advanced electric machines and control strategies for electric vehicles,” Proc. IEEE, vol. 109, no. 6, pp. 2657–2668, 2021.

[131] A. Swaminathan, K. Malavika, N. Narayanan and M. Jayakumar, “Review on different topologies of power electronic converters and control strategies for motors in electric vehicles,” 2021 Innovations in Power and Advanced Computing Technologies (i-PACT), Kuala Lumpur, Malaysia, vol. 2021, pp. 1–7, 2021.

[132] D. Mohanraj, J. Gopalakrishnan, B. Chokkalingam and L. Mihet-Popa, “Critical aspects of electric motor drive controllers and mitigation of torque ripple—Review,” IEEE Access, vol. 10, pp. 73635–73674, 2022.

[133] T. Kimoto, “Material science and device physics in SiC technology for high-voltage power devices,” Jpn. J. Appl. Phys. , vol. 54, no. 4, pp. 04010, 2015.

[134] H. Matsunami, “Fundamental research on semiconductor SiC and its applications to power electronics,” Proc. Jpn. Acad., Ser. B., vol. 96, no. 7, pp. 235–254, 2020.

[135] S. Chabi, and K. Kadel, “Two-Dimensional Silicon Carbide: Emerging Direct Band Gap Semiconductor,” Nanomaterials, vol. 10, no. 11, pp. 2226, 2020.

[136] X. She, A. Q. Huang, Ó. Lucía and B, “Ozpineci. Review of Silicon Carbide Power Devices and Their Applications,” IEEE Trans. Ind. Electron., vol. 64, no. 10, pp. 8193–8205, 2017.

[137] S. Anwar, Z. J. Wang and M. Chinthavali, “Characterization and Comparison of Trench and Planar Silicon Carbide (SiC) MOSFET at Different Temperatures,” 2018 IEEE Transportation Electrification Conference and Expo (ITEC), Long Beach, CA, USA. vol. 2018, pp. 1039–1045,2018.

[138] L. Sun, B. Duan, Y. Wang and Y. Yang, “Fast-Switching Lateral IGBT with Trench/Planar Gate and Integrated Schottky Barrier Diode (SBD),” 2019 31st International Symposium on Power Semiconductor Devices and ICs (ISPSD). Shanghai, China. vol. 2019, pp. 379–382, 2019.

[139] M. Chaturvedi, S. Dimitrijev, D. Haasmann, H. A. Moghadam, P. Pande and U. Jadli, “Comparison of Commercial Planar and Trench SiC MOSFETs by Electrical Characterization of Performance-Degrading Near-Interface Traps,” IEEE Trans. Electron Devices, vol. 69, no. 11, pp. 6225–6230, 2022.

[140] B. Asllani, A. Castellazzi, O. A. Salvado, A. Fayyaz, H. Morel and D. Planson, “VTH-Hysteresis and Interface States Characterisation in SiC Power MOSFETs with Planar and Trench Gate,” 2019 IEEE International Reliability Physics Symposium (IRPS), Monterey, CA, USA, vol. 2019, pp. 1–6,2019.

[141] S. Z. Zhang, “Influence of driving and parasitic parameters on the switching behaviors of the SiC MOSFET,” Front. Energy Res., vol. 10, pp. 1079623, 2022.

[142] S. H. Liu, M. M. Huang, M. J. Wang, M. Zhang, and J. Wei, “Considerations for SiC super junction MOSFET: On-resistance, gate structure, and oxide shield,” Microelectron. J., vol. 137, pp. 105823, 2023.

[143] N. Oswald, P. Anthony, N. McNeill and B. H. Stark, “An Experimental Investigation of the Tradeoff between Switching Losses and EMI Generation With Hard-Switched All-Si, Si-SiC, and All-SiC Device Combinations,” IEEE Trans. Power Electron., vol. 29, no. 5, pp. 2393–2407, 2014.

[144] A. Babaie, B. Karami and A. Abrishamifar, “Improved equations of switching loss and conduction loss in SPWM multilevel inverters,” 2016 7th Power Electronics and Drive Systems Technologies Conference (PEDSTC), Tehran, Iran, vol. 2016, pp. 559–564, 2016.

[145] A. K. Sadigh, V. Dargahi and K. A. Corzine, “Analytical Determination of Conduction and Switching Power Losses in Flying-Capacitor-Based Active Neutral-Point-Clamped Multilevel Converter,” IEEE Trans. Power Electron., vol. 31, no. 8, pp. 5473–5494, 2016.

[146] Z. Zhang, F. Wang, L. M. Tolbert, B. J. Blalock and D. J. Costinett, “Active gate driver for fast switching and cross-talk suppression of SiC devices in a phase-leg configuration,” 2015 IEEE Applied Power Electronics Conference and Exposition (APEC), Charlotte, NC, USA. vol. 2015, 774–781, 2015.

[147] Y. Noge and M. Shoyama, “High Bandwidth Active Gate Driver for Simultaneous Reduction of Switching Surge and Switching Loss of SiC-MOSFET,” 2022 International Power Electronics Conference (IPEC-Himeji 2022- ECCE Asia), Himeji, Japan, vol. 2022, pp. 2097–2103, 2022.

[148] S. Fukunaga, H. Takayama and T. Hikihara, “A Study on Switching Surge Voltage Suppression of SiC MOSFET by Digital Active Gate Drive,” 2021 IEEE 12th Energy Conversion Congress & Exposition - Asia (ECCE-Asia), Singapore, Singapore, vol. 2021, pp. 1325–1330, 2021.

[149] J. V. P. S. Chennu, R. Maheshwari and H. Li, “New Resonant Gate Driver Circuit for High-Frequency Application of Silicon Carbide MOSFETs,” IEEE Trans. Ind. Electron., vol. 64, no. 10, pp. 8277–8287, 2017.

[150] B. Sun, Z. Zhang and M. A. E. Andersen, “Review of Resonant Gate Driver in Power Conversion,” 018 International Power Electronics Conference (IPEC-Niigata 2018 -ECCE Asia), Niigata, Japan, vol. 2018, pp. 607–613, 2018.

[151] X. Wang, H. Wu and V. Pickert, “A cost-efficient Current-Source Gate Driver for SiC MOSFET Module and its Comparison with Voltage-Source Gate Driver,” 2020 IEEE 9th International Power Electronics and Motion Control Conference (IPEMC2020-ECCE Asia), Nanjing, China, vol. 2020, pp. 979–984, 2020.

[152] H. Wu, X. Wang, J. Ortiz-Gonzalez, O. Alatise and V. Pickert, “Investigation into the Switching Transient of SiC MOSFET Using Voltage/Current Source Gate Driver,” The 10th International Conference on Power Electronics, Machines and Drives (PEMD 2020), Online Conference, vol. 2020, pp. 657–662, 2020.

[153] A. Sagehashi, K. Kusaka, K. Orikawa and J. -i. Itoh, “Current source gate drive circuits with low power consumption for high frequency power converters,” 2015 9th International Conference on Power Electronics and ECCE Asia (ICPE-ECCE Asia), Seoul, Korea (South), vol. 2015, pp. 1017–1024, 2015.

[154] Q. Zheng, C. Chen and Y. Kang, “Modeling and Comparison of Switching Loss between SiC MOSFETs with Current Source and Voltage Source Gate Driver,” 2021 IEEE Workshop on Wide Bandgap Power Devices and Applications in Asia (WiPDA Asia), Wuhan, China, 2021, pp. 1-5, 2021.

[155] A. Kumar, M. Losito, M. Moradpour and G. Gatto, “Current Source Gate Driver for SiC MOSFETs in Power Electronics Applications,” 2022 International Symposium on Power Electronics, Electrical Drives, Automation and Motion (SPEEDAM), Sorrento, Italy, vol. 2022, pp. 523–527, 2022.

[156] M. Moradpour, W. -T. Franke, P. Pirino and G. Gatto, “Current Source Gate Driver for GaN E-HEMT in Hard-Switched High Power Applications,” 2020 International Symposium on Power Electronics, Electrical Drives, Automation and Motion (SPEEDAM), Sorrento, Italy, vol. 2020, pp. 408–413, 2020.

[157] Z. Zhang, C. Liu, M. Wang, Y. Si, Y. Liu and Q. Lei, “A Novel Current-Source-Based Gate Driver With Active Voltage Balancing Control for Series-Connected GaN HEMTs,” IEEE Open J. Power Electron., vol. 2021, no. 2, pp. 346–367, 2021.

[158] A. Schindler, B. Koeppl and B. Wicht, “EMC analysis of current source gate drivers,” 2013 9th International Workshop on Electromagnetic Compatibility of Integrated Circuits (EMC Compo), Nara, Japan, vol. 2013, pp. 101–106, 2013.

[159] Y. He, X. Wang, S. Shao and J. M. Zhang, “Active Gate Driver for Dynamic Current Balancing of Parallel-Connected SiC MOSFETs,” IEEE Trans. Power Electron., vol. 38, no. 5, pp. 6116–6127, 2023.

[160] H. T. Tian, Y. H. Li, Q. Zhang, N. R. Xiao, J. J. Wang, H. W. Liu, Y. Q. Li, “Improved Current-Sharing Imbalance Control Model Based on Magnetic Ferrite Inductance and a Gate Drive Circuit,” Machines, vol. 11, no. 2, pp. 197, 2023.

[161] D. A. Philipps, P. Xue, T. N. Ubostad, F. Iannuzzo and D. Peftitsis, “Low Inductive Characterization of Fast-Switching SiC MOSFETs and Active Gate Driver Units,” IEEE Trans. Ind. Appl., vol. 59, no. 5, pp. 6384–6398, 2023.

[162] T. Liu, T. T. Y. Wong and Z. J. Shen, “A Survey on Switching Oscillations in Power Converters,” IEEE J. Emerging Sel. Top. Power Electron., vol. 8, no. 1, pp. 893-908, 2020.

[163] H. Chen and D. Divan, “High speed switching issues of high power rated silicon-carbide devices and the mitigation methods,” 2015 IEEE Energy Conversion Congress and Exposition (ECCE), Montreal, QC, Canada, vol. 2015, pp. 2254–2260, 2015.

[164] D. Xu, M. Yang, J. Long and D. Xu, “Design and Multi-constraint Evaluation of Passive dv/dt Filter for SiC-based Motor Drives,” 2022 25th International Conference on Electrical Machines and Systems (ICEMS), Chiang Mai, Thailand, vol. 2022, pp. 1–5, 2022.

[165] S. Sivakumar, M. J. Sathik, P. S. Manoj, and G. Sundararajan, “An assessment on performance of DC–DC converters for renewable energy applications,” Renewable Sustainable Energy Rev., vol. 58, pp. 1475–1485, 2016.

[166] M. ElMenshawy, and A. Massoud, “Medium-Voltage DC-DC Converter Topologies for Electric Bus Fast Charging Stations: State-of-the-Art Review,” Energies, vol. 15, no. 15, pp. 5487, 2022.

[167] S. A. Q. Mohammed, and J. W. Jung, “A State-of-the-Art Review on Soft-Switching Techniques for DC–DC, DC–AC, AC–DC, and AC–AC Power Converters,” IEEE Trans. Ind. Inf., vol. 17, no. 10, pp. 6569–6582, 2021.

[168] M. Z. Hossain, N. A. Rahim, and J. Selvaraj, “Recent progress and development on power DC-DC converter topology, control, design and applications: A review,” Renewable Sustainable Energy Rev., vol. 81, no. 1, pp. 205–230, 2018.

[169] D. Nayanasiri, and Y. W. Li, “Step-Down DC–DC Converters: An Overview and Outlook,” Electronics, vol. 11, no. 11, pp. 1693, 2022.

[170] I. Alhurayyis, A. Elkhateb and J. Morrow, “Isolated and Nonisolated DC-to-DC Converters for Medium-Voltage DC Networks: A Review,” IEEE J. Emerging Sel. Top. Power Electron., vol. 9, no. 6, pp. 7486–7500, 2021.

[171] X. F. Cheng, C. Y. Liu, D. L. Wang, and Y. Zhang, “State-of-the-Art Review on Soft-Switching Technologies for Non-Isolated DC-DC Converters,” IEEE Access, vol. 9, pp. 119235–119249, 2021.

[172] F. Mumtaz, N. Z. Yahaya, S. T. Meraj, B. Singh, R. Kannan, and O. Ibrahim, “Review on non-isolated DC-DC converters and their control techniques for renewable energy applications,” Ain Shams Eng. J., vol. 12, no. 4, pp. 3747–3763, 2021.

[173] M. H. Taghvaee, M. A. M. Radzi, S. M. Moosavain, H. Hizam, M. H. Marhaban, “A current and future study on non-isolated DC–DC converters for photovoltaic applications,” Renewable Sustainable Energy Rev., vol. 17, pp. 216–227, 2013.

[174] F. A. Abbas, T. A. Abdul-Jabbar, A. A. Obed, A. Kersten, M. Kuder, T. Weyh, “A Comprehensive Review and Analytical Comparison of Non-Isolated DC-DC Converters for Fuel Cell Applications,” Energies, vol. 16, no. 8, pp. 3493, 2023.

[175] R. Venugopal, B. Chandrasekar, A. D. Savio, R. Narayanamoorthi, K. M. Aboras, H. Kotb, Y. Y. Ghadi, M. Shouran, and E. Elgamli, “Review on Unidirectional Non-Isolated High Gain DC–DC Converters for EV Sustainable DC Fast Charging Applications,” IEEE Access, vol. 11, pp. 78299–78338, 2023.

[176] I. Alhurayyis, A. Elkhateb and J. Morrow, “Isolated and Nonisolated DC-to-DC Converters for Medium-Voltage DC Networks: A Review,” IEEE J. Emerging Sel. Top. Power Electron., vol. 9, no. 6, pp. 7486–7500, 2021.

[177] H. Meshael, A. Elkhateb, and R. Best, “Topologies and Design Characteristics of Isolated High Step-Up DC–DC Converters for Photovoltaic Systems,” Electronics, vol. 12, no. 18, pp. 3913, 2023.

[178] S. B. Sudarshan, and G. Arunkumar, “Isolated DC-DC Power Converters for Simultaneous Charging of Electric Vehicle Batteries: Research Review, Design, High-Frequency Transformer Testing, Power Quality Concerns, and Future,” Sustainability, vol. 15, no. 3, pp. 2813, 2023.

[179] W. Hu, J. T. Tao, Z. K. Ding, and H. Yang, “Analysis and control of partial power processing nonisolated bidirectional DC-DC converter,” Int. J. Circuit Theory Appl., vol. 51, no. 9, pp. 4427–4441, 2021.

[180] T. Jalilzadeh, and N. Rostami, “New multi-operational multi-port DC–DC converter with bidirectional capability,” IET Renewable Power Gener., vol. 17, no. 6, pp. 1518–1534, 2023.

[181] T. Sojoudi, M. Sarhangzadeh, J. Olamaei and J. F. Ardashir, “An Extendable Bidirectional High-Gain DC–DC Converter for Electric Vehicle Applications Equipped With IOFL Controller,” IEEE Trans. Power Electron., vol. 38, no. 8, pp. 9767–9779, 2023.

[182] M. Z. Malik, S. Q. Zhang, A. Ali, A. Farooq, “A. Design and implementation of a multi-port bidirectional converter for electric vehicle applications,” Int. J. Circuit Theory Appl., vol. 51, no. 10, pp. 4728–4753, 2023.

[183] Y. L. Li, Y. J. Wang, Y. S. Guan, and D. G. Xu, “Design and Optimization of High-Gain Bidirectional DC–DC Converter for Electric Vehicles,” IEEE Trans. Power Electron., vol. 38, no. 9, pp. 11221–11232, 2023.

[184] W. S. Lee, S. Y. Bae, D. H. Cho, H. S. Yoon, and I. O. Lee, “High-efficiency bidirectional low-voltage power converter for fuel-cell electric vehicles,” J. Power Electron., vol. 23, no. 9, pp. 1307–1320, 2023.

[185] F. L. Yi, and F. Q. Wang, “Review of Voltage-Bucking/Boosting Techniques, Topologies, and Applications,” Energies, vol. 16, no. 2, pp. 842, 2023.

[186] F. L. Tofoli, D. D. Pereira, W. J. de Paula, and D. D. Oliveira, “Survey on non-isolated high-voltage step-up dc–dc topologies based on the boost converter,” IET Power Electron., vol. 8, no. 10, pp. 2044–2057, 2015.

[187] F. G. Nimitti, J. C. Giacomini and A. M. S. S. Andrade, “Dual-Stacked Bidirectional Boost/Buck DC–DC Converter,” IEEE Trans. Ind. Electron, vol. 70, no. 9, pp. 8873–8882, 2023.

[188] M. S. Khan, S. S. Nag, A. Das and C. Yoon, “Analysis and Control of an Input-Parallel Output-Series Connected Buck-Boost DC–DC Converter for Electric Vehicle Powertrains,” IEEE Trans. Transp. Electrif., vol. 9, no. 2, pp. 2015–2025, 2023.

[189] C. P. Mehta and Balamurugan P, “Buck-Boost Converter as Power Factor Correction Controller for Plug-In Electric Vehicles and Battery Charging Application,” In Proceedings of the IEEE 6th International Conference on Power Systems (ICPS), New Delhi, India, vol. 2016, pp. 1–6, 2016.

[190] P. Gray, P. Lehn and S. Wang, “An Integrated Bidirectional Three-Phase AC Charger for Vehicle Applications with Buck-Boost Capability,” In Proceedings of the IEEE Energy Conversion Congress and Exposition (ECCE), Portland, OR, USA, vol. 2018, pp. 517–523, 2018.

[191] P. S. R. Nayak, K. Kamalapathi, N. Laxman and V. K. Tyagi, “Design and Simulation of Buck-Boost Type Dual Input DC-DC Converter for Battery Charging Application in Electric Vehicle,” In Proceedings of the International Conference on Sustainable Energy and Future Electric Transportation (SEFET), Hyderabad, India, vol. 2021, pp. 1–6, 2021.

[192] H. Moradisizkoohi, N. Elsayad, A. Berzoy, C. R. Lashway and O. A. Mohammed, “A Multi-Level Bi-Directional Buck-Boost Converter Using GaN Devices for Electric Vehicle Applications,” In Proceedings of the 17 IEEE Transportation Electrification Conference and Expo (ITEC), Chicago, IL, USA, vol. 2017, pp. 742–746, 2017.

[193] K. L. Liu, Z. L. Yang, X. P. Tang, and W. P. Cao, “Automotive Battery Equalizers Based on Joint Switched-Capacitor and Buck-Boost Converters,” IEEE Trans. Veh. Technol., vol. 69, no. 11, pp. 12716–12724,2020.

[194] R. Georgious, S. Saeed, J. Garcia and P. Garcia, “Switching Schemes of the Bidirectional Buck-Boost Converter for Energy Storage System,” In Proceedings of the IEEE Vehicle Power and Propulsion Conference (VPPC), Gijon, Spain, vol. 2020, pp. 1–5, 2020.

[195] M. S. Khan, S. S. Nag, A. Das and C. Yoon, “A Novel Buck-Boost Type DC-DC Converter Topology for Electric Vehicle Applications,” In Proceedings of the IEEE Energy Conversion Congress and Exposition (ECCE), Vancouver, BC, Canada, vol. 2021, pp, 1534–1539, 2021.

[196] D. A. Barkas, G. C. Ioannidis, C. S. Psomopoulos, S. D. Kaminaris, and G. A. Vokas, “Brushed DC Motor Drives for Industrial and Automobile Applications with Emphasis on Control Techniques: A Comprehensive Review,” Electronics, vol. 9, no. 6, pp. 887, 2020.

[197] S. A. Odhano, P. Pescetto, H. A. A. Awan, M. Hinkkanen, G. Pellegrino and R. Bojoi, “Parameter Identification and Self-Commissioning in AC Motor Drives: A Technology Status Review,” IEEE Trans. Power Electron., vol. 34, no. 4, pp. 3603–3614, 2019.

[198] J. Cui, M. Kramer, L. Zhou, F. Liu, A. Gabay, G. Hadjipanayis, B. Balasubramanian, and D. Sellmyer, “Current progress and future challenges in rare-earth-free permanent magnets,” Acta Mater., vol. 158, pp. 118–137, 2018.

[199] K. Takagi, Y. Hirayama, S. Okada, A. Hosokawa, and W. Yamaguchi, “Recent Research Trend in Powder Process Technology for High-Performance Rare-Earth Permanent Magnets,” Kona Powder Part. J., vol. 40, pp. 74–93, 2023.

[200] K. S. Stegen, “Heavy rare earths, permanent magnets, and renewable energies: An imminent crisis,” Energy Policy, vol. 79, pp. 1–8, 2015.

[201] J. Zuščak, V. Kujan, and F. Janíček, “Simulations and measurements on a self-excited induction generator,” J. Electr. Eng., vol. 69, no. 5, pp. 359–365, 2018.

[202] K. Sumin, H. S. Lee, and L. W. Young, “Current Status and Prospect of Rare Earth Magnet,” Journal of the Korean Magnetics Society, vol. 28, no. 6, pp. 248–259, 2018.

[203] J. Fischbacher, A. Kovacs, M. Gusenbauer, H. Oezelt, L. Exl, S. Bance, and T. Schrefl, “Micromagnetics of rare-earth efficient permanent magnets,” J. Phys. D: Appl. Phys., vol. 51, no. 19, pp. 193002, 2018.

[204] Z. W. Li, A. Kedous-Lebouc, J. M. Dubus, L. Garbuio, and S. Personnaz, “Direct reuse strategies of rare earth permanent magnets for PM electrical machines – an overview study,” Eur. Phys. J. Appl. Phys., vol. 86, no. 2, pp. 1–10, 2019.

[205] P Mercorelli, “Control of Permanent Magnet Synchronous Motors for Track Applications,” Electronics, vol. 12, no. 15, pp. 3285, 2023.

[206] K. Kolano, “New Method of Vector Control in PMSM Motors,” IEEE Access, vol. 11, pp. 43882–43890, 2023.

[207] T. D. C. Busarello, A. Bubshait, O. V. S. R. Varaprasad, A. Alsaleem and M. G. Simões, “Comprehensive Design Approach for Field-Oriented Control of Interior Permanent Magnet Synchronous Machines,” 2022 4th Global Power, Energy and Communication Conference (GPECOM), Nevsehir, Turkey, 2022, pp. 168–173, 2022.

[208] B. Yousef, M. Ghanbari, and R. Ebrahimi, “A Modified FOC for FTC of Induction Motor Drives,” Arabian J. Sci. Eng., vol. 48, no. 5, pp. 6747–6764, 2023.

[209] P. Ramesh, M. Umavathi, C. Bharatiraja, G. Ramanathan, and S. Athikkal, “A Development of a PMSM motor field-oriented control algorithm for electrical vehicles,” Mater. Today: Proc., vol. 65, no. 1, pp. 176–187, 2022.

[210] D. Galindo, E. F. Palomeque, “FOC Control Design of VSI-SiC Power Converter for an Electric Traction System,” Intelligent Technologies: Design and Applications for Society (CITIS), Springer, Cham, 2022, vol. 607, pp. 357–367, 2023.

[211] A. Nasr, C. Y. Gu, X. C. Wang, G. Buticchi, S. Bozhko and C. Gerada, “Torque-Performance Improvement for Direct Torque-Controlled PMSM Drives Based on Duty-Ratio Regulation,” IEEE Trans. Power Electron., vol. 37, no. 1, pp. 749–760, 2022.

[212] T. E. Sola, H. J. Chiu, Y. C. Liu and A. N. Rahman, “Improved Direct Torque Control of Induction Motor for Torque Ripple Minimization,” IEEE Access, vol. 10, pp. 131980–131995, 2022.

[213] J. Y. Peng, and M. Yao, “Overview of Predictive Control Technology for Permanent Magnet Synchronous Motor Systems,” Appl. Sci, vol. 13, no. 10, pp. 6255, 2023.

[214] X. G. Zhang and J. Li, “Model Predictive Switching Control for PMSM Drives,” IEEE J. Emerging Sel. Top. Power Electron., vol. 11, no. 1, pp. 942–951, 2023.

[215] X. G. Zhang, C. G. Zhang, C. Xu, and S. W. Fan, “Multimode Model Predictive Control for PMSM Drive System,” IEEE Trans. Transp. Electrif., vol. 9, no. 1, pp. 667–677, 2023.

[216] H. L. Liu, W. Y. Lin, Z. T. Liu, C. Buccella, and C. Cecati, “Model Predictive Current Control With Model-Aid Extended State Observer Compensation for PMSM Drive,” IEEE Trans. Power Electron., vol. 38, no. 3, pp. 3152–3162, 2023.

[217] L. X. Gao, and F. Chai, “Model Predictive Direct Motion Control for Distributed Drive Electric Vehicles,” IEEE Access, vol. 11, pp. 67443–67459, 2023.

[218] X. G. Zhang, and C. G. Zhang, "Model Predictive Control for Open Winding PMSM Considering Dead-Zone Effect," IEEE J. Emerging Sel. Top. Power Electron. , vol. 11, no. 1, pp. 874–885, 2023.

[219] P. Ubare, V. Patne, and D. Sonawane, "Enhancing performance of permanent magnet motor for electric vehicle drives using model predictive control," Proc. Inst. Mech. Eng., Part D: J. Automob. Eng., vol. 9, no. 1, pp. 667–677, 2023.

[220] Q. C. Meng, and G. Q. Bao, "A Novel Low-Complexity Cascaded Model Predictive Control Method for PMSM," Actuators, vol. 12, no. 9, pp. 349, 2023.

[221] J. T. Huang, G. X. Jiang, P. Zhang, J. X. Chen, "A Low Switching Frequency Model Predictive Control Method for an Induction Motor Fed by a 3-Level Inverter," Electronics, vol. 12, no. 17, pp. 3609, 2023.

[222] M. W. Zhao, S. Zhang, X. P. Li, C. N. Zhang and Y. Zhou, "Parameter Robust Deadbeat Predictive Current Control for Open-Winding Surface Permanent Magnet Synchronous Motor Drives," IEEE J. Emerging Sel. Top. Power Electron. , vol. 11, no. 3, pp. 3117–3126, 2023.

[223] S. G. Petkar and V. K. Thippiripati, "A Simplified Predictive Current Control of Open-End Winding Permanent Magnet Synchronous Motor," IEEE Trans. Power Electron., vol. 38, no. 1, pp. 816–826, 2023.

[224] H. F. Li, J. Y. Shao and Z. Y. Liu, "Incremental Model Predictive Current Control for PMSM With Online Compensation for Parameter Mismatch," IEEE Trans. Energy Convers., vol. 38, no. 2, pp. 1050–1059, 2023.

[225] H. Wang, T. Wu, Y. G. Guo, G. Lei, and X. M. Wang, "Predictive Current Control of Sensorless Linear Permanent Magnet Synchronous Motor," Energies, vol. 16, no. 2, pp. 628, 2023.

[226] Z. Y. Sun, S. Xu, G. Z. Ren, C. X. Yao and G. T. Ma, "A Cascaded Band Based Model Predictive Current Control for PMSM Drives," IEEE Trans. Ind. Electron., vol. 70, no. 4, pp. 3503–3514, 2023

[227] L. P. Zhao, B. J. Ge, H. Y. Gao, and D. J. Tao, "Model Predictive Current Control for Dual Three-Phase Permanent Magnet Synchronous Motor Based on Active Disturbance Rejection," J. Electr. Eng. Technol., vol. 18, no. 5, pp. 3721–3732, 2023.

[228] L. W. Luo, F. Yu, L. Ren, and C. Lu, "Parameter-Free Model Predictive Current Control for PMSM Based on Current Variation Estimation without Position Sensor," Energies, vol. 16, no. 19, pp. 6792, 2023.

[229] X. Gu, W. Y. Xu, G. Z. Zhang, W. Chen, and X. F. Jin, "Three-Level Inverter-PMSM Model Predictive Current Control Based on the Extended Control Set," Electronics, vol. 12, no. 3, pp. 557, 2023.

[230] W. Ding, J. L. Li and J. N. Yuan, "An Improved Model Predictive Torque Control for Switched Reluctance Motors With Candidate Voltage Vectors Optimization," IEEE Trans. Ind. Electron., vol. 70, no. 5, pp. 4595–4607, 2023.

[231] W. Zhang, Y. Yang, M. D. Fan, L. Q. He, A. M. Ji, Y. Xiao, H. Q. Wen, X. N. Zhang, T. Yang, S. Mekhilef, and J. Rodriguez, "An Improved Model Predictive Torque Control for PMSM Drives Based on Discrete Space Vector Modulation," IEEE Trans. Power Electron., vol. 38, no. 6, pp. 7535–7545, 2023.

[232] M. S. Mousavi, S. A. Davari, V. Nekoukar, C. Garcia, L. He, F. X. Wang, and J. Rodriguez, "Predictive Torque Control of Induction Motor Based on a Robust Integral Sliding Mode Observer," IEEE Trans. Ind. Electron., vol. 70, no. 3, pp. 2339–2350, 2023.

[233] L. F. Ge, J. X. Zhong, J. L. Huang, N. F. Jiao, S. J. Song and R. W. De Doncker, "A Novel Model Predictive Torque Control of SRMs With Low Measurement Effort," IEEE Trans. Ind. Electron. , vol. 70, no. 4, pp. 3561–3570, 2023.

[234] M. Hassan, X. L. Ge, A. T. Woldegiorgis, M. S. Mastoi, M. B. Shahid, R. Atif, M. S. Shaikh, and S. Kumar, "Research on atmospheric pollutant and greenhouse gas emission reductions of trucks by substituting fuel oil with green hydrogen: A case study," ISA Trans., vol. 138, pp. 670–686, 2023.

[235] M. Karimi, M. A. Rostami, and H. Zamani, "Continuous Control Set Model Predictive Control for the optimal current control of Permanent Magnet Synchronous Motors," Control Eng. Pract., vol. 138, pp. 105590, 2023.

[236] F. X. Wang, Y. Wei, H. Young, D. L. Ke, H. T. Xie and J. Rodríguez, "Continuous-Control-Set Model-Free Predictive Fundamental Current Control for PMSM System," IEEE Trans. Power Electron., vol. 38, no. 5, pp. 5928–5938, 2023.

[237] C. S. Lim, S. S. Lee and E. Levi, "Continuous-Control-Set Model Predictive Current Control of Asymmetrical Six-Phase Drives Considering System Nonidealities," IEEE Trans. Ind. Electron., vol. 70, no. 8, pp. 7615–7626, 2023.

[238] B. Z. Wang, J. Y. Jiao and Z. Y. Xue, "Implementation of Continuous Control Set Model Predictive Control Method for PMSM on FPGA," IEEE Access, vol. 11, pp. 12414–12425, 2023.

[239] X. S. Wu, C. Xue, L. Ding, Z. Y. Quan and Y. W. Li, "Improved Finite Control Set Model Predictive Control for Parallel Dual-Converter-Fed PMSM Drives," IEEE Trans. Ind. Electron., vol. 70, no. 4, pp. 3581–3592, 2023.

[240] M. X. Gu, Y. Yang, M. D. Fan, Y. Xiao, P. Liu, X. A. Zhang, H. Yang, and J. Rodriguez, "Finite Control Set Model Predictive Torque Control With Reduced Computation Burden for PMSM Based on Discrete Space Vector Modulation," IEEE Trans. Energy Convers., vol. 38, no. 1, pp. 703–712, 2023.

[241] H. Kawai, J. Cordier, R. Kennel and S. Doki, "Application of Finite Control Set–Model Predictive Control for Servo Brake Motion in PMSM Drives," IEEE Can. J. Electr. Comput. Eng. , vol. 46, no. 2, pp. 117–129, 2023.

[242] C. Zhou, H. M. Li, L. G. Yang, R. D. Liu, and H. A. Zhao, "Finite Control Set Model Predictive Torque Control Considering Dynamic and Steady-State Control Performance for SMPMSM Drives," IEEJ Trans. Electr. Electron. Eng. , vol. 18, no. 9, pp. 1503–1513, 2023.

[243] A. Brosch, O. Wallscheid and J. Böcker, "Long-Term Memory Recursive Least Squares Online Identification of Highly Utilized Permanent Magnet Synchronous Motors for Finite-Control-Set Model Predictive Control," IEEE Trans. Power Electron., vol. 38, no. 2, pp. 1451–1467, 2023.

[244] T. B. D. Santos, I. Oliani, R. Figueiredo, D. Albieiro, A. Pelizari and A. J. Sguarezi Filho, "Robust Finite Control Set Model Predictive Current Control for Induction Motor Using Deadbeat Approach in Stationary Frame," IEEE Access, vol. 11, pp. 13067–13078, 2023.

[245] H. Kawai, J. Cordier, R. Kennel, and S. Doki, "Model predictive current control with a finite set of novel voltages and modulator in permanent magnet synchronous motor drives," IET Electr. Power Appl., vol. 17, no. 9, pp. 1197–1211, 2023.

[246] M. Pereira and R. E. Araújo, "Model-Free Finite-Set Predictive Current Control With Optimal Cycle Time for a Switched Reluctance Motor," IEEE Trans. Ind. Electron., vol. 70, no. 8, pp. 8355–8364, 2023.

[247] Z. Sun, Y. T. Deng, J. L. Wang, T. Yang, Z. Wei and H. Y. Cao, "Finite Control Set Model-Free Predictive Current Control of PMSM With Two Voltage Vectors Based on Ultralocal Model," IEEE Trans. Power Electron., vol. 38, no. 1, pp. 776–788, 2023.

[248] B. Cao, B. M. Grainger, X. Wang, Y. Zou, G. F. Reed and Z. H. Mao, "Direct torque model predictive control of a five-phase permanent magnet synchronous motor," IEEE Trans. Power Electron., vol. 36, no. 2, pp. 2346–2360, 2021.

[249] W. Chen, S. Zeng, G. Zhang, T. Shi and C. Xia, "A modified double vectors model predictive torque control of permanent magnet synchronous motor," IEEE Trans. Power Electron., vol. 34, no. 11, pp. 11419–11428, 2019.

[250] M. Hassan, X. L. Ge, R. Atif, A. T. Woldegiorgis, M. S. Mastoi, and M. B. Shahid, "Computational efficient model predictive current control for interior permanent magnet synchronous motor drives," IET Power Electron., vol., 15, no. 12, pp. 1111–1133, 2022.

[251] S. J. Zhu, and H. S. Zhang, "Simplified model predictive current control strategy for open‑winding permanent magnet synchronous motor drives," J. Power Electron., vol. 21, no. 6, pp. 911–920, 2021.

[252] D. D. Su, C. N. Zhang and Y. G. Dong, "Finite-state model predictive current control for surface-mounted permanent magnet synchronous motors based on current locus," IEEE Access, vol. 5, pp. 27366–27375, 2017.

[253] L. Gao and T. H. Pan, "Composite Multi-Vector Model Predictive Control for Permanent Magnet Synchronous Motor," 2023 IEEE 12th Data Driven Control and Learning Systems Conference (DDCLS), Xiangtan, China, 2023, pp. 1824–1829, 2023.

[254] J. Z. Qu, J. Jatskevich, C. N. Zhang, and S. Zhang, "Improved multiple vector model predictive torque control of permanent magnet synchronous motor for reducing torque ripple," IET Electr. Power Appl., vol. 15, no. 6, pp. 681–695, 2021.

[255] H. H. Dong, Y. B. Wang, "Multi-vector Robust Model Predictive Current Control for PMSM Based on Incremental Model," J. Electr. Eng. Technol., vol. 18, no. 5, pp. 3657–3669, 2023.

[256] M. S. R. Saeed, W. S. Song, L. Huang and B. Yu, "Double-Vector-Based Finite Control Set Model Predictive Control for Five-Phase PMSMs With High Tracking Accuracy and DC-Link Voltage Utilization," in IEEE Trans. Power Electron., vol. 37, no. 12, pp. 15234–15244, 2022.

[257] D. Jin, H. S. Zhang, S. J. Zhu, A. Wang, J. J. Jiang, "Two-vector predictive current control strategy based on maximum torque per ampere control for PMSMs," J. Power Electron., vol. 22, no. 8, pp. 1313–1323, 2022.

[258] B. Xu, Q. Jiang, W. Ji and S. H. Ding, "An Improved Three-Vector-Based Model Predictive Current Control Method for Surface-Mounted PMSM Drives," IEEE Trans. Transp. Electrif., vol. 8, no. 4, pp. 4418–4430, 2022.

[259] J. H. Ji, S. B. Jin, W. X. Zhao, D. Z. Xu, L. S. Huang and X. Q. Qiu, "Simplified Three-Vector-Based Model Predictive Direct Power Control for Dual Three-Phase PMSG," IEEE Trans. Energy Convers., vol. 37, no. 2, pp. 1145–1155, 2022.

[260] Y. H. Li, J. S. Su, H. Qin, and C. H. Zhao, "Simplified multi-step predictive control for surface permanent magnet synchronous motor," Energy Rep., vol. 6, no. 9, pp. 379–384, 2020.

[261] W. Chen, X. H. Zhang, X. Gu, Y. Yan and T. N. Shi, "Band-Based Multi-Step Predictive Torque Control Strategy for PMSM Drives," IEEE Access, vol. 7, pp. 171411–171422, 2019.

[262] Y. P. Xu, Y. F. Sun, and Y. L. Hou, "Multi-step model predictive current control of permanent-magnet synchronous motor," J. Power Electron., vol. 20, no. 1, pp. 176–187, 2020.

[263] Y. H. Li, X. Y. Wang, Z. K. Liu, G. X. Chen, D. M. Liu and C. Ren, "Simplified Multi-Step Predictive Current Control for Surface Permanent Magnet Synchronous Motor," 2021 IEEE International Conference on Predictive Control of Electrical Drives and Power Electronics (PRECEDE), Jinan, China, vol. 2021, pp. 207–212, 2021.

[264] Z. Y. Chen, J. Q. Qiu and M. J. Jin, "Prediction-error-driven position estimation method for finite-control-set model predictive control of interior permanent-magnet synchronous motors," IEEE J. Emerging Sel. Top. Power Electron. , vol. 7, no. 1, pp. 282–295, 2019.

[265] C. A. Agustin, J. T. Yu, C. K. Lin, and X. Y. Fu, "A Modulated Model Predictive Current Controller for Interior Permanent-Magnet Synchronous Motors," Energies, vol. 12, no. 15, pp. 2885, 2019.

[266] Z. J. Gong, C. N. Zhang, X. Ba, and Y. G. Guo, "Improved deadbeat predictive current control of permanent magnet synchronous motor using a novel stator current and disturbance observer," IEEE Access, vol. 9, pp. 142815–142826, 2021.

[267] C. Bai, Z. G. Yin, Y. P. Zhang, and J. Liu, "Multiple-models adaptive disturbance observer-based predictive control for linear permanent-magnet synchronous motor vector drive," IEEE Trans. Power Electron., vol. 37, no. 8, pp. 9596–9611, 2022.

[268] C. Bai, Z. G. Yin, Y. Q. Zhang, and J. Liu, "Robust predictive control for linear permanent magnet synchronous motor drives based on an augmented internal model disturbance observer," IEEE Trans. Ind. Electron., vol. 69, no. 10, pp. 9771–9782, 2022.

[269] Q. Fei, Y. T. Deng, H. W. Li, J. Liu, and M. Shao, “Speed ripple minimization of permanent magnet synchronous motor based on model predictive and iterative learning controls,” IEEE Access, vol. 7, pp. 31791–31800, 2019.

[270] T. Yang, T. Kawaguchi, S. Hashimoto, and W. Jiang, “Switching Sequence Model Predictive Direct Torque Control of IPMSMs for EVs in Switch Open-Circuit Fault-Tolerant Mode,” Energies, vol. 13, no. 21, pp. 5593, 2020.

[271] L. M. Hou, J. H. Ma, and W. Wang, “Sliding mode predictive current control of permanent magnet synchronous motor with cascaded variable rate sliding mode speed controller,” IEEE Access, vol. 10, pp. 33992–34002, 2022.

[272] C. M. Zheng, J. F. Yang, Z. Gong, Z. Y. Xiao, and X. X. Dong, “Cascade-Free Modulated Predictive Direct Speed Control of PMSM Drives,” Energies, vol. 15, no. 19, pp. 7200, 2022.

[273] J. S. Chen, and Y. Zhang, “Dual-vector model predictive current control of permanent magnet synchronous motor drives with the segment golden search method,” IEEE Access, vol. 8, pp. 183826–183846, 2020.

[274] L. L. Xu, G. M. Chen, and Q. Y. Li, “Ultra-local model-free predictive current control based on nonlinear disturbance compensation for permanent magnet synchronous motor,” IEEE Access, vol. 8, pp. 127690–127699, 2020.

[275] A. Brosch, S. Hanke, O. Wallscheid, and J. Böcker, “Data-driven recursive least squares estimation for model predictive current control of permanent magnet synchronous motors,” IEEE Trans. Power Electron., vol. 36, vol. 2, pp. 2179–2190, 2021.

[276] B. Kiani, S. Soleymani, B. Mozafari, and H. M. Shourkaei, “Model predictive based direct torque control for induction motor drives by sole-evaluation of two parameter independence duty ratios for each voltage vector,” Electr. Power Compon. Syst., vol. 48, no. 19–20, pp. 2019–2036, 2021.

[277] I. M. Alsofyani, and K. B. Lee, “Three-level inverter-fed model predictive torque control of a permanent magnet synchronous motor with discrete space vector modulation and simplified neutral point voltage balancing,” J. Power Electron., vol. 22, no. 1, pp. 22–30, 2022.

[278] R. R. Kumar, and K. Alok, “Adoption of electric vehicle: A literature review and prospects for sustainability,” J. Cleaner Prod., vol. 253, pp. 119911, 2020.

[279] A. Kalair, N. Abas, M. S. Saleem, A. R. Kalair, and N. Khan, “Role of energy storage systems in energy transition from fossil fuels to renewables,” Energy Storage, vol. 3, no. 1, pp. e135, 2021.

[280] L. Mihet-Popa, and S. Saponara, “Toward Green Vehicles Digitalization for the Next Generation of Connected and Electrified Transport Systems,” Energies, vol. 11, no. 11, pp. 3124, 2018.

[281] U. Buenger, and J. Michalski, “The Impact of E-Mobility in a Future Energy System Dominated by Renewable Electricity,” Chem. Ing. Tech., vol. 90, no. 1–2, pp. 113–126, 2018.

[282] M. S. Hossain, L. Kumar, M. E. Assad, R. Alayi, “Advancements and Future Prospects of Electric Vehicle Technologies: A Comprehensive Review,” Complexity, vol. 2022, pp. 3304796, 2022.

[283] Q. Cheok, N. H. Husaini, and M. M. Nauman, “Economic feasibility of electric vehicles: A case study,” Energy Storage, vol. 4, no. 3, pp. e302, 2022.

[284] M. S. Hossain, L. Kumar, M. M. Islam, and J. Selvaraj, “A Comprehensive Review on the Integration of Electric Vehicles for Sustainable Development,” J. Adv. Transp., vol. 2022, pp. 3868388, 2022.

[285] R. Kene, T. Olwal, and B. J. van Wyk, “Sustainable Electric Vehicle Transportation,” Sustainability, vol. 13, no. 22, pp. 12379, 2021.

[286] X. L. Zhao, L. Wang, Y. L. Zhou, B. X. Pan, R. C. Wang, L. M. Wang, and X. Q. Yan, “Energy management strategies for fuel cell hybrid electric vehicles: Classification, comparison, and outlook,” Energy Convers. Manage., vol. 270, pp. 116179, 2022.

[287] D. D. Tran, M. Vafaeipour, M. El Baghdadi, R. Barrero, J. Van Mierlo, O. Hegazy, “Thorough state-of-the-art analysis of electric and hybrid vehicle powertrains: Topologies and integrated energy management strategies,” Renewable Sustainable Energy Rev., vol. 119, pp. 109596, 2020.

[288] C. H. Liu, K. T. Chau, C. H. T. Lee, and Z. X. Song, “A Critical Review of Advanced Electric Machines and Control Strategies for Electric Vehicles,” Proc. IEEE, vol. 109, no. 6, pp. 1004–1028, 2021.

[289] D. G. Barroso, Y. Yang, F. A. Machado and A. Emadi, “Electrified Automotive Propulsion Systems: State-of-the-Art Review,” IEEE Trans. Transp. Electrif., vol. 8, no. 2, pp. 2898–2914, 2022.

[290] Y. Yang, Q. He, C. Y. Fu, S. P. Liao, and P. Tan, “Efficiency improvement of permanent magnet synchronous motor for electric vehicles,” Energy, vol. 213, pp. 118859, 2020.

[291] I. López, E. Ibarra, A. Matallana, J. Andreu, and I. Kortabarria, “Next generation electric drives for HEV/EV propulsion systems: Technology, trends and challenges,” Renewable Sustainable Energy Rev., vol. 114, pp. 109336. 2019

[292] X. S. Hu, J. Han, X. L. Tang, and X. K. Lin, “Powertrain Design and Control in Electrified Vehicles: A Critical Review,” IEEE Trans. Transp. Electrif., vol. 7, no. 3, pp. 1990–2009, 2021.

[293] G. Q. Ma, M. Ghasemi, and X. Y. Song, “Integrated Powertrain Energy Management and Vehicle Coordination for Multiple Connected Hybrid Electric Vehicles,” IEEE Trans. Veh. Technol., vol. 67, no. 4, pp. 2893–2899, 2018.

[294] N. Oswald, P. Anthony, N. McNeill and B. H. Stark, “An Experimental Investigation of the Tradeoff between Switching Losses and EMI Generation With Hard-Switched All-Si, Si-SiC, and All-SiC Device Combinations,” IEEE Trans. Power Electron., vol. 29, no. 5, pp. 2393-2407, 2014.

[295] X. Y. Jia, C. S. Hu, B. T. Dong, F. C. He, H. Wang and D. H. Xu, “System-Level Conducted EMI Model for SiC Powertrain of Electric Vehicles,” 2020 IEEE Applied Power Electronics Conference and Exposition (APEC), New Orleans, LA, USA, 2020, pp. 885–892, 2020.

[296] B. Y. Zhang and S. Wang, “Radiated Electromagnetic Interference Modeling for Three Phase Motor Drive Systems with SiC Power Modules,” 2021 IEEE Applied Power Electronics Conference and Exposition (APEC), Phoenix, AZ, USA, 2021, pp. 2243–2250, 2021.

[297] X. F. Ding, P. Lu, Z. Y. Shan, “A high-accuracy switching loss model of SiC MOSFETs in a motor drive for electric vehicles,” Appl. Energy, vol. 291, pp. 116827, 2021.

[298] Y. S. Wang, H. Guo, T. Yuan, L. F. Ma, and C. C. Wang, “Electromagnetic noise analysis and optimization for permanent magnet synchronous motor used on electric vehicles,” Eng. Comput., vol. 38, no. 2, pp. 699–719, 2021.

[299] X. Y. Jia, C. S. Hu, B. T. Dong, F. C. He, H. Wang, and D. H. Xu, “Influence of system layout on CM EMI noise of SiC electric vehicle powertrains,” CPSS Trans. Power Electron. Appl., vol. 6, no. 4, pp. 298–309, 2021.

[300] M. Rif'an, E. Media's, and H. Firmansyah, “Intelligent control system for high efficiency Electric Vehicles,” IOP Conf. Ser.: Mater. Sci. Eng., vol. 1098, no. 4, pp. 042072, 2021.

[301] M. Didat, C. D. New, S. Choi and A. Lemmon, “Improved Methodology for Conducted EMI Assessment of Wide Band-Gap Power Electronics,” IEEE Open J. Power Electron., vol. 3, pp. 731–740, 2020.

[302] R. J. He, Y. Xu, S. Walunj, S. H. Yong, V. Khilkevich, D. Pommerenke, H. L. Aichele, M. Boettcher, P. Hillenbrand, and A. Klaedtke, “Modeling Strategy for EMI Filters,” IEEE Trans. Electromagn. Compat., vol. 62, no. 4, pp. 298-309, 2020.

[303] T. Ozaki, T. Funaki and T. Ibuchi, “An experimental study on conducted noise emission for PMSM drive with SiC inverter Conducted noise reduction by snubber circuit,” 2017 IV International Electromagnetic Compatibility Conference (EMC Turkiye), Ankara, Turkey, vol. 2017, 1–6, 2017.

[304] J. Hu, X. Xu, D. D. Cao and G. B. Liu, “Analysis and optimization of electromagnetic compatibility for electric vehicles,” IEEE Electromagn. Compat. Mag., vol. 8, no. 4, pp. 50-55, 2018.

[305] H. Rao, B. R. Zhou, F. Zhang, Y. Xu, C. Hong and J. Yang, “Electromagnetic Compatibility of Power Electronic Devices in Electric Vehicle Drive System. 2021 IEEE 4th International Conference on Electronics Technology (ICET), Chengdu, China, vol. 2021, pp. 509–512, 2021.

[306] X. Gong and J. A. Ferreira, “Extracting the parameters of a common mode EMI equivalent circuit model for a drive inverter,” The 2010 International Power Electronics Conference - ECCE ASIA -, Sapporo, Japan. vol. 2010, 892–899, pp. 2010.

[307] K. B. Wang; H. M. Lu, C. C. Chen, and Y. Xiong, “Modeling of System-Level Conducted EMI of the High-Voltage Electric Drive System in Electric Vehicles,” IEEE Trans. Electromagn. Compat., vol. 64, no. 3, pp. 741–749, 2022.

[308] A. Safayet and M. Islam, “Modeling of Conducted Emission for a Three-Phase Motor Control Inverter,” IEEE Trans. Ind. Appl., vol. 37, no. 2, pp. 1202–1211, 2021.

[309] Y. Liu, K. Y. See, S. Yin, R. Simanjorang, A. K. Gupta and J. -S. Lai, “Equivalent circuit model of high power density SiC converter for common-mode conducted emission prediction and analysis,” IEEE Electromagn. Compat. Mag., vol. 8, no. 1, pp. 67–74, 2019.

[310] M. Kumar and K. Jayaraman, “Design of a Modified Single-Stage and Multistage EMI Filter to Attenuate Common-Mode and Differential-Mode Noises in SiC Inverter,” IEEE J. Emerging Sel. Top. Power Electron., vol. 10, no. 4, pp. 4290–4302, 2022.

[311] L. Zhai, G. X. Hu, C. Song, M. Lv and X. Y. Zhang, “Comparison of Two Filter Design Methods for Conducted EMI Suppression of PMSM Drive System for Electric Vehicle,” IEEE Trans. Veh. Technol., vol. 70, no. 7, pp. 6472–6484, 2021.

[312] S. Waffler and J. W. Kolar, “Efficiency Optimization of An Automotive Multi-Phase Bi-Directional DC-DC Converter,” In Proceedings of the IEEE 6th International Power Electronics and Motion Control Conference (IPEMC), Wuhan, China, vol. 2009, pp. 566–572, 2009.

[313] S. Waffler, J. Biela and J. W. Kolar, “Output Ripple Reduction of An Automotive Multi-Phase Bi-Directional DC-DC Converter,” In Proceedings of the IEEE Energy Conversion Congress and Exposition (ECCE), San Jose, CA, USA, vol. 2009, pp. 2184–2190,2009.

[314] Q. Zhang, Y.L. Shang, Y. Li, N.X. Cui, B. Duan, and C.H. Zhang, “A Novel Fractional Variable-Order Equivalent Circuit Model and Parameter Identification of Electric Vehicle Li-Ion Batteries,” ISA Trans., vol. 97, pp.448–457, 2020.

[315] Q. Zhang, N.X. Cui, Y. Li, B. Duan, and C.H. Zhang, “Fractional Calculus Based Modeling of Open Circuit Voltage of Lithium-Ion Batteries for Electric Vehicles,” J. Energy Storage, vol. 27, pp. 100945, 2020.

BIODATA OF STUDENT

Chi Zhang was born at Shaanxi, China in 1996. He received the B.S. and M.S. degrees at the College of Electrical and Control Engineering from Shaanxi University of Science & Technology, Xi'an 710021, China, in 2018 and 2021, respectively. He is currently pursuing toward the Ph.D. degree at the Advanced Lightning, Power and Energy Research Centre (ALPER) within the Department of Electrical and Electronics Engineering in the Faculty of Engineering from Universiti Putra Malaysia, Serdang 43400, Selangor, Malaysia. He is a joint training of PhD candidate in Tsinghua University, Beijing 100084, China. Since 2021, he has been employed with the laboratory of Infineon Technologies AG, Neubiberg 85579, Germany, and ABB Asea Brown Boveri Ltd, Zurich CH-8050, Switzerland. His current research interests include power electronics converter, motor control strategy, electromagnetic interference and compatibility, energy storage systems, SiC MOSFET degradation mechanism and failure analysis.

LIST OF PUBLICATIONS

Journals

Chi, Zhang, Binyue Xu, Jasronita Jasni, Mohd Amran Mohd Radzi, Norhafiz Azis, and Qi Zhang. Model Control and Digital Implementation of the Three Phase Interleaved Parallel Bidirectional Buck–Boost Converter for New Energy Electric Vehicles. Energies, 15(19):7178, 2022. https://doi.org/10.3390/en15197178. (SCIE, JCR: Q3, IF: 3)

Chi, Zhang, Binyue Xu, Jasronita Jasni, Mohd Amran Mohd Radzi, Norhafiz Azis, and Qi Zhang. Three Voltage Vector Duty Cycle Optimization Strategy of the Permanent Magnet Synchronous Motor Driving System for New Energy Electric Vehicles Based on Finite Set Model Predictive Control. Energies, 16(6):2684, 2023. https://doi.org/10.3390/en16062684. (SCIE, JCR: Q3, IF: 3)

Chi, Zhang, Jasronita Jasni, Mohd Amran Mohd Radzi, Norhafiz Azis, and He, Xiangming. A Comprehensive Review of stage-of-the-art Subsystems Configurations, Technical Methodologies, Advancements and Prospects for New Energy Electric Vehicles. Ionics, 29(7): 2529-2547, 2023. https://doi.org/10.1007/s11581-023-05062-3. (SCIE, JCR: Q3, IF: 2.4)

Chi, Zhang, Jasronita Jasni, Mohd Amran Mohd Radzi, Norhafiz Azis, and He, Xiangming. Research and Analysis of Electromagnetic Interference of a Motor Drive Control System Based on PMSM With SiC MOSFET for New Energy Electric Vehicles. Frontiers in Energy Research, 11:1338212, 2023. https://doi.org/10.3389/fenrg.2023.1338212. (SCIE, JCR: Q3, IF: 2.6)

Chi, Zhang, Jasronita Jasni, Mohd Amran Mohd Radzi, Norhafiz Azis, and He, Xiangming. Influence Analysis and Countermeasure Research of Motor Drive Control System under High Switching Frequency with Silicon Carbide (SiC) MOSFET for New Energy Electric Vehicles. Edelweiss Applied Science and Technology, accepted. (Scopus)

Chi, Zhang, Jasronita Jasni, Mohd Amran Mohd Radzi, Norhafiz Azis, and He, Xiangming. A Comprehensive Review of the Current Landscape and the Impending Advancements for Energy Storage Systems. Energy Technology, under review. (SCIE, JCR: Q3, IF: 3.6)

Chi, Zhang, Jasronita Jasni, Mohd Amran Mohd Radzi, Norhafiz Azis, and He, Xiangming. Degradation Mechanism and Failure Analysis on the Gate Oxide and Body Diode of SiC MOSFET under Repetitive Power Cycling Stress. Journal of Power Electronics, under review. (SCIE, JCR: Q3, IF: 1.3)